Imperial College London

Investigating the role of chemotaxis in the natural source zone depletion of petroleum hydrocarbons

By Cameron William Michael Murphy

A thesis submitted for the degree of Doctor of Philosophy (PhD) in Sustainable Civil Engineering, Environmental and Water Resources Engineering Section

Department of Civil and Environmental Engineering, Imperial College London

June 2023

Supervisors: Adrian P. Butler, Po-Heng Lee, Claire E. Stanley, Geoffrey J. Puzon and Matthew J. Morgan

Declaration of originality

All materials presented in the accompanying work is entirely my own work except where explicitly and individually indicated, and that all sources used in its preparation and quotations are clearly cited.

Copyright Declaration

The copyright of this thesis rests with the author. Unless otherwise indicated, its contents are licensed under a Creative Commons Attribution-Non Commercial 4.0 International License (CC BY-NC). Under this license, you may copy and redistribute the material in any medium or format. You may also create and distribute modified versions of the work. This is on the condition that: you credit the author and do not use it, or any derivative works, for a commercial purpose. When reusing or sharing this work, ensure you make the licence terms clear to others by naming the licence and linking to the licence text. Where a work has been adapted, you should indicate that the work has been changed and describe those changes. Please seek permission from the copyright holder for uses of this work that are not included in this licence or permitted under UK Copyright Law.

Abstract

Industrial sites contaminated by petroleum hydrocarbons present complex groundwater challenges and environmental risks. Remediation efforts are costly and efficiencies vary over time. Natural source zone depletion (NSZD) involves the gradual degradation of petroleum hydrocarbons through biogeochemical processes. Microbes aid in this degradation, utilising chemotaxis to move towards hydrocarbon sources. This thesis investigates the distribution and interactions of chemotactic and hydrocarbon degrading (CD) microbes through field and laboratory studies. The first study utilised predictive metagenomic profiling (PMP) and ecological analysis to infer functionality and the spatial relationships existing within core samples collected from a legacy site. The second study assessed how microbial communities of varying degrees of chemotactic ability might interact, via the creation of genetically engineered *Pseudomonas* strains. This "chemotaxis mutant toolkit" was used in conjunction with a novel quantitative soft-agar swim fluorescent chemotaxis laser scanning assay to investigate microbial interaction and biomobilisation. The first study found that naphthalene drives the occurrence of CD taxa, including members of the *Pseudomonadaceae* family. The second study found that a co-culture of chemotactic and non-chemotactic petroleum hydrocarbon degrading Pseudomonas strains has a significantly greater colony perimeter than an equal biomass of non-chemotactic mutants, therefore potentially carrying greater biodegradation potential. This study also found evidence of microbial interaction and biomobilisation of *P. putida* F1 cheA by *P. putida* F1 due to variations in the fluorescent intensity profiles producing radial distributions atypical of non-chemotactic bacteria. In conclusion, chemotactic and microbial transport parameters within existing NSZD models should be reviewed to accommodate for CD accumulation in areas of naphthalene contamination. Models should also account for the interactions of chemotactic and non-chemotactic microbes that may occur within the subsurface. Thereby providing a more accurate quantification of risk posed by petroleum hydrocarbon contamination to groundwater as well as providing insight into how to design or manage bioremediation strategy.

Acknowledgements

First and foremost, I would like to thank my family and friends for all their resolute support. I express my sincere gratitude to my principal supervisor at Imperial College London, Adrian P. Butler, for his continuous support and guidance throughout my PhD journey. His unwavering supervision has made my time at Imperial College London truly fulfilling, both academically and personally. Secondly, I am immensely grateful to Matthew J. Morgan from the Commonwealth and Scientific Research Organisation (CSIRO) for providing me with invaluable academic and emotional support throughout my PhD. Whether it was during my stay in Perth, WA or my visits to Canberra, ACT, Matthew's presence and guidance has been instrumental to my development as a research scientist. I also extend my heartfelt acknowledgement and appreciation to Geoffrey Puzon for his consistent support, supervision, and laboratory training. Despite the geographical distance, and copious fieldwork, Geoffrey's unwavering commitment to my progress was evident through numerous video calls to my office at Imperial College London, as well as during my year in Perth, Australia.

Additionally, I would like to express my personal thanks to the scientists and staff at CSIRO, including Greg Davis, John Rayner, Yasuko Geste, Tom Walsh, and Trevor Bastow, for their academic and technical support in the field of site geochemistry and sampling. Tom Walsh was also an excellent soundboard for ideas and advice, from both a personal and academic basis. I am also grateful to Mike Donn, Jason Wylie, Melanie Bruckberger, and Robert Woodbury for their assistance in sample processing, and to Suzanne Metcalfe for her support with 16S amplicon sequencing. Kaveh Sookhak Lari's help in assessing the unknowns within existing NSZD models is also acknowledged.

I am deeply appreciative of Claire E. Stanley for her supervision and granting me access to the Department of Bioengineering at Imperial College London. I extend my gratitude to my fifth supervisor, Po-Heng Lee, for his valuable guidance and advice throughout my research. I would also like to thank Angeles Hueso-Gil's

for her enduring support, patience, and genetic engineering advice during our time together in the SynBio Laboratories.

I would like to thank Fionnuala Ni Dhonnabhain, Angela Frederick and Sarah Willis for their assistance in general office tasks, expense claims, and administrative support. Special thanks also go to Chris Cheeseman and Robert Vollum for their training, academic and personal support. I am also grateful to the Environmental and Water Resource Engineering (EWRE) research group, my colleagues in Room 302, and fellow scientists in the SynBio Laboratories. Notably, I would like to extend my personal gratitude and thanks to Duncan Ingram, Gediz Kocaoğlan, Kyler Roy, Kiyan F. Shabestary, Davina Patel, Francesca Smith, Felix Richter, Léa Bernier, and William Newell for their support and group camaraderie, particularly Kyler Roy for his editing of chapter four.

Finally, I express my sincere gratitude to BP Australia for their support in granting site access, which was vital for the success of my investigation.

Dedicated to my late father Dr Anthony Murphy

Contents

1 Introduction **15**

1.1 Petroleum hydrocarbon contamination 16

1.1.1 Health effects 19

1.2 Natural source zone depletion (NSZD) 20

1.3 Brief description of chemotactic function 24

1.3.1 Energy burden of chemotaxis and flagella formation 25

1.3.2 Non-flagella driven chemotactic response mechanisms 27

1.4 Aim and objectives 28

1.4.1 Thesis outline 29

2 Literature review **30**

2.1 Historical review of chemotaxis 30

2.1.1 Examples of microbial chemotaxis 31

2.1.1.1 Metabolism-independent chemotaxis 31

2.1.1.2 Metabolism-dependent chemotaxis and other taxis types 34

2.1.2 Further historical advances in chemotaxis research 36

2.2 Chemotaxis assays at microcosm and field scales 38

2.3 Computational modelling 40

2.4 Community dynamics and plasmid exchange 41

2.4.1 Chemotactically enhanced NSZD and chemotactically assisted biomobilisation 45

3 Field-based study **49**

3.1 Authorship Statement 49
3.2 Introduction 50
3.3 Field study at legacy site and biostatistics 52
3.3.1 Summary of field study plan and design 52
3.3.2 Overview of the site and chemical analysis 53
3.4 Materials and methods 54
3.4.1 Site description and soil core recovery 54
3.4.2 Petroleum hydrocarbon chemical analysis 57
3.4.3 16S rRNA gene amplification and bioinformatics 57
3.4.4 Predictive metagenomic profiling 59
3.5 Results 60
3.5.1 Molecular ecology, genetic diversity and statistical analysis . . 60
3.5.2 Alpha diversity analysis 62
3.5.3 Community composition analysis 63
3.5.4 Beta diversity analysis 65
3.5.5 Environmental drivers of community structure and CD group OTU distribution 66
3.6 Discussion 69
3.6.1 The role of predicted chemotactic and hydrocarbon degrading communities in NSZD 69
3.6.2 Community connections between CD and D group microbes . 72
3.6.3 Relevance of the microbial interaction triggering a shift in the *Geobacteraceae* distribution within the subsurface 73

4 Methods of bioengineering bacteria and development of a novel quantitative soft-swim fluorescent chemotaxis laser scanning assay (qSS-FCLSA) 75

4.1 Introduction 75
4.2 Laboratory set-up, safety and microscopy 77
4.3 Microbial strains, construction of mutants and preparation 78

4.3.1 Construction of the chemotactic *P. putida* F1 mScarlet-I (pMRE135) and the non-chemotactic *P. putida* F1 cheA mScarlet-I (pMRE135) mutants . . . 81
4.3.2 Construction of non-chemotactic and non-motile *P. putida* F1 cheA ΔfliM mScarlet-I (pMRE135) mutants . . . 83
4.3.2.1 Construction of the pEMG-fliM plasmid . . . 83
4.3.2.2 Deletion of the fliM gene . . . 89
4.4 Chemotaxis assay development and testing . . . 93
4.4.1 Agarose in-plug assays . . . 93
4.4.1.1 Agarose in plug-assays: imaging and example assay . 96
4.4.2 Fungal-fungal interaction (FFI) device . . . 96
4.4.2.1 Fungal-fungal interaction (FFI) device: imaging and example assay . . . 99
4.4.3 Gene frame agarose in-plug assays . . . 100
4.4.3.1 Gene frame agarose in-plug assays: imaging and example assay . . . 102
4.4.4 Novel quantitative soft-swim fluorescent chemotaxis laser scanning assay (qSS-FCLSA) . . . 102
4.4.4.1 Novel quantitative soft-swim fluorescent chemotaxis laser scanning assay (qSS-FCLSA): imaging and example assay . . . 104
4.5 Summary of assay development . . . 110

5 Assessing the interaction of chemotactic and non-chemotactic bacteria 112

5.1 Introduction . . . 112
5.2 Material and methods . . . 120
5.2.1 qSS-FCLSA experimental design . . . 120
5.2.2 Microbial interaction and biomobilisation experimental design 122
5.2.3 Statistical methodology and model selection . . . 124
5.3 Results . . . 127

5.3.1 Perimeter results using the qSS-FCLSA . . . 127
5.3.2 Perimeter comparisons . . . 129
5.3.2.1 F1 . . . 129
5.3.2.2 F1 & WT . . . 129
5.3.2.3 cheA . . . 129
5.3.2.4 cheA & WT . . . 129
5.3.2.5 F1 & cheA . . . 129
5.3.2.6 cheA vs. F1 . . . 130
5.3.2.7 cheA & WT vs. cheA . . . 130
5.3.2.8 cheA & WT vs. F1 & WT . . . 130
5.3.2.9 F1 & WT vs. F1 . . . 130
5.3.2.10 F1 & cheA vs. F1 . . . 130
5.3.2.11 F1 & cheA vs. cheA . . . 130
5.4 Intensity curve analysis . . . 133
5.4.1 Mono-culture and co-culture comparisons . . . 133
5.4.2 Microbial interaction and biomobilisation comparison . . . 135
5.4.2.1 Intensity profile (10 mM succinate) . . . 135
5.4.2.2 Intensity profile (1 mM succinate) . . . 136
5.4.2.3 Intensity profile (0 mM succinate) . . . 137
5.5 Discussion . . . 140
5.5.1 Mono-culture treatment comparisons . . . 140
5.5.2 Chemotactic behaviour in carbon low environments . . . 143
5.5.3 Microbial interactions, co-culture comparisons and biomobilisation . . . 145
5.5.4 Evidence of intra-colony biomobilisation . . . 147

6 General discussion **152**

6.1 Summary of key questions and objectives . . . 152
6.2 Unification of the field and laboratory studies . . . 154
6.3 Field and laboratory studies in context with current literature . . . 155

6.3.1 1. Are chemotactic and hydrocarbon degrading bacteria and archaea present at a contaminated petroleum hydrocarbon legacy site undergoing NSZD? . . . 155
6.3.2 2. What environmental factors and hydrocarbons drive the distributions of chemotactic and hydrocarbon degrading bacteria and archaea? . . . 157
6.3.3 3. How do bacteria of varying degrees of chemotactic ability and motility interact with one another? . . . 159

7 Conclusions **162**

7.1 Conclusions of field-study . . . 162
7.2 Conclusions of laboratory-based study . . . 163
7.3 Summary of field and laboratory limitations . . . 164
7.3.1 Data analysis limitations . . . 164
7.3.2 Laboratory limitations . . . 164
7.4 Research recommendations . . . 165
7.4.1 Bioinformatic approaches and future work based on fieldwork 165
7.4.2 Laboratory-based bioengineering approaches . . . 167
7.5 Concluding statement . . . 172

List of Figures

Fig. 1.1 Petroleum hydrocarbon structures

Fig. 1.2 Natural source zone depletion (NSZD) schematic

Fig. 1.3 Key questions and objectives addressed

Fig. 2.1 Chemotactic *E. coli* cell schematic

Fig. 2.2 Schematic of microbial cell conjugation and the transfer of a plasmid carrying genes involved in chemotaxis and hydrocarbon degradation in a contaminated groundwater aquifer

Fig. 3.1 Field study plan and design

Fig. 3.2 Map of sampling sites

Fig. 3.3 Microbial community heatmap

Fig. 3.4 Non-metric multidimensional scaling (NMDS) Bray-Curtis

Fig. 3.5 Distance-based Bray-Curtis constrained redundancy ordination analysis (db-RDA)

Fig. 4.1 Development and testing of chemotaxis assays

Fig. 4.2 Chemotaxis gene order of *P. putida* F1 cheA

Fig. 4.3 Fluorescent colonies under ultraviolet (UV) light

Fig. 4.4 Genetic engineering flow-chart for the deletion of fliM gene from *P. putida* F1 cheA

Fig. 4.5 Synthetically engineered architecture of pEMG-fliM plasmid and the successful deletion of the fliM gene

Fig. 4.6 Agarose in-plug chemotaxis assay

Fig. 4.7 Fungal-fungal interaction (FFI) device chemotaxis assay

Fig. 4.8 Gene frame chemotaxis assay

Fig. 4.9 Novel quantitative soft-agar swim fluorescent chemotaxis laser scanning assay (qSS-FCLSA) development

Fig. 4.10 Other qSS-FCLSA trials using the fluorescence gel scanner

Fig. 4.11 Visualisation of the analysis pathway for the qSS-FCLSA

Fig. 4.12 Assay selection

Fig. 5.1 Biomobilisation mechanisms

Fig. 5.2 Microbial "curtain" enveloping a petroleum hydrocarbon plume

Fig. 5.3 Interactions of chemotactic and hydrocarbon degrading microbes at the contaminant interface

Fig. 5.4 Colony range expansion

Fig. 5.5 Model logarithmic transformation

Fig. 5.6 Linear mixed model batch effect comparison

Fig. 5.7 Raw colony perimeters

Fig. 5.8 Colony radial intensity curve profiles

Fig. 5.9 Colony intensity curve profile comparisons providing evidence for biomobilisation and microbial transport

Fig. 5.10 Schematic comparing expected vs. measured radial intensity profiles

Fig. 5.11 "Tug of war" biomobilisation mechanism

Fig. 6.1 General discussion summary

List of Tables

Table. 3.1 Generalised linear model

Table. 4.1 List of strains and mutants used in this study

Table. 4.2 Plasmids used in this study

Table. 4.3 Primers used in this study

Table. 5.1 *Pseudomonas putida* F1 reference table

Table. 5.2 qSS-FCLSA experimental design

Table. 5.3 Intensity curve profile reference table

Table. 5.4 Linear mixed model treatment comparison using pairwise comparisons of estimated marginal means

Table. 5.5 Linear mixed model strain comparison using pairwise comparisons of estimated marginal means

Table. 5.6 Area under curve (AUC) comparisons for strain and treatments

Table. 5.7 Area under curve (AUC) comparisons providing evidence for microbial interaction and biomobilisation

List of Abbreviations

ATP Adenosine triphosphate

AUC Area under curve

bp Base pairs

BTEX Benzene, toluene, ethylbenzene and xylene

C Chemotactic and non-hydrocarbon degrading taxa

CD Chemotactic and hydrocarbon degrading taxa

CDD Chemotactic and non-chemotactic hydrocarbon degrading taxa

CHD Coronary heart disease

DIET Direct inter-species electron transfer

DNA Deoxyribonucleic acid

DNAPL Dense non-aqueous phase liquids

D Non-chemotactic and hydrocarbon degrading taxa

Fe Iron

g Gravitational force equivalent

LB Lysogeny broth (Miller)

LNAPL Light non-aqueous phase liquids

MCP Methyl-accepting chemotaxis proteins

MCS Multiple cloning sites

Mn Manganese

MRI Magnetic resonance imaging

NA Natural attenuation

NSZD Natural source zone depletion (NSZD)

NCND Non-chemotactic and non-hydrocarbon degrading taxa

OD Optical density

PDMS Polydimethylsiloxane

PMP Predictive metagenomic profiling

PMT Photo-multiplier tube

POI Point of inoculation

PPM Parts per million

qSS-FCLSA Quantitative soft-agar swim fluorescent chemotaxis laser scanning assay

RNA Ribonucleic acid

rRNA Ribosomal ribonucleic acid

rpm Revolutions per minute

TPH Total petroleum hydrocarbon

UNSDG United Nations Sustainable Development Goals

UV Ultraviolet

VOC Volatile organic carbons

WT Wild-type

16S These are components of the 30S subunit (prokaryotic ribosome)

Chapter 1

Introduction

Groundwater provides a vital source of drinking water for many communities worldwide, fast becoming the primary source of water in arid and semi-arid regions (*1*). However this essential resource is vulnerable to contamination, especially with a growing worldwide population, increased industrial expansion and changes in agricultural practices. This has led to the release of various contaminants, such as toxic heavy metals, pesticides, microplastics and petroleum hydrocarbons into the groundwater supply (*2*, *3*). Combined with contamination from natural sources such as the leaching of arsenic from natural mineral deposits, there is a growing global concern and desire to ensure there is a sustainable and safe supply of drinking water worldwide for future use (*4*, *5*).

Extreme climatic variability poses an additional risk, due to the increased need to over-abstract in times of drought and seasonable variability limiting groundwater recharge. This further highlights the importance of maintaining and shielding this resource from contamination (*6*). The following chapter outlines how groundwater can be contaminated by petroleum hydrocarbon compounds and how it is remediated by both abiotic and biotic processes, with a focus on how microbes within the subsurface can assist in the bioremediation process.

1.1 Petroleum hydrocarbon contamination

Petroleum hydrocarbon contamination is a major issue worldwide and could mean the some of the current United Nations Sustainable Development Goals (UNSDG) are not met. These are highlighted in the "Global assessment of soil pollution" report, which list a number of goals directly and indirectly impacted by petroleum contamination (*7–9*). The UNSDGs 1, 2, 3, relate to providing food for all, and achieving "zero hunger", as well as improving human health. Petroleum contamination poses a risk to the attainment of these goals by impacting soil health and in-turn food security. UNSDGs 6, 11, 14, 15 are also directly affected as they relate to providing clean and "safe drinking water" for all, both in cities and the countryside, as well as reducing the impact of contamination on "land degradation and loss of terrestrial" and "aquatic biodiversity" (*7–9*).

Naturally occurring petroleum hydrocarbons originate from the deposition of dead microorganisms, zooplankton and other flora and fauna. This matter has then been deposited within a layer of sedimentary rock, which has then been subsequently encapsulated below an impermeable geological layer and subjected to high pressures and temperatures over millions of years. These petroleum hydrocarbon compounds are generally extracted by production wells and separated into various petroleum products via fractional distillation. It is at this point that they can pose a risk to the surrounding environment (*10*).

Total petroleum hydrocarbons (TPH) can be released into the subsurface in the form of crude oil, diesel fuels and jet fuels and pose a significant risk to the surrounding marine and terrestrial ecosystems (Fig. 1.1) (*10–12*). Crude oils are comprised of short chain alkanes (C_6-C_{10}), as well as monoaromatic hydrocarbon compounds like benzene, toluene, ethylbenzene, and xylenes (BTEX). Crude oil also contains polycyclic aromatic hydrocarbons (PAHs), such as phenanthrene, a prevalent contaminant at legacy sites, with other major sources being the incomplete combustion of fuels. These compounds contain 2 or more aromatic rings. The structure of phenanthrene, along with other common petroleum hydrocarbon compounds are

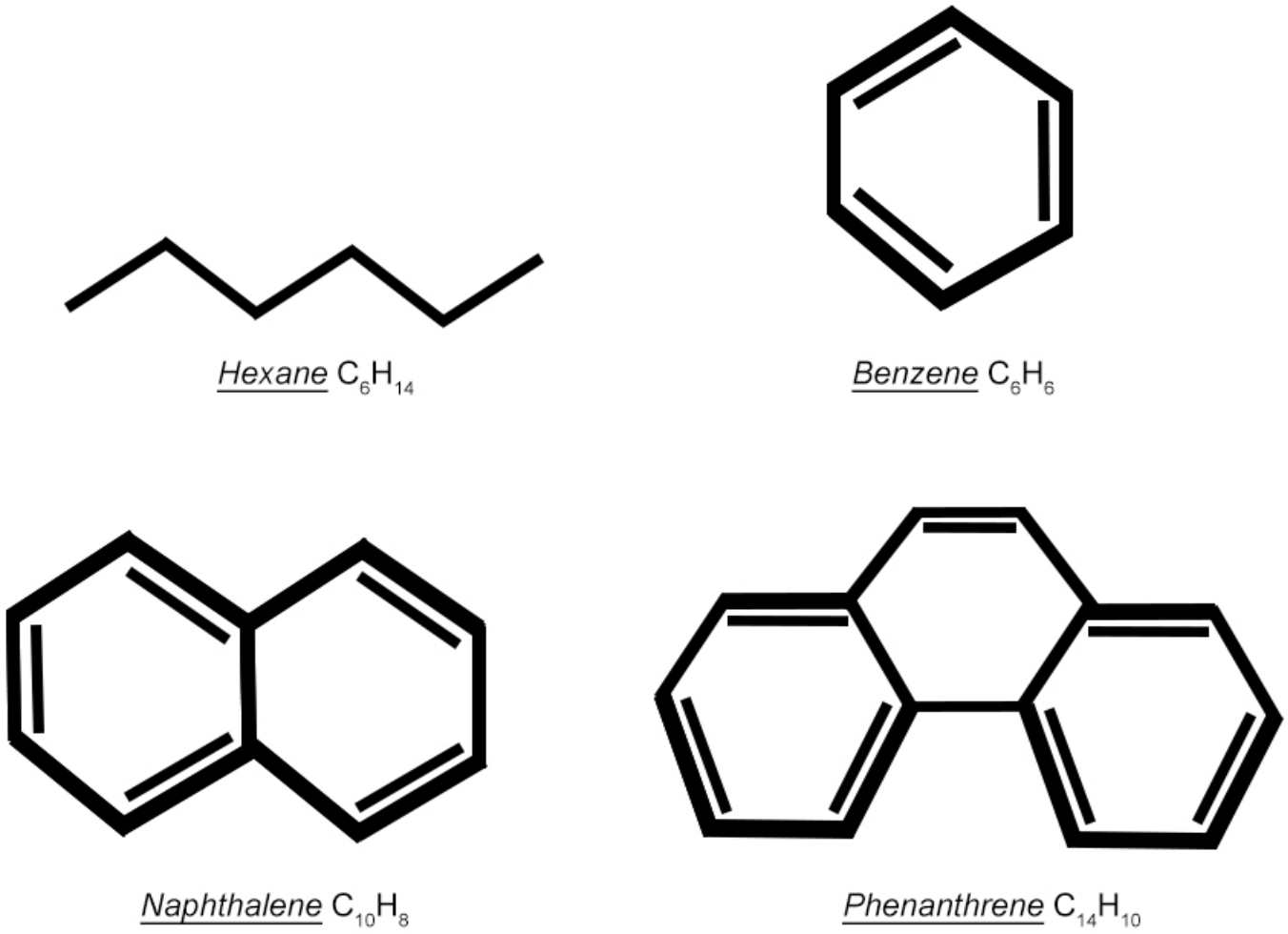


Fig. 1.1. Petroleum hydrocarbon structures. Chemical structures of petroleum hydrocarbon compounds; hexane, benzene, naphthalene, and phenanthrene.

shown in figure 1.1 (Fig. 1.1) (*13–15*). In contrast, diesel range fuels contain longer carbon chained alkanes (C_{10}-C_{40}) and effectively no BTEX. Diesel range fuels also contain paraffin (C_nH_{2n+2}) and some PAHs. Jet fuels generally contain 10 to 16 carbon atoms, as well as numerous additives to ensure stability (*10*, *16*, *17*). These oils and fuels are all generally described as being light non-aqueous phase liquids (LNAPLs), with densities less than that of water (*18*). Coal tar and extra heavy crude oil fractions are examples of dense non-aqueous phase liquids (DNAPLs), due to their densities being greater than that of water (*19*).

Leakages or spills from refined petroleum hydrocarbons are the most common cause of petroleum hydrocarbon contamination, as the spills permeate the neighbouring

soil, migrating downward towards the water table and putting the groundwater supply and health of the surrounding ecosystem and population at risk (*11*, *20*). It has been reported that 30 % of spills are caused by human error, including poor operations, handling of materials and substandard maintenance, with other causes being lightning, static electricity and structural failure (*21*). Groundwater contamination differs from surface water contamination as it is harder to assess the total extent of the contamination plume below the surface and therefore more difficult to assess the most efficient remedial measures (*11*).

LNAPLs pose a significant contamination risk, due to the fact that their free-phase layer can partition between air and water phases and reside on the top of the capillary fringe, thereby allowing for the lateral proliferation of contaminants within the subsurface (*22*). The density of DNAPLs means they often fall below the water table, descending laterally along downward sloping strata to regions of lower permeability until they are trapped or advance further downwards through a more permeable feature, such as fracture, making the total volume of contamination and extent of contamination plume difficult to gauge. The extent of a petroleum hydrocarbon spill is often estimated by measuring the distance from the source to the farthest edge of the contamination plume. Plumes have been calculated reaching ca. 64 m, from underground storage tanks in Los Angeles, CA, with a contamination plume 270 m in diameter and 350 m in length being measured around ruptured diesel storage tanks at a train station in Yogyakarta City, Indonesia. In Perth, Western Australia, petroleum leaked from a subsurface fuel storage tank and entered the groundwater, travelling further than 400 m horizontally from the service station (*23*). Kilometer scale contamination plumes have also been recorded, such as in the case of the "Deepwater Horizon" subsurface hydrocarbon spill, with a plume ranging from 22-35 km (*24*, *25*). This variance in plume extent highlights the site-specific nature of contamination plumes and that a myriad of factors such as the geology and composition of the spill (e.g. LNAPL/DNAPL ratio) govern the extent of a contamination plume (*26–28*).

Enhanced climatic variability can also trigger a change in the contamination profile of previously localised pockets of hydrocarbon, which initially did not pose a threat by altering their distribution through fluctuations in the water table level (*1*, *29*). The need for more drinking water wells and irrigation systems, in periods of drought further highlights this emerging risk (*1*, *29*). These factors makes NAPLs generally very difficult to remediate and as well as increasing the risk of human exposure (*30*, *31*).

1.1.1 Health effects

Petroleum hydrocarbons that enter the groundwater system can pose a significant risk to human health, with their levels being restricted by various laws depending on the country and environment in which they are found (*32*). It is also important to note that the toxicological effects of just a small fraction of these compounds are characterised, thereby limiting the knowledge of the plethora of health effects associated with individual petroleum compounds (*20*, *33*).

Acute short-term exposure to ethylbenzene, for example, over a period of around 15 minutes can lead to dizziness and chest constriction, whilst exposure over longer timescales can lead to changes in blood lymphocyte levels in humans, and possibly cancer (*34*, *35*). Another dangerous NAPL compound, naphthalene, can cause hemolytic anemia in children, as well as a myriad of other serious health effects and is prevalent in petroleum hydrocarbon contaminated sites globally (*36–38*). Hypertension, a key risk factor in coronary heart disease (CHD), is a commonly reported effect of worker exposure during clean-up at spill sites, due to release of volatile organic carbons (VOC). PAHs have been recorded crossing the placenta blood barrier, with their metabolites being found in breast-milk. Both of these have the potential to cause developmental issues (*39*, *40*).

These compounds also have the ability to inhibit the development of terrestrial ecosystems, altering the health and growth of plants by modulating their salt in-

take. This causes errors in the plants natural metabolic function, resulting in the deficiency of nutrients and chlorophyll, ultimately deforming the plants and altering the hydraulic conductivity of the soil (*20*).

These factors along with their carcinogenic risk profile and ability to enter the essential groundwater supply make petroleum hydrocarbon contamination remediation an essential avenue of research worldwide (*33*, *38*, *41*, *42*).

1.2 Natural source zone depletion (NSZD)

Many engineering techniques, such as air-sparging and solvent washing, have been developed to deal with contaminated sites, in order to hinder the spread of contaminants and facilitate their removal from groundwater (*10*, *43–46*).

Air-sparging involves the injection of air at high pressures below the lowest extent of the contamination plume (*47*). This air then rises through the saturated pores, interacting with the existing NAPL contaminants, creating a transient state, with air filling the existing pore space (*47*). The trapped contaminants in the soil matrix which coat the pores then diffuse into the injected air and are removed from the saturated zone by advection for further degradation processes (*47*). This process however, requires sophisticated equipment, which can be expensive and is highly site specific (*48*). Solvent washing on the other hand works by flushing solvents mixed with water to remove NAPLs from contaminated pores, working most effectively with hydrophobic organic contaminants. However, the more efficient solvents are often expensive (*49*, *50*).

An alternative, sustainable, and low cost approach is to utilise biological and abiotic processes naturally present in the subsurface, to breakdown these compounds into less hazardous and ultimately benign substances. This *in situ* natural degradation of petroleum hydrocarbon contamination is known as natural source zone depletion (NSZD) (*10*, *31*, *43–46*, *51*). This involves the partitioning of LNAPLs, with some

DNAPL components, into other phases (soil, water, and air) and their degradation into less harmful and hazardous compounds by biogeochemical reactions, with natural attenuation (NA) generally being used to describe exclusively the biological degradation (*31*, *52*, *53*).

Owing to the high cost of engineered contamination clean-up practices, it is extremely important to rigorously evaluate the cost of site specific remediation methods (*51*, *54*). In Houston, Texas, USA for example, NSZD reportedly saved $12 million when it was chosen as the preferred remediation option for a petroleum contaminated "French Limited Superfund Site" waste site in Harris County, Texas, over conventional pump-and-treat industrial practices. NSZD is also being used at other petroleum hydrocarbon spill sites, such as Bemidji, Minnesota (*10*, *43–46*, *55*).

NSZD processes become increasingly important over time, as products weather and decay, with the indigenous microbes playing a key role in the remediation of remaining and recalcitrant contaminants. This long established bioremediation technique has recently become increasingly favoured over more traditional industrial practices (*32*, *51*, *56–60*).

NSZD relies on natural groundwater dissolution and biodegradation mechanisms, which are governed by effective solubility, availability of electron acceptors and groundwater flow in the vicinity of contamination sources (*31*, *44*, *61*, *62*). Chemical reactions and physical mechanisms such as, volatilisation and dissolution, also assist in the NSZD of volatile petroleum compounds at the outset of a contamination event (*31*). Measuring the abundance of electron acceptors in the soil is commonly used as a tool to measure the rate of NSZD, along with emissions of soil gas and pilot site testing (*54*). Oxygen consumption gradients are generally calculated to assist in this process, with carbon traps also used to calculate carbon dioxide flux in conjunction with carbon-14 analysis (*54*). A thermal profile of can also be used to monitor the heat generated from the biodegradation processes (Fig. 1.2) (*54*, *63*, *64*).

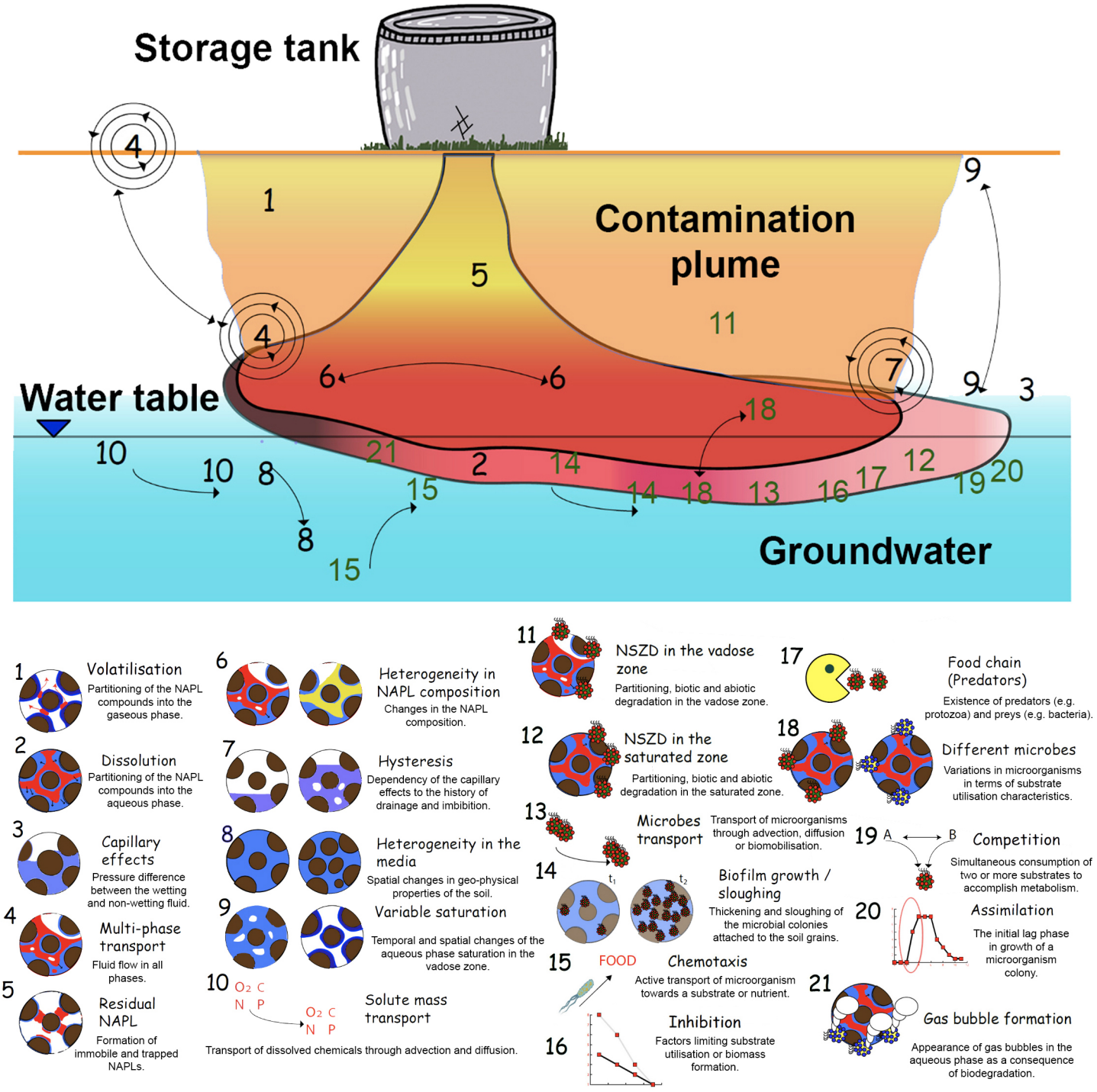


Fig. 1.2. Natural source zone depletion (NSZD) schematic. Brief description of the abiotic and biotic processes which control NSZD. The figure shows a fracture in a petroleum hydrocarbon stage tank, with the contamination plume originating from the source of the leak (After Lari et al., (2019)).

There is a myriad of other factors which have been shown to contribute to NSZD these are shown in figure. 1.2 (*31*). These NSZD processes can be divided into 4 groups; physicochemical processes governing fluid transport, partitioning and compositional changes of the NAPLs, reactions and processes in the vadose zone and groundwater, and microbiological processes (*31*). Rivett and Sweeney (2019) wrote a short technical bulletin further outlining NSZD, which contains some helpful visual aids, of the processes involved (*65*). The microbial degradation of the BTEX petroleum hydrocarbon compounds is usually carried out by multi-component enzymatic, hydrolytic, mono-oxygenase and di-oxygenase systems. Mono-oxygenase, uses one oxygen atom, whilst di-oxygenases uses two oxygen atoms to cleave the aromatic rings, with lycolipids and hydrolytic enzymes excreted from the cells also playing a role (*66*). This results in pyrocatechols and 2-hydroxy-substituted compounds respectively, which are channeled into the TCA cycle via a range of pathways (*67*). Anaerobic BTEX degradation utilises other pathways such as hydroxylation, methylation, carboxylation and the reduction of the benzene ring following transformation of the central aromatic intermediate benzoyl-CoA and ring cleavage, with anaerobic and aerobic communities potentially coexisting (*68*, *69*). Degradation by oxidoreductase families are key to the degradation of recalitrant hydrocarbons. Bacteria carry the oxidoreductase cytochrome P450, this enzyme plays a key role in biodegradation, however it is less effective with high molecular weight PAHs (*70*).

This thesis will focus on microbial processes, specifically chemotaxis (No. 15) and its interlinked role with microbial transport (interaction) and biomobilisation (No. 13). Chemotaxis has recently been highlighted as a parameter within NSZD in need of further investigation and quantification, if the NSZD of petroleum hydrocarbons is to be fully quantified and modelled (Fig. 1.2) (*31*). The current microbial transport parameter within NSZD traditionally focuses on advection and diffusion of cells, with this thesis aiming to investigate transport of a more biotic nature as chemotactic cells interact with other non-chemotactic cells. Therefore, this transport effect is commonly refereed to as microbial interaction and/or biomobilisation throughout the thesis (*31*).

1.3 Brief description of chemotactic function

Chemotaxis has recently been highlighted as a biodegradation mechanism which needs to be understood in more detail to fully quantify its impact on NSZD (Fig. 1.2) (*55*). This biological function grants certain microorganisms the ability to transport themselves in response to a chemical concentration gradient and enhance NSZD (*71–74*). This is defined as movement towards or away from a chemical source (*75*). Generally, movement is in one direction, with the organisms rapidly rotating their flagella via an ion flux motor. The flagella are leash like appendages that have a diameter of around 20 nm (*71*, *76–78*).

Pseudomonas putida cells can have several flagella in a polar lophotrichous arrangement on the anterior of the cell, the cells flagella work together determining if the cell "runs" or "tumbles" (*79*, *80*). A counter-clockwise rotation aligns the flagella and bunches them together, allowing the bacteria to swim in a straight line, whilst a clockwise rotation de-couples the flagella, thereby causing the bacteria to tumble into place, with the direction of rotation being down the flagella towards the cell (*81–85*).

Various flagella arrangements and swim patterns exist (*76*). *Spirillum volutans*, has a polar flagella arrangement, with flagella on both poles of the cell (*76*). *Rhizobium leguminosarum*, a bacteria which is prevalent in soil systems, does not control directional movement via changing flagella rotation direction, rather direction is controlled by rate of clockwise rotation (*86*). This is perhaps related to an evolutionary adaption to swimming in viscous fluids in the soil and aids them when swimming in contaminated environments (*86*). Some *Rhizobium leguminosarum bv. trifolii* strains for example, have been inferred to form a symbiotic association with plant root systems and assist in the degradation of the petroleum hydrocarbon, chrysene (*87*). If the chemotactic microbes become trapped in the pore space, they must re-organise their flagella to break-free or come back in the way they came, with their general movement being more akin to "hopping" and a Lévy walk with rests (*52*, *88*).

Microbial species that exhibit chemotaxis-assisted hydrocarbon degradation have been shown to enhance the rate of NSZD in column and microcosm experiments (*89–91*). In a laboratory experiment, a chemotactic *Pseudomonas putida* G7 (PpG7) strain degraded 90 % of naphthalene in six hours, compared to 30 hours for a non-chemotactic mutant strain and a non-motile mutant strain. This was hypothesised to be due to improved bioaccessibility attributed to chemotaxis (*91*). Indigenous microbes present in the subsurface have been reported to possess the ability for chemotactic assisted petroleum hydrocarbon biodegradation, such as; *Alcaligenaceae* to alkanes extracted from a crude oil-polluted seawater in Daya Bay, South China Sea and other PAHs isolated from a contaminated refinery in Mathura, India (*92*, *93*). Exploitation of this chemotaxis mechanism to manipulate microbe-driven NSZD could therefore have far reaching bioremediation potential at sites undergoing NSZD (*89–91*).

1.3.1 Energy burden of chemotaxis and flagella formation

Flagella bundles in *E. coli* rotate at a rate of ∼130 Hz, with the cell swimming at ∼25 μm s^{-1}, with other microbes such as *P. putida* recorded at higher swim speeds of ∼44 μm s^{-1} (*76*, *94*). The shape of the cell and how elongated it is also controls the degree of chemotactic response, and ultimately its speed (*95*). The energy burden of a chemotactic response by *E. coli* is estimated to be $10^3 - 10^4$ ATP s^{-1} from *in vivo* baseline measurements and an additional 10^3 ATP s^{-1} for sensory adaptation (*96*). The cell's propulsion has an energy requirement of $10^4 - 10^6$ ATP s^{-1}. This means that at high speeds chemotaxis is thought to only require a small increase in energy cost relative to the energy required for propulsion. However, at moderate speeds of ∼25 μm s^{-1} the burden of propulsion and chemotaxis is comparable (*96*). Chemotactic response thresholds vary depending on microbe (archaea or bacteria) and attractant types, with chemoattractant thresholds on the order of mM or μM and distances of μ, mm, and cm (*97–100*). For example *E. coli* cells can detect attractants at a distance of 0.6 mm, from the tip of a capillary tube, containing 1 mM of the attractant aspartate which formed a gradient of steepness 0.02 mM at a mean

concentration of around 8μM (*99*, *100*). Recent research has also investigated the metabolic cost and energy burden of flagella formation and chemotaxis. Expression of motility and chemotaxis proteins accounts for around 2-4 % of the total cellular expressed proteins, these proteins could be expressed in other processes that lead to improved growth rates, therefore a trade-off between growth and motility can thus be hypothesised (*96*).

An experimental study by Ni et al., (2020) at the Max Planck Institute for Terrestrial Microbiology found that a motile and chemotactic *E. coli* wild-type (WT) was outcompeted by a chemotactic *E. coli* ΔflhC mutant, completely devoid of motility in a well-mixed liquid environment containing an attractant (glucose or ribose), the same occurred in a non-stirred environment (*101*). As the quality and source of the carbon and attractant decreased in the co-culture the fraction of *E. coli* WT cells decreased (with ribose being of a higher quality carbon source compared to glucose). A similar result also occurred when a co-culture of *E. coli* wild-type (WT) and a *E. coli* ΔfliC mutant, which only lacks the flagella protein flagellin was undertaken. The metabolic cost of biosynthesis of the flagella is thought to be the primary reason for this (*96*, *101*). Therefore, during periods of starvation, motility would become the overriding source of energy consumption, with prolonged starvation leading to a decrease in the total number of motile cells (*96*). This may be part of an energy saving mechanism, with some microbes being able to disrupt flagella function via the binding of proteins to the flagella motor switch, thereby giving microbes the ability to actively turn on and off motility (*102*).

Given the energy burden associated with flagella formation and their diversity in function. It is essential to develop mutants of varying degrees of chemotactic ability and motility, to investigate how they interact with each other in the presence of a chemical gradient. This would provide a clearer pictures as to how chemotactic cells may respond to petroleum hydrocarbon contamination in real-world porous environments.

1.3.2 Non-flagella driven chemotactic response mechanisms

It is also important to note that, chemotactic movement does not have to be driven by the rotation of flagella; gliding, twitching, and sliding are alternative mechanisms of chemotactic movement. *Flavobacterium johnsoniae*, for example, exhibits a gliding response by the helical cycling of adhesion proteins along the substratum of the cell, to propel themselves forward (*76*). Some *Pseudomonas* and *E. coli* utilise type IV pili fibers for chemotactic movement via twitching and sliding. These are 5-7 nm fibers that can be used for motility. Type IV pili can extend, tether and retract across surfaces much like a rock climber abseiling, often in conjunction with thin curli fibers which aid with cell adhesion (*76*, *103*, *104*). It is these type IV pili that play a pivotal role in the chronic viral infections such as cystic fibrosis (*105*).

Other microbes favour the use of fungal networks over flagella, they use these intricate networks created by fungi and hyphae to speed-up movement towards chemoattractants and other nutrients (*106–110*). Bacteria have been shown to use the hyphae to cross air gaps, with movement generally occurring inside the hyphae. However, the bacteria are also thought to move on the outside of the fungal hyphae, on a thin fluid film (*107*, *110*, *111*). The bacteria *Paraburkholderia terrae* BS001 have been shown to travel 2.6 mm/day in combination with the hyphae of the saprotroph *Lyophyllum sp.* strain Karsten, this provides an idea of the scale of the transport. Another fungus the oomycete *Pythium ultimum* has been shown to transport *Pseudomonas putida* PpG7 and provide improved access to areas of phenanthrene contamination (Fig. 1.1) (*97*, *112*, *113*). These mechanisms are worthy of further experimental and field observations, however they are outside the scope of this thesis.

The next section provides an outline of the principal aim of the thesis and its structure. It is followed by a chapter focusing on the historical review of chemotaxis.

1.4 Aim and objectives

The overarching aim of this thesis to determine the key petroleum compounds, environmental variables, and microbial interactions which shape the distribution of chemotactic and hydrocarbon degrading microbes. The key research questions and associated objectives are outlined in figure 1.3 (Fig. 1.3). The introductory chapter outlined the role of chemotaxis in the NSZD of petroleum hydrocarbons. This thesis aims to answer three key questions which can improve the understanding of NSZD; **1.** Are chemotactic and hydrocarbon degrading bacteria and archaea present at a contaminated petroleum hydrocarbon legacy site undergoing NSZD? **2.** What environmental factors and hydrocarbons drive the distributions of chemotactic and hydrocarbon degrading bacteria and archaea? **3.** How do bacteria of varying degrees of chemotactic ability and motility interact with one another?

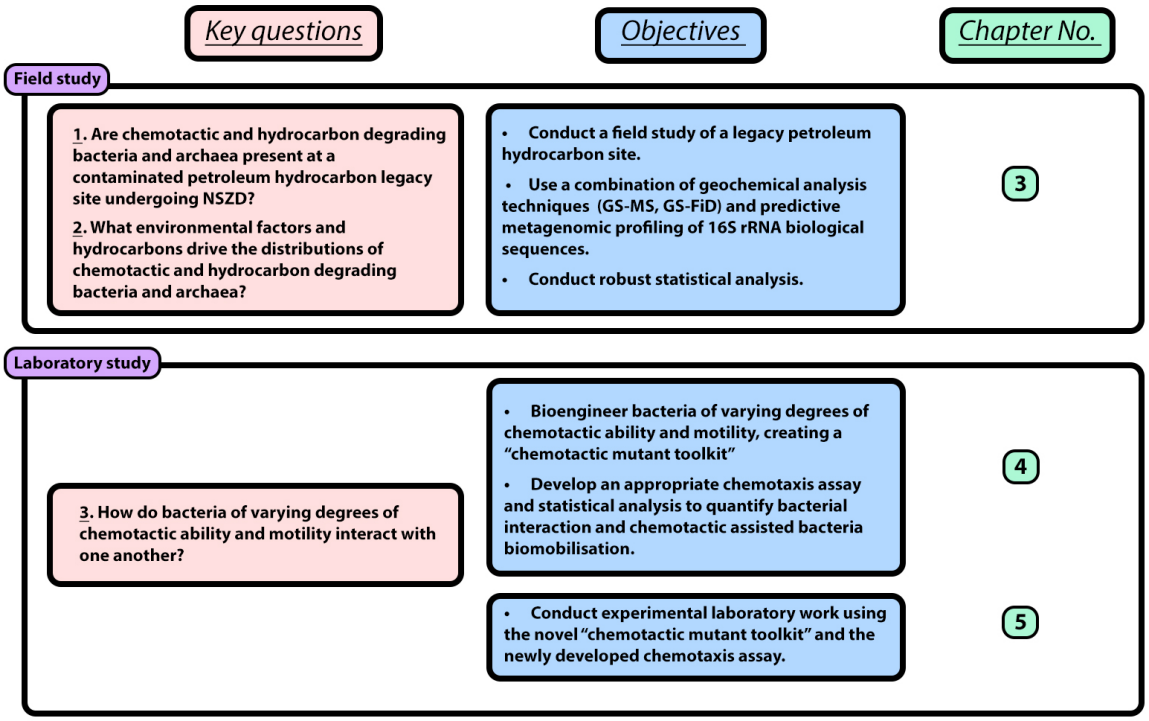


Fig. 1.3. Key questions and objectives addressed.

1.4.1 Thesis outline

The introductory chapter outlined the role of chemotaxis in the NSZD of petroleum hydrocarbons, this is followed by a historical literature review of chemotaxis and chemotactically assisted biomobilisation in chapter two. This review explores the initial discovery of the phenomenon and provides further details on: chemotactic function and variety, the development of chemotactic assays, and the evolution of computational and modelling techniques. In addition, the role of chemotaxis on plasmid transfer and community dynamics within the subsurface is assessed. The third chapter addresses key questions **1.** and **2.** with regards to the distribution of chemotactic and hydrocarbon degrading bacteria and archaea at a legacy petroleum hydrocarbon site undergoing NSZD by means of a field-based study (Fig. 1.3).

The fourth chapter outlines the methods for the development of novel chemotaxis assay, along with the bioengineering of bacteria required to answer question **3.** Subsequently the fifth chapter outlines the results of the experimental study and its outcomes, with regards to bacterial interaction and chemotactically assisted biomobilisation. Chapter six provides a general discussion of the field and laboratory-based studies and how they relate to current literature, with chapter seven highlighting the thesis conclusions and some of the limitations with the current work, which leads on to further research recommendations.

Chapter 2

Literature review

2.1 Historical review of chemotaxis

Chemotaxis was first witnessed by the Dutch pioneering scientist Antonie Philips van Leeuwenhoek (*10*, *73*, *114*). Dubbed the "Father of Microbiology", he was puzzled by the movement and swarming of bacteria within pepper-water in 1676, it is suspected this was chemotactic response (*10*, *73*, *114*).

The first systematic studies which provide evidence of bacterial swimming motility and preferential community banding towards a food source, did not appear until 1881-1884, with Pfeffer publishing his pioneering work on chemotaxis in 1884 (*73*, *114*, *115*). *Bacillus termo* and *Spirillum undula* bacteria were suspended in solution with a capillary tube partially filled with a chemoattractant inside, with the initial concentrations being 1 % meat extract or 1 % asparagine (*73*). A chemical gradient was therefore formed by the diffusion of the attractant, which drew the bacteria to the mouth of the tube and later inside (*73*).

Different scenarios and chemoattractants were tested, with bacterial movement being seen in seconds. However, when the bacteria *S. undula*, were exposed to a mixture of 1 % meat extract and 4 % potassium nitrate, the chemotactic response was subdued by the toxicity of the potassium nitrate (*73*). Pfeffer's work also highlighted for the first time that in some situations chemicals were attractants at one concentration and repellents at another, as well as the fact that attraction occurred even if the

media could not support growth (*73*).

Henry Harris further developed quantitative and qualitative methods to analyse bacterial chemotaxis during the second half of the 20^{th} Century (*116*, *117*). It wasn't until 1969 that significant advances were made, with researchers investigating if bacteria detected the attractants themselves or if their response was due to a chemical gradient of a metabolite involved in the adenosine triphosphate (ATP) or Kerbs cycle, as they degraded the attractant (*114*). The latter was ruled out, due to several factors: a) some extensively metabolised chemicals are not attractants, b) some essentially non-metabolisable chemicals attract bacteria, c) bacteria can be attracted to chemicals even in the presence of metabolisable non-attractable chemicals, d) chemical attractants, which are similar in structure, compete with one another, but not with structurally unrelated attractants, e) the transport of chemicals into the cells themselves is not necessary for it to attract, and f) the fact that mutant bacteria which lack a chemotactic detection mechanism can still be isolated if they metabolise normally (*73*, *114*, *118*, *119*).

Julius Adler, the American biochemist and geneticist, discovered that the above statements can be explained by the fact that bacteria sense attractants and repellents using chemoreceptors, to measure changes in the chemical gradient and report the signal to the flagella (*72*, *114*, *118*). An overview of the differences in function between metabolism-dependent and metabolism-independent chemotaxis follows.

2.1.1 Examples of microbial chemotaxis

2.1.1.1 Metabolism-independent chemotaxis

Archaeal and bacterial chemotactic movement is governed by a variety of sensory systems as they respond to environmental fluxes, these systems control most biological signal transduction pathways (*122*). Most bacteria contain signalling proteins called HAMP domain signalling motifs; histidine kinases, adenylyl cyclases, methyl-accepting chemotaxis proteins (MCPs), and phosphatases (Fig. 2.1) (*120*, *122*).

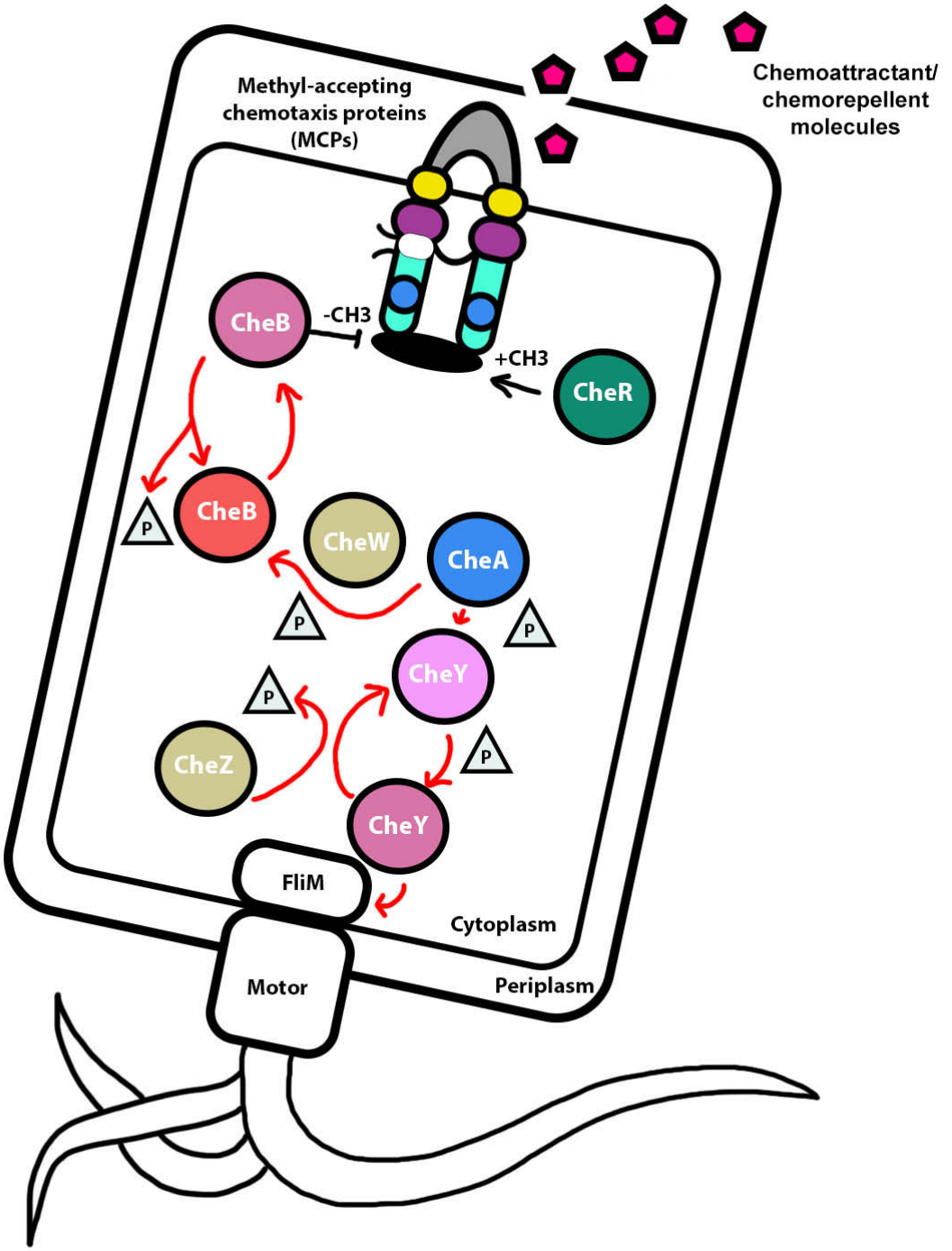


Fig. 2.1. Chemotactic *E. coli* cell schematic. Schematic of the simplified HAMP region and chemotactic signaling subdomain (SSD), responding to a chemoattractant/chemorepellent. The HAMP and SSD hairpin region is located at the tip of the cytoplasm, which interacts with the chemotaxis genes, particularly CheW and CheA for the modulation of flagella rotation. The kinase-activating hairpin tip of the SSD, has the highest amino acid sequence conservation among MCPs. A typical MCP receptor also consists of a ligand-binding domain which recognises and senses the chemoattractant molecules and other environmental cues and is usually located on the extracellular side of the cell membrane. The fliM gene which governs flagella function is also highlighted along with the phosphate groups; triangles, involved in cell signalling (*120*, *121*).

It has been discovered that the metabolism-independent chemosensing mechanism generally occurs via the triggering of transmembrane protein chemoreceptors and transducers (Fig. 2.1) (*123*, *124*). These chemotaxis transducers transmit information to the flagella through a two-component regulatory systems to sense a change in the biological or physical environment and relay the signal to the bacterial nucleoid, where modulation of gene expression occurs. This is explained in more detail below with a chemotactic cell schematic displayed in figure 2.1 (*123*, *124*).

The transmembrane signaling in *E. coli* is a typical example of metabolism-independent chemotaxis, this method of chemical sensing is present in several other bacteria such as *Salmonella sp.*, *Bacillus subtilis* and *Pseudomonas sp.*, to a vast number of petroleum hydrocarbons (*123*). Several genetic and biochemical investigations of *E. coli* have been undertaken and it has been determined that four chemoreceptors out of five are transmembrane proteins and are utilised in the signaling process: Tar for aspartate, Trg for ribose, Tap for peptides, Tsr for serine and galactose (*103*, *123*, *125*). These proteins are homologous MCPs and all contain a periplasmic sensing domain, as well as a cytoplasmic signalling domain (Fig. 2.1) (*123*, *126*).

The binding of an effector molecule to these proteins results in the emission of a signal that is transduced to the flagella via the CheW gene and the sensor histidine kinase CheA protein, this triggers a phosphorelay of proteins that control the direction of flagella rotation and function of the motor, such as the fliM gene, along with regulating the CheY protein (Fig. 2.1) (*121*, *123*, *127*).

This pathway is similar to albeit slightly more complex than other two-component signal transduction systems in bacteria with CheY protein controlling swimming behaviour and binding to the flagella to reverse the swim direction (Fig. 2.1) (*123*). The phosphatase CheZ gene, terminates the signal via the removal of a phosphate group from CheY-P, ceasing the response (*120*, *121*). Adaption of this system is also governed by methylation and demethylation of certain glutamyl residues present on

the MCPs via the methyltransferase CheR protein and the methylesterase CheB protein, with elevated methylation resulting in the inhibition of MCP signaling and the cessation of a chemotactic response (Fig. 2.1) (*121*).

2.1.1.2 Metabolism-dependent chemotaxis and other taxis types

Metabolism-dependent chemotaxis, however, occurs when bacteria require metabolism of a chemotactic molecules and is present in more archaic α-proteobacterium, such as *Azospirillum brasilense* (*123*). There are three key criteria for this: a) the inhibition of the metabolism of a chemical attractant stops the chemotactic response, b) non-metabolisable analogues of metabolisable chemoattractants are not attractants, and c) the presence of another metabolisable chemical deters a chemotactic response (*123*). *A. brasilense* contains a major chemotaxis receptor for sensing oxygen and other metabolism-related parameters critical to the colonisation of the wheat root surface (*128*).

This metabolism-dependent chemotactic mechanism may also be the key driver in steering *Rhodobacter sphaeroides*, another remediative bacteria to a favourable chemical environment via a "selective stopping" strategy (*129*). This chemotactic strategy also utilises similar biochemical signalling pathways to the chemotaxis phenomenon, known as energy taxis and is defined as the response to stimuli affecting cellular energy levels, with notable examples being phototaxis and aerotaxis, however phototaxis would be almost negligible in the subsurface (*123*). These mechanisms involve an electron transport chain; this is when a change in the rate of electron transport or other related energy parameter, is detected by the signal transduction system (*123*, *130*, *131*). This system allows metabolisable substrates to stimulate behavioral responses as long as there is a receptor sensing change in the cellular energy gradient (*123*).

Aerotaxis may be a key player in the oxidative biodegradation of different compounds such as petroleum hydrocarbons due to the fact that different oxygenase enzymes, which are crucial in the degradation of contaminants, require molecular oxygen

to function (*123*, *131*). However, anaerobic and microaerophilic organisms may find it favourable to penetrate deeper into the soils and sediment and degrade toxic contaminants, exhibiting a negative aerotactic response and move towards chemicals such as DNAPLs (*123*, *132*, *133*).

Other taxis phenomena also exist, such as magnetotaxis, rheotaxis, and haptotaxis. A magnetotactic response is governed by an electric field, where bacteria have the ability to form magnetosomes, which have organelles containing dedicated vesicles, which synthesise magnetic iron crystals. These act as sensors of the Earth's magnetic field, with chemotaxis possibly enhancing this effect in certain environments with the alignment of cells (*134*).

The movement of bacteria triggered by fluid velocity gradients and shear is known as rheotaxis, with chemotactic bacteria being unable to detect shear (*135*). In high shear environments where flow is perpendicular to chemotactic gradients there is expected to be a negative interaction reducing the effectiveness of motility, however if shear is parallel no interaction with chemotaxis and rheotaxis is thought to occur (*135*). Nevertheless, it has been suggested that flow and shear in porous media has a more complex relationship and influence on chemotactic cells than initially thought (*136*). A recent study found that the pores caused heterogeneity in the fluid flow field, resulting in the unexpected accumulation of chemotactic cells in high abundances, in stagnant flow fields within micro-pockets (*136*). This suggests further research needs to be undertaken to elucidate the relationship between chemotaxis and rheotaxis.

Thirdly, haptotaxis is a taxis phenomena related to chemotaxis directly. This is defined as directional movement on exclusively solid immobilised non-saturated attractants, with this phenomenon being shown to increase the residence times of surface-colliding bacteria to naphthalene rich sites by relocation (*137*). Further research is required to investigate these other taxis phenomena more and their interplay with chemotaxis. However this is outside the scope of this thesis. Since it is clear chemotactic movement can revolve around dependent and in-dependent

metabolism of nutrients or energy sources, an alternative hypothesis of the original ecological drive for a chemotactic response should be considered such as the drive to explore new territories or other microbial interactions (*96*). The next subsection continues the historical review of chemotaxis and the development of the assays used to investigate its role in the NSZD of petroleum hydrocarbons.

2.1.2 Further historical advances in chemotaxis research

In the early 1970's, Adler's group also discovered there is a low threshold of sensitivity to attractant concentration Δc, with the sensitivity following Weber's law or fold-change detection. This is defined as relative change in attractant concentrations ($\Delta c/c0$), rather than absolute change. This results in chemotactic cells exhibiting a "logarithmic" tracking or sensing regime. This is characterised by a sustained and constant amplitude response when moving in a chemical gradient that increases exponentially or close to exponentially (*138*, *139*).

A significant amount of chemotaxis research and development of chemotaxis assays was spearheaded by the late Howard C. Berg of Harvard University during the 1980s. Mainly focusing on biochemical changes within systems as a proxy for multiple environments, primarily via the tethering of flagella to a surface and exposing the cells to different chemicals and environmental conditions (*76*, *140–142*). This monitors the cells direction of movement through the analysis of a series of intermittent pauses, with attractants decreasing pauses and repellents increasing pauses. This technique also allowed for the novel calculation of the torsional compliance force (*76*, *140*, *141*).

The aforementioned capillary tube method of observation was initially highly subjective, until quantitative analysis of the bacteria was achieved by constructing well defined chemical gradients. This allowed for the determination of positive or negative chemotactic responses and analysis of the distribution of bacteria in the gradient by measuring the scattering of light by laser beam (*143–146*). The development

of other assays, such as soft-agar chemotaxis assays, agarose plug and chemical-in-plug assays, where the attractant is uniformly distributed or diffuses outwards in semi-solid agar or agarose, paved the way for further analysis on how chemotaxis operates at a colony or community level (*143–146*).

Soft-agar chemotaxis assays traditionally work by placing a petri-dish with soft-agar assays on an experimental dark-field illumination kit, known as a "bucket of light". The colony perimeters can be then be measured to study chemotactic behaviour (*147*). The assay works by the microbes forming self-generated chemical gradients (*101*, *103*).

The development of microfluidic assays has also further advanced the field (*103*). A microfluidic study by Mehdi Salek in 2019, yielded a key result. It utilised a T-maze microfluidic device shape and found that within chemotactic mono-cultures there is significant phenotype variation of sensitivity towards chemoattractants. Phenotypes are created from environmental variation and variation in the expression of a cells genetic code. This suggests a bet-hedging strategy may cause variation to typical chemotactic responses (*148*).

Advances in the study of twitching motility of cells has been more gradual due to the subtle twitching motion of cells. Tracking techniques and imaging in recent years has however gradually evolved, and has allowed for the twitching oscillation of cells to be studied in more detail (*149*, *150*). It has been shown that movement mediated by type IV pili is independent of flagella driven rotation, with the flagella possibly acting as a stabilising anchor during surface-based movement within and upon biofilms (*149*). Biofilms form when clusters of bacteria attach themselves to a surface (*151*). This was investigated using inverted microscopy, the TrackMate plug-in within ImageJ, and exposing mutants of *P. aeruginosa* to chemoattractants within microfluidic devices (*149*, *150*).

Advances in microscopy, with high magnification lenses of x 400 being made more commonly available, has spurred the advance of more sophisticated computer pro-

gramming software which can quantitatively analyse chemotaxis at a single cell level. TaxisPy is an example of such software. This freely available Python programme investigates the tumble frequency of cells and was developed in 2020 (*152*).

2.2 Chemotaxis assays at microcosm and field scales

Studies using microcosm chemotaxis assays have also been undertaken to investigate chemotactic responses to multiple attractants, such as *Pseudomonas putida* F1 to the chlorocarbon, trichloroethylene (TCE), along with sodium benzoate and sodium acetate (*90*, *98*). The idea being bench-scale and microcosm studies are a better representation of field sites.

A study by Olson et al., (2004), assessed the chemotactic response and spatial distribution of *P. putida* F1 using magnetic resonance imaging (MRI), responding to the attractant trichloroethylene (TCE). It labelled the bacteria with magnetite particles in a porous media matrix to mimic a field environment, packing a column, with a bed length of 8 cm, injecting the column at a flow rate of 2 mL/min, and imaging the distribution shift over a period of 16 hours. The study found a statistically significant effect on bacterial migration and chemotaxis through porous media in the presence of a chemical concentration gradient (*90*). The outcome of this microcosm study supports the idea that chemotactically assisted movement within groundwater systems could potentially improve the overall effectiveness of NSZD by enhancing the abundance of biomass in regions of contamination (*98*).

However, Gomes and his colleagues found that the naphthalene degradation rate of an indigenous microbial population decreased when a chemotactic and hydrocarbon degrading *Pseudomonas putida* KT2442 (pNF142) strain was introduced (*37*). This inoculate is suspected to have suppressed nutrient availability, due to the *Pseudomonas putida* KT2442 (pNF142) strain dominating (*37*). This strain however is not reported to be directly chemotactic towards naphthalene, repeating the study with a microbe chemotactic towards naphthalene, may wield different result (i.e.

there might be a more constructive relationship) (*103*). Another study by Strobel et al., (2011), used a similar microcosm set-up to mimic a porous environment with subsurface groundwater flow. It found that a chemotactic *P. putida* F1 strain preferentially accumulated transverse to fluid flow, compared to a non-chemotactic *P. putida* F1 cheA smooth swimming mutant, which maintained a more random distribution (*98*). The center of mass of the chemotactic bacteria plume effectively moved upward toward the level at which the chemoattractant benzoate was injected, relative to the movement of non-chemotactic *P. putida* F1 cheA bacteria. A similar response was seen when acetate was used as the chemoattractant (*98*).

Historically field-based studies of chemotaxis in groundwater environments are scarce, and focus more on motility and non-motile cells rather than chemotactic responses. Nevertheless, a USGS toxicology study involving injection and recovery at a field site in Cape Cod, MA, found that a motile pseudomonad advected through a sandy aquifer under natural-gradient conditions, ahead of a non-motile mutant (*153*). Roseanne M. Ford and Ronald W. Harvey calculated that chemotaxis may have been a significant driver in their distribution, providing evidence of free swimming responses of chemotaxis at an aquifer scale (*153*). Another injection and recovery study in fractured volcanic rock found that the non-motile bacteria were more abundant at a down-gradient well in heavily fractured granite rock in Mirror Lake, NH, compared to motile bacteria. This is thought to be consistent with the idea, that motile bacteria have higher diffusion coefficients and thus more collisions with surfaces, resulting in their presence declining at lower gradients (*153*). It is worth mentioning, motile bacteria are potentially more likely to swim into stagnant pore space of no flow, within fractured rock and exhaust nutrient supply (*136*, *153*). There is also a possibility of them entombing themselves within their extracellular polymeric substance (EPS) secretions, which eventually form a biofilm, clogging pores, potentially limiting chemotaxis due to the blocking of chemotactic signals in pore space and most of the bacteria shifting to a growth phase (*96*, *153*, *154*). This highlights the pivotal role the geology of the site plays.

It is also worth noting that the clogging of pores by biofilm and EPS created and secreted by microbes alters the heterogeneous porous network, thereby altering chemical transport and groundwater flow within the subsurface. This indirectly also influences the NSZD of contaminates (*154*). Attaining data across such a plethora of different scales, geology and environments from cellular to field scale, using multiple chemotaxis assays, will assist in decreasing the uncertainties associated with scale-dependency variation. Therefore improving the understanding of chemotactic activity and the role it plays in NSZD of petroleum hydrocarbons (*153*).

2.3 Computational modelling

The computational modelling of chemotaxis, also assists in the gauging of the role it plays in the NSZD of petroleum hydrocarbons. Modelling has advanced over the past 50 years, from the classic Keller and Segel chemotactic cell aggregation model in the early 1970s, to more advanced models in the past decade. The Keller and Segel model was initially introduced to explain the accumulation of *Dictyostelium discoideum*, a slime mold amoeba, towards a chemoattractant via the development of chemotaxis partial differential equations (PDE) which incorporated advection-diffusion equations used in standard groundwater contaminant transport modelling (*155*, *156*). In the model the cells can move left, right and forward, and assumes the chemoreceptors are on the external portion of the cell, with the model taking into account the cells effective size. It also utilises components of Brownian motion, however not metabolism of attractants (*155*). Several modifications of the Keller and Segel model have been made over the years, such as improving the consumption rate of attractants, with a recent 2020 review by Arumugam and Tyagi, describing the different model variations and gaps in the literature (*157*). The development of other model types, such as smoothed particle numerical meshless Lagrangian methods has also advanced (*71*).

A 2020 study by Adam Gosztolai and Mauricio Barahona used an analytical model of microbial chemotactic drift velocities in rugged environments to incorporate a

microbial memory component. This memory component is used to extract spatio-temporal information from the landscape, which microbes are thought to store to alter their chemotactic navigation and spatial distribution. The model provides numerical solutions which concur, with the outer limits of some of the models created by Keller and Segel equations (*158*). However, such models are hard to quantify at both a Darcy and field scale (*55*, *159*).

Recently, multiphase biogeochemical models have been developed to include chemotaxis and model NSZD on various scales, such as TMVOCBio (*55*). This model acts as a "digital twin", mimicking the NSZD of petroleum hydrocarbon at the aforementioned Bemidji, Minnesota site. However, further research is needed to adequately include chemotaxis and microbial transport, with the distribution of chemotactic and hydrocarbon degrading cells within the subsurface and their interaction being vital parameters to quantify, with chemotaxis and microbial transport recently highlighted as research "hot topics" (*31*, *55*).

This overview of chemotactic function, historical literature review and analysis of the different methodologies used to investigate the phenomenon provides a clear grounding of the topic of chemotaxis. The next section will further investigate how microbial communities of varying degrees of chemotactic and hydrocarbon degrading ability interact and transfer degradative ability within the subsurface.

2.4 Community dynamics and plasmid exchange

Microbial community degradation research has mainly concentrated on the degradation of structurally similar aromatic compounds, focusing on the remediation of more recalcitrant aromatic compounds and not necessarily chemotactic activity within bacterial communities (*103*, *121*, *123*, *160*). It is therefore important to understand the nature of the impact of chemotaxis on degradation rate and plasmid transfer within microbial communities in the subsurface. Parales & Ditty in 2018 wrote ; "...the ability of an organism to sense and follow a gradient of a particular

chemical or class of chemicals that it is unable to degrade could bring it into close contact with other organism carrying relevant transmissible catabolic plasmids for the degradation of these chemicals. In this way, chemotaxis could stimulate the dissemination of catabolic plasmids among environmental bacteria, and hence could enhance the biodegradative capacity of the population" (*121*, *146*).

Catabolic plasmids are large (80-1100 kilo base pairs (kb)) circular or linear accessory deoxyribonucleic acid (DNA) elements, which are present inside the cytoplasm of most bacteria on Earth (*161*). Recent research has studied these catabolic gene clusters and their evolution and subsequent ability to degrade environmental recalcitrant contaminants (*162*). The transfer of catabolic plasmids, which can carry the genes encoding degradation pathway enzymes, chemoreceptors, and transporters can transfer the degradation ability to neighbouring bacteria, along with potentially expanding the range of contaminates the bacteria can degrade and is chemotactic to (Fig. 2.2) (*125*, *162*, *163*).

The plasmids are generally transferred by cell-to-cell conjugation, which can be enhanced when plants are present, as these may harbour localised populations of microbes which have not been exposed to these travelling chemotactic communities (Fig. 2.2).This is also, in part, due to some chemotactic bacteria being attracted to plant exudates, with most of the conjugation activity occurring inside the plant leaf as well as on the surface of the leaf itself. This has been witnessed, when *Pseudomonas syringae* transferred the antibiotic resistant plasmid RP1 to epiphytically grown bacteria within the bush bean *Phaseolus vulgaris*. The transfer of the toluene monooxygenase operon; involved in toluene degradation, from *Burkholderia cepacia* L.S.2.4 to endophytic bacteria, within the yellow lupine plant has also been recorded (*10*, *121*, *125*, *162*, *165–167*).

Furthermore, from a fundamental genetic perspective, the presence of chemoreceptor genes on certain catabolic plasmids suggest that chemotaxis is a principal driver in biodegradation and has been throughout bacterial evolution (Fig. 2.2) (*125*, *162*).

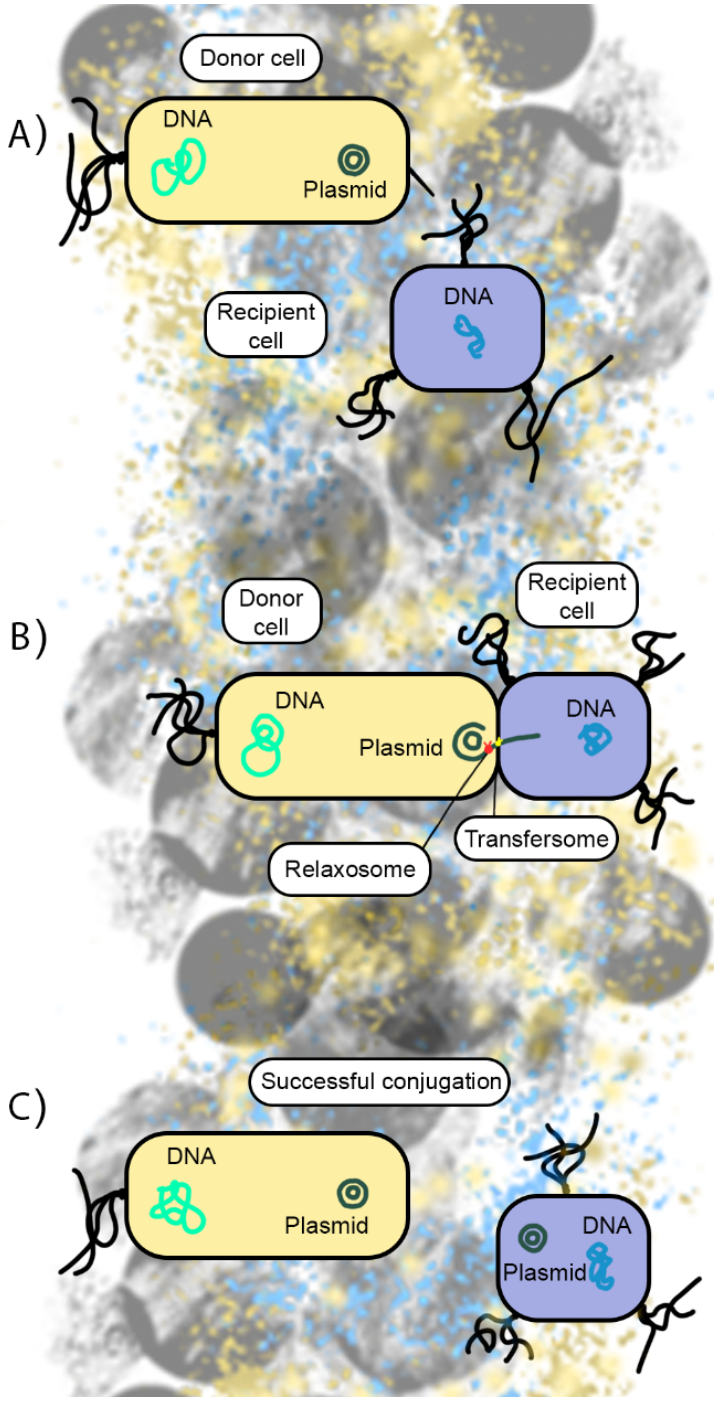


Fig. 2.2. Schematic of microbial cell conjugation and the transfer of a plasmid carrying genes involved in chemotaxis and hydrocarbon degradation in a contaminated groundwater aquifer. A) The schematic shows a chemotactic donor cell, which can degrade petroleum hydrocarbon, due to the fact is carrying a plasmid. The donor cell outstretches its pili, towards the chemotactic recipient cell which cannot degrade the hydrocarbon. B) The pili attaches and retracts, bringing the cells together, with chemotaxis possibly boosting the frequency of this occurrence. The plasmid is then nicked, this process relaxes the torsional strain needed to maintain supercoiling and allows for a single strand of DNA from the nicked plasmid to be transferred. C) Successful transfer of plasmids after recircularisation, allowing both cells to degrade hydrocarbon and likely increasing the plethora of attractants the recipient cell is chemotactic towards (*125*, *162–164*).

Is also thought that an increase in the amount anthropogenic contamination and an increase in competition for food in the subsurface, led an increase in chemotactic activity to attain energy and food (*52*, *123*). This is supported by the fact it is common for the degradation genes to be located in close proximity to the chemotactic genes, with the exact nature of this relationship not being fully understood (*103*, *121*, *168*).

The plasmid pJP4 which is carried by *Ralstonia eutropha* JMP134, assists in the degradation of the organochlorine herbicide 2,4-D, as well as 3-chlorobenzoate degradation and possesses chemotactic properties, it can also be readily exchanged by conjugation with similar bacteria transferring chemotactic and hydrocarbon degradative ability (*162*). The hydrocarbon degrading *P. putida* G7 strain and other *Pseudomonas* species are chemotactic towards naphthalene, however they generally need to be grown in the presence of naphthalene to initiate a chemotactic response. They degrade naphthalene and similar hydrocarbons through the use of the Nah7 and pDTG1 plasmids (*123*). The Nah7 plasmid works in partnership with the NahY naphthalene chemoreceptor, this chemoreceptor exhibits significant homology to the aforementioned MCPs (*123*). These plasmids can be disseminated to similar microbes in the surrounding area and can assist in the NSZD of naphthalene contamination (*123*, *169*, *170*). Another *Pseudomonas* strain, *P. putida* F1, exhibits a chemotactic response to toluene, when grown in its presence, with its ability to degrade toluene reliant on the utilisation of the broad substrate plasmid, toluene dioxygenase (TOL). The TOL plasmid allows the bacteria to oxidise other hydrocarbons and some organocholides, such as chlorobenzenes and chlorophenol. This functionality can also be transferred by conjugation and exchange the plasmid to other genera such as *Rhizobium*, which have recently been shown to degrade phenanthrene (Fig. 2.2) (*168*, *171–175*).

Chemotaxis has also been shown to possibly increase the rate of plasmid exchange, due to an increase in the amount of physical collisions and cell-to-cell contact. Further research into how microbes interact would also improve the understanding on

how the NSZD rate could be impacted by plasmid exchange (*103*, *121*, *125*, *153*, *162*). The next section will further investigate chemotactic function, by reviewing the interaction of bacteria of varying degrees of chemotactic ability and motility and the enhanced degradation which is possible in the subsurface through biomobilisation, concluding this literature review of chemotaxis.

2.4.1 Chemotactically enhanced NSZD and chemotactically assisted biomobilisation

Exploitation of this chemotactic mechanism has far reaching remedial potential, it can enhance the mass transfer of biodegrading bacteria to regions of contamination and increase the rate of NSZD (*72*, *176*, *177*). NAPLs for example can become entrapped within soil and rock, forming "blobs" or "pockets" of contamination (*132*). In order for successful bioremediation to occur, degradative bacteria require access to the target contaminants; either by biofilm formation, direct adhesion of the bacteria to the NAPL water interface or via dissolution of the target compound in the aqueous phase (*123*, *151*). Biofilms assist in this process allowing bacteria to move along the periphery of the contaminated region, permitting growth, enhancing degradation rate and decreasing the environmental health risk (*52*, *123*, *125*, *178*).

Chemotaxis is naturally advantageous in such instances, allowing bacteria better access to entrapped NAPL blobs prior to biofilm formation (*132*). However it can be difficult for non-chemotactic bacteria to make their way to NAPL blobs, due to their inability to sense a gradient, they travel along fluid flow paths of high conductivity (*89*, *103*, *121*, *123*, *125*, *132*, *179*). This enhancement of biomass in zones and areas of hydrocarbon degradation, is why knowledge of the distribution of microbes of varying degrees of chemotactic ability and motility, needs to be improved to adequately gauge NSZD (*89*, *103*, *121*, *123*, *125*, *132*, *179*).

Flagellated chemotactic bacteria can swim between $\sim$19.7-40.5 μm s^{-1} and have the ability to swim up-gradient and transverse to typical groundwater flow velocities

(*90*). However, their response is most efficient at the lower flow velocities, considering that groundwater flow velocities can vary from approximately ∼5.8-121.5 μm s^{-1} (*89*, *180*). This may allow bacteria and archaea to swim freely within the subsurface (*90*). Bacteria such as the motile Gram-positive model microbe *Bacillus subtilis*, sourced from from sewage contamination have been recorded to travel 10.7 m in 8 weeks in clay and sandy clay (*181*). However, percolation and groundwater transport are also driving factors, with motility assisting.

Chemotactic bacteria encircle a contaminant, generating a "curtain" of chemotactic and hydrocarbon degrading taxa, the distribution of such communities at a contaminated legacy petroleum hydrocarbon site has not been previously investigated (*52*, *89*, *123*, *125*, *178*). This encircling of petroleum hydrocarbons also occurs in seawater (*182*). The curtain of microbes that forms around NAPL plumes assists in reducing the spread of contaminants in source zones; particularly smaller petroleum droplets and potentially influences the distribution of other microbes (*183*).

Initially it was thought that the distribution of non-motile microbes through the subsurface was only enhanced by physical factors such as fluid movement from rainwater drainage or water table fluctuation, with the typical distances between microbes within the soil being calculated to be 50-100 μm, with chemotaxis having the potential to alter this within pore space on μm, mm & cm scales (*97–100*). However, biological drivers have recently been discovered, such as fungal hyphae transporting cells or the direct attachment of the cells to the skin of earthworms as they move within the subsurface (*184*, *185*). Recently, microbial biomobilisation has also been shown to occur via several mechanisms, such as "piggybacking", where the non-motile microbes physically attach to the motile chemotactic microbes, effectively acting as cargo carriers (*186*, *187*). An example of this is when the non-motile anaerobic bacterium *Porphyromonas gingivalis* physically attaches itself to the motile bacteria *Treponema denticola*, as *T. denticola* responds chemotactically towards sucrose (*186*). A similar biomobilisation mechanism has been seen in certain motile and non-motile cancer cells (*188*).

Another biomobilisation mechanism occurs because of hydrodynamic entrapment, when motile and chemotactic *Paenibacillus vortex* cells entrap fungal conidia in their wake (*189*). The zoospore *Pythium aphanidermatum* has also been shown to biomobilise the chemotactic and hydrocarbon degrading bacteria *P. putida* G7 and non-motile petroleum hydrocarbon degrading bacteria *Mycobacterium gilvum* VM552 towards ethanol (*190*). This is interesting as microbes which are already chemotactic are biomobilised more efficiently by the larger zoospores, which exert a thrust force during flagella propulsion, resulting in the formation of eddies within the fluid. The zoospore is responding to ethanol, which it uses as a "homing inducer" (*190*, *191*). The biomobilisation of *P. putida* G7 in the subsurface will further assist in the dissemination of the aforementioned hydrocarbon degrading plasmids, mentioned in above.

M. gilvum cells have also been shown to be biomobilised by chemotactic *P. putida* G7 cells, when exposed to a chemoattractant in a capillary microfluidic assay, and a bulk suspensions bioreactor (*184*). Therefore, biomobilisation is also involved in enhancing the distribution of microbes into new territories and expanding the spatial range distribution (*96*). In this case, the biomobilisation effect is triggered by hydrodynamic forces and a mechanical "push / pull" biomobilisation effect, with the bulk suspensions bioreactor working more effectively at increasing the degree of transport (*184*). This biomobilisation is significant as it involves solely bacteria of similar sizes (*184*, *190*). The capillary microfluidic assay, however showed a three-fold decrease in biomobilisation displacement. This was due to the cells blocking the capillary channels as they diffuse, highlighting the importance of pore size and the geology at a real-world site. Interestingly, it has been reported that there is a 50% reduction in pore size and in chemotaxis and motility for a similar reduction in pore size. Clay soils, for instance, hinder the spread of microbes as the saturated pore space is reportedly too small, however, *E. coli* have been shown to be less effected by this due to their shorter swimming run lengths (*52*, *184*, *192*, *193*). This biomobilisation mechanism, enhanced the biomass potentially capable of petroleum degradation due to enhanced transport towards the contaminant interface (*96*).

However, it is not clear if chemotactic microbes in the field, physically alter the distribution of other motile but non-chemotactic microbes, potentially transporting them closer to the contaminated region and increasing NSZD (*52*, *123*, *125*, *178*, *184*). It has also recently been shown that individual bacteria can synchronise their flagella, so they do not tangle, possibly enhancing the biomobilisation effect amongst microbes which are motile but non-chemotactic to the attractants such as petroleum hydrocarbons (*194*). The thrust force of the motile but non-chemotactic cell has thus also been theorised to assist if any piggybacking occurred (*195*).

Understanding this microbial transport phenomenon in more detail and how microbes of varying degrees of chemotactic ability and motility behave in a porous matrix, is important, as it has the potential to increase the abundance of biomass capable of degradation closer to the contaminant interface (Fig. 1.2). It could also lead to a net decrease in degradation potential, if the bacteria collide and come to loggerheads with one another, hindering expansion and this could result in clusters of cells blocking pore throats.

Improving the understanding of chemotaxis and its influence upon the microbial transport of other microbes, will provide a clearer picture of the NSZD rate. This is key to updating and improve the accuracy of NSZD models (Fig. 1.2) (*31*). This may also assist in the bioprospecting, screening, and subsequent identification of chemotactic and hydrocarbon degrading microbes capable of enhancing NSZD (*196*). These microbes could then be added to the site, to assist in the degradation, in a process known as bioaugmentation (*197*, *198*).

Chapter 3

Field-based study

.

3.1 Authorship Statement

This chapter contains a field study which was submitted to the *Journal of Hazardous Materials* is inserted in full at the end of the thesis, with inserts used throughout; "Under Creative Commons License Open Access Guidelines" and with full permission directly from the "Elsevier" publishing house (*199*).

I declare I am responsible for the studies conceptualisation and analysis of the chemical and 16S rRNA sequencing analysis, as well as the development of the "bioinformatic pipeline". I am the principal author and responsible for the investigation. Below is the statement of authorship:

"Cameron W. M. Murphy: Conceptualization, Methodology, Investigation, Formal analysis, Writing. Greg B. Davis: Investigation, Formal analysis, Writing. John L. Rayner: Investigation, Formal analysis. Tom Walsh: Investigation, Formal analysis, Writing. Trevor P. Bastow: Investigation, Formal analysis, Writing. Adrian P. Butler: Formal analysis, Writing, Supervision. Geoffrey J. Puzon: Investigation, Formal analysis, Writing, Supervision, Project administration. Matthew J. Morgan: Methodology, Investigation, Formal analysis, Writing, Supervision.

Paper Acknowledgment: Yasuko Geste is thanked for technical help with chemistry.

Mike Donn, Jason Wylie, Melanie Bruckberger and Robert Woodbury are thanked for their help in sample processing. Suzanne Metcalfe is thanked for her assistance with amplicon sequencing. Kaveh Sookhak Lari is thanked for his help with the graphical abstract. BP Australia is acknowledged for supporting the investigation. This work is financially supported by the Commonwealth Scientific and Industrial Research Organisation (CSIRO)".

The aim of this field study was to explore the association of the predicted functional potential of microbial communities at these sites with these legacy contaminants, and test whether the distribution of petroleum hydrocarbon and LNAPL compounds influences the abundance of the inferred chemotactic and hydrocarbon degrading microbes. As well as, determining the relative abundances of microbes that possess these properties. This was achieved by comparing the predicted metagenome profiles of operational taxonomic units (OTUs) derived from 16S rRNA marker gene sequences, to the distribution and concentration of legacy petroleum hydrocarbon and LNAPL compounds across the site. Investigating the preferential occurrence of the predicted chemotactic and hydrocarbon degrading microbes to various petroleum products and depth allows for the development of more accurate NSZD models (*55*). The methodology applied in this study assists in potential bioprospecting and screening of chemotactic and hydrocarbon degrading microbes potentially capable of enhancing NSZD. This will provide a clearer picture of risk to groundwater resource (*200*).

3.2 Introduction

Understanding how microbial communities interact with specific chemical contaminants is an important step towards predictive modelling and manipulation of sites to promote NSZD. A number of studies have investigated the microbial communities and physical conditions that may contribute to the NSZD of petroleum hydrocarbon compounds (*201–203*). These studies have considered the role of different redox conditions on biodegradation and the role of microorganisms in constraining con-

taminant expansion in the subsurface (*204–206*). Research has also highlighted the role of microorganisms in degrading more recalcitrant contaminants, and the role of maintaining a diverse biodegrading population (*207*, *208*), along with investigating the formation of biodegradation by-products (e.g. polar compounds) in weathered diesel and their fate (*23*, *209–211*). Chemotaxis is an important mechanism used by microbes to exploit otherwise inaccessible resources, including petroleum hydrocarbons (*146*). Many microbes have been demonstrated to be capable of chemotaxis-assisted degradation of alkanes and other hydrocarbon compounds (*212*, *213*).

The distribution of chemotactic microbes and the exact nature of the role chemotaxis plays in the NSZD of petroleum hydrocarbons under field conditions remains unclear (*31*). Addressing this challenge requires characterising microbial diversity, community composition and the functional potential of community members for hydrocarbon degradation and chemotaxis. Although culturing specific bacteria can provide direct evidence of chemotaxis and degrading functions, the vast majority of soil microbes are not culturable and environmental samples are typically too diverse to make this feasible for characterising communities (*214*). Alternatively, shotgun metagenomic sequencing, which aims to assemble whole genomes from short fragments, can be used to determine gene content and thus functional potential of microbial communities. However, it is limited if there is little community biomass or host contamination, and remains a significant bioinformatic challenge (*215*). An alternative approach indirectly infers the functional potential of individual species by comparing community-derived marker gene sequences against a database of reference genomes from organisms with known functions (*215*). For example, Crampon et al. (2018) used this approach to infer that operational taxonomic units based on 16S rRNA amplicon sequences were abundant in metabolic pathways linked to higher polycyclic aromatic hydrocarbon degradation potential. The widespread use of this approach for inferring community functional potential and the recent improvements in database coverage and optimised genome prediction algorithms make this a robust option for microbial community functional inference (*215*, *216*).

To achieve the aim of this thesis and address research objectives and aims, it was

necessary to conduct a real-world field study (Fig. 3.1).

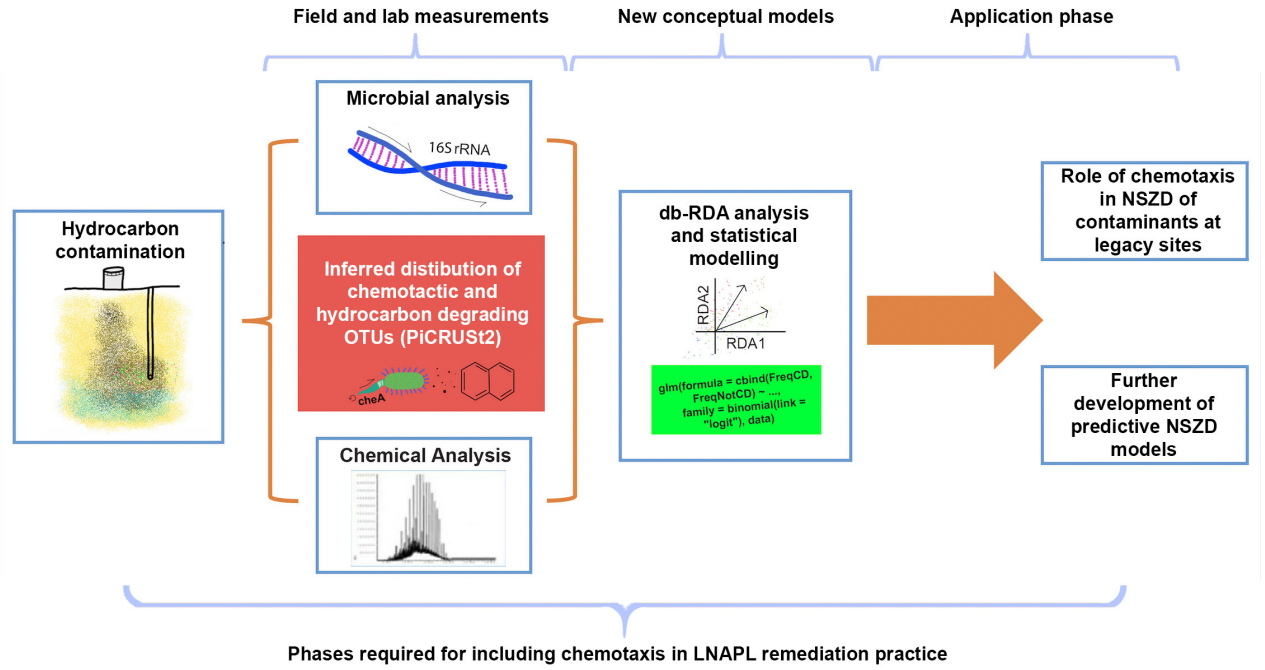


Fig. 3.1. Field study plan and design. After Murphy et al., (2022) (*177*).

The purpose of this study was to investigate the presence of chemotactic and hydrocarbon degrading microbes at a contaminated legacy petroleum hydrocarbon site undergoing NSZD, as well as to determine the variables driving their occurrence and distribution (Fig. 3.1).

3.3 Field study at legacy site and biostatistics

3.3.1 Summary of field study plan and design

This study investigates the distribution of potentially chemotactic and hydrocarbon degrading microbes (CD) across the water table of a legacy petroleum hydrocarbon site near Perth, Western Australia in areas impacted by crude oil, diesel and jet fuel. Core samples were recovered and analysed for hydrocarbon contamination using gas chromatography. Predictive metagenomic profiling was undertaken to infer functionality using a combination of 16S rRNA sequencing and PICRUSt2 analysis.

3.3.2 Overview of the site and chemical analysis

Soil cores collected from the site had different ranges of petroleum hydrocarbon (crude oil, diesel fuel and jet fuel) contamination as well as a representative background core (Fig. 3.2). Cores were analysed for concentrations of TPH, LNAPL components, and selected aromatic compounds (the main water soluble aromatic compounds present in significant abundances) (Fig. 3.2). The representative background control location was found to contain negligible concentrations of TPH and LNAPL components (data not shown). Across all core locations contaminated with different petroleum types, TPH had peak concentrations of 20–100 g/kg, which generally occurred below the water table (Fig. 3.2). The Crude oil contaminated cores contained a limited range of identifiable LNAPL components; primarily these were the aromatic components 2-MN, naphthalene, 1-MN, phenanthrene and ethylbenzene. These were generally found in two of the three Crude oil cores. The diesel cores were generally dominated by 2-MN, 1-MN, naphthalene and phenanthrene, with a more diverse range of up to a dozen dominant aromatic components in the LNAPL detected in the Jet Fuel cores (Fig. 3.2). In the Water Table and Middle sections of the Crude oil cores (T7, D10a), concentrations peaked at approximately 10–100 mg/kg for ethylbenzene, naphthalene, 1-MN, 2-MN and phenanthrene, although highest concentrations were in the Middle section (Fig. 3.2). D10b was similar, however the core did not contain ethylbenzene and had lower concentrations of naphthalene and phenanthrene, with the highest concentrations in the Middle section. D10b also contained very low concentrations of 2-MN in the Bottom section. Concentrations in core T7 were above detection levels in the Top section, with low concentrations of 2-MN in the Bottom section. In the Diesel cores (T3, D6), naphthalene, phenanthrene, 1-MN and 2-MN had peak concentrations in the range 10–100 mg/kg. TPH and 1-MN were detected in the Bottom section of D6 (Fig. 3.2).

The two Jet Fuel cores, D9 and T5, were found to contain elevated concentrations of selected aromatic components in the Middle section of the cores, with concentrations ranging from approximately 10 to 3000 mg/kg (Fig. 3.2). Notably, all the BTEX

(benzene, toluene, ethylbenzene and xylenes) and trimethylbenzene (TMB) isomers were detected in these cores, as well as 1-MN, 2-MN and naphthalene. Phenanthrene was only detected in T5. Exceptionally elevated concentrations of m/p-xylene and 1,2,4-TMB were recorded in the Middle section of both cores. In D9, the shallower Water Table section, a smaller range of the selected aromatic compounds were recorded (1,2,3-TMB, 1,3,4-TMB, 1,3,5-TMB, m/p-xylene, o-xylene, ethylbenzene), with toluene and benzene not being detected. However, all compounds were detected in the Bottom section of this core. In contrast, no TPH was detected in the Water Table section of the T5 Jet Fuel core, and ethylbenzene, 1-MN, naphthalene and 2-MN were the only LNAPL components detected in the Bottom section of this core (Fig. 3.2).

3.4 Materials and methods

3.4.1 Site description and soil core recovery

The study site has stored significant volumes of crude oil, as well as diesel and jet fuels, for over 50 years. It is approximately 50 km south of Perth, Western Australia. The site overlies a shallow superficial unconfined sand aquifer, which is located on the Swan Coastal Plain (Fig. 3.2) (*38*). The dominant surficial lithology is a Safety Bay Sands unit with deeper Becher Sand units; these lithographic units are relatively homogenous and composed of sub-horizontal layered aeolian and littoral calcareous sands (*38*). The sand is predominately fine to medium grained, with hydrophobic properties and some thin inter-bedded layers of course grained sands and gravel, with low concentrations of organic matter (*217*). Cores recovered from the site were taken from the predominantly homogenous aeolian and littoral calcareous sands as described in detail by Johnston et al. (1998) (*38*). Limited air-sparging, bioventing, LNAPL skimming, slurping, vacuum extraction and a mixture of such remediation techniques have been trialled on the site over time, however the site is now undergoing assessment and management through NSZD (*42*, *45*).

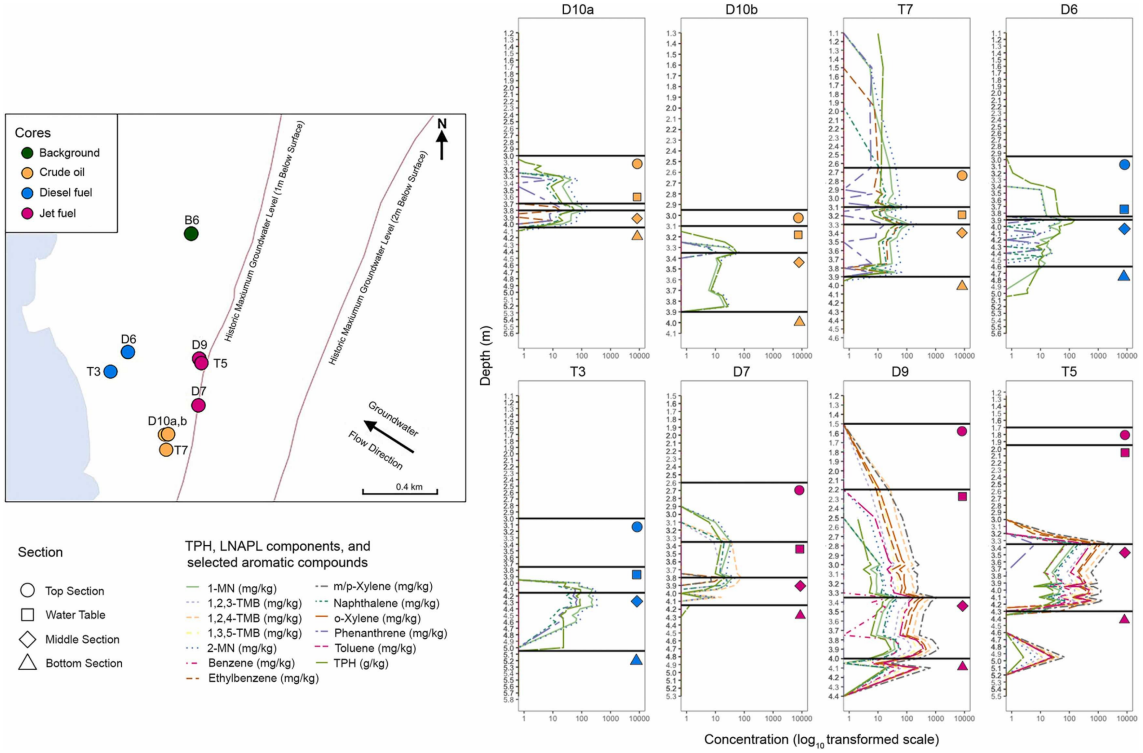


Fig. 3.2. Map of sampling sites. Map of sampling sites showing position of contaminated zones relative to maximum historic groundwater levels, and proximity to the Indian Ocean. The figure also shows the depth profile of the contaminated core sections after GC-FID and GC-MS analysis. The concentrations of TPH and the selected aromatic LNAPL components identified (1-methylnaphthalene (1-MN), 1,3,5-trimethylbenzene (1,3,5-TMB), ethylbenzene, o-xylene, 1,2,3-trimethylbenzene (1,2,3-TMB), 2-methylnaphthalene (2-MN), m/p-xylene, phenanthrene, 1,2,4-trimethylbenzene (1,2,4-TMB), benzene, naphthalene, and toluene) are shown. The solid horizonal black lines indicate the subsections within the core, along with concentrations at each sample section. Inferred and extrapolated linear lines are then used to postulate concentrations between the core sample sections. Different line types are used to differentiate between individual contaminants. The Background core is green, the Crude Oil cores are orange, the Diesel Fuel cores are blue and the Jet Fuel cores are pink. On the right-hand side of the figure, circles represent the Top section, squares represent Water Table section, rhombuses represent the Middle section and triangles represent the Bottom section (*176*).

Groundwater at the site is typically fresh with a low electrical conductivity (50–160 mS/m), has an average 2.28 m in depth (however this is seasonally dependent), and has a pH typically in the range 7.5–8.5 buffered by the calcareous nature of the superficial sand formation. Regionally nitrate and sulfate are present in groundwater due to agricultural and urban influences. However, within the site these electron acceptors (along with oxygen) are strongly depleted within groundwater due to natural attenuation processes (*23*). Bicarbonate ranges from 250 to 940 mg/L and dissolved methane is found across large areas of the groundwater due to hydrocarbon degradation processes (*218*). Methane production also indicates that other electron acceptors are strongly depleted (*219*).

Soil cores were recovered using a Geoprobe 6620 drilling rig (*220*). One core was recovered from a representative background control area unaffected by petroleum hydrocarbon contamination (B6), three cores were recovered from the crude oil contaminated area (T7, D10a and D10b), two cores were recovered from the diesel contaminated area (D6, T3), and three cores were recovered from the jet fuel contaminated area (D7, D9 and T5) (Fig. 3.2). The nine core locations were sampled from depths of 1.50–5.10 m below ground level. Each core was cut into 0.05 m sections, sealed in tins and immediately transported on ice to the CSIRO laboratory. Upon arrival at the laboratory, tins were sub-sampled for chemical and biological analysis. For each core, four representative sections were selected from the Top section (above the water table at an average of 2.28 m in depth), Water Table section (an average of 3.05 m in depth), Middle section (an average of 3.78 m in depth and below the water table), and Bottom section (an average of 4.48 m in depth) (Fig. 3.2) (*220*). Chemical analysis using GC-MS and GC-FID was undertaken on these 36 section samples. For biological analysis, triplicate samples (5 g), from each of the 36 sections, were collected using sterile techniques and stored at -80°C until DNA extraction. For chemical analysis, 3–5 g were sampled and immediately extracted using 4 mL of dichloromethane (containing deuterated internal standards) (d6-benzene, d8-toluene, d10-p-xylene, d8-naphthalene, d14-p-terphenyl) as described in Bruckberger et al. (2021). The Water Table section of the core was

differentiated from the other core sections by re-weighing the remaining core samples before and after drying, and comparing the moisture loss (*209*). This was achieved by initially air-drying a portion of the core section to remove excess chemicals for 48 h, and then heating it in an oven for 24 h at 105°C to calculate moisture loss (%) (*220*). Geochemical analysis of a subset of soil cores samples (24 in total) for a range of parameters (TOC, N, P, pH, moisture, electrical conductivity, Al, As, B, Ca, Cd, Co, Cr, Cu, Fe, K, Mg, Mn, Mo, Na, Ni, Pb, S, and Zn) was conducted at a government NATA accredited laboratory (ChemCentre, Western Australia) using standard methods (Fig. 3.2) (*221*).

3.4.2 Petroleum hydrocarbon chemical analysis

Total petroleum hydrocarbon (TPH) analysis of the core sample extracts was carried out using an Agilent 6890 gas chromatography–flame ionisation detector (GC-FID) system (*220*). Internal and petroleum hydrocarbon external standards were used. Gas chromatography–mass spectrometry (GC–MS) analysis of the core sample extracts was carried out using an Agilent 7890 gas chromatograph and an Agilent 7000B mass spectrometer (*220*). Quantitation of selected analytes was performed using external standards (benzene, toluene, ethylbenzene, m-xylene, p-xylene, o-xylene, 1,3,5-trimethylbenzene (1,3,5-TMB), 1,2,4-trimethylbenzene (1,2,4-TMB), naphthalene, 2-methylnaphthalene (2-MN), 1-methylnaphthalene (1-MN) and phenanthrene) containing the same internal standards used for the samples (Fig. 3.2).

3.4.3 16S rRNA gene amplification and bioinformatics

Genomic DNA was extracted from the 36 core sections in triplicate (36 × 3), using 0.5 g of soil and the PowerBiofilm DNA Isolation Kit (MoBio Laboratories, Inc., Carlsbad, CA, USA), and quantified with a Qubit fluorometer (Invitrogen) (*209*). A 300 base pair (bp) area of the V4 region of the 16S rRNA was amplified using the 515f (5'-GTGCCAGCMGCCGCGGTAA-3') and 806rcbc (5'-GGACTACHVGGGTWTCTAAT-3') primer set (*222*), following the Earth Micro-

biome Project protocol (https://earthmicrobiome.org/protocols-and-standards/16s/) and barcoding and sequencing library preparation followed the Illumina 16S protocol (Illumina, USA). After amplification the PCR products were individually purified with SPRI beads (Ampure XP beads, Beckman Coulter) and then barcodes added through a second round of PCR. Following a second round of bead-based purification, samples were quantified and pooled in an equimolar manner ready for sequencing. Forward and reverse sequencing was undertaken on the Illumina MiSeq (v3 600 cycle), following the manufacturer's instructions (Illumina, USA) (*209*). Data has been published online (https://data.csiro.au/collections/collection/CIcsiro:49662v1). Sequences were processed using QIIME2 version 2019.1 (*223*). The imported paired-end sequences were denoised and merged using the DADA2 workflow, which involved trimming the first 19 nucleotide bases from each read and truncating at 190 bases (*224*). This process utilises exact amplicon sequence variants (ASVs) instead of conventional OTU workflows. The ASVs were clustered using the de novo "q2-vsearch" clustering algorithm at 97% similarity, with borderline chimeras being retained (*225*). Representative OTU sequences were classified against the Silva 138 515F/806R database using the "classify-sklearn" algorithm (*226–228*). OTUs which were not classified as prokaryotes were removed. R Studio version 4.0.3 (*229*). Alpha diversity metrics (the number of OTUs and Chao1 estimator) were calculated from a single rarefaction at 10,000 reads per sample, this was selected after manual inspection of rarefaction curves and Good's coverage calculation (Fig. 3.2, 3.3). The Water Table and Middle section of the Jet Fuel core T3 failed to pass the rarefaction threshold and were excluded from further analysis. Homogeneity of variance for each metric grouped by Zone (Background, Crude Oil, Diesel or Jet Fuel) and Section (Top, Water Table, Middle, Bottom) were tested with Levene's test implemented in the "car" package. Two-way ANOVA tests of the alpha diversity estimates were used to test for statistically significant differences in microbial diversity between Zone and Section.

3.4.4 Predictive metagenomic profiling

For further analyses the dataset was rarefied 1000 times at 10,000 reads and averaged relative abundances retained. The resulting OTUs were then imported into PICRUSt2 v2.3.0 and placed into a reference phylogenetic tree, with metagenome content being predicted using an ancestral-state reconstruction algorithm to predict the metagenomes based on 16S marker gene information (*215*). The resulting tree was used for functional metabolic prediction, through the utilisation of Kyoto Encyclopedia of Genes and Genomes (KEGG) reaction pathways, with a minimal nearest-sequenced taxon index (NSTI) value of 2 set to improve accuracy of pathway assignment (*215*, *230*, *231*). The OTUs were split into four groupings, based on the predicted presence of chemotaxis and petroleum hydrocarbon KEGG degradation pathways.

The chemotactic and hydrocarbon degrading (CD) group included OTUs inferred to possess the pathways associated with bacterial chemotaxis (ko02030) as well as at least one of the hydrocarbon degradation pathways; benzoate degradation (ko00362), bisphenol degradation (ko00363), chloroalkane and chloroalkene degradation (ko00625), chlorocyclohexane and chlorobenzene degradation (ko00361), toluene degradation (ko00623), nitrotoluene degradation (ko00633), xylene degradation (ko00622), caprolactam degradation (ko00930), ethylbenzene degradation (ko00642), naphthalene degradation (ko00626) and/or polycyclic aromatic hydrocarbon degradation (ko00624) (*232*). It is important to highlight here that this does not explicitly mean that a given CD OTU is necessarily chemotactic directly towards one of the hydrocarbons, but that it may also include microbes that are chemotactic towards other compounds. The chemotactic (C) group included OTUs inferred to possess only the chemotaxis pathway and none of the hydrocarbon degradation pathways. The hydrocarbon degrading group (D) included OTUs inferred to possess at least one of the hydrocarbon degradation pathways and no bacterial chemotaxis pathway. Finally, the non-chemotactic and non-hydrocarbon degrading (NCND) group contains OTUs without inferred bacterial chemotaxis or any of the hydrocarbon degradation pathways. It is important to note that individual OTUs are assigned to a single

group based on their inferred functionality. Since OTUs within the same family may differ in their inferred functional grouping, it is possible for a single family to contain OTUs assigned to different functional groups.

3.5 Results

3.5.1 Molecular ecology, genetic diversity and statistical analysis

Family-level relative abundance heatmaps were generated to visualise the alpha diversity and taxonomic community composition of the predicted metagenomic groupings and their distribution across the site. A heatmap of the community composition of the groupings at a genera level is present in the supplementary information (Supplementary Information). The "vegan" package was used to visualise the beta diversity among the samples through non-metric multidimensional scaling (NMDS) ordination of the Bray-Curtis dissimilarity matrix (*233*). This approach is commonly used to inspect the dissimilarity of contaminated petroleum hydrocarbon sites (*234*, *235*).

Environmental drivers of community composition and CD OTU distribution were identified independently using constrained ordination and Generalised Linear Modelling (GLM). For both analyses multicollinearity of the environmental variables was assessed using the vifcor function in the "usdm" package to calculate variance inflation factors, with a correlation threshold of 0.7 being implemented to remove any strong multicollinear signals. Nine of the 13 variables had collinearity issues and were removed for further analyses (*236*). The remaining environmental variables were Depth, Naphthalene, Phenanthrene and Benzene. TPH was also omitted from further analysis due to a confounding relationship with the LNAPLs (*237*). This is because TPH can also be representative of colloids or sorbed phase hydrocarbons on particulate matter, as well as dissolved hydrocarbons and dissolved nonhydrocarbons, which leads to collinear relationship (*237*). The contaminant concentra-

tion and depth were standardised using the "decostand" function in the "vegan" package (*233*). Distance-based constrained redundancy analysis (db-RDA) of the Bray-Curtis dissimilarity matrix was performed using the "capscale" function in the "vegan" package in order to investigate which of the remaining parameters (depth, naphthalene, phenanthrene and benzene) drive structural differences between samples. Statistically significant variables were identified using step-wise model selection procedure implemented in the ordistep function in vegan with a cutoff p-value $<$ 0.05). This analysis was also used to explore the difference in the distribution of the various inferred functional chemotactic and hydrocarbon degrading groups. To aid clarity, the OTUs from each group were visualised separately on the common db-RDA axes.

A generalised linear model (GLM) assuming a binomial distribution, with a logit link function, was used to test the association between CD group microbes, depth and contaminant concentration. The model counts OTUs assigned to the CD group, as "successes" and OTUs assigned to the C, D and NCND groups as "failures". Variable selection was undertaken using a bi-directional step-wise model using the "MASS" package and the AIC criterion to select significant variables and model with a p-value of $<$0.05 (*238*).

This study tested the association and distribution of microbes and petroleum LNAPL contaminants based on their inferred chemotactic and hydrocarbon degrading ability across multiple vertical transects across the water table of a legacy petroleum hydrocarbon site undergoing NSZD. Samples with low contaminant concentrations, including all Background sections and the Top sections of the Diesel, Crude Oil and Jet Fuel cores, tended to have similar community structure and composition, whereas the composition of deeper, more contaminated sections was more influenced by contaminant type. Two independent analyses identified naphthalene concentration as a driver of community structure and CD OTU distribution. Concentrations of naphthalene were found to have a significantly positive relationship with the occurrence of predicted CD group microbes, while concentrations of benzene and

phenanthrene, along with depth, were significantly negatively related (Table. 3.1, Fig. 3.2). OTUs that were particularly influenced by naphthalene concentration were assigned to the four microbial families, *Pseudomonadaceae*, *Desulfocapsaceae*, *Comamonadaceae* and *Geobacteraceae*. Existing NSZD models do not incorporate the role of CD microbial taxa and the results presented here provide further evidence supporting their inclusion to improve prediction of risk and remediation of petroleum in subsurface environments.

3.5.2 Alpha diversity analysis

The 250 bp paired-end MiSeq run produced 5,057,077 reads, of which 4,786,072 reads passed all quality control, denoising and chimera removal steps. Rarefaction curves of observed and Shannon's diversity and a Good's coverage of 96.5–99.8% for all samples in the rarefied dataset suggest that 10,000 reads was appropriate and captures the vast majority of microbial diversity in most samples (Supplementary Information Fig. S2, S3). The Chao1 diversity estimator ranged from 169.5 (T5 Jet Fuel Bottom section) to 1377.003 (B6 Background Water Table) (Supplementary Information Fig. S3). Background 'Zone' samples had the highest alpha diversity within each section, except the Top section of D10b (Supplementary Information Fig. S3). Two-way ANOVA showed that the Zone (Background, Crude, Diesel or Jet Fuel) had a significant effect on the Chao1 diversity across the site ($F = 5.267$, $df = 3$, $P = 0.009$), but neither Section ($F = 2.665$, $df = 3$, $P = 0.08$) nor the interaction of Zone and Section ($F = 0.725$, $df = 9$, $P = 0.681$) had a statistically significant effect. Pairwise Wilcoxon rank sum tests using a Benjamin-Hochberg correction for multiple tests showed that Background samples had significantly higher alpha diversity than Diesel ($P = 0.048$) and Jet Fuel ($P = 0.024$) samples, but not Crude oil samples ($P = 0.059$) (Supplementary Information Fig. S2, S3). Multivariate dispersion was significantly lower for the Background Zone than all other Zones (betadisper $F = 13.26$, $df = 3$, $P < 0.001$; TukeyHSD $P < 0.001$ for all Background Zone pairwise comparisons), which indicated that Background sample Sections were highly similar to each other. After rarefaction, averaging and predictive metagenomic sequencing

analysis, 7583 unique bacterial and archaeal OTUs were identified and were assigned to Prokaryote taxa (Supplementary Information Fig. S2-S4).

3.5.3 Community composition analysis

Background Sections at all depths and Top Sections (Fig. 3.3) of most cores were characterised by high abundance of OTUs in the *Methylomirabilaceae*, *Nitrosopumilaceae*, *Nitrosotaleaceae*, *Nitrososphaeraceae*, and *Rokubacteriales*. Community composition was more variable in deeper sections of contaminated cores, but some common patterns were evident. The Middle and Bottom sections of most contaminated cores were charactersied by high abundance of OTUs in the *Anaerolineaceae*, *Methanocellaceae* and *Methanosaetaceae*, which are obligate anaerobes. *Aminicenantales* OTUs were common in the Crude and Diesel cores only, whereas *Smithellaceae* and *Methanoreulaceae* were more abundant in Diesel and Jet Fuel cores. In contrast, the Middle Sections of Crude core T7 and Jet Fuel core D9 were characterised by communities that included a high abundance of OTUs in the *Geobacteraceae* and *Pseudomonadaceae*. No *Geobacteraceae* OTUs were detected in the Background core, with *Pseudomonadaceae* OTUs only being detected in low abundances in the Bottom section. Methanogenic families (e.g. *Methanocellaceae* and *Methanosaetaceae*) were notably present throughout the site (Fig. 3.3).

After grouping by inferred functional potential, the CD group contained 1831 OTUs, and were most commonly assigned to *Geobacteraceae*, *Comamonadaceae*, *Smithellaceae*, *Methanoregulaceae*, *Methanocellaceae*, *Nitrosopumilaceae*, *Pseudomonadaceae*, and *Desulfocapsaceae* (Supplementary Information Fig. S5a). The D group contained 3411 OTUs, which were most commonly assigned to families including *Nitrosotaleaceae*, *Anaerolineaceae*, *Methylomirabilaceae*, *Woesearchaeales*, *Methanocellaceae*, *Methanobacteriaceae*, *Rokubacteriales*, *Dysgonomonadaceae*, and *Nitrosopumilaceae*. The C group contained 938 OTUs, with high abundance families including *Rokubacteriales*, *Hungateiclostridiaceae* and *Omnitrophaceae*. Finally, the NCND contained 1403 OTUs with those assigned to *Anaerolineaceae*, *Aminicenan-*

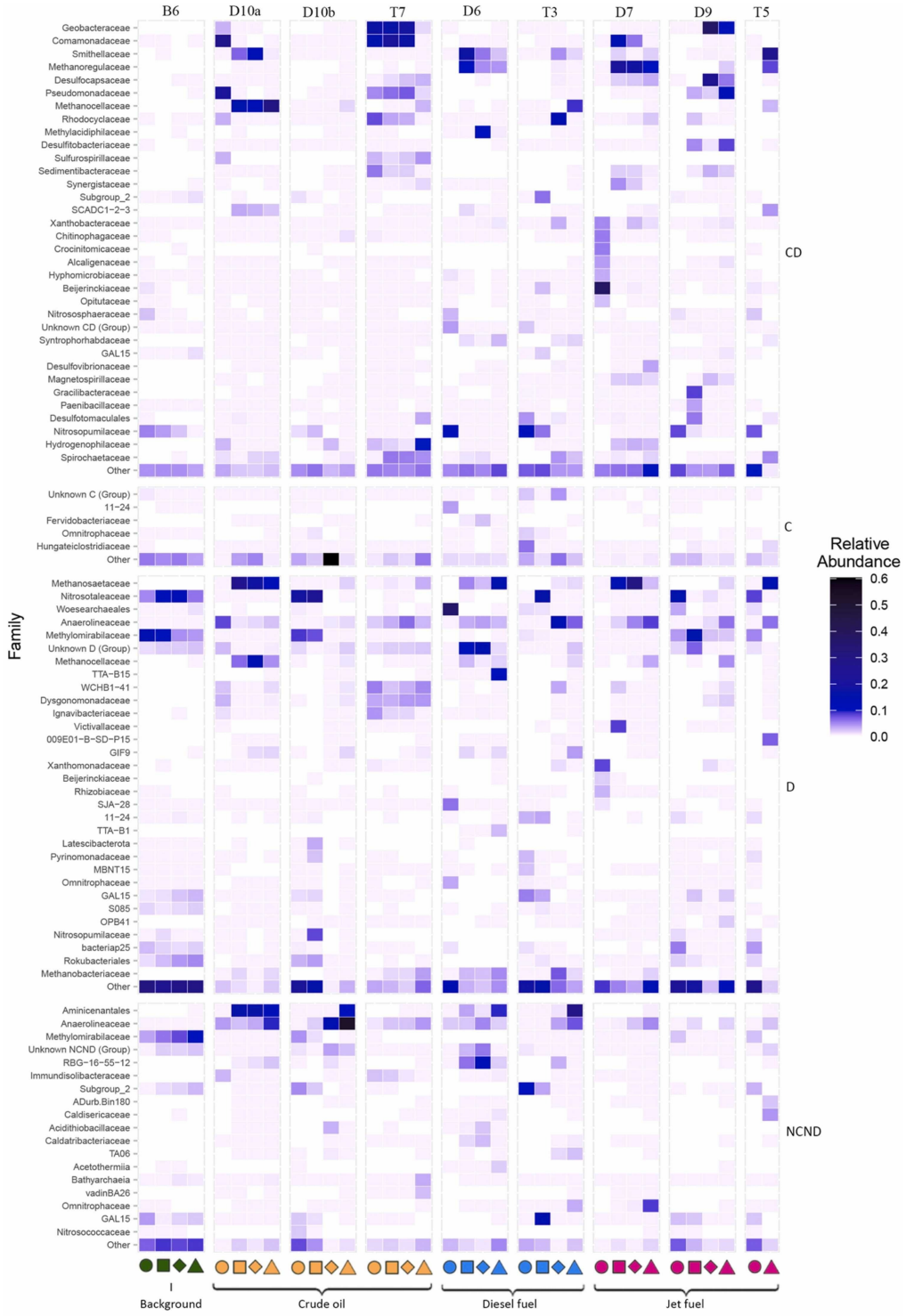


Fig. 3.3. Microbial community heatmap. Community composition heatmap of relative abundances arranged by similarity of distribution of the families in their chemotactic and hydrocarbon degrading groups based on predictive metagenomic profiling. The heatmap is faceted by group, with the purple shading representing their relative abundance. The Other taxa of each group contains microbes with a maximum relative abundance <2%; including uncultured taxa, with unknown taxa also being shown. The y-axis is arranged by similarity of distribution, with the x-axis being arranged by core section and contamination zone. The Background core is green, the Crude Oil cores are orange, the Diesel Fuel cores are blue and the Jet Fuel cores are pink. On the right-hand side of the figure circles represent the Top section, squares represent Water Table section, rhombuses represent the Middle section and triangles represent the Bottom section (*176*).

tales and *Methylomirabilaceae* being most abundant (Fig. 3.3).

3.5.4 Beta diversity analysis

Non-metric multidimensional scaling (NMDS) ordination was undertaken on the cores across the site. NMDS enabled a way to condense information from multidimensional data, into an interpretable two-dimensional dissimilarity ordination plot. In this molecular ecological ordination, if the points were closer, then the corresponding OTUs within the samples were more closely related (Fig. 3.4).

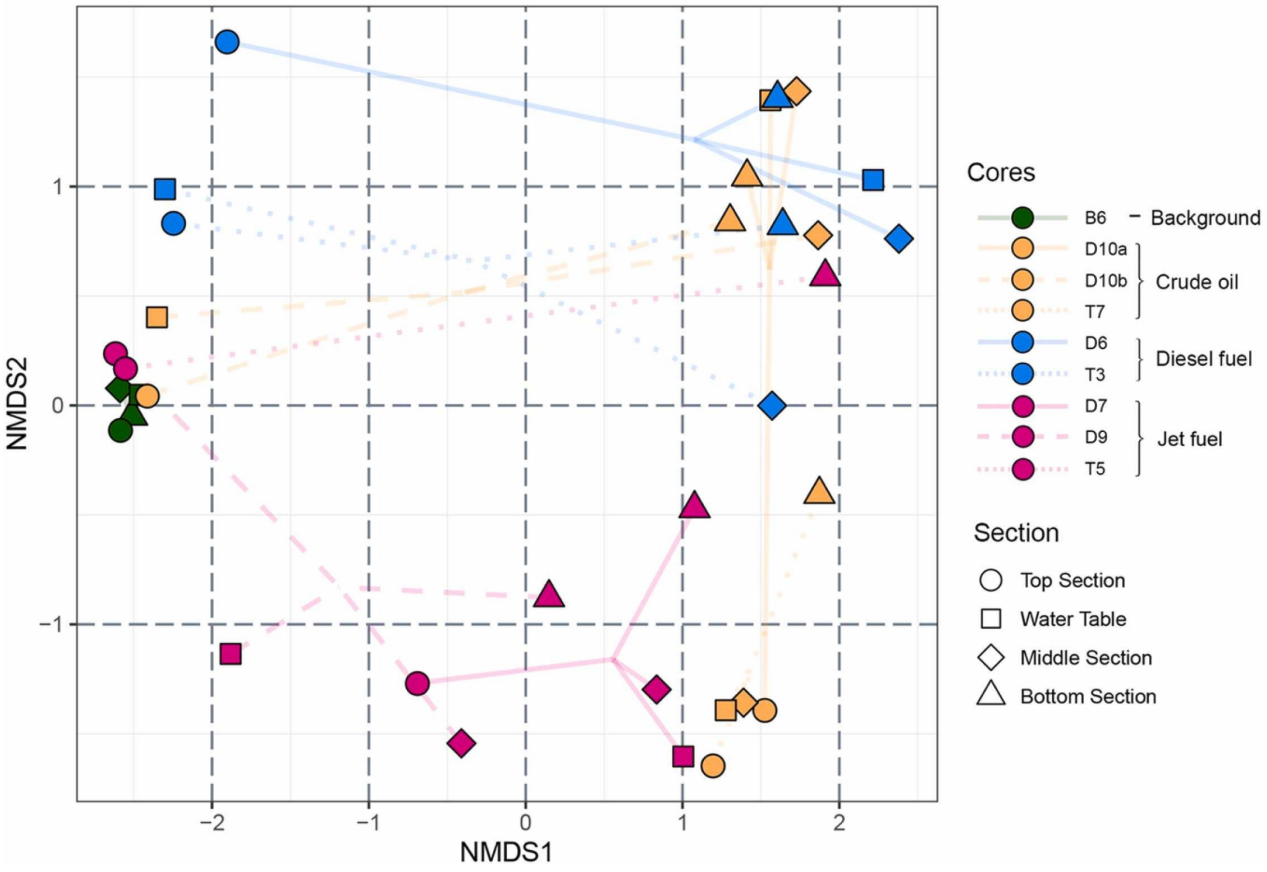


Fig. 3.4. Non-metric multidimensional scaling (NMDS) Bray-Curtis. Dissimilarity plot of core sections representing beta diversity. The stress of the ordination is 0.07 and has been computed in 3 dimensions, with the first and second axis being presented. The Background samples are green, Crude Oil is orange, Diesel Fuel is blue and Jet Fuel is pink. Circles represent the Top section, squares represent Water Table section, diamonds represent the Middle section and triangles represent the Bottom section, various line-types are used to connect samples from the same core (*176*).

The Background core samples from all depths clustered together, indicating that they were highly similar in composition (Fig. 3.4). The majority of the Top sections of the Jet fuel, Diesel and Crude Oil clustered with the Background. The other contaminated sections formed two loose clusters: one comprised the Middle and the Bottom sections of the Diesel and Crude Oil cores; the other comprised samples from the Jet Fuel cores, T7 core and Top section of D10a (both Crude Oil).

3.5.5 Environmental drivers of community structure and CD group OTU distribution

Constrained ordination analysis was performed in order to better understand the drivers of differences in community composition. The stepwise model selection procedure selected depth and naphthalene contamination as significant variables (Fig. 3.5 and Supplementary Information Fig. S6). Constrained ordination of a subset of samples for which a more extensive chemical analysis was available further confirmed naphthalene and depth as significant variables in addition to pH and arsenic concentration (Supplementary Information Fig. S7). The following results and discussion focused on the results for the statistically robust full sample dataset since both analyses identified naphthalene as a major explanatory vector orthogonal to depth, and the pH vector was congruent with the depth vector. Congruent with the NMDS result, Background Zone samples clustered with samples from Top and Water Table Sections and were influenced by low naphthalene and depth with low contamination levels (Fig. 3.5A). The additional analysis of the subset of samples suggests that higher arsenic may also contribute to this observation (Supplementary Information Fig. S7). However, the composition of samples from some Jet Fuel and Crude Oil Zones were strongly influenced by high naphthalene levels (Fig. 3.5A).
The side-by-side comparison of the db-RDA plots enabled easier interpretation of the relationship between the OTUs in the predicted chemotactic and hydrocarbon degrading groups and depth and naphthalene (Fig. 3.5B, Table. 3.1). The distribu-

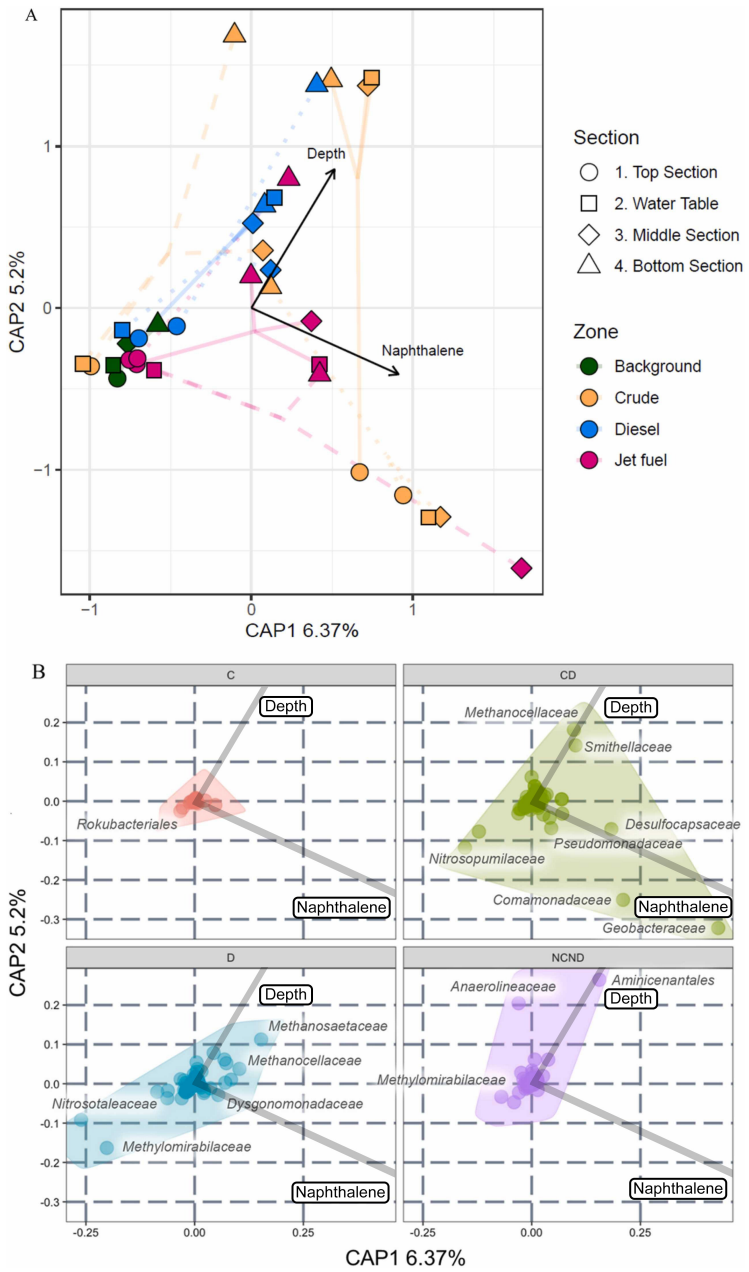


Fig. 3.5. Distance-based Bray-Curtis constrained redundancy ordination analysis (db-RDA). The figures show both samples and individual OTUs. In both figures naphthalene and depth are the significant variables. (A) A db-RDA of samples and significant variables ($p < 0.05$) following step-wise model selection. Naphthalene and depth are the significant variables, with the length of the arrows gauging relative significance of each variable, the longer the arrow the greater the influence the variable has. The first axis (CAP1) explains 6.37% of variation across samples, with the second axis (CAP2) explaining 5.2% of variation, with the db-RDA explaining 13.2% of total variation. The Background samples are green, Crude Oil is orange, Diesel Fuel is blue and Jet Fuel is pink, with core sections through the water table being illustrated by shapes, and the different line types showing the differences between the cores. Circles represent the Top section, squares represent the Water Table section, diamonds represent the Middle section and triangles represent the Bottom section, line-types link core samples. (B) Different chemotactic and hydrocarbon degrading groups, the taxa of notable OTUs and how they are driven by significant variables within the db-RDA. The C group is red, the CD group is green, the D group is blue and the NCND group is purple (*176*).

Table. 3.1. Generalised linear model. Statistical summary of the generalised linear model developed to investigate chemotaxis and hydrocarbon degradation across the legacy petroleum hydrocarbon site.

	Dependentvariable
	Frequency of CD OTUs vs.non-CD OTUs
Depth	*Estimate* –0.040
	Pr(>|z|) = 0.0137*
Benzene	*Estimate* –0.201
	Pr(>|z|) = <2e-16***
Naphthalene	*Estimate* 0.273
	Pr(>|z|) = <2e-16***
Phenanthrene	*Estimate* –0.125
	Pr(>|z|) = 1.1e-11*
Constant	*Estimate* –0.936
	Pr(>|z|) = <2e-16***
Observations	34
Log Likelihood	–545.707
Akaike Inf. Crit	1,101.413

Note: *p < 0.1; **p < 0.05; ***p < 0.01

tion of a subset of OTUs appeared to be influenced by naphthalene contamination and all were assigned to the CD group (Fig. 3.5B). Separate subsets of OTUs assigned to the CD, D, and NCND groups were predicted to be influenced by depth. The OTUs assigned to the C group were not strongly influenced by either variable.

The subset of CD OTUs influenced by naphthalene were assigned to the four microbial families, *Pseudomonadaceae*, *Desulfocapsaceae*, *Comamonadaceae* and *Geobac-*

teraceae. The subset of CD OTUs influenced by depth were assigned to three families, *Methanocellaceae*, *Nitrosopumilaceaes* and *Smithellaceae*.

A generalised linear model (GLM) assuming a binomial distribution with a logit link function was used to test the relationship between the occurrence of CD OTUs vs. Non-CD (C, D, NCND) OTUs and contaminant concentration and depth (Table. 3.1). CD OTU occurrence was found to be significantly influenced by naphthalene contamination across the site, with a significantly negative relationship with depth, as well as the concentration of the soluble aromatic components, benzene and phenanthrene, across multiple vertical transects across the water table (Table 3.1).

3.6 Discussion

3.6.1 The role of predicted chemotactic and hydrocarbon degrading communities in NSZD

As expected, CD OTUs were found to have higher relative abundances in the contaminated cores (Crude Oil, Jet Fuel and Diesel) in contrast to the Background core (Fig. 3.3). Naphthalene concentration was identified as a driver of CD OTUs distribution (Fig. 3.5 A & B, Table. 3.1). These CD OTUs were assigned to the microbial families *Geobacteraceae*, *Comamonadaceae*, *Pseudomonadaceae* and *Desulfocapsaceae*, and appear to co-occur in samples with similar community composition (Fig. 3.3, 3.5 B). Furthermore, the families *Pseudomonadaceae*, *Comamonadaceae* and *Geobacteraceae* have been noted to contain members which are electroactive microbes and family members are involved in the formation of biofilms which can further enhance the degradation of petroleum hydrocarbon compounds (*239*, *240*).

Comamonadaceae family members have been reported in other legacy contaminated sites in Kuwait (*241*). The family includes specific genera, such as *Comamonas*

which is similar to some *Pseudomonas* species in its biology, ecology and ability to metabolise aromatic compounds (*242*). However, they generally do not assimilate carbohydrates for growth, preferring organic acids and aromatic compounds (*243*). The *Acidovorax sp.* strain JS42 is a notable example of a CD group microbe of the *Comamonadaceae* family and has been specifically associated with aromatic and nitroaromatic degradation at manufacturing sites (*244*).

All *Geobacteraceae* OTUs were classified as CD group taxa. Previous work has shown that members of this family can degrade multiple hydrocarbons in LNAPLs and are strictly anaerobic (*245*, *246*). However, chemotaxis towards hydrocarbons has not been observed; this does not mean it is impossible, however *Geobacteraceae* species have been shown to be chemotactic towards Fe (II) or Mn (II) oxide (*177*, *247*, *248*). It is therefore likely that *Geobacteraceae* OTUs are chemotactic towards compounds other than hydrocarbons, and that they may instead be considered part of the D group.

Pseudomonadaceae are part of the *Gammaproteobacteria* class of microbes, with this class being reported previously in high abundances throughout cores of a legacy petroleum hydrocarbon contaminated site in Kuwait (*241*, *249*). All of the CD group OTUs from this family were from the genus Pseudomonas, species of which are generally aerobic Gram-negative rod-like bacteria, however some members can also survive in certain anaerobic environments, due to their facultatively anaerobic nature (Supplementary Information Fig. S4) (*103*, *250*). Many *Pseudomonas* species are able to degrade and/or metabolise many petroleum hydrocarbon compounds, as well as being highly chemotactic towards aromatic hydrocarbons found in petroleum LNAPL zones, thereby potentially assisting in NSZD (*103*, *250*, *251*).

Members of *Geobacteraceae* and *Pseudomonadaceae*, *G. sulfurreducens* and *P. aeruginosa*, have been reported to facilitate interspecies electron transfer (IET). This permits extracellular electron exchange in environments of mixed resources (*252*). *P. aeruginosa* has been reported to exhibit both direct interspecies electron transfer (DIET) and hydrogen interspecies electron transfer (IET) with *G. sulfurreducens*

(*252*). This could be another reason for their co-occurrence and is worthy of further investigation. The scope and nature of chemotaxis in the *Geobacteraceae* family poses compelling questions (*247*). Further research needs to be undertaken to determine if members of the *Geobacteraceae* family are chemotactic toward hydrocarbons, and their co-occurrence with *Pseudomonadaceae* species is due to their synergetic DIET relationship (*252*). Alternatively, their positioning within the subsurface could be due to a bacteria-bacteria transport (*190*). This mode of transport is where *Pseudomonadaceae* or other microbes which are chemotactic directly towards petroleum hydrocarbons drag the generally non-motile *Geobacteraceae* along its chemotactic gradient towards hydrocarbon compounds (*186*, *187*, *190*).

The other CD OTU influenced by naphthalene is assigned to the genus *Desulfoprunum*, in the *Desulfocapsaceae* family (Supplementary Information Fig. S5 B and S5 C, Fig. 3.5B). This genus has been recorded at hydrocarbon contaminated sites previously and are capable of using benzoate during sulfate reduction (*253*, *254*). Chemotactic responses of this family and genera however have not been directly observed but were inferred from the functional potential of genes present in metagenome-assembled genomes (MAGs) found as epibionts in *Rimicaris exoculata* shrimp in deep-sea hydrothermal vents and assigned to this family (*255*). The KEGG pathway for naphthalene degradation includes benzoate degradation as a possible next step in naphthalene degradation, as well as being a central intermediary in the degradation of other petroleum hydrocarbons (*253*, *254*). OTUs assigned to the families *Pseudomonadaceae*, *Comamonadaceae* and *Geobacteraceae* all possess this pathway (Supplementary Information Fig. S5 B). The negative relationship with depth and CD OTU presence could be explained by the fact many of the CD microbes are more tolerant of various environments and prefer to be where the attractant (food source) is present (*103*, *160*, *245*, *246*).

Overall, these results indicate the presence of CD group OTUs (that is, OTUs that were predicted to have the functional potential for chemotaxis and hydrocarbon degradation) is positively associated with naphthalene contamination and thus sug-

gests a role for chemotaxis assisted degradation contributing to NSZD of petroleum hydrocarbons. In addition, these results have generated novel hypotheses regarding the contribution of the four OTUs significantly associated with naphthalene. Further research is needed to characterise the role of the CD OTUs in the families *Pseudomonadaceae*, *Desulfocapsaceae*, *Comamonadaceae* and *Geobacteraceae* in order to define their contribution to NSZD. Further research will lead to a more accurate understanding of the role chemotaxis plays in NSZD and lead to better mitigation of risk from petroleum releases.

3.6.2 Community connections between CD and D group microbes

A subset of CD OTUs assigned to *Smithellaceae* (assigned to the genus *Smithella*) and *Methanocellaceae* (assigned to the genus *Methanocella*) were found to be significantly associated with increasing depth. *Smithellaceae* were recorded throughout the site, however at an elevated presence in the cores D10a (Crude Oil), T5 (Jet Fuel), and D6 (Diesel). Members of the family are sulfate-reducing, strictly anaerobic and hydrocarbon degrading microbes, which may possess the ability for chemotaxis (*256–258*). Family members have been linked with playing a role in anaerobic syntrophic food chains (*257*, *258*). Interestingly, a CD OTU in the *Methanocellaceae*, a petroleum hydrocarbon degrading and potentially chemotactic family co-occurred with a CD OTU in the *Smithellaceae* (Fig. 3.3). Co-occurrence of these families has been previously reported by others (*258–260*). Members of the *Methanocellaceae* are capable of both anoxic and oxic methanogenesis (*261*). Methanogenesis has been commonly reported in groundwater at the site (*218*). This could explain its presence above and below the water table in cores D6 and D7, where it has been hypothesised to act as scavengers for hydrogen, working with Smithellaceae and other related families (*258*).

Although our study has focused on inferred chemotaxis assisted hydrocarbon degradation, the role of other non-chemotactic functional groups in NSZD is of inter-

est. For example, Tischer et al. (2013), described a methanogenic and potentially hydrocarbon degrading consortium that included CD group taxa, such as *Smithellaceae* and *Methanocellaceae* and D grouped taxa such as members of the acetoclastic *Methanosaetaceae* family and the hydrogenotrophic family *Methanoregulaceae* (*258*). Interestingly, this consortium was able to reduce volatile fatty acid accumulation, therefore liberating the molecules required to enhance chemotactic activity within the subsurface (*262*). Methanogenic families, such as *Methanobacteriaceae* have been reported previously at legacy petroleum hydrocarbon sites such as the Huabei Oilfield, China (*263*). Interestingly, some *Acinetobacter* species are known to be capable of chemotaxis assisted alkane and hydrocarbon degradation, however the OTUs assigned to *Acinetobacter* species in this study were found to be assigned to the D group which were predicted to be non-chemotactic. This further emphasises the importance of this functional group in NSZD. In summary, the D group microbes are potentially a valuable avenue of further study, both to evaluate CD community interaction and to understand their combined role in NSZD (*212*, *213*).

3.6.3 Relevance of the microbial interaction triggering a shift in the *Geobacteraceae* distribution within the subsurface

Finally, the study also found that the spatial distribution of *Geobacteraceae* within the subsurface may be influenced by the chemotactic movement and interactions of *Comamonadaceae* or *Pseudomonadaceae* towards petroleum hydrocarbons within the subsurface (*177*).

Geobacteraceae is a member of obligate anaerobic family of microbes, which are sensitive to oxygen. In this study however, it was detected at shallower depths within the subsurface than expected, where oxic zones existed (*177*). It is thought it may have been transported to the shallower subsurface by biomobilisation, resulting in a change in their natural spatial distribution (*177*). The *Geobacteraceae* family

contains various petroleum hydrocarbon degrading genera, notably *Geobacter*, a widely reported degrader of aromatic hydrocarbons, such as benzene (*245*, *246*). This genus is inferred to have three primary mechanisms for anaerobic activation and degradation of benzene: carboxylation to benzoate, methylation to toluene, or hydroxylation to phenol, as the genome encodes pathways for anaerobic benzoate, toluene and phenol (*264*). The lack of monooxygenase genes in the genome of some *Geobacter* strains, indicates that anaerobic degradation pathways are preferred over aerobic metabolism pathways (*264*).

It is worth noting *Geobacter* has also been reported under certain environmental conditions to be motile, when grown on insoluble iron; Fe (III) or manganese; Mn (IV) oxide, and responds chemotactically to Fe (II) or Mn (II) oxides (*247*, *265*). Therefore it is important to assess if such conditions were present at the legacy site near Perth, Western Australia. Geochemical analysis of soil cores was conducted as part of the study and no significant relationship with a range of parameters including: Fe (ppm), Mn (ppm) and electrical conductivity was found (Supplementary Information Fig. S1, S5). This supports the idea that chemotactically assisted biomobilisation by bacteria in the *Comamonadaceae* or *Pseudomonadaceae* families, could be the cause of the unusual distribution of *Geobacteraceae* families within the subsurface (*177*). This phenomenon could also influence the distribution of non-chemotactic hydrocarbon degrading (D) taxa at the site.

Interestingly, if the CD taxa and the D taxa detected at the site are combined into a mixed community (CDD), the preferential accumulation in areas of naphthalene contamination still occurs (*177*). This could suggest that the distribution of other functional groups, could be influenced by a biomobilisation effect (*177*, *266*). This microbial transport and biomobilisation triggered by a potential chemotactic response is important to explore and quantify in order to produce an accurate reflection of NSZD and risk to the groundwater supply and reiterates the fact that the third key question of this thesis needs to be addressed (Fig. 1.2).

Chapter 4

Methods of bioengineering bacteria and development of a novel quantitative soft-swim fluorescent chemotaxis laser scanning assay (qSS-FCLSA)

4.1 Introduction

In order to achieve the study's objectives and answer the third key question relating to determining how chemotactic bacteria interact with non-chemotactic bacteria the third question was necessary to use a laboratory-based approach and construct several strains of bacteria of varying degrees of chemotactic ability and motility. It is also was necessary to conducted exploratory laboratory analysis to develop a novel quantitative soft-agar swim fluorescent chemotaxis laser scanning assay (qSS-FCLSA).

The various chemotaxis assays and methodologies utilised investigating in tackling this problem are outlined in figure 4.1.

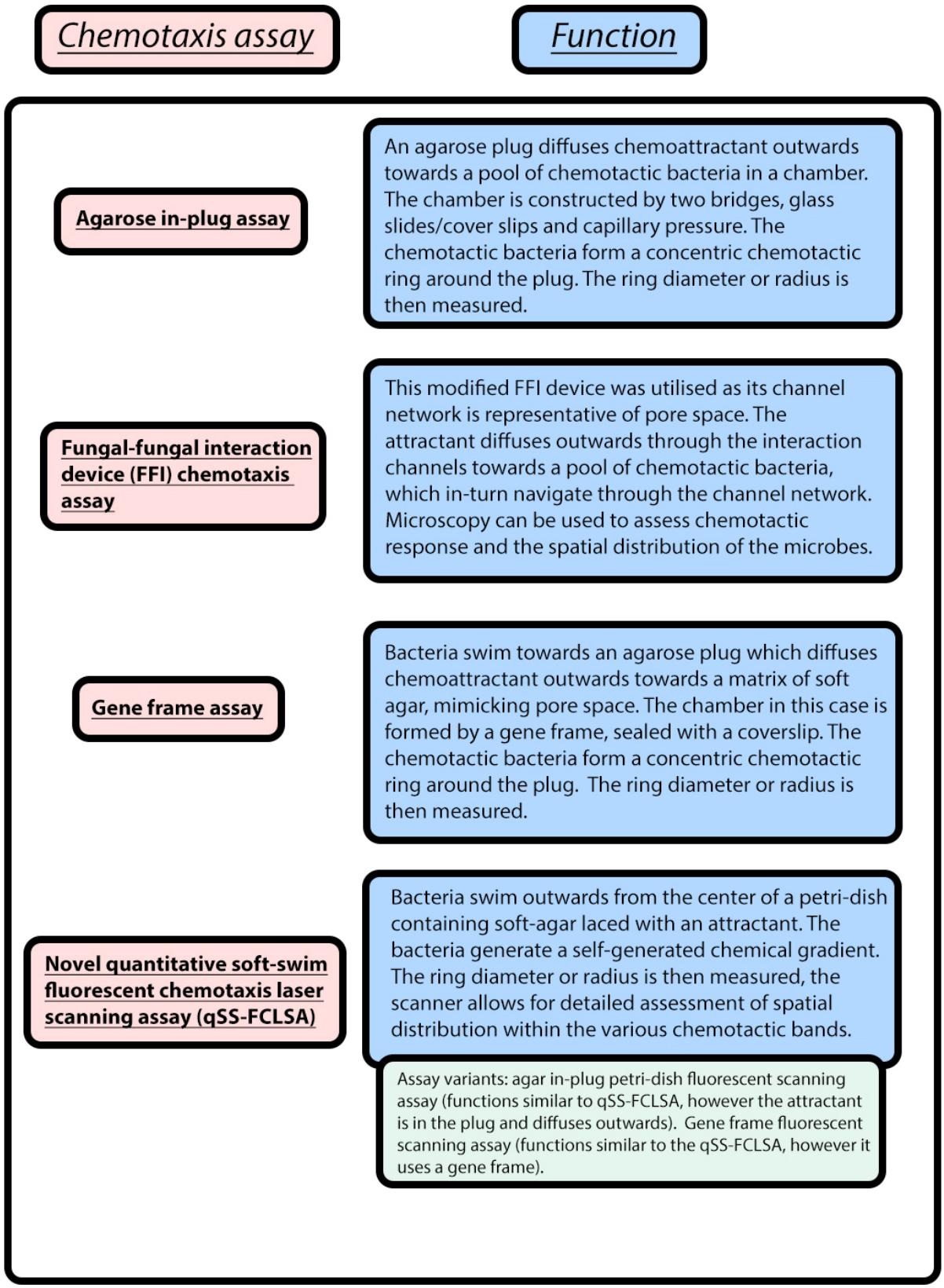


Fig. 4.1. Development and testing of chemotaxis assays. This figure highlights the four different assays; agarose in-plug assay, fungal-fungal interaction device (FFI) chemotaxis assay, gene frame assay and the novel quantitative soft swim agar chemotaxis laser assays, which were developed and tested.

Pseudomonas, as previously mentioned, is an aerobic Gram-negative rod-like bacterium prevalent in chemotactic and hydrocarbon degrading bacteria, commonly extracted from contaminated environments. Therefore, *P. putida* was chosen for genetic engineering work to create mutants of varying degrees of chemotactic ability and motility. In-part this is also due to its versatility and amenability to genetic engineering (*267*). The goal of this second laboratory-based study was to construct strains of varying degrees of chemotactic ability and the methodology of construction follows.

4.2 Laboratory set-up, safety and microscopy

A BioMAT 2 Class 2 Microbiological Safety Cabinet (MSC) was used when sub-culturing and handling all bacterial strains. This was always sterilised under UV light (254 nm) for 30 minutes to avoid contamination. Chemical fume hoods (Clean Air Ltd) were used when handling toxic or noxious chemicals, along with all standard health and safety procedures and aseptic techniques.

All petri-dishes used for plating were standard 90 mm x 15 mm petri-dishes (Fisherb rand^{TM}), with the Gibson©P1000 pippete range and associated tips being used throughout. Parafilm was commonly used to close the petri-dishes and reduce the risk of contamination (Bemis^{TM} Parafilm^{TM} M). All biological and chemical waste was treated with Rely+On^{TM}Virkon and autoclaved as required. Controls were used throughout the ProFlex^{TM} PCR process, with autoclaved Milli-Q© being used as a negative control, with antibiotics being used primarily to maintain plasmid fluoresce, selection and to protect against contamination. All H_2O mentioned henceforth in the methodology is autoclaved Milli-Q© and all the antibiotics are Sigma, unless otherwise stated.

Random checks for cell motility and contamination were undertaken throughout, using a Nikon Eclipse Ts2 inverted microscope and a Nikon Eclipse Ti inverted microscope, both equipped with an air immersed $\times 20/0.3$ numerical aperture and

Plan Fluor objective (Nikon, Switzerland).

Both microscopes were equipped with; a high-power light emitting diode (LED) light engine (LedHUB, Omicron-Laserage Laserprodukte GmbH, Germany) which was used as the source of excitation to produce fluorescence images. An LED of 465 nm was employed to excite the *P. putida* strains which expressing eGFP and GFP, and a LED of 544 nm being used to excite *P. putida* strains expressing dsRed and mScarlet-I. The microscope was also equipped with the following filters: a) band pass filters (Omicron-Laserage Laserprodukte GmbH; 465 nm), b) beam splitters (AHF Analysentechnik AG, Germany; 495 nm and 565 nm) and c) emission filters (AHF Analysentechnik AG; 525/50 nm and 605/70 nm) (*268*). The Nikon Eclipse Ti microscope was also combined with a Retiga R1 CCD camera (Qimaging, Canada) (*268*). Additionally, a motorised stage (Scan III, Prior Scientific, UK), mounted within a dark temperature-controlled incubator (Okolab, Italy), was set to 30°C. The Nikon Eclipse Ts2 was also equipped with a Nikon Digital Sight 1000. The NIS-Elements Advanced Research imaging software (Nikon, Switzerland) was used to view the devices and fluorescent cells.

4.3 Microbial strains, construction of mutants and preparation

This study utilised eleven *Pseudomonas putida* strains and mutants, along with three *E. coli* strains and mutants (Table. 4.1). Several existing strains of *P. putida* F1 and *P. putida* KT2440 are also used during assay development and evaluation. The advantage of the "chemotaxis mutant toolkit" is they can all metabolise the same attractant, succinate, with toluene and acetate also being used (*269*). It is important to note here that the *P. putida* F1 wild-type (WT) strain generally has a lophotrichous flagella arrangement, i.e., several flagella at one of the poles of the cell (*80*). Additionally, *E. coli* was used throughout this study to carry plasmids and assist in the bioengineering of the *P. putida* F1 cells (Table. 4.1) (*82*, *83*, *103*).

Table. 4.1. List of strains and mutants used in this study.

Bacteria	Chemotaxis	Motility	Fluorescence	Description	Source/Reference
P. putida **F1 wild-type (WT)**	+	+	-	Type strain isolated from a polluted creek in Urbana, Illinois.	Provided by Rebecca Parales, The University of California, Davis, USA [99]
P. putida **F1 cheA**	-	+	-	Smooth swimming non-chemotactic mutant (cheA::mini-Tn5; Km^{Res}).	Kind gift from Rebecca Parales, The University of California, Davis, USA [139]
P. putida **F1 mScarlet-I (pMRE135)**	+	+	+	Insertion of broad-host range plasmid to constitutively express red fluorescent protein genes within the *P. putida* F1 chemotactic wild-type (WT).	This study
P. putida **F1 cheA mScarlet-I (pMRE135)**	-	+	+	Insertion of broad-host range plasmid to constitutively express red fluorescent protein genes within the *P. putida* F1 cheA mutant.	This study
P. putida **F1 cheA pEMG-fliM**	-	+	-	Smooth swimming non-chemotactic mutant (cheA::mini-Tn5; KmRes), carrying the pEMG-fliM plasmid.	This study
P. putida **F1 cheA pEMG-fliM pSW-I**	-	+	-	Smooth swimming non-chemotactic mutant (cheA::mini-Tn5; KmRes), carrying the pEMG-fliM & pSW-I cointegrate.	This study
P. putida **F1 cheA ΔfliM**	-	-	-	Deletion of the fliM gene within the *P. putida* F1 cheA mutant.	This study
P. putida **F1 cheA ΔfliM mScarlet-I (pMRE135)**	-	-	+	Insertion of broad-host range plasmid to constitutively express red fluorescent protein genes within the non-chemotactic and non-motile *P. putida* F1 cheA ΔfliM.	This study
P. putida **KT2440 GFP**	+	+	+	Insertion of miniTn7-gfp at an extragenic location near glmS within the chemotactic *P. putida* KT2440 strain.	Provided by Isha Hashmi at the University of Neuchâtel, Switzerland [195]
P. putida **KT2440 ΔfliM dsRed**	+	-	+	Deletion of the fliM gene by allelic exchange, rendering the mutant non-motile, with insertion of a dsRed fluorescent protein-encoding gene at a neutral position in the genome.	Provided by Isha Hashmi at the University of Neuchâtel, Switzerland [149]
P. putida **F1 eGFP**	+	+	+	Mini Tn5-Pcirc-egfp inserted chromosome into the chemotactic *P. putida* F1 WT strain.	Provided by Vladimir Sentchilo, University of Lausanne, Switzerland [256]

Bacteria	Function	Source/Reference
E. coli **DH5 αλpir (pEMG)**	Carrying the pEMG plasmid.	Provided by Angeles Hueso-Gil, Centro de Biotecnología y Genómica de Plantas, Spain [150]
E. coli **DH5 αλpir (pSW-I)**	Carrying the pSW-I helper plasmid.	Provided by Angeles Hueso-Gil, Centro de Biotecnología y Genómica de Plantas, Spain [150, 277]
E. coli **S17-1 λpir mScarlet-I (pMRE135)**	Carrier of the mScarlet-I (pMRE135) plasmid.	Purchased from Addgene (Plasmid #118489) [222]

A summary of the strains used follows:

Pseudomonas putida F1 WT and *P. putida* F1 cheA were kindly provided by Rebecca Parales, The University of California, Davis, USA. The *P. putida* F1 WT strain as previously mentioned in the literature review of chapter two and the paper in chapter three, is hydrocarbon degrading and chemotactic to a wide range of petroleum hydrocarbon compounds. Meanwhile, the *Pseudomonas putida* F1 cheA mutant, is a smooth swimming, non-chemotactic petroleum hydrocarbon degrading mutant (*270*). *P. putida* F1 cheA has one of the longest known *cheA* polypetides and is 747 amino acids long (*270*). The removal of the *cheA* gene interferes with the

transmission of chemotactic signals to the *cheY* proteins which govern the "switch proteins" in the flagella motor (Fig. 4.2) (*270*). This modified strain also carries kanamycin resistance inside the mini-Tn5 derived transposon, with figure 4.2 illustrating the location of the genes upstream/downstream of the *cheA* gene (Fig. 4.2) (*103*, *270*, *271*).

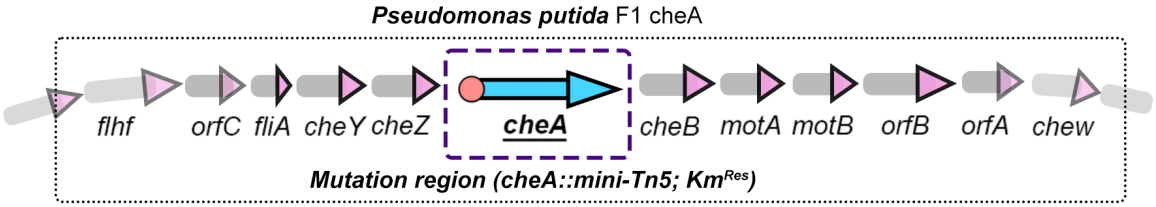


Fig. 4.2. Chemotaxis gene order of *P. putida* F1 cheA Chemotaxis genes are generally found in clusters and are shown in transparent grey and pink. However, gene organisation is not absolutely conserved and can deviate in order. The cheA gene is highlighted in blue and underlined, along with the site of the mini-Tn5-Km^{Res} insertion in vermilion. After Ditty et al., (1998) (*270*).

Pseudomonas putida F1 mScarlet-I (pMRE135), *P. putida* F1 cheA mScarlet-I (pMRE135) and *P. putida* F1 cheA ΔfliM mScarlet-I (pMRE135) are novel strains constructed for this thesis. The mScarlet-I fluorescent protein is part of a series of red synthetic proteins and is used because of its fast maturation rate. Upon cell death the fluorescence lingers, then decreases due to protein breakdown, with the rate governed by various conditions (*272*, *273*). The methodology for the construction of these mutants construction is outlined below. *P. putida* KT2440 GFP and *P. putida* KT2440 ΔfliM dsRed strains were graciously provided by Dr Isha Hashmi at the University of Neuchâtel, Switzerland. Lastly, a further *P. putida* F1 eGFP strain was provided by Vladimir Sentchilo at the University of Lausanne, Switzerland. This is tagged with a mini Tn5-Pcirc-egfp chromosomal insert, which allowed for constitutively expression of the enhanced green fluorescent protein (eGFP).

4.3.1 Construction of the chemotactic *P. putida* F1 mScarlet-I (pMRE135) and the non-chemotactic *P. putida* F1 cheA mScarlet-I (pMRE135) mutants

The *P. putida* F1 WT strain was modified by incorporating a mScarlet-I (pMRE135) plasmid inside the *P. putida* F1 WT strain. A single *P. putida* F1 WT colony was selected from a nutrient agar (Oxoid) plate, which had been incubated overnight (Thermo Scientific MaxQ^{TM} 6000) at 30°C. The *P. putida* F1 WT strain was initially streaked from a -80°C (New Brunswick Scientific U535) glycerol stock (50% autoclaved Milli-Q© and 50% 0.2 μm filtered (Corning©) glycerol $\geq$ 99.5% (Fisher BioReagents^{TM}). This colony was subsequently incubated overnight in 5 ml lysogeny broth (LB) (Miller, Fisher BioReagents^{TM}) within a 14 ml culture tube (Starlab), shaking at 250 rpm and 30°C (*127*).

The overnight culture was then centrifuged; 4000 x *g* (Eppendorf Centrifuge 5810 R), pelleted and washed twice at room temperature (21°C), for 10 minutes in 0.2 μm vacuum filtered 300 mM sucrose (Sigma). This method of making electrocompetent cells is adapted from (*274*). This sucrose was dissolved in H_2O using a magnetic stirrer (Fisherbrand^{TM}). All centrifugations occur at room temperature, unless otherwise stated. The electrocompetent cell culture was then concentrated by centrifugation, and 1 mL was pipetted into a 2 ml Eppendorf, with vortexing (Corning© LSE). This suspension was then centrifuged for 8 minutes at 2000 x *g* using an Eppendorf 5453 MiniSpin table-top centrifuge. The supernatant was then discarded and the pellet was resuspended in 0.5 ml of 300 mM sucrose solution (*274*).

An *E. coli* S17-1 λpir strain carrying the mScarlet-I (pMRE135) plasmid colony was selected from a LB agar (Miller, Supelco©) plate dosed with 50 μg/ml kanamycin and 25 μg/ml chloramphenicol, which had been had been incubated overnight at 30°C. Visual confirmation of the fluorescence was achieved using a UV light box (Alpha Innotech) (Fig. 4.3). A fluorescent colony was incubated overnight in 5 ml

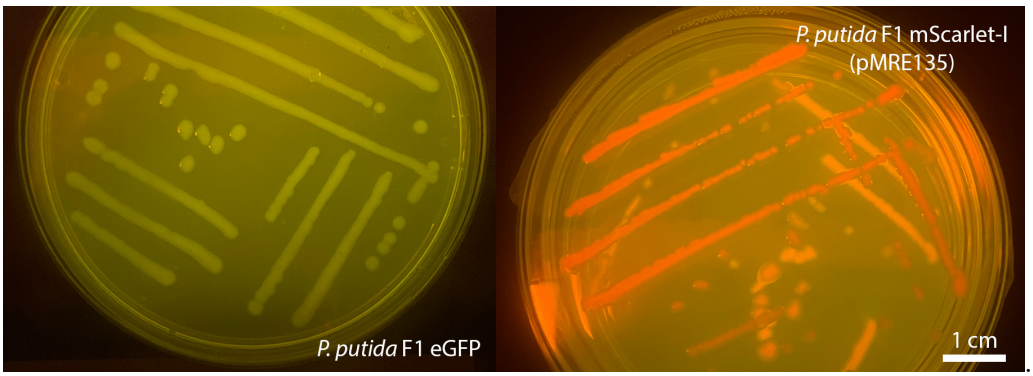


Fig. 4.3. Fluorescent colonies under ultraviolet (UV) light. Photo taken of the UV light box of two nutrient agar petri-dishes containing *P. putida* F1 strains, dosed with the relevant antibiotics. The left shows the green fluorescence of the *P. putida* F1 eGFP strain. This is contrasted, with the red fluorescence of the mScarlet-I (pMRE135) plasmid electroporated within the *P. putida* F1 WT strain on the right.

LB within a 14 ml culture tube at 37°C and 250 rpm (Fig. 4.3). It was then dosed with 50 μg/ml kanamycin and chloramphenicol 25 μg/ml, to maintain the presence of the fluorescent mScarlet-I plasmid (Addgene, Bacterial resistance: kanamycin, Backbone selectable markers: chloramphenicol #118489) (*273*). The colony was then pelleted twice in H_2O at 4000 x g for 10 minutes.

A QIAprep Spin Miniprep kit from Qiagen was then used to extract the plasmid to a concentration of 50 ng/ml, which was measured on a Thermo Scientific^{TM} NanoDrop 1000 spectrophotometer. A 100 μl aliquot of the concentrated electrocompetent *P. putida* F1 WT cell suspension was then pipetted into a 2 ml electroporation cuvette (Bio-Rad) after vortexing, along with 1.25 μl of the mScarlet-I pMRE135 plasmid DNA and electroporated (2 ml Bio-Rad MicroPulsar, Standard *E. coli.* 2 set-up; 2.5 kV) (*274*). One ml of autoclaved LB was immediately added, and cells were incubated in a spinning incubator at 250 rpm and 30°C for 1 hour. This mixture was then centrifuged for 8 minutes at 2000 x g and spread on an LB plate using a Microspec E6 Spreader (Fisher Scientific^{TM}). The plate was also dosed with 50 μg/ml kanamycin and 25 μg/ml chloramphenicol and incubated at 33.5°C (Cole-Parmer^{TM} Stuart^{TM} SI-200) overnight.

Plates were screened for positively fluorescence colonies using a UV light box, then

overnight cultures were prepared in 5 ml LB within a 14 ml culture tube dosed with 50 μg/ml kanamycin and 25 μg/ml chloramphenicol at 30°C to make glycerol stocks (Fig. 4.3). The new *P. putida* F1 mScarlet-I (pMRE135) strain was then placed in the -80°C freezer in glycerol stock using the same ratios previously described. This process was repeated with the *P. putida* F1 cheA strain, although the initial colony was selected from 50 μg/ml kanamycin nutrient agar plates with the resultant *P. putida* F1 cheA mScarlet-I (pMRE135) strain being placed in glycerol stocks in the -80°C freezer.

4.3.2 Construction of non-chemotactic and non-motile *P. putida* F1 cheA ΔfliM mScarlet-I (pMRE135) mutants

In order to create the *P. putida* F1 cheA ΔfliM mScarlet-I (pMRE135) strain, the fliM gene was deleted using a similar protocol to the scar-less gene deletion methodology outlined by Martínez-García and de Lorenzo in 2012 (*275–277*). The fliM gene controls the flagella motor switch and formation of the lophotrichous flagella, its deletion generally renders *P. putida* non-flagellated and thus non-motile, aside from pili and curli activity (Fig. 2.1) (*76*, *103*, *104*, *278*). A detailed description of the methodology; a variation of the SOEing PCR method of splicing by overlap extension follows, with a simplified flow-chart illustrating key stages in the process in fig. 4.4 (*275*).

4.3.2.1 Construction of the pEMG-fliM plasmid

Primers were designed around the flanking regions of fliM gene; TS1F-KpnI (atgcatgactGGTACCAGAGCGAAGCAGTCAAAGAC) and TS1R (GTAAGCGACCGGCACACCGTGCGGACTCCTACTGCAATAC), along with TS2F (CGGTGTGCCGGTCGCTTAC) and TS2R-XbaI (aatcctctacTCTAGACTTGATACGTTCGCTGGGGC) (Fig. 4.4 A, Table. 4.2). A Phusion© PCR was run using *P. putida* F1 cheA as a colony template. This colony selected from a -80°C freezer glycerol stock, which had been streaked onto a nutrient agar plate containing 50 μg/ml kanamycin

Table. 4.2. Primers used in this study.

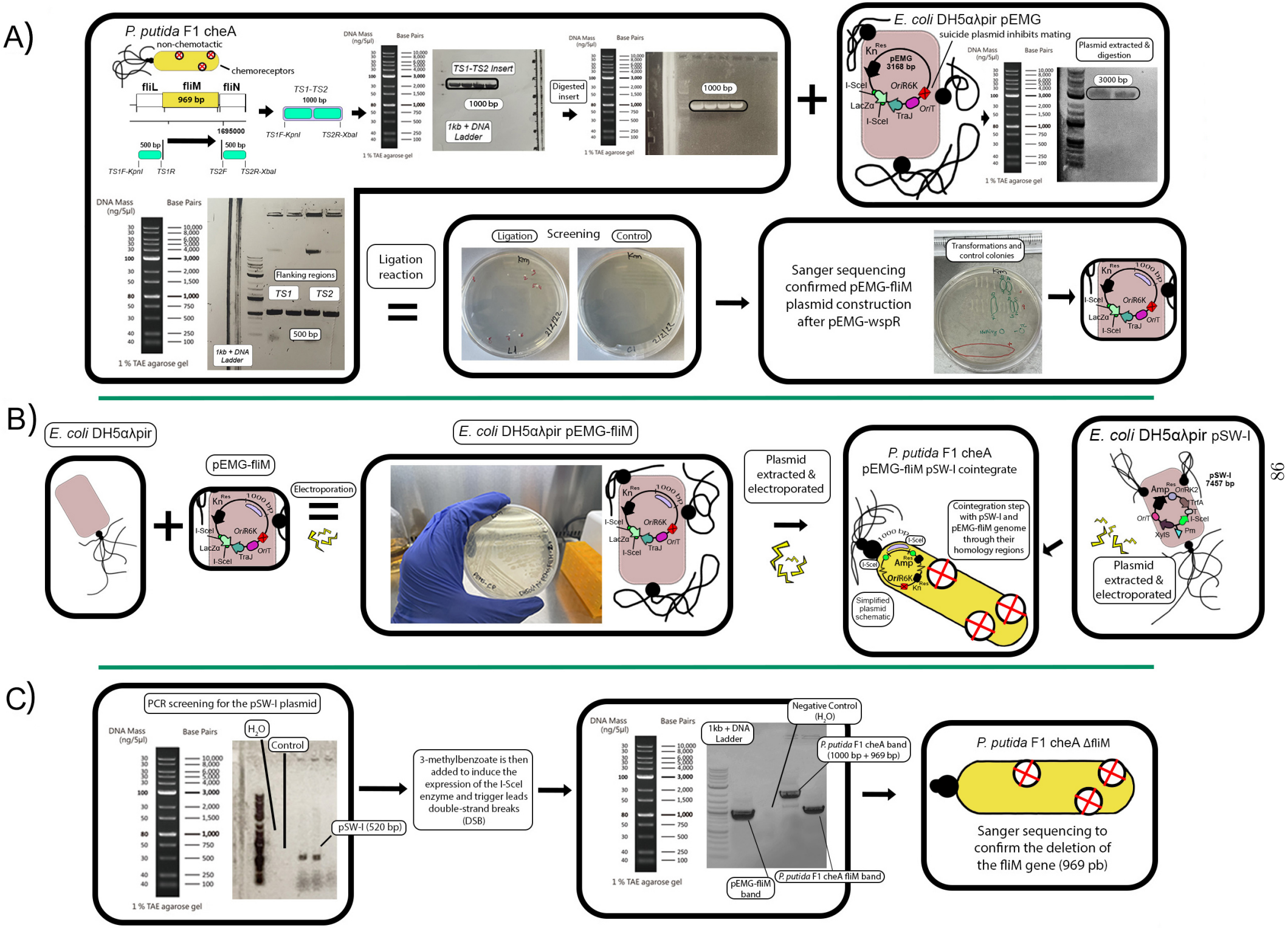
Primers	Sequence	Source/Reference
TS1F-KpnI	atgcatgactGGTACCAGAGCGAAGCAGTCAAAGAC	Purchased from Integrated DNA Technologies IDT, United States [This study]
TS1R	GTAAGCGACCGGCACACCGTGCGGACTCCTACTGCAATAC	Purchased from Integrated DNA Technologies IDT, United States [This study]
TS2F	CGGTGTGCCGGTCGCTTAC	Purchased from Integrated DNA Technologies IDT, United States [This study]
TS2R-XbaI	aatcctctacTCTAGACTTGATACGTTCGCTGGGGC	Purchased from Integrated DNA Technologies IDT, United States [This study]
pSW-I-F	5'-GGACGCTTCGCTGAAAACTA-3'	Purchased from Integrated DNA Technologies IDT, United States [150]
pSW-I-R	5'-AACGTCGTGACTGGGAAAAC-3'	Purchased from Integrated DNA Technologies IDT, United States [150]

and incubated overnight at 30°C (Fig. 4.4 A) (*275*). This colony template was then combined with 4 μl of Phusion© GC Buffer (New England BioLabs), 0.4 μl 10 mM dNTP (Thermo Scientific^{TM}), 0.2 μl Phusion© High-Fidelity DNA Polymerase (New England BioLabs) and 13.4 μl H_2O and 1 μl 10 μM of primers. This PCR was run for the each of the flanking regions TS1 (500 bp) (TS1F-KpnI, TS1R) and TS2 (500 bp) (TS2F, TS2R-XbaI) (Table. 4.2). A ProFlex^{TM} PCR machine was used to amplify the TS1 and TS2 with the following conditions; 95°C 5 minutes, 30 cycles (95°C 20 seconds, Veriflex (62°C-57°C) 20 seconds, 20 seconds 72°C) and a final cycle of 72°C 5 minutes (Fig. 4.4 A). A SciSpin Mini centrifuge was used prior to all PCRs, to make sure all mixtures were concentrated at bottom of the small 0.2 ml PCR tubes (Table. 4.2).

The resulting PCR product was run through an electrophoresis gel (Sub-Cell GT Horizontal Electrophoresis Cell, 15 x 15 cm tray, with PowerPac Basic Power Supply and gel caster #1640302) using 1 % agarose (Sigma) 1 x TAE (Sigma) (250 V, 30 A, 300 W, 30 minutes). A 1 kb plus DNA ladder (Invitrogen) was used in all PCRs run, with the reaction products being mixed with purple dye (New England BioLabs), to illuminate under UV light to assist in the sizing and approximate quantification of the DNA (Fig. 4.4 A). The TS1 and TS2 bands at 500 bp were cutout of the gel using a scalpel (Fisherbrand^{TM}) and DNA was recovered using a Zymoclean Gel DNA Recovery Kit and concentrated using a Eppendorf Concentrator Plus for 15 minutes at 45°C (Fig. 4.4 A). The gels can be viewed in figure 4.4 A on the next page.

Fig. 4.4. Genetic engineering flow-chart for the deletion of fliM gene from *P. putida* F1 cheA. A) Shows the initial construction of the delivery pEMG-fliM plasmid. It is designed to exchange DNA segments of the target genome by corresponding homologous sequences which are inserted into multiple cloning sites (MCS). Note the poly-linker MCS which is flanked by I-SceI site engineered within a lacZα segment (*279*). B) Illustrates the insertion of the novel pEMG-fliM plasmid inside *P. putida* F1 cheA and the creation of the pSW-I cointegrate, with C) depicting the fliM gene deletion transformation and induction. The I-SceI sites nuclease after activation of the Pm promoter by XylS, in the presence of 3-methylbenzoate (MB) (*279*). Note the presence of the transcriptional terminator (T), this is necessary to avoid transcriptional-readthrough (*279*).

NB: The crosses over the chemoreceptors are used to highlight the fact the cell is non-chemotactic, rather than any direct alteration of the chemoreceptors themselves (*275–277*, *279*).


A)
P. putida F1 cheA
non-chemotactic
chemoreceptors
fliL
fliM
fliN
969 bp
1695000
500 bp
500 bp
TS1F-KpnI
TS1R
TS2F
TS2R-XbaI
TS1-TS2
1000 bp
TS1F-KpnI
TS2R-XbaI
DNA Mass (ng/5µl)
Base Pairs
1 % TAE agarose gel
TS1-TS2 Insert
1000 bp
1kb + DNA Ladder
Digested insert
1000 bp
E. coli DH5αλpir pEMG
suicide plasmid inhibits mating
pEMG 3168 bp
Kn
Res
I-SceI
OriR6K
LacZα
TraJ
OriT
I-SceI
Plasmid extracted & digestion
3000 bp
Flanking regions
TS1
TS2
500 bp
1kb + DNA Ladder
Ligation reaction
Ligation
Screening
Control
Sanger sequencing confirmed pEMG-fliM plasmid construction after pEMG-wspR
Transformations and control colonies
B)
E. coli DH5αλpir
pEMG-fliM
Electroporation
E. coli DH5αλpir pEMG-fliM
Plasmid extracted & electroporated
P. putida F1 cheA
pEMG-fliM pSW-I cointegrate
Cointegration step with pSW-I and pEMG-fliM genome through their homology regions
Simplified plasmid schematic
E. coli DH5αλpir pSW-I
pSW-I 7457 bp
Amp
OriRK2
TrfA
TraJ
OriT
I-SceI
Pm
XylS
Plasmid extracted & electroporated
C)
PCR screening for the pSW-I plasmid
H2O
Control
pSW-I (520 bp)
1 % TAE agarose gel
3-methylbenzoate is then added to induce the expression of the I-SceI enzyme and trigger leads double-strand breaks (DSB)
1kb + DNA Ladder
Negative Control (H2O)
P. putida F1 cheA band (1000 bp + 969 bp)
pEMG-fliM band
P. putida F1 cheA fliM band
P. putida F1 cheA ΔfliM
Sanger sequencing to confirm the deletion of the fliM gene (969 pb)

A second PCR reaction was run using 1 μl of the TS1 and TS2 DNA product as a reaction template, along with; 4 μl of Phusion© GC Buffer (New England BioLabs), 0.4 μl 10 mM dNTP, 0.2 μl Phusion© High-Fidelity DNA Polymerase (New England BioLabs), 13.4 μl H_2O and 1 μl 10 μM of the TS1F-KpnI and TS2R-XbaI primers (Table. 4.2). The second PCR conditions were 95°C 5 minutes, 30 cycles (95°C 30 seconds, 57°C 30 seconds, 72°C 1 minute 15 seconds) and a final cycle of 72°C for 10 minutes (*275*). This work was conducted prior to cloning the target sequences into pEMG and the digestion reaction (Fig. 4.4 A) (*275*).

A *E. coli* DH5$\alpha\lambda$pir carrying the pEMG plasmid and an *Ori*R6K-based suicide vector was streaked onto LB plates (from glycerol stock) with 50 μg/ml kanamycin and incubated overnight at 37°C (Table. 4.4) (*275*). A colony was then selected and incubated at 37°C and 250 rpm in 5 ml LB within a 14 ml culture tube and 50 μg/ml kanamycin. This culture was then centrifuged at 4000 x *g* for 10 minutes and the supernatant was washed off and vortexed. A QIAprep Spin Miniprep kit from Qiagen was used to extract the plasmid to a concentration of 100 ng/ml using a spectrophotometer (Fig. 4.4 A) (*275*).

Table. 4.3. Plasmids used in this study.

Plasmid	Description	Source/Reference
pSW-I	Used to induce the expression of I-SceI.	Provided by Angeles Hueso-Gil, Centro de Biotecnología y Genómica de Plantas, Spain [150]
pEMG	Tailored to facilitate chromosomal engineering and gene deletion.	Provided by Angeles Hueso-Gil, Centro de Biotecnología y Genómica de Plantas, Spain [150]
pEMG-fliM	Tailored to delete the fliM region and render.	This study
pEMG-wspR	Used as a positive control for pEMG.	Provided by Angeles Hueso-Gil, Centro de Biotecnología y Genómica de Plantas, Spain [98]
mScarlet-I (pMRE135)	Plasmid used to constitutively express fluorescent protein genes in bacteria.	Purchased from Addgene (Plasmid #118489) [222]

A restriction digest reaction was carried using 3 μl of H_2O, 1 μl of KpnI-HF enzyme (New England BioLabs), 1 μl of XbaI enzyme (New England BioLabs), 4 μl of CutSmart Buffer (New England BioLabs) and 40 μl of the TS1-TS2 1000 bp insert, along with 40 μl of the pEMG plasmid (*275*). This was then run through an electrophoresis gel, using the same equipment, and run times as mentioned above; the plasmid band was detected at 3000 bp and the TS1-TS2 insert was recorded at 1000

bp (Fig. 4.4 A). These were then cutout and the DNA fragment was concentrated using a Zymoclean Gel DNA Recovery Kit along with a speed vacuum (15 minutes at 45°C) to concentrate the DNA fragment to 100 ng/ml. A ligation reaction was then undertaken using 4 μl T4 Buffer (New England BioLabs), 1 μl T4 ligase (New England BioLabs), 0.5 μl of the pEMG plasmid, 5 μl of the TS1-TS2 1000 bp insert and 12.5 μl of H_2O and incubated at 16°C for 16 hours in stasis within a PCR machine. This pEMG-fliM ligate product was then dialysed on a MF-Millipore 3.0 μm filter membrane disk 25 mm in a H_2O bath for 15 minutes to allow for osmosis purification (Fig. 4.4 A).

E. coli DH5$\alpha\lambda$pir electrocompetent cells were then prepared (*274*, *275*). A *E. coli* DH5$\alpha\lambda$pir colony was selected from a LB plate which had been streaked from a -80°C freezer glycerol the night before and incubated at 37°C overnight. The colony was then incubated at 37°C in 5 ml of LB within a 14 ml culture tube at 250 rpm overnight. An aliquot (50 μl) of this overnight culture was then pipetted into 50 ml fresh LB the next day. This new sub-culture was incubated at 37°C and 250 rpm until an of OD_{600nm} of 0.4 was reached, which was analysed using an Eppendorf BioPhotometer. The day culture was then centrifuged at 1000 x *g* for 10 minutes at 4°C and washed with ice-cold H_2O and ice-cold pipette tips three times.

The pEMG-fliM plasmid was concentrated in tandem, using an Eppendorf Concentrator Plus. It was then subsequently electroporated inside chilled electroporation cuvettes. One ml of LB was then immediately added to the transformed *E. coli* DH5$\alpha\lambda$pir pEMG-fliM strain and it was incubated in a shaking incubator at 250 rpm and 37°C for 1 hour 30 minutes. This was then centrifuged at 2000 x *g* for 8 minutes and spread on LB agar with 50 μg/ml kanamycin and incubated overnight at 37°C for 1 hour 30 minutes (Fig. 4.4 A).

Transformed colonies were then screened by colony PCR to check for successful insertion of the bespoke pEMG-fliM plasmid within *E. coli* DH5$\alpha\lambda$pir, against a negative control of H_2O and positive control plasmid of pEMG-wspR provided by Angeles Hueso-Gil, Centro de Biotecnología y Genómica de Plantas (Table. 4.2, 4.3)

(*280*). Each reaction involved 5 μl of H_2O, 0.625 μl of pEMG-F, 0.625 μl of pEMG-R, 6.25 μl of GoTaq© Green Master Mix (Promega) and a colony as a template for each reaction, aside for the negative control. PCR conditions were 95°C 5 minutes, 30 cycles (95°C 30 seconds, 55.8°C 30 seconds, 72°C 1 minute 15 seconds) and a final cycle of 72°C for 10 minutes. The PCR product was then run on a gel using the same electrophoresis conditions, with a band being present at 1000 bp, with the positive control being 980 bp (Fig. 4.4 A).

If the PCR was successful, with a band present at 1000 bp, it was cut out from the gel with a scalpel and a QIAprep Spin Miniprep kit from Qiagen was used to extract the DNA from the gel (Fig. 4.4 A, B). The DNA fragment was then concentrated as above and Sanger sequencing (Source Bioscience, Synthetic Biology, Imperial College London) confirmed the creation of the pEMG-fliM plasmid. This is displayed in figure. 4.4 A, using Benchling (Fig. 4.4 A, B, 4.5 A, Supplementary Information Data. S9) (*281*).

4.3.2.2 Deletion of the fliM gene

The *E. coli* DH5$\alpha\lambda$pir colonies which carried the newly constructed pEMG-fliM plasmid were then grown overnight in 5 ml LB within a 14 ml culture tube containing 50 μg/ml kanamycin. Glycerol stocks were then prepared, and the new *E. coli* DH5$\alpha\lambda$pir pEMG-fliM strain was placed in the -80°C freezer (Fig. 4.4 A, B).

In order to prepare for gene deletion, *E. coli* DH5$\alpha\lambda$pir pEMG-fliM was streaked onto LB plates with 50 μg/ml kanamycin from -80°C glycerol freezer stock and grown overnight at 37°C in the incubator. A colony was then selected and incubated overnight in 5 ml LB within a 14 ml culture tube at 37°C and 250 rpm. This strain was then pelleted at 4000 x *g* for 10 min and a QIAprep Spin Miniprep kit from Qiagen was used to extract the pEMG-fliM plasmid. The next step in the gene deletion process was the incorporation of the pEMG-fliM plasmid inside the *P. putida* F1 cheA strain (Fig. 4.4 b).

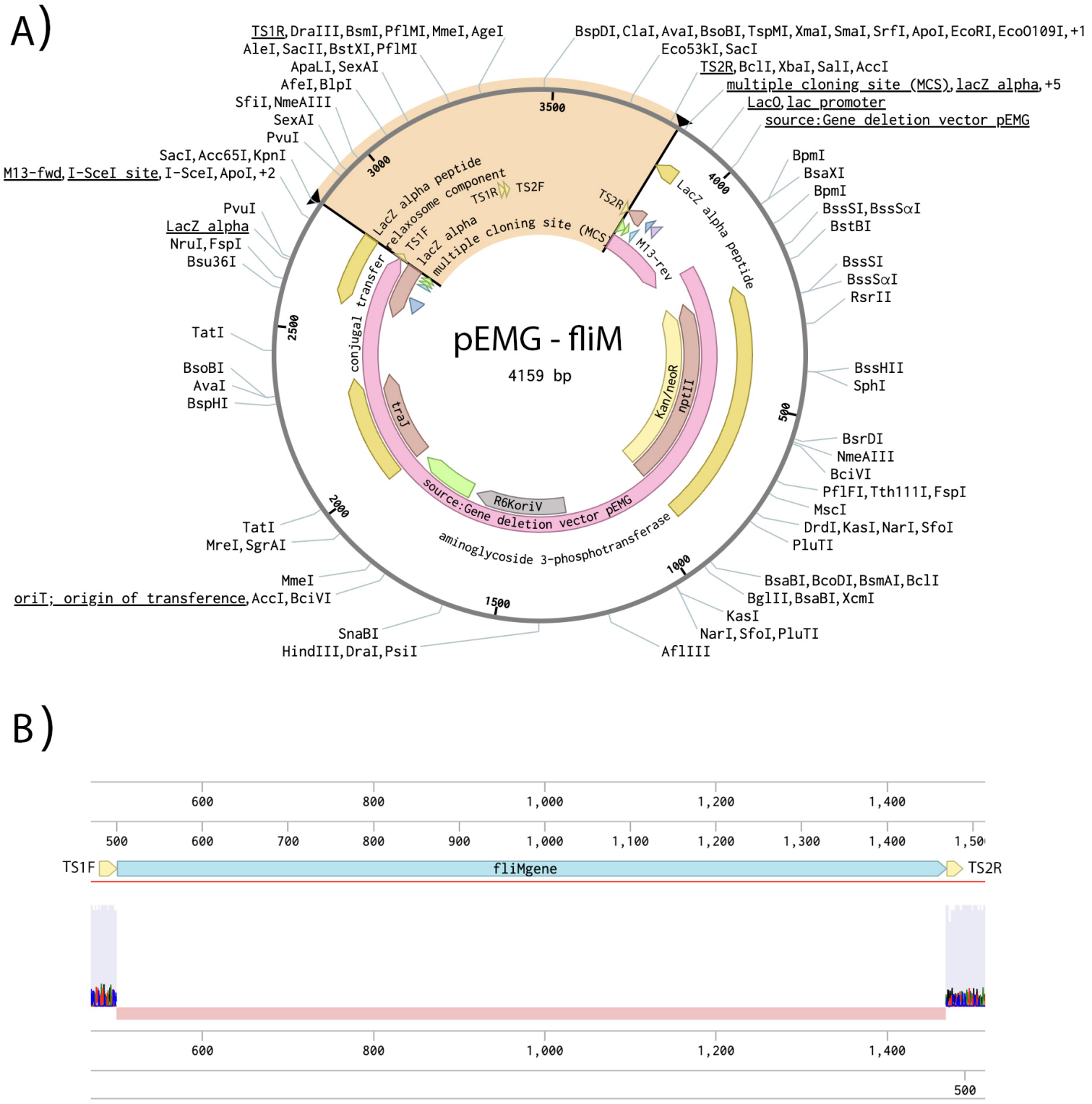


Fig. 4.5. Synthetically engineered architecture of pEMG-fliM plasmid and the successful deletion of the fliM gene. A) Plasmid map of proteins and genes, such as the *Ori*R6K-based suicide vector. The highlighted region shown in orange, denotes the area for the fliM gene deletion, with the flanking regions (TS1F, TS1R, TS2F and TS2R bp) also visible insert. B) This figure shows the gene deletion of the fliM gene within a *P. putida* F1 cheA strain, resulting in the genetic construction of the *P. putida* F1 cheA ΔfliM mutant, with the start (TS1F) and end (TS2R) of the empty gene deletion marked next to the yellow arrows (Supplementary Information Data. S9) (*276*, *277*, *281*).

A *P. putida* F1 cheA colony was selected from a nutrient agar plate with 50 μg/ml kanamycin, which was freshly streaked plate from a -80°C freezer glycerol stock that had been incubated overnight at 30 °C (*275*). This colony was then incubated overnight in 5 ml LB within a 14 ml culture tube with 50 μg/ml kanamycin at 30°C and shaken at 250 rpm. The culture was then pelleted and washed twice by centrifugation at 1000 x *g* for 10 minutes in 0.2 μm filtered 300 mM sucrose solution (prepared as above). One mL was pipetted into a 2 ml Eppendorf, with vortexing being used after each centrifugation of 8 minutes at 2000 x *g*.

The supernatant was then discarded, and the pellet was resuspended in 0.5 ml of 300 mM sucrose solution, then 1.25 μl of the concentrated extracted pEMG-fliM plasmid (100 ng/ml) was mixed into a 100 μl aliquot of the concentrated electrocompetent *P. putida* F1 cheA cells (*274*). The cells were electroporated in a 1.5 ml Eppendorf. One ml of LB was then pipetted immediately inside, and cells were incubated in a shaking incubator at 250 rpm and 30°C for 1 hour. This mixture was then centrifuged for 8 minutes at 2000 x *g* and spread on an LB plate with 75 μg/ml kanamycin and incubated at 33.5°C. A higher kanamycin concentration led to enhanced successful transformation, possibly due to the latent kanamycin resistance from the *P. putida* F1 cheA mutant construction (Fig. 4.4 A, B) (*127*).

A *E. coli* DH5$\alpha\lambda$pir pSW-I strain, which carries the pSW-I plasmid was then taken from -80°C glycerol stock and spread on LB agar dosed with 500 μg/ml ampicillin (Sigma) and incubated at 37 ° C overnight. A schematic of the pSW-I plasmid can be seen in figure 4.4 B, C, with the corresponding I-SceI site to the left hand side of the plasmid in fig 4.4 A, and these are key to the bioengineering of the *P. putida* strain (*275*, *279*). The plasmid was extracted to 100 ng/ml using a QIAprep Spin Miniprep kit from Qiagen. Electrocompetent *P. putida* F1 cheA pEMG-fliM cells were made using the same 300 mM sucrose method mentioned above and transformed with 1.25 μl of the concentrated pSW-I plasmid via electroporation (*274*). After electroporation, cells and 1 ml LB were incubated at 33.5°C for 1 hour, centrifuged at 2000 x *g* for 8 minutes and then spread on nutrient agar petri-dishes with

75 μg/ml kanamycin and 500 μg/ml ampicillin, and incubated overnight at 33.5°C (Fig. 4.4 A, B, C).

A colony PCR was then run to check for the presence of the pSW-I cointegrate in this new *P. putida* F1 cheA pEMG-fliM pSW-I strain. This was achieved with ampicillin resistance screening (Fig. 4.4 C). This screening utilised two primers; pSW-F: 5'-GGACGCTTCGCTGAAAACTA-3' and pSW-R: 5'-AACGTCGTGACTGGGAAAAC-3', with the PCR conditions being 5 minutes at 95°C, and 25 cycles (30 seconds at 95°C, 30 seconds at 55°C, 30 seconds at 72°C) and 5 minutes at 72°C (Table. 4.4). Each PCR screening reaction involved 5 μl of H_2O, 0.625 μl of pSW-F, 0.625 μl of pSW-R, 6.25 μl of GoTaq© Green Master Mix and a colony as a template for each reaction, aside for the negative control, and the pSW-I plasmid concentrate being used as a positive control (Fig. 4.4 B, C). This was then run on an electrophoresis gel against a 1 kb plus DNA ladder, as described above, with a 520 bp band indicating the presence of the pSW-I plasmid (Fig. 4.4 C). Overnights of the *P. putida* F1 cheA pEMG-fliM pSW-I strain, which contained the pSW-I plasmid were prepared in 5 ml LB, which was dosed with 75 μg/ml kanamycin and 500 μg/ml ampicillin, with glycerol stocks being made the following day.

A separate overnight of the *P. putida* F1 cheA pEMG-fliM pSW-I cointegrate was prepared in 5 ml LB and 20 μl of 0.5 M 3-methylbenzoate (MB) (Fluka # 89890), this induces the expression of the I-SceI enzyme and leads to double-strand breaks (DSB) and the subsequent fliM gene deletion. The I-SceI induction sites are marked in (Fig. 4.4 B, 4.5 A). This induction was run at 250 rpm at 30°C for 15 hours (*275*). The culture was then pelleted and centrifuged at 1000 x *g* for 10 minutes and streaked onto nutrient agar plate containing 50 μg/ml kanamycin overnight (Fig. 3).

Random colony PCR screening was then used to check for the deletion of the fliM gene, as most reverted to the *P. putida* F1 cheA strain template. Successful transformations were then grown overnight in 5 ml LB and 50 μg/ml kanamycin. The initial expectation was a 50:50 success rate ratio of gene deletion to failures, which

reverted to motile *P. putida* F1 cheA strain. However, a lower ratio of successful deletions was found, potentially as a result of variable changes in laboratory conditions and plasmid transformation efficiency (*275*). Sanger sequencing (Source Bioscience, Synthetic Biology, Imperial College London) confirmed the creation of the new strain, and this was again aligned in Benchling (Fig. 4.5 B, Supplementary Information Data. S9) (*281*). Glycerol stocks of this new *P. putida* F1 cheA ΔfliM mutant strain were then prepared as outlined above. The delta (Δ) symbol is used to designate deletion of the fliM gene. Cells were also transformed with the mScarlet-I (pMRE135) plasmid, to construct the *P. putida* F1 cheA ΔfliM mScarlet-I (pMRE135) mutant (Fig. 4.4 C, 4.5, Table. 4.1, 4.2, 4.3).

4.4 Chemotaxis assay development and testing

The applicability and repeatability of various chemotaxis assays mentioned in the literature review, were tested along with the development of a new quantitative soft-agar chemotaxis swim assay. In co-culture experiments 50:50 mixtures were utilised to investigate microbial interactions of chemotactic bacteria of varying degrees of chemotactic ability, and evaluate evidence of chemotactically assisted biomobilisation (Fig. 4.1).

4.4.1 Agarose in-plug assays

Agarose in-plug chemotaxis assays were initially trialed as they can be used to quantify a chemotactic response via the assessment of the chemotactic ring diameter (*103*). More modern adaptations utilised a "bucket of light", as previously mentioned in the literature review in chapter two (*103*, *147*). To evaluate and develop this technique, colonies of *P. putida* F1 eGFP were streaked onto a LB agar plate containing 15 μg/ml tetracycline from -80°C glycerol stock and then incubated overnight at 30°C (Fig. 4.2, 4.5, 4.6).

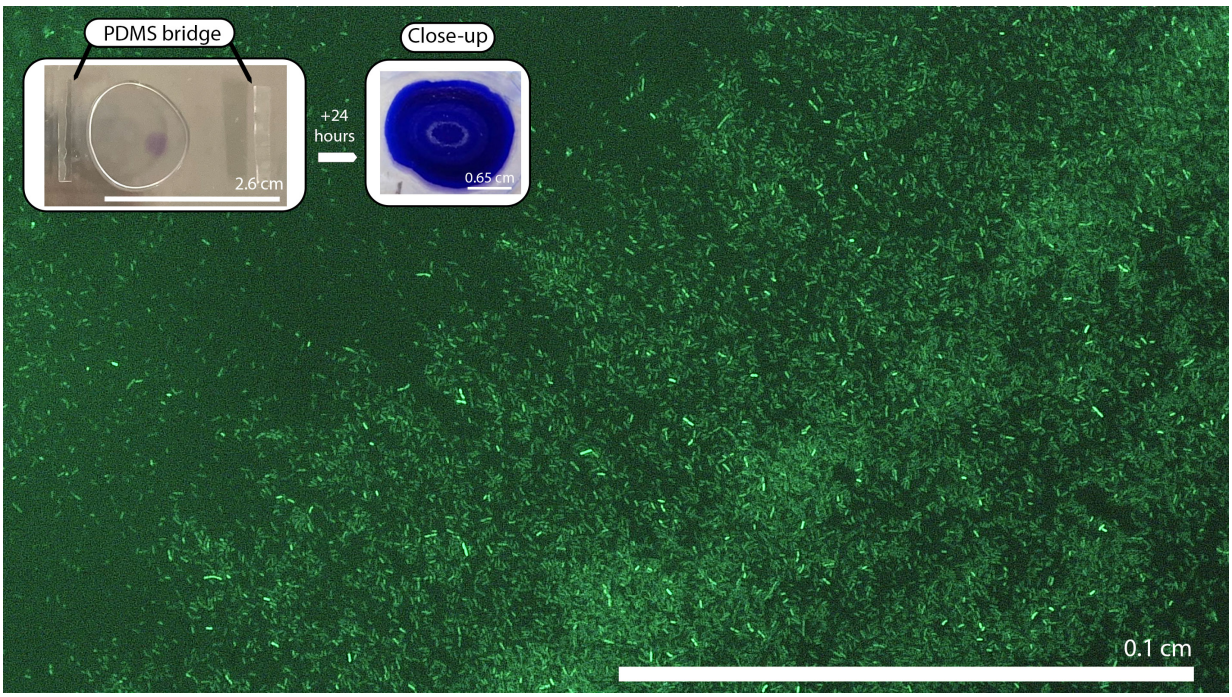


Fig. 4.6. Agarose in-plug chemotaxis assay. *P. putida* F1 eGFP responding to an agarose plug of 10 % (vol/vol) toluene, forming chemotactic rings. The "fuzzy" or blurred edges of the colony can also be seen, which is indicative of the improved run/tumble swimming bias associated with a chemotactic response (*147*, *282*, *283*). Image captured using the Nikon Eclipse Ts2 Microscope (Nikon, Switzerland) set-up as described at the start of the chapter with a x 20 objective at 465 nm excitation. A shot of the dried chemotactic ring (white cells) is also shown after 24 hours, along with the chamber which is created due to capillary action and the PDMS bridge (*284*).

A colony was then selected and incubated in 10 ml of M9 minimal media salts (Gibco^{TM}) within a 20 ml conical Erlenmeyer glass flask (Pyrex^{TM}) along with 15 μg/ml tetracycline (Sigma) and 10 % (vol/vol) toluene, long with 2.5 mM of sodium benzoate (Sigma) (*168*). This acted as an alternative source of carbon, allowing the cells to accustom themselves with the toluene. Exposing *P. putida* F1 to NAPLs and solvents, such as toluene, interferes with the cells structure in a process known as toluene or solvent shock. Therefore, this acclimatisation step is necessary (*103*, *159*, *285–287*). The flask for this overnight culture was then capped with cotton wool balls (Williams), foil (AluminaSeal^{TM}) and parafilm (Bemis^{TM} Parafilm^{TM} M) and incubated at 30°C and 250 rpm.

This acclimatisation process is also important as it helps trigger a chemotactic response of *P. putida* F1 towards toluene (*103*). The overnight cultures were pelleted

at 1000 x g for 10 minutes and washed twice in autoclaved phosphate buffer solution (PBS); made by dissolving PBS tablets (Fisher BioReagents^{TM}) in Milli-Q© and autoclaved. The centrifuged supernatant was poured off and vortexed between each stage. The cells were then diluted in PBS to obtain an optical density in the mid-exponential growth phase of OD_{600nm} 0.5. This optical density was used as this is considered to fall within the idealised concentration to investigate bacterial chemotaxis (OD_{600nm} 0.3-0.7), with a density above 0.7 considered too high as it disguises the chemotactic signal, with the flagella of individual bacteria being often unable to work as a group (Fig. 4.6) (*168*, *194*, *284*, *288*). The upper limit however is up for debate, as Tian et al., (2021) reported that *E. coli* had an enhanced chemotactic response due to overcrowding (*289*).

The agarose in-plug chemotaxis assay was constructed by bonding two slabs of the elastomeric polymer, polydimethylsiloxane (PDMS), onto a microscope slide (75 by 26 mm) to create a bridge and covered with a coverslip, as described in detail below (Fig. 4.6).

The PDMS was formulated using a 10:1 ratio of base to curing agent (Sylgard^{TM} 184, Dow Corning©, USA), degassed in a vacuum desiccator for 1 hour. It was then poured onto a silanised silicon wafer; until approximately 5 mm in height and cured overnight at 70°C in a drying oven (Fisher BINDER™). A scalpel was then used to cutout two PDMS slabs (20 mm long, 6 mm wide and 5 mm in height). These were then plasma bonded using a Zepto plasma cleaner (Diener Electronic, Germany; vacuum pressure 0.75 mbar, power 50%, coating time 1 minute) to a microscope slide (75 by 26 mm) (Fisherbrand^{TM}).

The plug was made of 2% UltraPure^{TM} low-melting point agarose (Life Technologies) in random motility buffer (RMB: 11.2 g/l K_2HPO_4 (Sigma); 4.8 g/l KH_2PO_4 (Sigma); 0.029 g/l EDTA (Sigma); 3.93 g/l NaCl (Sigma)), with the plug being melted on a 65°C block heater (Fisherbrand^{TM}) (*290*). This RMB is commonly used in chemotactic experiments to wash chemotactic cultures and as a control (*290*). Ten percent (vol/vol) toluene was added to the mix briefly after heating,

with the same volume of RMB being added as a control (*168*).

A few crystals of Coomassie blue (R-250 Dye, Thermo Scientific^{TM}) were dissolved in the agarose to provide visual contrast for the plug. An aliquot (12 μL) of the agarose plug mixture was then quickly pipetted onto the microscope slide between the two PDMS strips, and 30 seconds was allowed for the plug to cool before sealing with a glass coverslip (75 by 26 mm) (Fisherbrand^{TM}) (Fig. 4.6) (*284*). A cell suspension of *P. putida* F1 eGFP motile cells (230 μL of the OD_{600nm} 0.5) was carefully pipetted into the chamber (Fig. 4.5).

4.4.1.1 Agarose in plug-assays: imaging and example assay

After 15 minutes the assay was imaged using the Nikon Eclipse Ts2 Microscope (Nikon, Switzerland), set-up as described at the start of the chapter with a x 20 objective and 465 nm excitation (*284*).

A successful run is shown in figure 4.6 (Fig. 4.6). This assay, overall had several issues, mainly associated with the handling of the toluene. It evaporated quickly; within minutes, and it was hard to gauge how much was absorbed into the plug. Dimethyl sulfoxide (DMSO) (Sigma) was added, to assist in its absorbance, however this proved unfruitful due to cell death attributed to toluene shock (*103*, *159*, *285–287*, *291*). Taking this into consideration, along with the fact that air bubble formation frequently occurred, and leakage of the cell culture out of the chamber led to inconsistent results. It was decided to test other chemotaxis assays (Fig. 4.5).

4.4.2 Fungal-fungal interaction (FFI) device

A microfluidic approach was then trialed using a FFI device (Fig. 4.5, 4.7) (*268*). This device was designed originally to assess the interaction and confrontation of two fungi (Fig. 4.7 A). Two holes are typically punched at each end, using a precision cutter (Ø 4.75 mm; Syneo, USA). These holes create entrances to inoculate the system with fungal spores. In this case, one hole was cut for microbial inoculation

and the other for the placement of the plug containing the chemoattractant (*268*).

The FFI device was created by preparing PDMS and degassing the mixture, as described above. It was then poured onto a FFI master mould wafer, which contained the template of the FFI (kindly provided by Claire E. Stanley) and cured overnight at 70°C in a drying oven (Fisher BINDER™) (*268*). Two holes were then punched in the FFI device and it was plasma bonded to a glass bottomed petri-dish (WPI FluoroDish^{TM}, 35mm). It was then filled with 80 μl PBS. A 4 % percent M9 minimal media salt Bacto^{TM} agar (Becton Dickinson) plug (Ø 4.75 mm; Syneo, USA) with or without 1 mM acetate (Sigma) was placed in the left open hole using sterile forceps (Fisher Scientific Ltd, Bent & sharp). These forceps were also sterilised by UV (254 nm) within the BioMAT 2 Class 2 Microbiological Safety Cabinet (MSC), with all the plugs being handled using best aseptic practice (Fig. 4.5).

An agar concentration of 4 % Bacto^{TM} (Becton Dickinson) was chosen as it was determined to be the best agar concentration for plug rigidity (Fig. 4.7 B). This was due to inconsistencies in plug consistency at lower concentrations, with the formation of fractures and other faults also occurring when using alternatives, such as agarose or Phytagel^{TM} (Sigma) (Fig. 4.7 B). Alginate beads were also trialed as a delivery method of the chemoattractant. This involved autoclaving 33 μL of sodium alginate (Sigma) solution and mixing it with 0.1 mol L^{-1} sterile $CaCl_2$ solution (Sigma) using an Heidolph Titramax 101 orbital lab shaker at 2 x *g* (Heidolph Instruments, Germany). This constant agitation leads to the formation of beads after 30 minutes. These beads were collected in a 100 μm sterilized nylon mesh (Corning©) and washed with H_2O. However, similar structural issues persisted with this medium (Fig. 4.7 B, C). It was also found that the best way to get consistent plug depths of 5 mm was to use a rectangular flat-bottomed petri-dishes (Fisher).

A *P. putida* KT2440 GFP culture, exhibiting green fluorescence, was streaked onto some nutrient agar containing 10 μg/ml gentamicin (Sigma) from -80°C freezer glycerol stock and then incubated overnight at 30°C (*292*). A colony was then selected and incubated in 5 ml of LB and 10 μg/ml gentamicin within a 14 ml

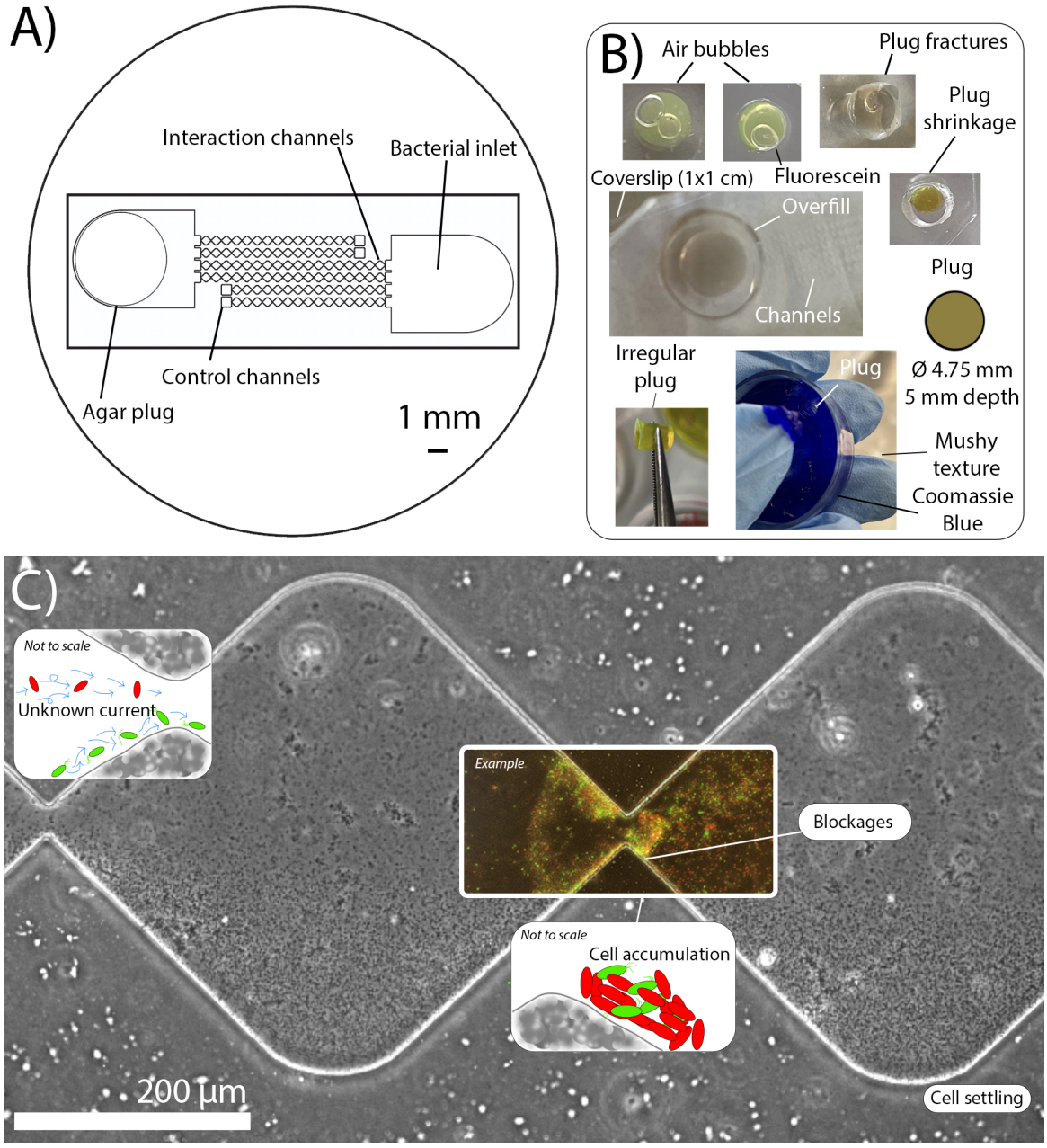


Fig. 4.7. Fungal-fungal interaction (FFI) device chemotaxis assay. A) Schematic of the FFI device, 1 mm for scale (After Gimeno et al., (2021) (*268*)). B) Highlights issues with air bubbles, plug shrinkage, fractures and irregular plugs, as well as mushy texture during plug construction; as in the case of the Coomassie blue (R-250 Dye, Thermo Scientific^{TM}) example. Overfill of the channels is also an issue as this leads to an uncertain total cell abundance within the channels. The scale of the plugs is also visible in relation to the device. C) Bright-field (x 20) close-up of the interaction channel. The schematics show the problems caused by currents, leading to an accumulation of settling cells in the lower half of the channels. This is further exemplified with the fluorescence channel inset showing an example of accumulation of cells within the channel gap at 465 nm (*P. putida* KT2440 GFP) and 544 nm (*P. putida* KT2440 ΔfliM dsRed), viewed using the Nikon Ti Microscope with a x 20 objective. Note the scale 200 μm.

culture tube overnight. This culture was pelleted at 1000 x g for 10 minutes and washed twice in autoclaved PBS, with the supernatant being poured off and vortexed between each stage. The same process was undertaken with the *P. putida* KT2440 ΔfliM dsRed strain, which is non-motile and exhibits a red fluorescence (Fig. 4.5) (*292*).

The cultures were prepared to an OD_{600nm} 0.5 in their mid-exponential growth phase, with 0.3 μl of a mixed-culture of *P. putida* KT2440 GFP and *P. putida* ΔfliM dsRed being inoculated into the right hole of the FFI (*293*). Both openings were then sealed with a 1 x 1 cm square cover glass (Fisherbrand^{TM}) (Fig. 4.5, 4.7).

4.4.2.1 Fungal-fungal interaction (FFI) device: imaging and example assay

This was then imaged on the Nikon Ti Microscope using a x 20 objective lens and a time series ran overnight taking images every 30 minutes, using a 465 nm and 544 nm excitation. This was undertaken to assess if the movement of the *P. putida* KT2440 GFP, chemotactically alters the distribution of the non-motile *P. putida* KT2440 ΔfliM dsRed mutant as *P. putida* KT2440 GFP responds chemotactically towards the acetate (Fig. 4.7 C) (*184*, *293*). A range of image stitching regimes were trialed to generate large images covering 14 x 8 fields of view, with 15% overlap. However, focusing on more than one field of view seemed to produce more inconsistent results. Issues arose from a current and flow of unknown origin, which dragged and transported the cells within the device (Fig. 4.7 C).

This caused a substantial build-up of bacteria within the small, pore-like channels; visible in the inset within figure. 4.7 C. Immediately after plasma bonding, the PDMS converts to a hydrophilic state, which assists in the uptake of fluids, such as PBS within the device via capillary action (*294*). This was initially seen as a possible origin for this current. However, different experimental variation, such as punching 1 hole into the system and waiting overnight for any latent hydrophilic

forces to subside, did not remedy the situation and the issues persisted wielding non-consistent results (Fig. 4.5) (*294*).

This was confirmed by visualising the inconsistent diffusion of 6.6 mg/l fluorescein (Sigma) dosed M9 minimal media salts agar plugs within the system (Fig. 4.7 B). Evaporation was also seen as a possible cause for the unknown current. Therefore several alternative combinations of experimental design were trialed such as filling the area around the FFI device with H_2O and covering the glass bottomed petri-dish with parafilm. However, this failed to stop the flow (4.7 B, C). It was therefore decided to trial further chemotactic assays after various combinations failed to provide repeatable results (Fig. 4.5).

4.4.3 Gene frame agarose in-plug assays

A Thermo Scientific^{TM} Gene Frame, with a total volume capacity of 25 μl, was bonded to a cover slip 24 x 32 mm, 0.13-0.17 mm thickness (Fisherbrand^{TM}) by a two-sided adhesive strip and filled with 25 μl of 0.3 % agar RMB (Fig. 4.5) (*290*). Soft 0.3 % agar was used as it allows for the movement of the cells and also mimics a porous environment, with the chemoattractant delivered to the system by a small rigid disk (*103*, *165*, *269*, *295*). This small disk was cutout using a precision cutter (Ø 1.02 mm; Syneo, USA) and placed at the center of the gene frame (Fig. 4.5). This was constructed to fill the chamber comfortably, by filling an empty chamber with the 4 % RMB agar dosed, with and without 1 mM acetate; the chemoattractant, and then punching out a neat fitting disk out after cooling. Bacterial suspensions (1 μl of a OD_{600nm} 0.5) were inoculated into the center of the assay during the cells mid-exponential phase and prepared the same way as for the FFI device (Fig. 4.8 A, B, C) (*90*, *98*).

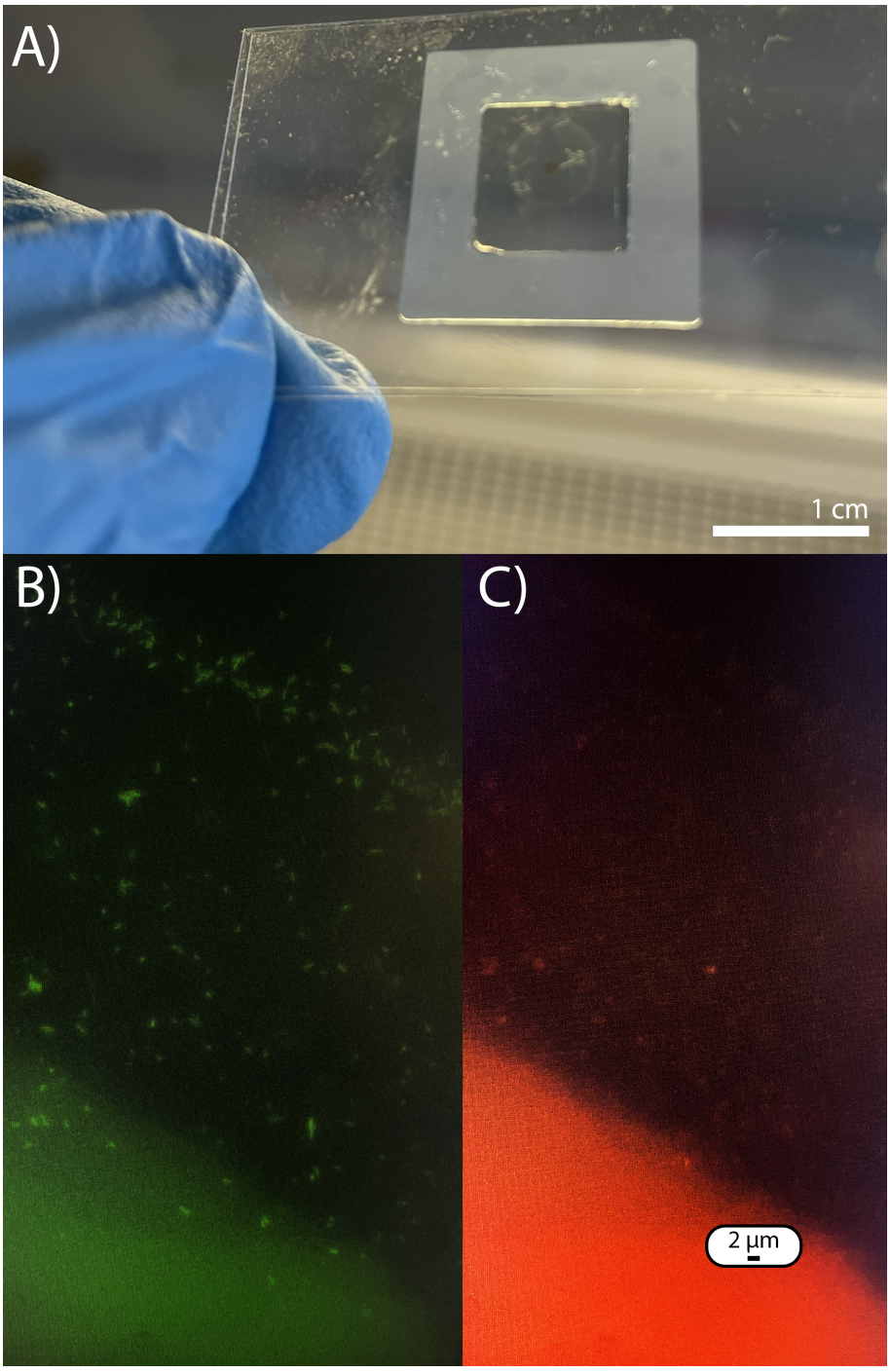


Fig. 4.8. Gene frame chemotaxis assay. A) Close-up of the gene frame and plug, the white bacterial ring encircling the plug is the bacteria responding chemotactically towards 1 mM acetate within the plug. A small fracture within the agar, resembling a small pair of scissors is visible, this highlights the issues caused by fracturing. B) *P. putida* KT2440 GFP showing a chemotactic ring forming (Nikon Ti Microscope x 20 465 nm), with C) showing the *P. putida* ΔfliM dsRed distribution, within the same culture, spread more evenly between the disk and limits of the gene frame after 12 hours, the lack of flagella make this mutant slightly smaller visually (Nikon Ti Microscope x 20 544 nm).

4.4.3.1 Gene frame agarose in-plug assays: imaging and example assay

Figure 4.8 illustrates a mixed-culture of mixed cells of *P. putida* KT2440 GFP and *P. putida* ΔfliM dsRed. Another cover slip 24 x 32 mm, 0.13-0.17 mm thickness (Fisherbrand^{TM}) was applied to seal the chamber (*293*). This assay worked well initially using the Nikon Ti Microscope with the x 20 objective and fluorescence channels at 465 nm and 544 nm excitation to analyse the fluorescence. However, the disk often deformed and led to an unequal dissemination of attractant within the gene frame, thereby not allowing for reliable and repeatable results, with air bubbles also commonly occurring (Fig. 4.5, 4.8).

Several other issues arose, such as overflow of the 0.3 % agar RMB and issues with the timing of the solidification of the agar, especially when sealing the chamber. The 4 % rigidity of the plug vs. rigidity of the 0.3 % RMB agar, often caused frequent fractures to form upon closing the assay. Attempts using RMB without agar were also trialed, however this resulted in the double counting of cells, as a result of chemotactic bacteria switching quickly between points, especially when time-lapses were trialed and image stitching was applied (Fig. 4.5, 4.8 A, B, C).

4.4.4 Novel quantitative soft-swim fluorescent chemotaxis laser scanning assay (qSS-FCLSA)

Quantitative soft-agar chemotaxis swim assays were set up similarly to previous studies. However this thesis developed a novel way to study the bacterial interaction and accumulation of bacteria within colonies, using an fluorescence laser scanning approach (Amersham Typhoon^{TM}) (Fig. 4.5, 4.9, 4.10) (*146*). Colonies were selected from nutrient agar plates (*296*), which had been incubated overnight at 30°C, containing the relevant antibiotic; 50 μg/ml kanamycin, 25 μg/ml chloramphenicol or 15 μg/ml tetracycline (*297*, *298*). These colonies were grown overnight in 5 ml LB within a 14 ml cell culture tube at 30°C with shaking at 1 x *g* containing the relevant *P. putida* F1 strain and antibiotic. The colonies were washed twice and pelleted in autoclaved M9 minimal media salts at 1000 x *g* for 10 minutes (*46*, *299*)

and diluted to an OD_{600nm} of 0.50, in accordance with their mid-exponential growth phase. Quantitative 0.25 % soft-agar swim plate assays with M9 minimal media salts were supplemented with succinate (Sigma) at 1 mM and 10 mM concentrations, and a control of no succinate and carbon source were prepared (Fig. 4.5) (*98*, *269*, *284*, *300*).

Higher concentrations of agar changed the chemotactic response from swimming to swarming, so concentrations below 0.5 % can be used to investigate the swimming response, with 0.25 % producing consistent results than the 0.3 % mixture (Fig. 4.5) (*103*, *165*, *269*, *295*, *301*).

Microbes in the qSS-FCLSA generate their own chemical gradient by metabolising a chemoattractant dispersed universally within soft-agar petri-dishes, with the innovation of this assay being the use of a fluorescent laser scanner to investigate how the chemotaxis and cells interact within a colony (*103*, *121*, *146*). The chemotactic response can be seen by the formation of circular chemotactic rings, with the size of the colony being measured to quantify a chemotactic response (Fig. 5.2, 5.4) (*146*, *244*, *302*). This pioneering chemotactic front at the perimeter of the colony, boosts the colonies chemotactic range. Subsequently these cells then replicate themselves and move outwards leaving behind settlers which occupy previously inhabited zones (Fig. 5.4) (*303*, *304*). This expansion has been thought of as being a vital driver for expanding bacterial diversity into foreign territories (*96*). Moreover, the outer chemotactic margin and perimeter of the chemotactic cell front is similar to a microbial curtain of petroleum hydrocarbon degrading taxa that envelopes contamination plumes in the field (Fig. 5.2) (*52*, *123*, *178*, *304*).

Succinate was used as the chemoattractant at concentrations of 1 mM and 10 mM (Fig. 4.9, 4.10 A). This compound is commonly used as a positive control, for the chemotactic response of *P. putida* F1, as it allows for the initial decoupling of energy and identification of normal chemotaxis behaviour (Fig. 4.5) (*98*, *269*, *284*, *300*). The compound is an intermediate compound in the Krebs cycle and a terminal compound in the degradation of petroleum hydrocarbons (*103*, *305*, *306*).

Its metabolism results in a flux of metabolites within the agar, with fumarate being extruded (*307*). The *P. putida* F1 strain contains the McfR (locus tag Pput 0339) chemoreceptor which detects succinate, along with malate and fumarate, with two other chemoreceptors McfS (locus tag Pput 4520) and McfQ (locus tag Pput 4894) also involved in the chemotactic response to succinate, with McfS (locus tag Pput 4520) having a more significant role compared to McfQ (*269*). This metabolism of succinate results in the formation of colonies of a greater perimeter than when no chemoattractant is present, with a stable expansion front being key to colony expansion (*103*, *121*, *300*, *308*). The *P. putida* F1 mScarlet-I (pMRE135) strain response was used as a control.

The 0.25 % soft-agar w/ M9 minimal media was then poured into a standard petri-dish for 15 minutes and left to cool (Fig. 4.9 A) (*146*). Succinate was uniformly distributed within the soft-agar at three different succinate treatment concentrations; 0mM, 1 mM and 10 mM (*269*, *300*). A 3.5 μl bacterial suspension of cells in their mid-exponential growth phase and at an OD_{600nm} of 0.50, was then inoculated in the center of the petri-dish (Fig. 4.5).

4.4.4.1 Novel quantitative soft-swim fluorescent chemotaxis laser scanning assay (qSS-FCLSA): imaging and example assay

An Amersham Typhoon^{TM} fluorescence gel scanner was used to analyse fluorescence intensity via the red fluorescence channel Cy3 (635 nm) and thus quantify the communities within the chemotactic bands and investigate chemotactic cell response, with the fluorescence acting as a proxy for bacterial abundance (Fig. 4.9, 4.10 A) (*303*). The *P. putida* F1 mScarlet-I (pMRE135) strain was used as a control. The bacterial communities usually extended from the bottom to the top of the soft-agar, although most cells remained submerged within agar, with the rings reflecting an increased concentration of cells near the outer peripheries of energy, nutrient, and/or electron-acceptor gradients (*147*). Microbes of varying degrees of chemotactic ability and motility will have slightly different colony shapes and sizes (Fig. 4.5) (*76*,

302).

It was also decided to inoculate the center of each of the quantitative soft-agar chemotaxis swim assays individually, rather than inoculate multiple strains on one dish as others have done previously (Fig. 4.9 A, B, C) (*103*). This is because *P. putida* has been shown to be capable of cell-cell communication and quorum sensing via the release of small signalling molecules, such as 3-oxo-C_{12}-AHL or c-di-GMP, although many are unidentified (*309–311*).

This type of communication is known as quorum sensing and could interfere with the aims of the thesis, i.e., studying the role of chemotaxis and microbial transport (Fig. 1.2, 4.9) (*309*). Figure 4.9 A is strikingly similar to figure. 15 of Adler's paper in 1966, where he witnessed the same "shadow zone", when *E. coli* was deposited on tryptone agar plates (*312*). This was suspected to be occurring due to some trials running successfully and some seeming to fail as a result of impeded chemotactic growth or a subdued chemotactic response (Fig. 4.9 A, B, C). Further research, could investigate this, to assess if some unknown chemical is released to spatially segregate the colonies and confirm if quorum sensing is indeed occurring (*310*). This can be tested by investigating the causes of the depletion zones when the colonies interact, sub-sampling this area and testing for expression of the ppuI and ppuR genes and abundances of the signalling molecule 3-oxo-C_{12}-AHL or similar chemicals (Fig. 4.9 A, B, C). Expression of ppuI and ppuR genes is used by many to gauge quorum sensing in *P. putida* F1 (*309*, *310*). Furthermore, inoculation closer to the edge of the petri-dish can also bias chemotactic responses, due to it altering the spatial flux of the chemoattractants within the petri-dish as a whole, further justifying inoculation at the center of the petri-dish. Note that all qSS-FCLSA experiments using the scanner were conducted at room temperature (*313*).

Co-cultures consisted of a 50:50 mix of cells prepared to a OD_{600nm} of 0.50 (Fig. 4.9, 4.11). The assay was incubated for 24 hours at 33.5°C after 24 hours. Increased temperature induced a more consistent chemotactic response, with *Pseudomonas*

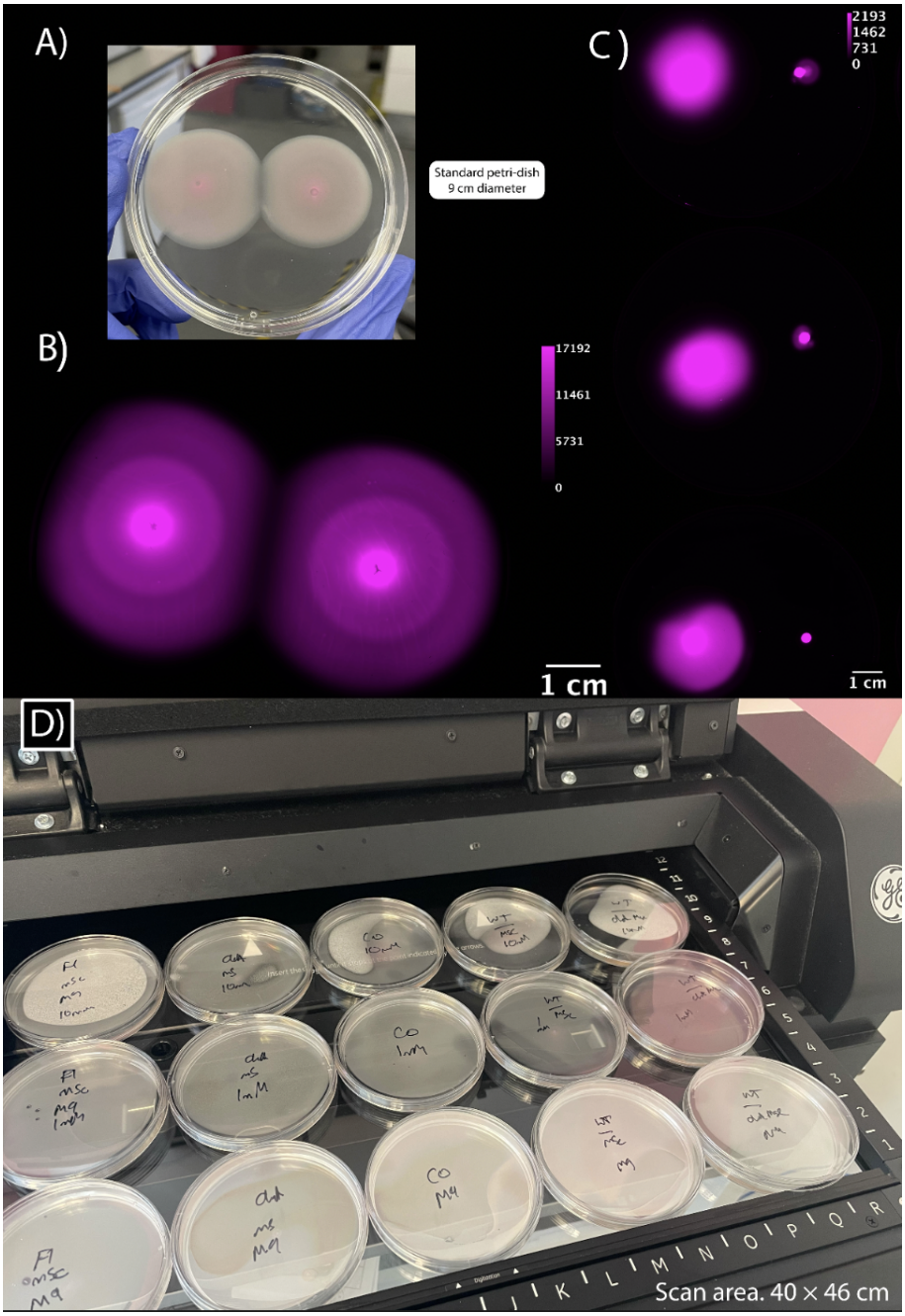


Fig. 4.9. Novel quantitative soft-swim fluorescent chemotaxis laser scanning assay (qSS-FCLSA) development. A) *P. putida* F1 mScarlet-I (pMRE135) 3.5 μl at OD_{600nm} 0.5 after 24 hours of incubation at 33.5°C in 1 mM succinate, inoculated at the left and the right side of a petri-dish. It displays biological replicates which show a "shadow zone" or zone of inhibition after 24 hours, suggesting some form of cell-cell communication is subduing growth in the center (*314*). B) Illustrates the fluorescence gel scan using the fluorescence channel Cy3 (635 nm) scan of the same dish. This is complicated by the results of C), where three biological replicates of *P. putida* F1 mScarlet-I (pMRE135) were prepared under the same conditions, along with technical replicates. Biological replicates of individual colonies are displayed vertically, with a technical replicate being inoculated to the right hand side of each dish. It suggests that there is an immediate secretion of molecules inhibiting the growth of the right technical replicate; the left colony was inoculated first, with the right colony inoculated ∼5 seconds later. D) Shows the Amersham Typhoon^{TM} scanner and a full experimental run.

species showing a broad range of chemotactic responses between 3 and 35°C and this temperature was used for similar assay by Gude et al., (2020) (Fig. 4.9 A) (*146*, *269*, *313*, *315*).

Other variants of the novel qSS-FCLSA were trialed; such as, using a small glass bottomed petri-dish with an attractant and a gene frame chemotaxis assay. The glass bottomed petri-dish often resulted in the scan producing Newton interference rings (Fig. 4.5 D, 4.10).

This made studying the chemotactic response or any diffusion patterns challenging, with the gene frame chemotaxis assay often resulting in non-repeatable results (Fig. 4.9 A, B). Its important to note here that cleaning of the fluorescence gel scanner glass shelf prior to use, using precision clean room wipes and 100 % ethanol was essential to avoid background interference (Kimtech Precision Wipes). Therefore it was decided to continue with the standard petri-dish assay (Fig. 4.5, 4.9 D).

The perimeter of the colonies, which formed at the point of inoculation (POI), were analysed via the "Multi-Otsu Threshold" add-on function in ImageJ. The 16-bit images had to be converted to 8-bit images to run the "Multi-Otsu Threshold" analysis; which was set to 5 levels, with the lowest region of contrast being selected (Fig. 4.11 B). The "magic wand" tool was set to a tolerance of 0 in ImageJ, this was done manually on a colony-by-colony basis (*150*, *313*, *317–319*). This method separates the edge of the colony from empty space, with this perimeter measurement being reported in centimeters (cm) (Fig. 4.5) (Supplementary Information Data. S10).

In order to investigate the fluorescent intensities of the colonies and the spatial distribution, the maximum and minimum brightness (B) and contrast (B & C) for each original scan was set at Min. 258 (B) and Max. 9474 (B) in ImageJ. A normalised radial distribution analysis was then run around the POI on the original 16-bit images in ImageJ using the built-in "Radial Profile" function to detect the

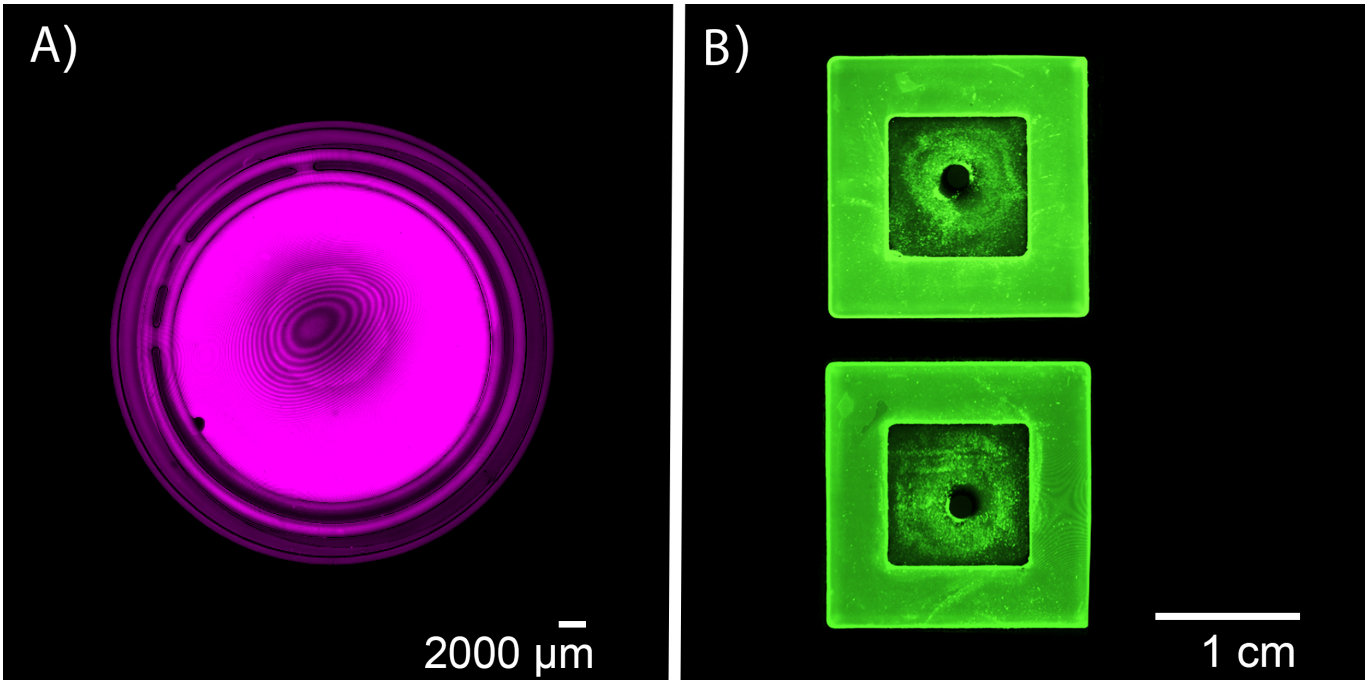


Fig. 4.10. Other qSS-FCLSA trials using the fluorescence gel scanner. A) *P. putida* F1 cheA mScarlet-I (pMRE135) cells, around a 4 % RMB agar plug in RMB buffer. The plug was dosed with 3 mg of fluorescein salt and 1 mM succinate inside a glass bottomed petri-dish, which was set-up to the red fluorescence channel Cy3 (635 nm). The initial aim of this variant of the assay, aside from trialing it as an alternative, was to view diffusion pattern of the fluorescein and see if it was impacted by the movement of the cells in response to 1 mM succinate *P. putida* F1 cheA mScarlet-I (pMRE135) cells. However, the shape of the glass bottomed petri-dish caused the development of Newton interference rings. These form due to the reflection of light between two surfaces. The use of standard petri-dishes subdued this effect (Fig. 4.5) (*316*). B) The gene frame chemotaxis assay was also trialed, set-up as previously described, however it was viewed using a fluorescence gel scanner. In this assay, the green fluorescence channel Cy2 (532 nm) and a current gain of PMT 343 gain was used to view the chemotactic response of *P. putida* KT2440 GFP cells towards 1mM acetate. The fact the cells are suspended in RMB without agar meant that overflow of the cells outside the device was common, also the fractures which formed during the sealing of the chamber led to an uneven and inconsistent asymmetric chemotactic response. This inconsistent asymmetric chemotactic response is indicative of the chemoattractant leaking out of the plugs in a non-uniform manner, and makes radial analysis of fluorescence complex. The two gene frame assays shown, also display significant autofluorescence, due in-part to the plastic adhesive surrounding the gene frames triggering interference.

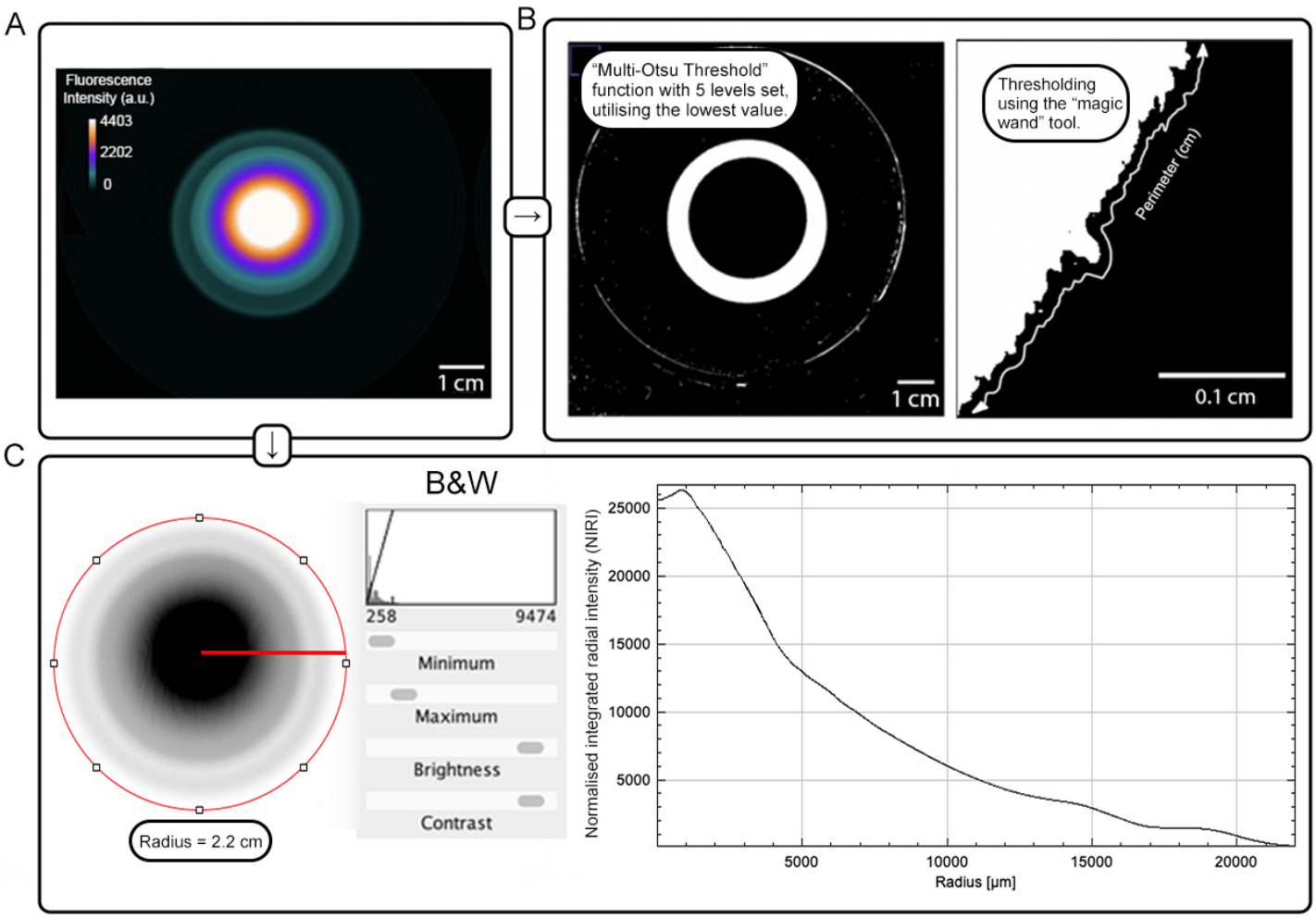


Fig. 4.11. Visualisation of the analysis pathway for the qSS-FCLSA. A) False colour image of the fluorescent intensity of *P. putida* F1 responding to 1 mM succinate at a OD_{600nm} of 0.5. The radial profile of the fluorescence intensity (a.u) emitted by the mScarlet-I (pMRE135) plasmid within the cells, highlights the intra-colony spatial distribution. B) "Multi-Otsu Threshold" analysis is used to assess the maximum extent of the community perimeter (cm) using the "magic wand" tool in ImageJ, with C) showing the built-in "Radial Profile" of fluorescent intensity profile (*150*, *313*, *317–319*).

microbial distribution throughout the assay, with the "Spatial Calibration" tick-box selected and the colony center being selected manually on colony-by-colony basis (Fig. 4.11) (*150*, *313*, *320*). The raw output of this "Radial Profile" function is a median normalised radial fluorescent intensity (a.u) around the POI (Fig. 4.5, 4.11) (Supplementary Information Data. S11).

The resolution of each pixel in the scan is 10 μm, with the radius of each circular profile being 2200 pixels / 2.2 cm (Fig. 4.9). If the scans contained any failures, such as: inoculation spatter around the POI, causing daughter colonies to form, interference in the scan, or if the soft-agar had structurally failed, the petri-dish was subsequently removed from all downstream analysis. The median normalised radial intensity curve for each treatment and strain was calculated, as this provides insight into the colony shape and intra-colony variation. The median value was chosen as it provides a better reflection of systems which may have high variability, such as the intensity signal around the POI, a log transformation was also used to improve clarity at lower intensities (Fig. 4.5) (*321*). Background noise was removed by arbitrarily selecting and subtracting the lowest median measured normalised radial intensity from the outer limit of all petri-dishes, with autofluorescence not being removed (*313*). The area under the curve (AUC) which is used as an estimation of bacterial abundance and spatial distribution, was calculated in *R* using the "AUC" function within the "DescTools" package (version 0.99.28) with the trapezoid rule option being selected for its calculation. It is a function of the median normalised radial intensity $\sim$ radius (cm), however it is written unit-less in this thesis (Fig. 4.5, 4.11) (*322*, *323*).

4.5 Summary of assay development

This chapter has provided an overview of some of the common chemotaxis assays outlined in the literature review, along with the creation and selection of a novel qSS-FCLSA (Fig. 4.12).

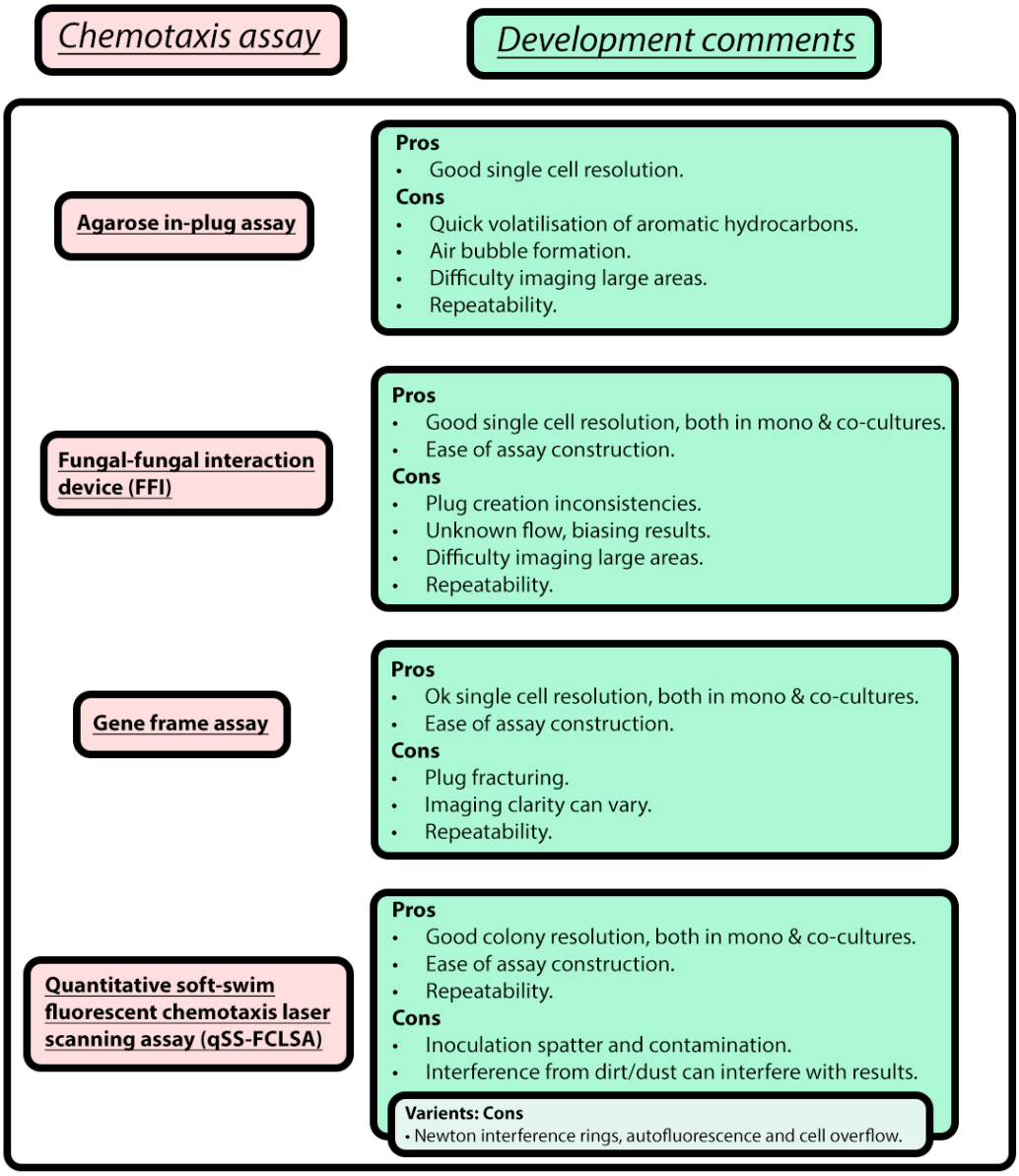


Fig. 4.12. Assay selection. "Pros and cons" list comparing the chemotaxis assay utilised, with the petri-dish novel quantitative soft-swim fluorescent chemotaxis laser scanning assay (qSS-FCLSA) chosen ahead of other experimental variants tested. This was primarily to check consistency.

This novel chemotaxis assay was the most robust and repeatable method tested, and can be used in conjunction with the chemotaxis mutant toolkit and statistical techniques, also highlighted in this chapter. This assay has improved intra-colony ring resolution than conventional soft-swim assays, providing a more detailed representation of distributional change in response to a chemoattractant (*146*) (Fig. 4.12).

Chapter 5

Assessing the interaction of chemotactic and non-chemotactic bacteria

5.1 Introduction

The goal of this laboratory-based study was to provide further information necessary to elucidate the chemotaxis parameter and the related microbial transport (interaction) parameter within existing NSZD models and answer the final question of this thesis; **3.** How do microbes of varying degrees of chemotactic ability and motility interact with one another ? (Fig. 1.3). Modifying parameters within NSZD should spur the development of new models which incorporate these phenomena, thereby providing a greater insight into the current NSZD rate, extent of contamination and evaluate site specific treatment options (Fig. 1.3) (*10*, *43–46*).

Chemotaxis has the potential to alter the distribution of microbes such as *Geobacteraceae*, a family of petroleum hydrocarbon degradation microbes which includes the genus *Geobacter*. Thereby potentially boosting the natural source zone depletion (NSZD) rate of petroleum hydrocarbons and reducing the risk to the groundwater supply (Fig. 1.1, 5.1, 5.2) (*31*, *176*, *184*, *324*). This chapter assesses the validity of the qSS-FCLSA by comparing the responses of the petroleum hydrocarbon de-

grading bacteria F1 and cheA to succinate. The interactions of the co-cultures of varying degrees of chemotactic ability are then assessed, as well as any evidence of biomobilisation (Fig. 1.3) (*103*, *121*, *300*, *308*).

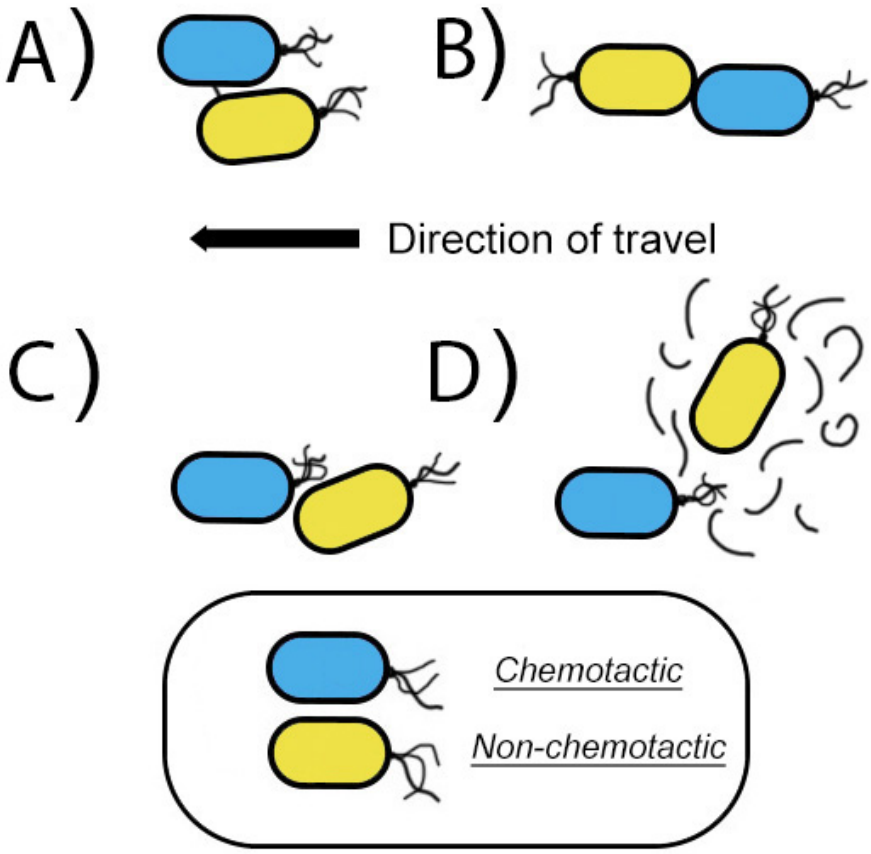


Fig. 5.1. Biomobilisation mechanisms. Illustrates the different biomobilisation mechanisms that may occur in a co-culture of chemotactic and non-chemotactic microbes. A) Piggybacking where microbes physically attach to each other, with one of the microbes being actively dragged along a gradient, like cargo carriers. B & C) Displays the push / pull mechanism, where a chemotactic cell either physically pushes or pulls a non-chemotactic cell along a gradient. D) Illustrates hydrodynamic entrapment, whereby non-chemotactic cells are entrapped in a hydrodynamic eddy created by the chemotactic cell (*184*, *190*).

As mentioned in section 2.4.1, chemotactic *P. putida* G7 cells have been shown to biomobilise non-motile *Mycobacterium gilvum* cells, as *P. putida* G7 responds chemotactically towards an attractant via push / pull interactions and hydrodynamic entrapment (Fig. 5.1, 5.2, 5.3). This biomobilisation mechanism can increase the petroleum hydrocarbon degradation potential, with the chemotactic microbes

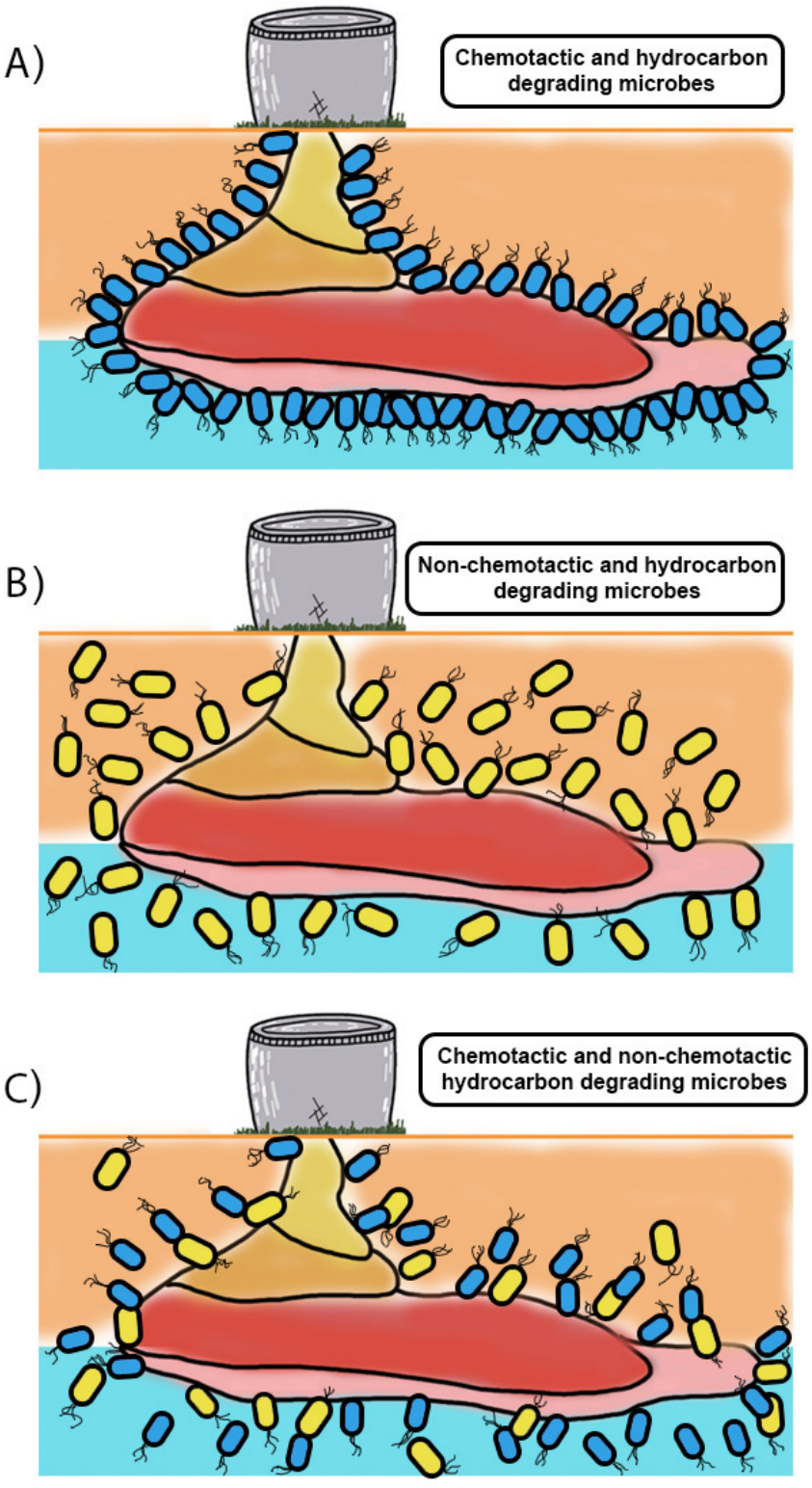


Fig. 5.2. Microbial "curtain" enveloping a petroleum hydrocarbon plume. Schematic of potential chemotaxis and microbial movement forming a curtain around a petroleum hydrocarbon contamination ganglia and blobs of degrading microbes. A) Chemotactic and hydrocarbon degrading microbes in blue, B) non-chemotactic and hydrocarbon degrading microbes in yellow, and C) co-culture of chemotactic and non-chemotactic hydrocarbon degrading microbes in blue and yellow. Not to scale (*52*, *136*).

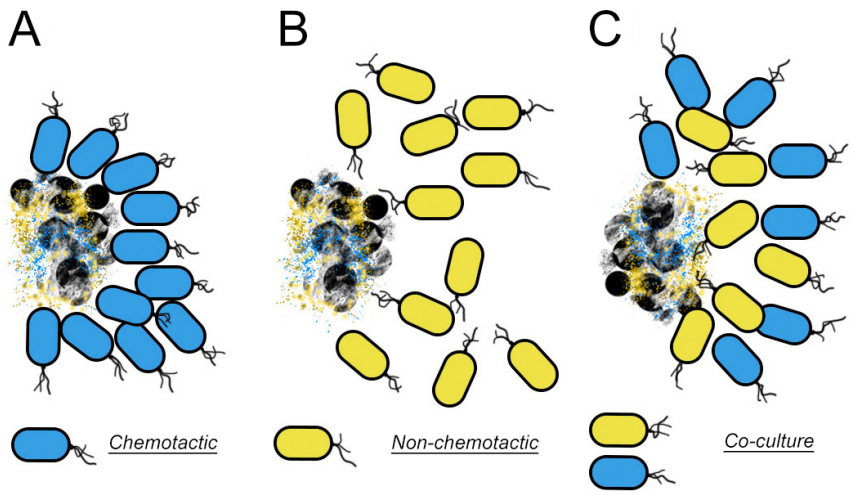


Fig. 5.3. Interactions of chemotactic and hydrocarbon degrading microbes at the contaminant interface. Schematic of chemotactic and hydrocarbon degrading microbes encircling petroleum hydrocarbons, a smaller scale version of figure 5.2; A) F1 (in blue) forming a tight group entombing the contaminant, B) cheA (in yellow) displaying a randomly distributed community, and C) displays a mixed-culture of F1 & cheA, with F1 inferred to biomobilise cheA closer to the contaminant interface. Not to scale (*52*, *136*).

acting as a "shuttle service" for bacteria or other microbes which cannot reach the contaminant interface unaided. It should also be noted, however that some will eventually arrive over time by advection through the pore space and advection (Fig. 5.1, 5.2, 5.3) (*184*, *190*). Piggybacking is another biomobilisation mechanism, where the cells physically attach to one another, with the active chemotactic cell governing the movement of the other non-motile cell. It is also likely that several more mechanisms exist (Fig. 5.1) (*190*). In addition, there is limited knowledge of the interaction and biomobilisation effects of chemotactic and non-chemotactic microbes interact (Fig. 1.1, 5.1, 5.2, 5.3).

This study developed a novel qSS-FCLSA in chapter four to address the third key question of this thesis and investigate microbial interaction (Fig. 1.3, 5.1, 5.4) (*103*). It utilised three strains from the chemotaxis mutant toolkit; a *P. putida* F1 mScarlet-I (pMRE135) strain, a *P. putida* F1 cheA mScarlet-I (pMRE135) mutant and a *P. putida* F1 wild-type (WT) strain. The names of these bacteria have been shortened to: F1, cheA and WT respectfully, for the majority of this chapter (Table.

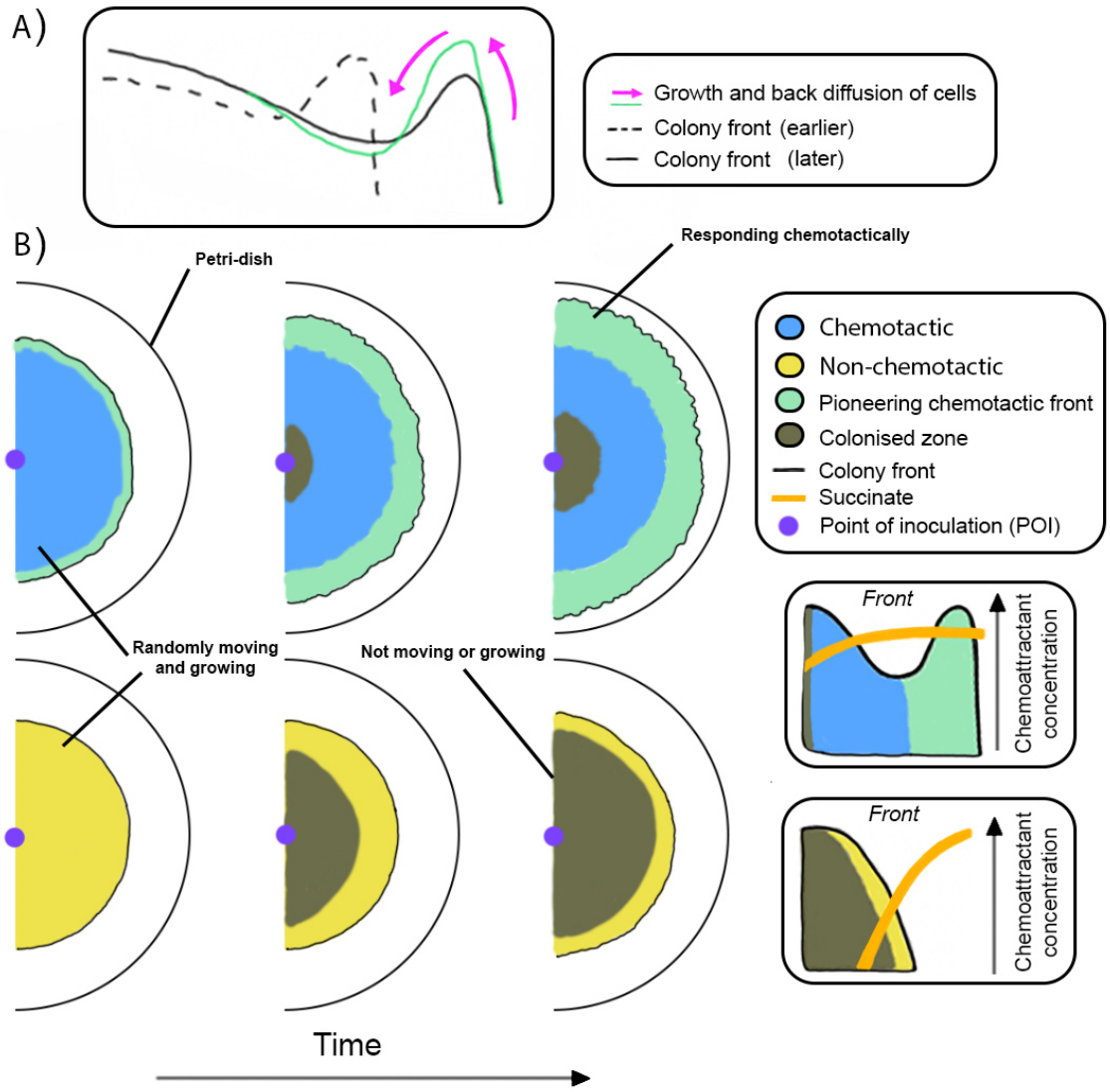
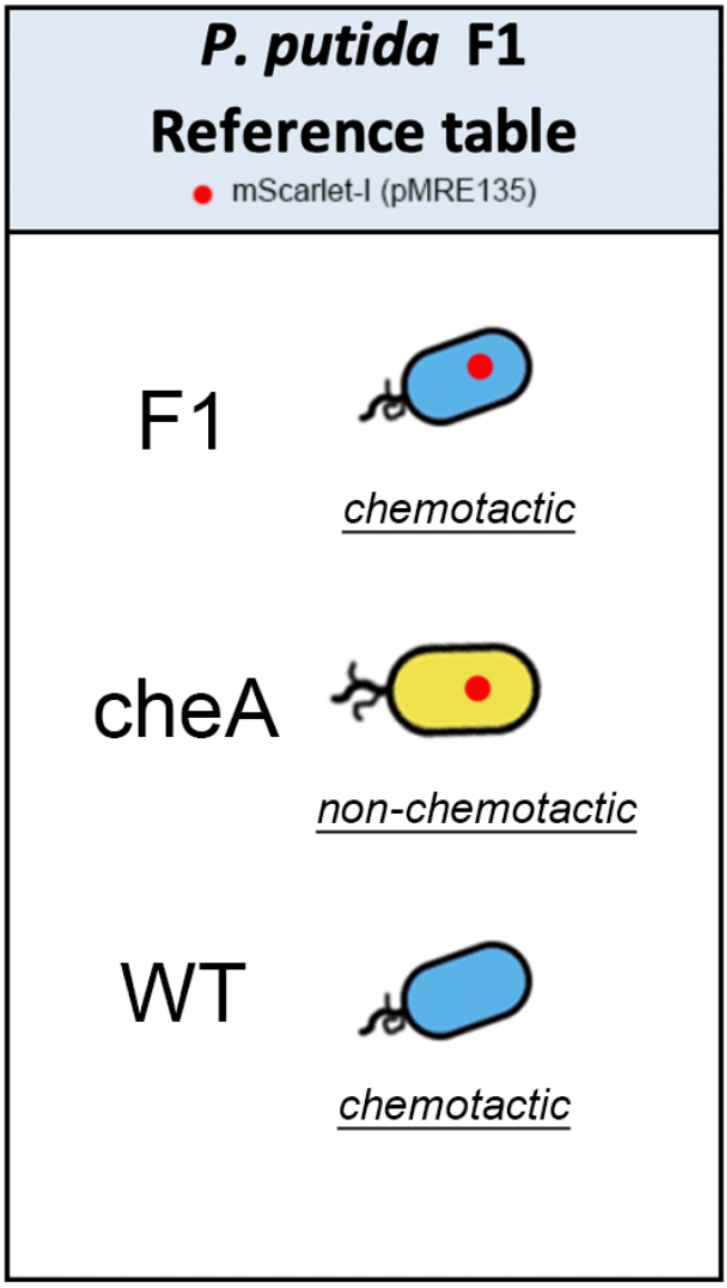


Fig. 5.4. Colony range expansion. Schematic of the expected chemotactic range expansion of chemotactic cells and the non-guided expansion of a non-chemotactic mono-culture radially outwards. A) Shows the development of the colony front and the migration of chemotactic cells (black line), with the previous extent of colony expansion (dashed black line), this exhibits the coupling of colony expansion and the formation of chemotactic ring "humps". The thin lime green line is indicative of the expected cell growth without diffusion, with the pink arrow displaying the impact of back-diffusion of cells (*304*). B) Illustrates the chemotactic range expansion of the chemotactic cells and the outer region of pioneering front. The sky blue front shows the settling chemotactic cells, with the yellow front showing the settling non-chemotactic cells (*304*). Both the chemotactic and non-chemotactic settling cells grow and swim randomly, with the non-chemotactic cells in-particular following Fisher–Kolmogorov wave dynamics (which is a model of wave propagation and cell growth) (*304*, *313*). The pioneering cells are shown in mint green. The non-chemotactic mutant however has a higher proportion of cells which colonise the inner region around the POI (mud brown), these cells are not growing and non-motile (*304*). The chemotactic strain has a shallower chemoattractant concentration gradient due to the fact its metabolism of the attractant is spread out over a greater range and it has access to more nutrients further away from the POI, whilst the non-chemotactic strain consumes nutrients during unguided migration and has limited access to further nutrients. After Cremer et al., (2019) (*304*, *313*).

Table. 5.1. *Pseudomonas putida* F1 reference table. Table of the three strains utilised from the chemotaxis mutant toolkit to investigate biomobilisation, developed in chapter four, with the functionality of the F1 strain, cheA mutant and WT strain underlined.



5.1). Note that the WT strain is un-tagged and does not contain the mScarlet-I (pMRE135) plasmid, therefore it can be used in conjunction with the cheA mutant and the F1 to investigate biomobilisation (Fig. 5.1). The study utilised succinate as a chemoattractant; it is an intermediate compound in the Krebs cycle and a terminal compound in the degradation of petroleum hydrocarbons, hence its selection (*103*, *305*, *306*). Further details on the chemotactic response of *P. putida* F1 are outlined in chapter four.

In chapter three it was shown that *Comamonadaceae*, *Pseudomonadaceae* and *Geobacteraceae* have been found to co-occur in the subsurface of a legacy petroleum hydrocarbon site and due to their distribution being influenced by chemotactic assisted biomobilisation. Therefore, using mutants of the *Pseudomonas* genus, within the *Pseudomonadaceae* family as a proxy for *Geobacteraceae* seems reasonable due to their shared ability to degrade petroleum hydrocarbons of a generally comparable cell size (*176*, *325–329*). *Pseudomonas* is an aerobic Gram-negative rod-like bacterium, however certain strains can survive in anaerobic environments, making it facultatively anaerobic (*103*, *160*).

Microbes in the qSS-FCLSA generate their own chemical gradient by metabolising a chemoattractant dispersed universally within soft-agar petri-dishes, with the innovation of this assay being the use of a fluorescent laser scanner to investigate how the chemotaxis and cells interact within a colony (*103*, *121*, *146*). The chemotactic response can be seen by the formation of circular chemotactic rings, with the size of the colony being measured to quantify a chemotactic response (Fig. 5.2, 5.3, 5.4) (*146*, *244*, *302*). This pioneering chemotactic front at the perimeter of the colony, boosts the colonies chemotactic range. Subsequently these cells then replicate themselves and move outwards leaving behind settlers which occupy previously inhabited zones (Fig. 5.4) (*303*, *304*). This expansion has been thought of as being a vital driver for expanding bacterial diversity into foreign territories (*96*). Moreover, the outer chemotactic margin and perimeter of the chemotactic cell front is similar to a microbial curtain of petroleum hydrocarbon degrading taxa that envelopes

contamination plumes in the field (Fig. 5.2, 5.3) (*52*, *123*, *178*, *304*).

Previous empirical and computer modeling work has shown that such chemotactic expansion, forms distinct chemotactic ring "humps" caused by the accumulation of chemotactic bacteria (Fig. 5.4) (*304*). The intensity profiles are used as a proxy for cell density. These hump structures also trigger back-diffusion of cells, which allows the cells again to swim outwards, following the self-generated gradient of the previous wave (Fig. 5.4 A, B, Table. 5.6) (*303*, *304*, *330*). These hump structures can be subtle, occurring intermittently within the colony (*304*, *331*). Behind these hump structures, settling cells grow and swim randomly; this has been shown previously in studies primarily using *E. coli* (Fig. 5.4) (*304*).

It can be theorised, based on phenotypical variation studied by Gude et al., (2020), how a colonies of mixed-culture of chemotactic and non-chemotactic cells may interact (*313*). This is achieved by substituting the *E. coli* pioneering cells and slow moving (less chemotactic) phenotypes in their study, with the F1 strain and cheA mutant respectfully (Table. 5.1) (*313*). In a mixed-culture the fast-moving F1 cells could constrain the movement of the slowly expanding cheA mutant. The F1 cells are then thought to consume the nutrients and chemoattractants at the edge of the colony, with these cells then triggering the flow of attractants inwards, towards the POI from the distal region of the colony, which the F1 cells which have been pushed back by back-diffusion utilise (*313*). This slowly blocks nutrient supply to the cheA growing near the POI and slows their expansion. Therefore allowing the F1 strain to migrate radially unimpeded. That being said the slower expanding cheA mutant may dominate the nutrient consumption near the POI which, in-turn stimulates the departure of the faster moving F1 cells. This resulting in more of a co-operative, bi-modal relationships based on spatial exclusion and segregation (*96*, *313*). However, biomobilisation, which would likely modify the relationship within this theorised system, has not been investigated. This study is the first to explore this and to quantify microbial interaction and biomobilisation within a colony composed of a mixed-culture F1 and cheA cells (Table. 5.1).

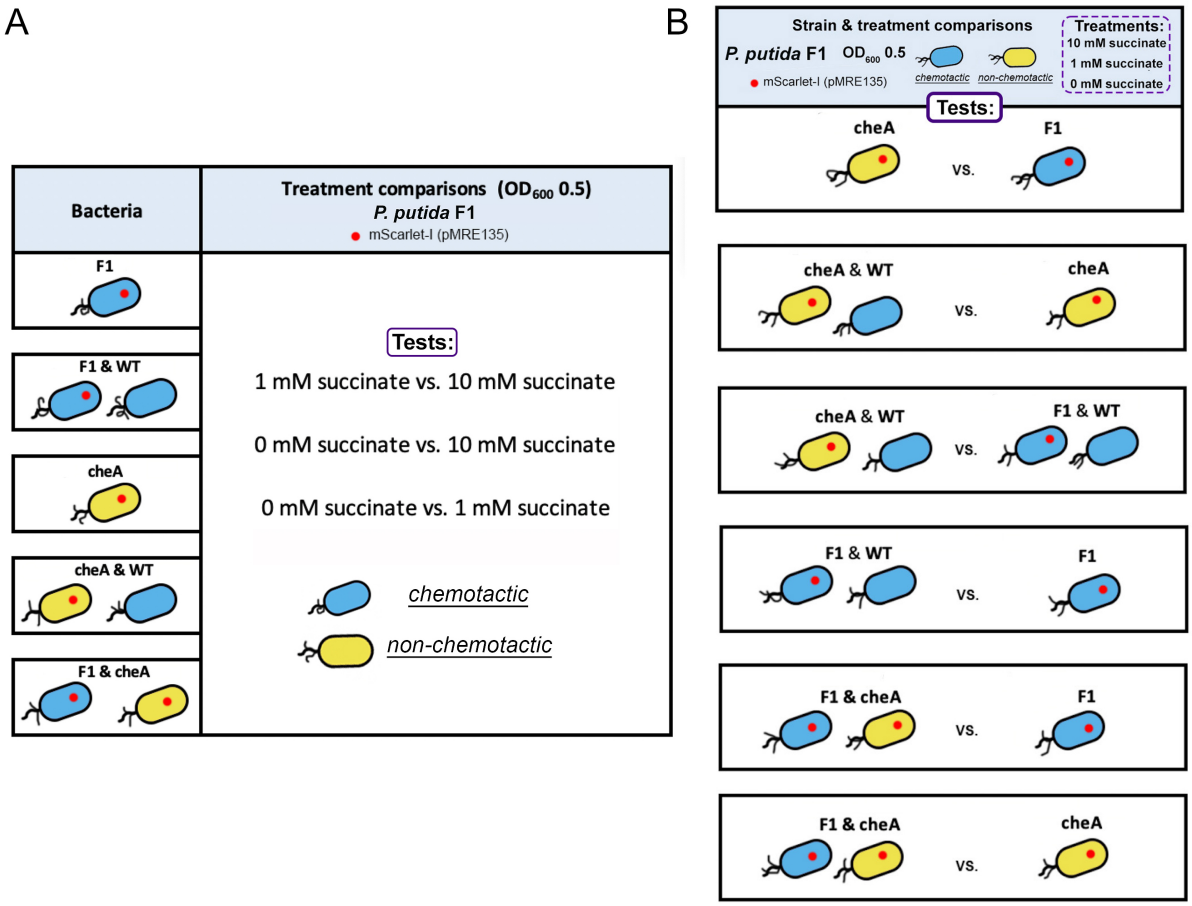
The qSS-FCLSA also allows for a more detailed study of the internal chemotactic humps structures and the "fuzzy" edges of the colony (Fig. 4.6, 4.9). The assay also has the ability to identify and characterise the intra-colony spatial distribution of the cheA cells, by leaving the WT cells un-tagged in a mixed-culture and decipher any interaction or biomobilisation that may occur. Therefore, possibly enhancing the rate NSZD of petroleum hydrocarbons (Fig. 4.5, 4.9, 5.2, 5.3, 5.4, Table. 5.1) (*52*, *123*, *147*, *178*, *304*, *332*).

5.2 Material and methods

5.2.1 qSS-FCLSA experimental design

Using the novel qSS-FCLSA, also developed in chapter four and following the methodology outlined previously, an experiment was conducted, applying the experimental design shown in table 5.2 (Table. 5.2). All mono-cultures were prepared to a OD_{600nm} of 0.50, in their mid-exponential growth phase with 3.5 μl being inoculated onto the 0.25 % soft-agar w/ M9 minimal media for 24 hours. Mixed-cultures consisted of a 50:50 mix of cells prepared to a OD_{600nm} of 0.50 (Fig. 4.9, 4.11). The qSS-FCLSA uses three different succinate treatment scenarios: 10mM, 1 mM and 0 mM, standard concentrations to investigate chemotaxis (*269*, *300*). The overnight qSS-FCLSAs were placed inside a fluorescence gel scanner to analyse intensity via the red fluorescence channel Cy3 (635 nm) (Fig. 4.9). The qSS-FCLSA assesses the spatial distribution of the F1 and cheA cells via the insertion of the mScarlet-I (pMRE135) plasmid, with the WT not containing the fluorescent plasmid. The presence of the mScarlet-I (pMRE135) plasmid is denoted by a red bullet point on the various schematics, tables and figures used throughout this chapter (Fig. 5.1 - 5.10). The laser scanner was set to a current gain of 377 PMT (V). This experiment was repeated 9 times to create batch biological replicates. The scans vary in length due to the image compression, with an average scan duration of 45 minutes (Fig. 4.9, 4.11).

Table. 5.2. qSS-FCLSA experimental design. The tables show the experimental design for the comparisons tested using the linear-mixed model batch effect and analysis of the estimates for the marginal means. A) Colony perimeters and intensity profiles tested for strain comparison, and B) colony perimeters tested for co-cultures, interaction and treatment comparison.



5.2.2 Microbial interaction and biomobilisation experimental design

In order to further investigate microbial interaction and biomobilisation, the intensity profiles of the strains were halved and summed together. This provided a theoretical representation of expected colony abundance at different OD_{600nm}. The shape of the intensity profiles and the AUC was then assessed.

The intensity of the F1 and cheA mono-culture curves were halved (from OD_{600nm} of $\sim$0.5) to give a representation of a curve reflecting an OD_{600nm} of $\sim$0.25. These curves were then halved to display what a co-culture of F1 and cheA might look like, this would then be compared to the intensity profile of the measured co-culture of F1 and cheA. In the measured co-culture it was assumed that there is a 50:50 split, for example in measured co-culture of F1 and cheA (OD_{600nm} $\sim$0.5), it was assumed there would be F1 OD_{600nm} $\sim$0.25 and F1 OD_{600nm} $\sim$0.25.

The intensity profiles of the cheA mutant OD_{600nm} $\sim$0.25 and 0.5 can be compared against the 50:50 co-cultures of cheA and the WT strain to assess any evidence of deviation from the expected profile, which would indicate some degree of biomobilisation (Table. 5.2, 5.3). This comparison was also undertaken on the intensity profiles of the F1 strain OD_{600nm} $\sim$0.25 and 0.5, against the F1 & WT co-culture, with similar curves expected (Table. 5.3). The co-cultures of F1 & WT and F1 & cheA were also summed to provide insight into the shape and perimeter of a colony containing only a quarter non-chemotactic cells. This theoretical exploratory analysis was conducted across all three succinate treatments (10 mM, 1 mM, and 0 mM) (Table. 5.3).

Further, theoretical curve profiles are also generated to investigate any biomobilisation effect using the selected strains from the chemotaxis mutant toolkit, with some cultures being halved or combined to estimate the curve at an OD_{600nm} of 0.25 (Table. 4.1, 5.1, 5.3). This is illustrated in the cell column of the table, inset in the top right. The co-culture is shown in forest green, the mono-culture of F1 is

Table. 5.3 Intensity curve profile reference table. A) The table shows the key for the mono and co-culture curve comparisons, and B) Design and reference table of the co-culture intensity profiles necessary to investigate biomobilisation.

A

Curve	Bacteria	Cells
	F1	
	cheA	
	F1 & cheA	
	F1	
	cheA	
	F1 & cheA	
	F1	
	cheA	
	F1 & cheA	

Treatment
10 mM succinate
1 mM succinate
0 mM succinate

B

Curve	OD_{600}	Bacteria	Cells
	0.5	F1 & cheA	
	0.5/2	F1	
	0.5/2	cheA	
	0.5	F1 & WT	
	0.5	cheA & WT	
	0.5/2+0.5/2	F1 & cheA	
	0.5+0.5	F1 & WT + cheA & WT	

Treatment
10 mM succinate
1 mM succinate
0 mM succinate

shown in sky blue, however it was halved, with the cheA strain in yellow also being halved. The magenta curve is the 50:50 co-culture of F1 and the WT strain, with the co-culture of the cheA and the WT strains being shown in black. The navy blue curve is half the F1 strain (OD_{600nm} of ∼0.25) plus half the cheA mutant cells (OD_{600nm} of ∼0.25). The vermilion curve is the co-culture of F1 strain and the WT strain plus the co-culture of the cheA mutant and the WT strain. A plot of the natural log of the intensity profiles is also included to bottom right of theoretical curve profiles in the results.

5.2.3 Statistical methodology and model selection

The perimeter data was analysed by running a linear mixed model using the "lmer" function within the *R* package "lme4" (version 1.1-31) (Model. 1). A linear mixed model statistical approach was undertaken to account for the random effects induced by having multiple experimental batches (*333*, *334*). Exploratory analysis showed that plotting the raw colony perimeter readings resulted in a multi-modal distribution (Fig. 5.5, Table. 5.2). A standardisation technique adopted by Maier et al., (2018), which studied colony size was trialed (*335*). This method standardised the measured values by calculating the median colony perimeter and dividing this figure by the standard deviation of the colony perimeters, however it failed to remove the skewed distribution, often present in biological systems (*335*). A standard natural log transformation remedied the multi-modal distribution and heteroskedastic nature of the perimeter distribution and residuals (Fig. 5.5 A) (*336*). This was confirmed by running a Levene's Test for homogeneity of variance by using the "leveneTest" function in *R* within the "car" package (version 3.1-1) (Model. 1). The qSS-FCLSA assay was validated by comparing the perimeter measurements of the F1 strain versus the cheA strain, and assessing the outcome of the mixed-linear model.

Model. 1. Linear mixed-effects model: *log*(Perimeter) ∼ Treatment*Bacteria+(1|Batch)

Model. 2. Linear model: *log*(Perimeter) ∼ Treatment*Bacteria

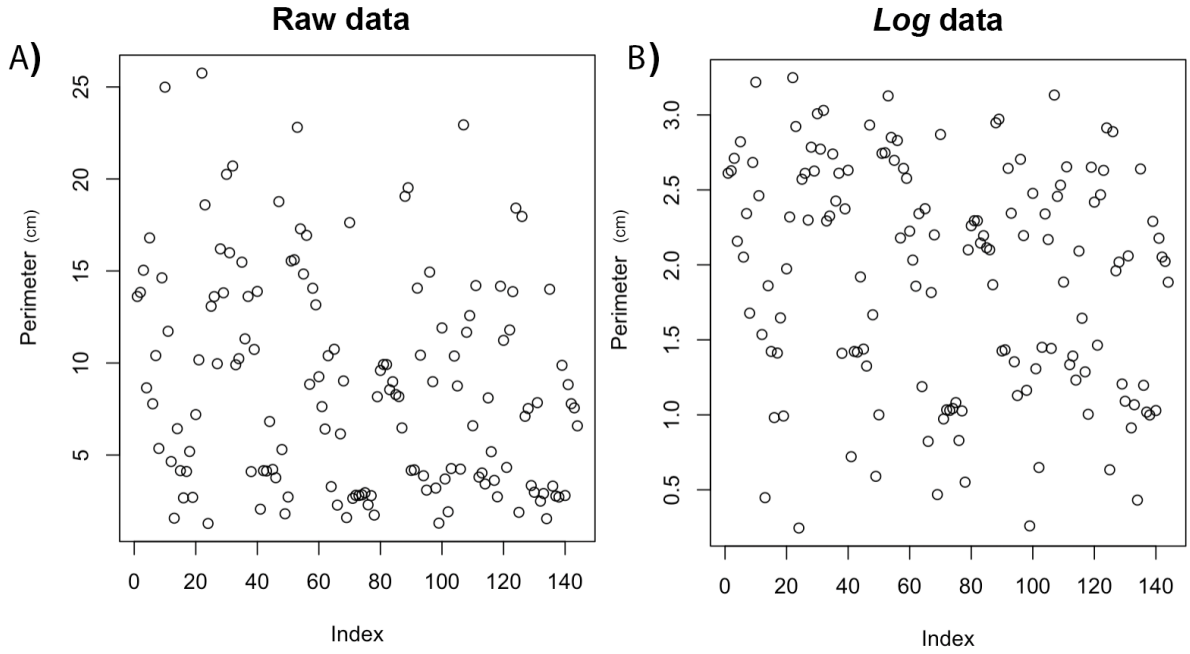


Fig. 5.5. Model logarithmic transformation. A) The distribution of the perimeters (cm). B) The natural *log* of the perimeters (cm).

There was a statistically significant difference in the model when accounting for batch effects of p-value $5.302e^{-08***}$, with the significance being calculated using the "anova" function within the "stats" package (version 3.6.2) in *R* (Model. 1, 2, Fig. 5.6). Therefore Model. 1. was selected for down-steam analysis. Comparisons between different strains and treatments were evaluated by analysis of the estimates for the marginal means using the "emmeans" function and package (version 1.3.2) in *R*.

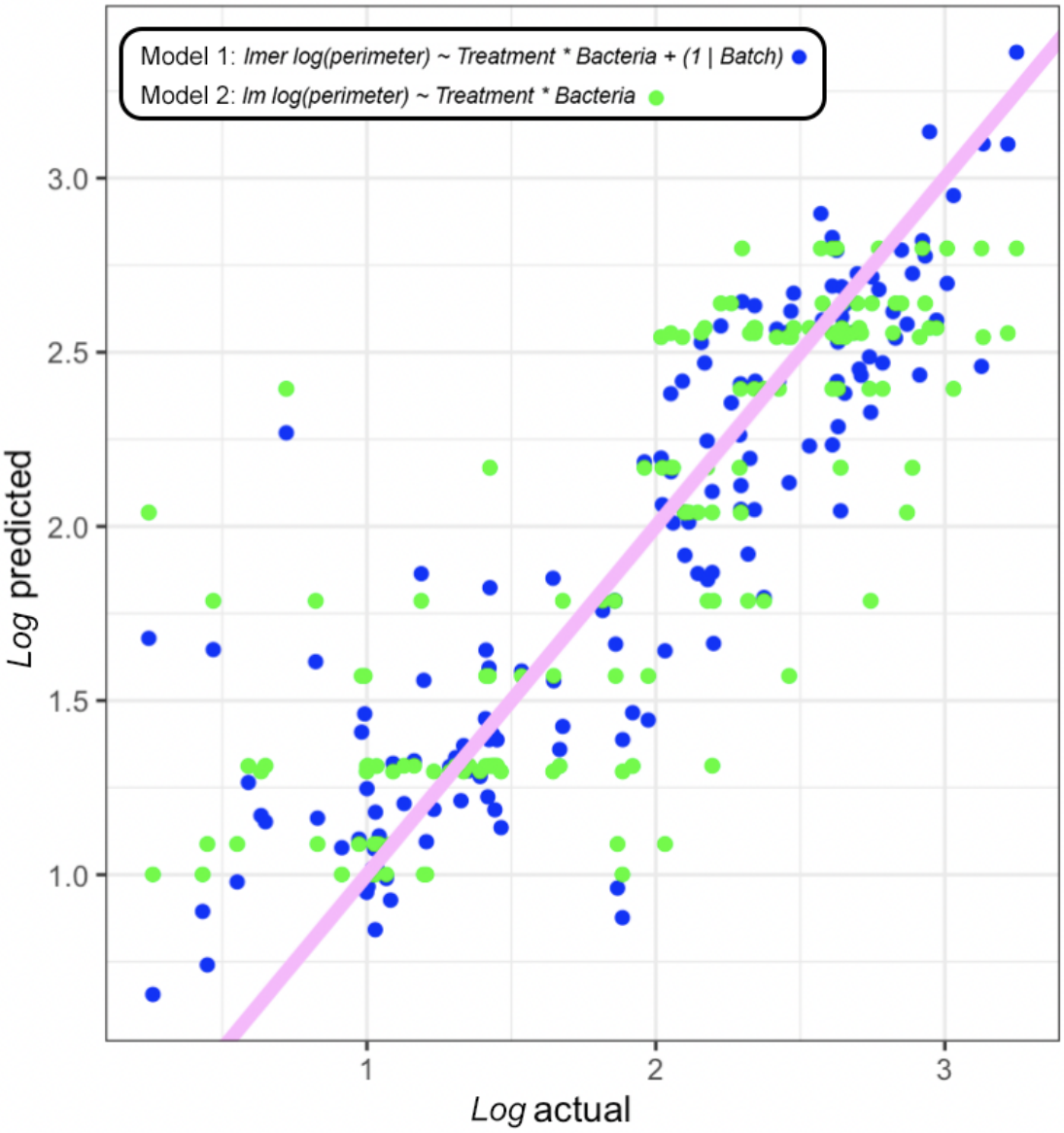


Fig. 5.6. Linear mixed model batch effect comparison. This figure shows the comparison of the predicted vs. actual measured perimeters of Model. 1 and Model. 2, with the model containing batch effects in navy blue and the model without in lime green. Model. 1 has a adjusted R^2: 0.4895; calculated using the "summary" base *R* function and Model. 2 has an R^2: 0.4999; calculated using the "r.squaredGLMM" function within the *R* "MuMIn" package (*337*). Note that the asterisk here (*) denotes an interaction term.

5.3 Results

5.3.1 Perimeter results using the qSS-FCLSA

The co-culture of F1 and cheA had the greatest mean perimeter across all treatments, with the F1 mono-culture generally being second highest (Fig. 5.7). The co-culture of F1 and cheA has a perimeter of ∼9 cm in the 0 mM succinate treatment, ∼14 cm in the 1 mM treatment and ∼16 cm in the 10 mM treatment. The F1 & cheA and F1 mono-cultures and F1 & WT have a similar elevated variance. The cheA mono-culture has a generally low mean perimeter across all treatments of between ∼3-5 cm. It also has a lower degree of variance (Fig. 5.7).

The cheA & WT co-cultures have similar mean perimeters across all three succinate treatments to the cheA mono-culture. This is also true at a succinate concentration of 10 mM for the F1 & WT co-culture when compared to the F1 mono-culture, however at lower concentrations the F1 is slightly smaller than the respective F1 & WT co-culture (Fig. 5.7).

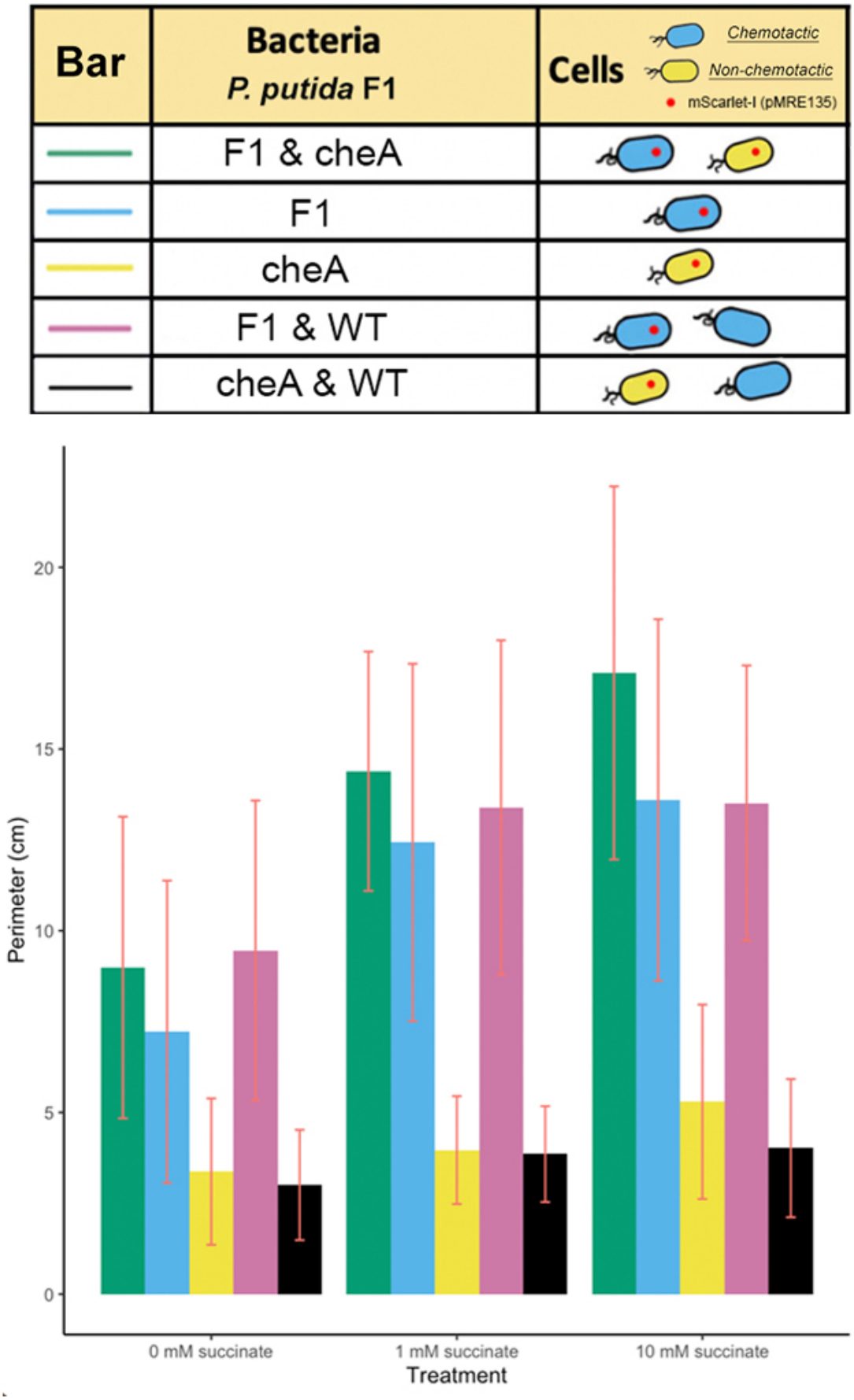


Fig. 5.7. Colony perimeters measured using the qSS-FCLSA. Plot of the raw colony perimeters (cm) of the mono and co-cultures; F1 & cheA (forest green), F1 (sky blue), cheA (yellow), F1 & WT (magenta), and cheA & WT (black). The standard deviation error bars are shown in red.

5.3.2 Perimeter comparisons

5.3.2.1 F1

The difference in the colony perimeters was assessed within the qSS-FCLSA. The perimeter of F1 was significantly greater in the presence of 1 mM and 10 mM succinate compared to when no attractant was present, with there being a non-significant difference in colony size between concentrations of 1 mM and 10 mM succinate (Table. 5.4).

5.3.2.2 F1 & WT

There was a non-significant change in the colony perimeters of a co-culture of F1 & WT in the presence of succinate. The co-culture is composed of a 50:50 mixture of both F1 & WT cells (Table. 5.4).

5.3.2.3 cheA

The cheA mutant shows no significant difference in the perimeter of the colony across the different chemoattractant treatments (Table. 5.4).

5.3.2.4 cheA & WT

The co-culture of the cheA mutant & WT strain shows a non-significant difference in the perimeter across the different succinate treatments (Table. 5.4).

5.3.2.5 F1 & cheA

The co-culture shows a significant difference in colony perimeter in the presence of a succinate, however a non-significant difference in perimeter between 1 mM to 10 mM succinate (Table. 5.4).

5.3.2.6 cheA vs. F1

F1 and cheA colonies had a significant difference in the colony perimeter across all succinate treatments, with cheA being significantly smaller (Table. 5.5).

5.3.2.7 cheA & WT vs. cheA

Co-cultures of cheA & WT had a non-significant difference in colony perimeter compared to the cheA mutant, with the cheA colony being slightly larger across all treatments; indicated by the negative t-ratio (Table. 5.5).

5.3.2.8 cheA & WT vs. F1 & WT

Co-cultures of cheA & WT versus F1 & WT had a significant difference in colony perimeter, with the F1 & WT having a greater perimeter across all treatments, indicated by the negative t-ratio (Table. 5.5).

5.3.2.9 F1 & WT vs. F1

Co-cultures of F1 and WT had a non-significant difference in colony perimeters versus a F1 mono-culture. The green text however, indicates a positive t-ratio of the co-culture perimeter size against the F1 mono-culture across all succinate treatments (Table. 5.5).

5.3.2.10 F1 & cheA vs. F1

Co-cultures of F1 & cheA had a non-significant difference in colony perimeters versus a F1 mono-culture, with the F1 strain mono-culture being larger (Table. 5.5).

5.3.2.11 F1 & cheA vs. cheA

Co-cultures of F1 & cheA had a significantly greater colony perimeter than cheA mutant mono-cultures, across all treatments (Table. 5.5).

Table. 5.4. Linear mixed model treatment comparison using pairwise comparisons of estimated marginal means. The table shows the treatment comparison of different mono-cultures and co-cultures. The t-ratio is calculated by dividing the difference between the means of the two treatment groups by the standard error of the difference. If the t-ratio is positive (green text), it means that the mean of the first treatment (left) is larger than the mean of the second treatment (right). If it is negative the first treatment is smaller (red text). The *p*-value and the significance asterisks are also illustrated (0-0.001 ***, 0.001-0.01 **, 0.01-0.05 *, 0.05-1 NS).

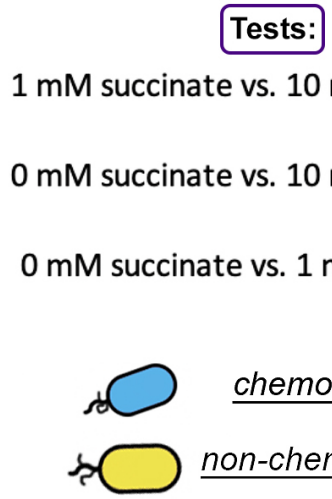
Bacteria	Treatment comparisons (OD_{600} 0.5) *P. putida* F1 ● mScarlet-I (pMRE135)	t-ratio	*p*-value	
F1 		-0.8398	0.9999	N.S.
		-4.5245	0.0013	**
		-3.6427	0.0291	*
F1 & WT 		-0.1938	1.0000	N.S.
		-2.2127	0.6552	N.S.
		-2.0813	0.7443	N.S.
cheA 		-1.1011	0.9987	N.S.
		-2.7770	0.2739	N.S.
		-1.5968	0.9562	N.S.
cheA & WT 		-0.0956	1.0000	N.S.
		-1.7309	0.9191	N.S.
		-1.6380	0.9465	N.S.
F1 & cheA 		-0.5683	1.0000	N.S.
		-4.2454	0.0038	**
		-3.6770	0.0262	*

Table. 5.5. Linear mixed model strain comparison using pairwise comparisons of estimated marginal means. The table shows the strain comparison of different mono-cultures and co-cultures. The t-ratio is calculated by dividing the difference between the means of the two culture groups by the standard error of the difference. If the t-ratio is positive (green text), it means that the mean of the first culture (left) is larger than the mean of the second culture (right). If it is negative, the first culture is smaller (red text). The p-value and the significance asterisks are also illustrated (0-0.001 ***, 0.001-0.01 **, 0.01-0.05 *, 0.05-1 NS).

Strain & treatment comparisons *P. putida* F1 OD_{600} 0.5 (chemotactic / non-chemotactic) mScarlet-I (pMRE135) Treatments: 10 mM succinate / 1 mM succinate / 0 mM succinate Tests:	t-ratio	*p*-value	
cheA vs. F1	-5.5419	1.78E-05	***
	-5.7106	8.50E-06	***
	-4.0078	0.0087	***
cheA & WT vs. cheA	-1.4830	0.9764	N.S.
	-0.4327	1.0000	N.S.
	-0.4740	1.0000	N.S.
cheA & WT vs. F1 & WT	-7.0731	1.16E-08	***
	-7.1766	6.88E-09	***
	-6.3755	3.71E-07	***
F1 & WT vs. F1	0.1978	1.0000	N.S.
	0.8533	0.9999	N.S.
	2.2627	0.6195	N.S.
F1 & cheA vs. F1	1.4633	0.9790	N.S.
	1.7154	0.9242	N.S.
	1.4379	0.9820	N.S.
F1 & cheA vs. cheA	6.9092	2.65E-08	***
	7.2514	4.69E-09	***
	5.2436	0.0001	***

5.4 Intensity curve analysis

5.4.1 Mono-culture and co-culture comparisons

The radial intensity profile plot shows the spatial distribution and interaction of F1, cheA and a co-culture of F1 and cheA in the different succinate treatments. The intensity signal comes from the expression of the mScarlet-I (pMRE135) around the POI. The F1 strain exposed to the 10 mM succinate treatment has the intensity of approximately 24000 a.u (at the POI; 0 cm), with a secondary peak occurring at 0.2 cm, with a peak intensity of approximately 21000 a.u (Fig. 5.8). The curve then lowers in intensity steeply until 0.4 cm, before decreasing more gradually. The F1 strain in the 1 mM succinate treatment curve shows a peak intensity of around 18000 a.u, with a small hump structure. This is followed by a fluctuating decline to around 5000 a.u around 0.25 cm from the POI, before exhibiting a more gradual undulating decline in intensity. The treatment with 0 mM displays an initial peak at 11000 a.u, followed by an undulating decline in intensity to approximately 1 cm (Fig. 5.8).

The insert of the natural log of the curves shows the distinct intensity humps that form at a radius of 0.7-2 cm (Fig. 5.8). These intensity humps also occur around the POI between 0-0.25 cm. The F1 10 mM succinate treatment curve has the greatest AUC of 11614.22, with the 1 mM succinate treatment being less than half (5985.36) and the 0 mM succinate treatment being the lowest at 3332.23 (Fig. 5.8, Table. 5.6).

The cheA intensity profile shows a steep drop in intensity, with the 10 mM succinate treatment following the initial trend of the F1 1 mM succinate treatment curve (Fig. 5.8). The intensity profile then drops to a greater degree at 0.25 cm from the POI, lowering towards 0 at around 0.6 cm from POI. The 1 mM and 0 mM succinate treatment curve following a similar slope. However they have lower initial peak intensities at approximately 12500 a.u, and similar AUCs of 2532.92 and 2248.93 respectively (Fig. 5.8, Table. 5.6).

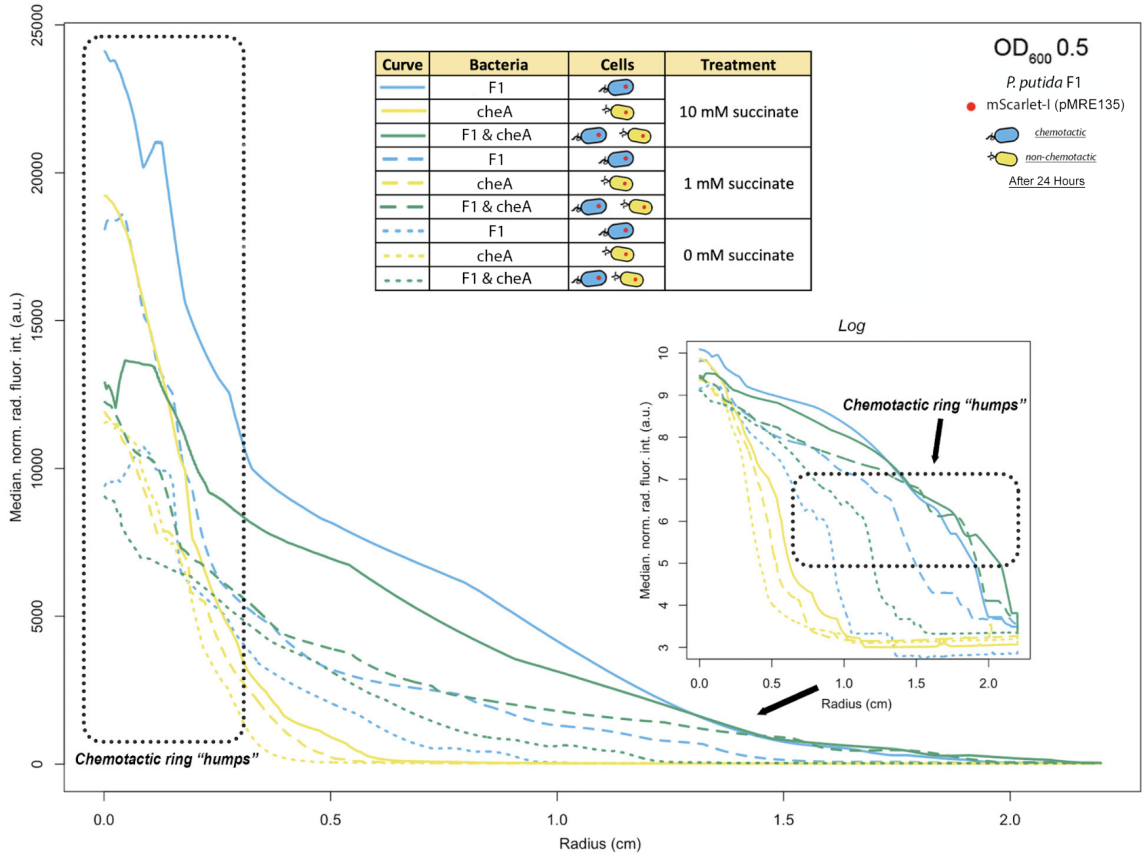


Fig. 5.8. Colony radial intensity curve profiles. This figure shows the median normalised radial fluoresce intensity profiles for the cultures; the F1 strain in sky blue, the cheA mutant in yellow and F1 and cheA co-culture in forest green, for all three succinate treatments (0 mM, 1 mM, and 10 mM). A plot showing the natural log of the intensity curves is also inset to bottom right of the figure.

The co-culture of F1 and cheA at 10 mM forms the lowest peak intensity of the three cultures, with a flatter initial intensity peak of 13500 a.u at 0.1-0.2 cm from the POI, with an AUC of 8594.99 (Table. 5.6). The F1 and cheA co-culture curve follow a similar decline in intensity to the F1 10 mM succinate curve, past 1.6 cm (Fig. 5.8). The F1 & cheA intensity profile and the 1 mM succinate treatment have a similar initial peak intensity to the 10 mM succinate treatment. However, it shows a more gradual undulating decline in intensity, with the 0 mM succinate treatment exhibiting a similar decline, with a lower initial intensity peak of 9500 a.u (Fig. 5.8, Table. 5.6). The co-culture had a greater AUC across all three treatments than the cheA mutant mono-cultures (Table. 5.6). The 1 mM succinate treatment of the F1 mono-culture and the co-culture have similar AUCs and curve profiles (Fig. 5.8, Table. 5.6, 5.8).

Table. 5.6. Area under curve (AUC) comparisons for strain and treatments. This table depicts the area under the median normalised radial intensity curve for the mono-cultures of F1 in sky blue, cheA in yellow and the co-culture of F1 and cheA. The green shading is used to highlight the ranges in AUC; a proxy for bacterial abundance across the different treatments.

Curve (OD_{600} 0.5)	Treatment	Area under curve (AUC)
F1 	10 mM succinate	11,614.22
		5,985.36
	1 mM succinate	3,332.23
cheA 		3,923.24
	0 mM succinate	2,532.92
		2,248.93
F1 & cheA 	*P. putida* F1 mScarlet-I (pMRE135) *chemotactic* *non-chemotactic*	8,594.99
		5,693.36
		3,673.81

5.4.2 Microbial interaction and biomobilisation comparison

5.4.2.1 Intensity profile (10 mM succinate)

Microbial interactions and biomobilisation of the F1 and cheA co-culture is assessed in figure. 5.9 with the forest green curve being plotted to benchmark how the profiles vary across the three treatments (Fig. 5.9 A, B, C). In figure 5.9 A, the F1 strain and cheA mutant curve profile is halved. This is to provide an approximation of what a curve OD_{600nm} of 0.25 may be. The black curve which represents a co-culture of cheA & WT had an AUC of 2421.9 and a secondary peak structure at around 1000 a.u (Fig. 5.9 A, Table. 5.7).

The F1 and WT co-culture, represented by the magenta curve had an initial peak intensity of approximately 1000 a.u. The magenta curve decreases gradually following the sky blue F1 curve, which represents an approximate OD_{600nm} of 0.25 (Fig. 5.9 A). The sky blue F1 curves had an AUC of 5807.11, this is higher than the magenta AUC of 5162.25 (Fig. 5.9 A, Table. 5.7). The navy blue curve; representing the sum of half the F1 mono-culture and half the cheA mono-culture, have an initial peak intensity of approximately 22000 a.u. The curves generally have a steep decline at 0.2 cm, however the vermilion curve; representing the sum of the co-cultures of

F1 and cheA with the WT, displays a more punctuated decline (Fig. 5.9 A). The navy blue and vermilion curves have similar plots and similar AUCs with values of 7768.73 and 7583.23 respectively (Table. 5.7).

5.4.2.2 Intensity profile (1 mM succinate)

The curves at 1 mM succinate are shown in figure 5.9 B. The vermilion and navy blue curves have an initial peak intensity of around 15000, with the vermilion curve starting higher (Fig. 5.9 B). The navy blue curve represents the sum of half the mono-cultures of F1 and cheA. It portrays a steep decline in intensity before leveling out at a radius of 0.5 cm (Fig. 5.9 B). The vermilion curve represents the combination of the F1 strain and the WT with the cheA mutant and the WT, displayed a slower decline and contained a secondary initial peak structure. The magenta curve representing the F1 and the WT co-culture, displayed an initial peak intensity of around 9000 a.u., and had a slow decline in intensity, following a similar path to the vermilion curve at around 0.6 cm. The yellow curve depicting approximately half the cheA mutant cells starts at approximately 6000 with a sloping decline, punctuated in places (Fig. 5.9 B).

The cheA mutant in co-culture with the WT strain (in black) exhibited a secondary peak at 0.2 cm, displayed a sloping decline, slightly steeper than the yellow curve, with both curves decreasing towards 0 at 0.5 cm, with the AUC of the yellow curve being 1266.46 and the black curve having a greater AUC of 1762.58 (Table. 5.7). The sky blue curve displayed a slightly punctuated decline to around 0.5 cm, it then levels out into a more gradual decline (Fig. 5.9 B). The co-culture of the F1 strain and cheA mutant shown in forest green displays a gradual decline from an initial peak intensity of 12500 a.u and an AUC of 5693.36, the curve intersects the magenta and vermilion curves, before decreasing at a slower rate, with a wavier decline (Fig. 5.9 B, Table. 5.7). Intensity humps between 1-2 cm are present for all curves, apart from the yellow curve depicting half the cheA cells and the black curve depicting the co-culture of cheA & WT (Fig. 5.9 B).

5.4.2.3 Intensity profile (0 mM succinate)

The treatment at 0 mM succinate without any attractant, shows curves of a more similar nature and shape, with generally a tighter initial intensity of between 5000-1000 a.u and AUC (Fig. 5.9 C, Table. 5.7). The vermilion curve representing a combination of the F1 strain and the WT with the cheA strain and the WT, shows the highest initial intensity of approximately 16000 a.u. It decreases steeply until an intensity of 5000 a.u at 0.25 cm, before decreasing at a slower rate towards 0 (Fig. 5.9 C). The magenta curve illustrates the F1 strain in combination with the WT strain, displaying an initial peak intensity of around 75000 a.u, declining towards 0.5 cm at a slow rate, before following the path of the vermilion curve towards 0 (Fig. 5.9 C).

There is a lack of any clear secondary peak structures between 0 and 0.25 cm. The black curve representing the cheA mutant and the WT strain exhibited a markedly steep decline at 0.25 cm, before following the decline of the yellow curve, with the AUC of the yellow curve (1124.46) being lower than the black curve (1985.13) (Fig. 5.9 C, Table. 5.7). The intensity humps occur at a radius of between 0.7-1.2 cm for the 0 mM succinate treatment. The intensity humps between 0.5-2 cm appear to decrease in intensity as succinate concentration decreases, along with a decrease in the spatial radius and extent of the intensity humps (Fig. 5.9).

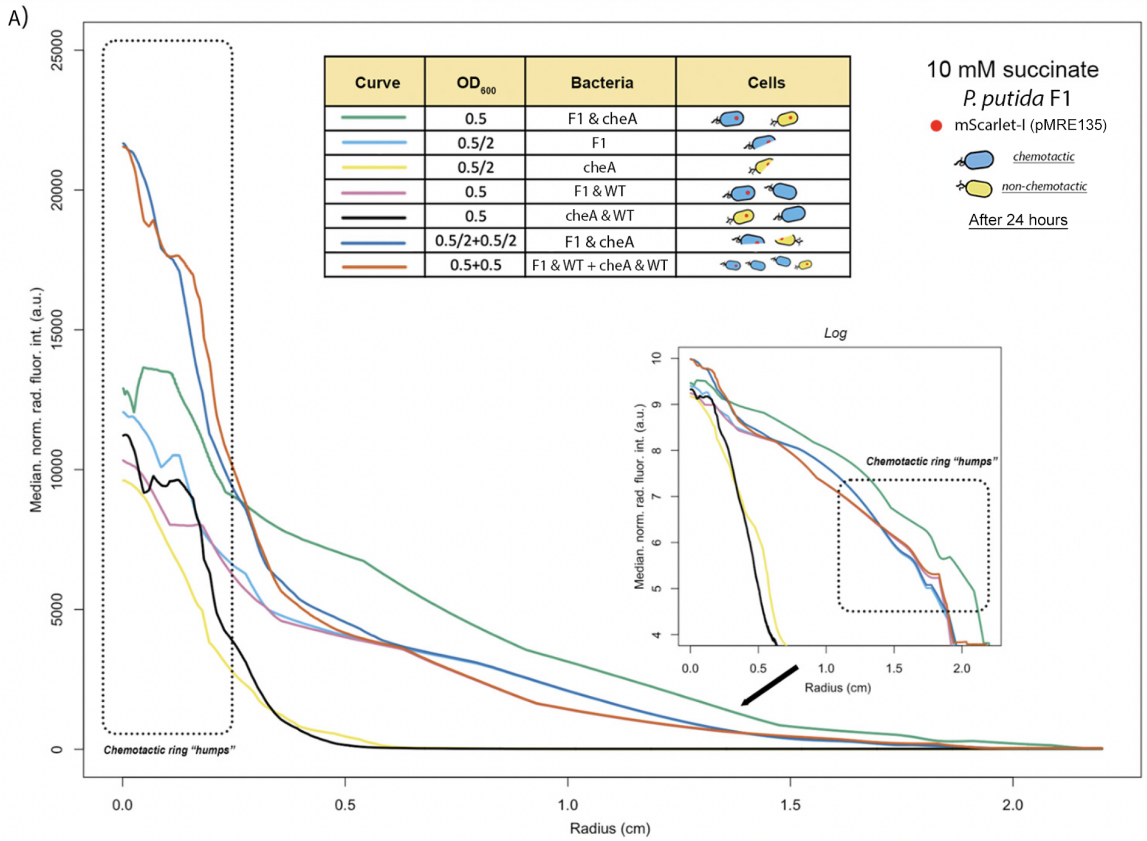


Fig. 5.9 A

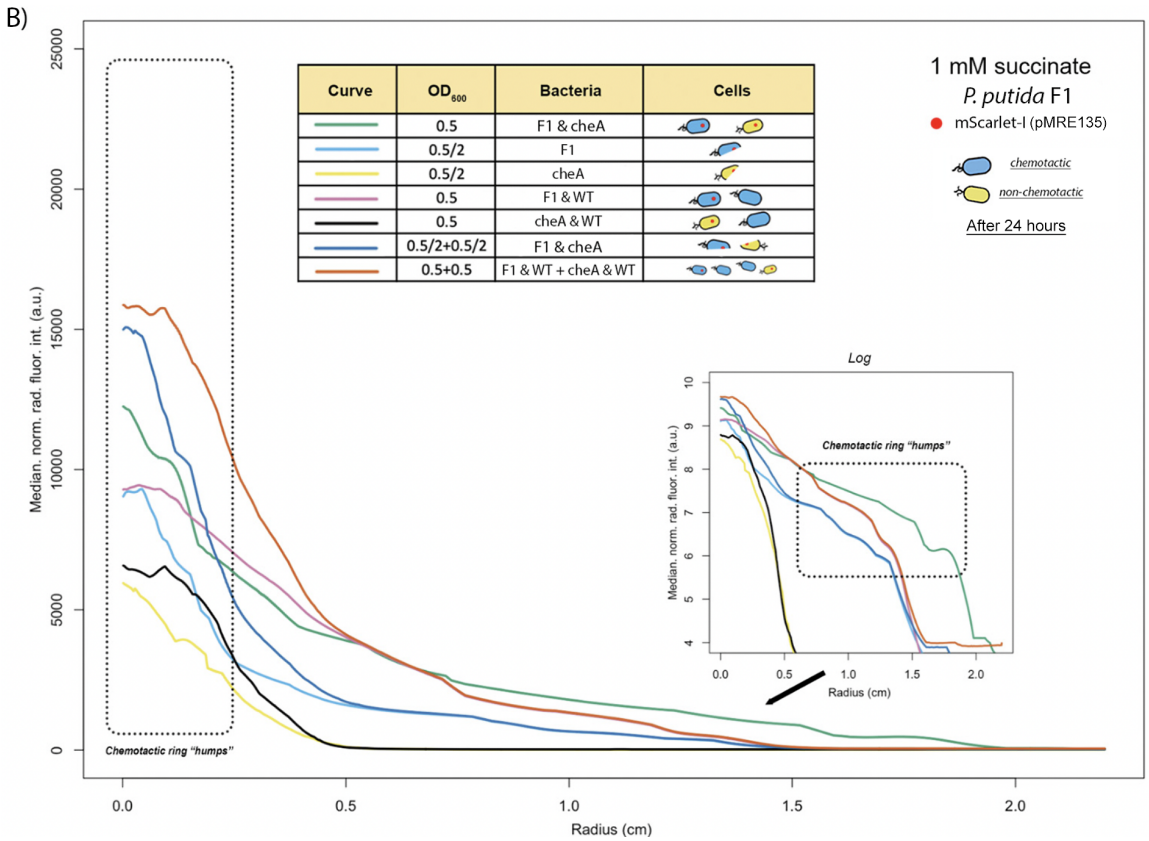


Fig. 5.9 B

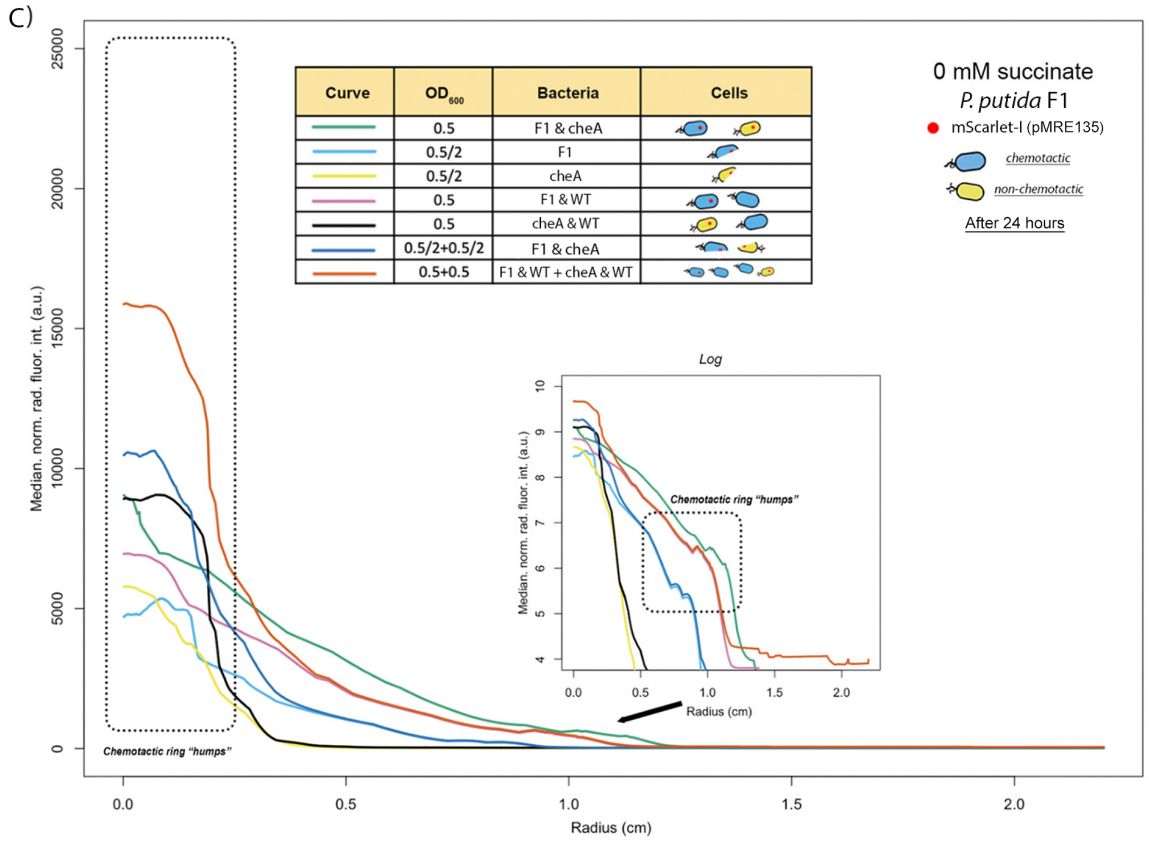
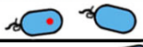
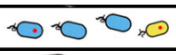
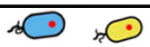
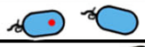
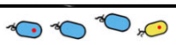


Fig. 5.9 C

Fig. 5.9. Colony intensity curve profile comparisons providing evidence for biomobilisation and microbial transport. The figure shows three different succinate treatments: A) 10 mM , B) 1 mM and C) 0 mM. The curves depict various combinations necessary to investigate any biomobilisation effect using the selected strains from the chemotaxis mutant toolkit, with some cultures being halved or combined to estimate the curve at an OD_{600nm} of 0.25 (Table. 4.1, 5.1). This is illustrated in the cell column of the table, inset in the top right. The co-culture is shown in forest green, the mono-culture of F1 is shown in sky blue, however it was halved, with the cheA strain in yellow also being halved. The magenta curve is the 50:50 co-culture of F1 and the WT strain, with the co-culture of the cheA and the WT strains being shown in black. The navy blue curve is half the F1 strain (OD_{600nm} of ∼0.25) plus half the cheA mutant cells (OD_{600nm} of ∼0.25). The vermilion curve is the co-culture of F1 strain and the WT strain plus the co-culture of the cheA mutant and the WT strain. A plot of the natural log of the intensity profiles is also included to bottom right of the figures.

Table. 5.7. Area under curve (AUC) comparisons providing evidence for microbial interaction and biomobilisation. This table depicts the area under curve (AUC) for the median normalised radial intensity profiles. It depicts the various combinations necessary to investigate any biomobilisation effect. Note that the cells drawn cut in half, represent half the amount of cells.

Curve	OD_{600}	Bacteria *P. putida* F1	Cells (chemotactic / non-chemotactic / mScarlet-I (pMRE135))	Treatment	Area under curve (AUC)
	0.5	F1 & cheA		10 mM succinate	8,594.99
	0.5/2	F1			5,807.11
	0.5/2	cheA			1,961.62
	0.5	F1 & WT			5,161.25
	0.5	cheA & WT			2,421.98
	0.5/2+0.5/2	F1 & cheA			7,768.73
	0.5+0.5	F1 & WT + cheA & WT			7,583.23
	0.5	F1 & cheA		1 mM succinate	5,693.36
	0.5/2	F1			2,992.68
	0.5/2	cheA			1,266.46
	0.5	F1 & WT			5,022.67
	0.5	cheA & WT			1,762.58
	0.5/2+0.5/2	F1 & cheA			4,259.14
	0.5+0.5	F1 & WT + cheA & WT			6,785.25
	0.5	F1 & cheA		0 mM succinate	3,673.81
	0.5/2	F1			1,666.11
	0.5/2	cheA			1,124.46
	0.5	F1 & WT			2,809.29
	0.5	cheA & WT			1,985.13
	0.5/2+0.5/2	F1 & cheA			2,790.58
	0.5+0.5	F1 & WT + cheA & WT			4,794.42

5.5 Discussion

5.5.1 Mono-culture treatment comparisons

The mono-cultures of the F1 strain show a significant difference in colony perimeter in the presence of succinate than without, as expected (Fig. 5.8, 5.10, Table. 5.4) (*269*, *307*, *338*, *339*). The F1 intensity curves, particularly when comparing 1 mM to 10 mM succinate show that, as the concentrations of chemoattractant increase, there is an increase in intensity profile and AUC (Fig. 5.8, Table. 5.5, 5.6). This is as a result of bacteria responding to increased chemoattractant concentrations and

nutrient gradients, created by the metabolism of the succinate (*269*, *307*, *338*, *339*).

However, there is a non-significant difference in the perimeter of the F1 colony, when there is an increase in succinate concentration between 1 mM and 10 mM succinate. This suggests that a "saturating concentration" may exist between 0-10 mM succinate. This occurs when most of the chemoreceptors (such as McfR, McfS and McfQ, mentioned in the chapter four), which run across the length of the cells are activated and saturated (*139*, *269*, *340–342*). This means the cells struggle to sense direction and become disoriented, with this saturating concentration being different for various attractant, cell types and microbes (Table. 5.4) (*139*, *340–342*). Generally, succinate concentrations of between 1 mM and 10 mM are used to demonstrate a chemotactic response (*127*, *269*). Further research with a wider range of succinate concentrations will explore the saturating concentration further and determine if this is case (*127*, *269*).

The F1 strain forms distinct chemotactic ring hump structures in figure 5.8, due to the accumulation of chemotactic bacteria (Fig. 5.3 A, 5.4, 5.8, 5.10) (*304*). This agrees with the expected curve profile mentioned in the introduction section of this chapter, which has been witnessed by direct experimental observation or numerically solving chemotactic growth expansion dynamics of chemotactic colonies in other studies. However most of these studies assessed the guided chemotactic expansion of *E. coli* cells, this suggests that *P. putida* F1 has the potential to form similar spatial distributions (Fig. 5.4, 5.8, 5.10, Table. 5.1) (*303*, *304*, *313*).

The cheA mutant shows no significant difference in colony perimeter when exposed to different concentrations of chemoattractant due to its inability to sense a chemical gradient (Table. 5.4) (*103*). This is due to the fact the cheA mutants lacks the guided response and collective colony dynamics qualities of the chemotactic F1 strain (Fig. 5.3 B, 5.4 B, 5.8, 5.10) (*189*, *289*, *304*). The intensity profiles for the cheA mutant support this with the profiles showing a characteristic steeply decreasing curve, which are governed by Fisher–Kolmogorov wave dynamics (Fig. 5.8, 5.10)

(*189*, *289*, *304*, *313*, *343*). This agrees with previous chemotaxis assays and studies where the non-chemotactic mutant has been shown not to form defined chemotactic rings (Fig. 5.8, 5.9) (*103*, *303*, *304*, *313*).

The lower AUC of the cheA mutant compared to the F1 mutant is likely due to an increased amount of cells colonising the zone around the POI and not growing (Fig. 5.4, Table. 5.6) (*304*, *313*). This is due to the fact they are trapped by more active growing settling cheA cells, which swim in an unguided random manner, and lack the pioneering cells which sense gradients and explore radially, allowing them access to the metabolisable attractants which govern increased growth (Fig. 5.3 A, B, 5.4, 5.8, Table. 5.6) (*304*, *313*). The cheA mutant is also unable to up-regulate motility assisted chemotaxis genes, to boost motility and spatial range when compared to the F1 strain, thus further contributing to this effect (Fig. 5.4) (*191*). It is important to note that, given time and a period of greater than 24 hours, the cheA strain should reach the same perimeter as the F1 strain and consume all the nutrients/chemoattractants present, however less efficiently and at a slower rate. This is based on results from the aforementioned Ni et al., (2020) study, which used chemotactic *E. coli* cells and non-chemotactic mutants (*101*).

The F1 strain forms a significantly greater perimeter than a cheA mutant and agrees with the curve profiles and general results of the study by Cremer et al., (2019) on chemotactic colony expansion (Fig. 5.4, Table. 5.5) (*304*). The qSS-FCLSA allows for a greater perspective of internal colony dynamics and chemotactic ring hump formation, with the raw scan from the fluorescence laser gel scanner being easily digitised and imported to ImageJ for further spatial distribution analysis (Fig. 4.9, 4.11). These results validate this novel method of imaging microbial chemotaxis and highlights the potential of chemotaxis to enhance biodegradation over non-chemotactic cells (Fig. 1.2, 1.3, 5.2). Therefore, it is the recommended that this qSS-FCLSA should be considered as a noteworthy alternative to the traditional "bucket of light" visualisation method (*147*, *150*).

5.5.2 Chemotactic behaviour in carbon low environments

In the qSS-FCLSA the F1 strain formed a significantly greater perimeter than the cheA mutant, even in the case of the 0 mM succinate treatment, with just the salts in the M9 minimal media and the agar present, with no other carbon source (Fig. 5.3 A, b, 5.8, Table. 5.5). This response can be explained by the natural advantage of chemotaxis over non-chemotactic cells (*101*). In carbon limited conditions, the colony perimeter of the F1 strain may still be significantly larger due to cohesive and collective bacterial behaviour of chemotactic cells. They can move outwards radially from the POI when they detect dead or dying cells, which liberate fresh sources of carbon and chemoattractants from their insides (*271*, *289*, *344*, *345*). This behaviour is supported by recent evidence of the up-regulation of chemotaxis and motility genes in chemotactic when cells when they are exposed to dead cells and in low carbon environments (*101*, *344*). The cheA mutant is unable to sense any carbon sources liberated from the dying cells and therefore unable to up-regulate chemotaxis genes accordingly, contributing to enhanced cell death compared to the F1 strain and a diminished perimeter in the 0 mM succinate treatment (Fig. 5.4, 5.8, Table. 5.1) (*191*).

Another reason for any growth at 0 mM succinate, could be that during the cell washing step with the M9 minimal media salts, some remnants of carbon from the culturing LB medium adhered to the cell walls, thereby providing a chemoattractant effect for the F1 strain (Fig. 5.8, 5.10, Table. 5.6). Interestingly, it has also been theorised that the slow growing or less chemotactically active phenotypes are naturally advantageous in heterogeneous porous media as they can have a sustainable and consistent growth rate, suggesting there may be alternative reasons for this result (*153*, *154*). Further qSS-FCLSA experiments with a step-wise increase in succinate concentration between 0-1 mM should elucidate this further, as well as the employment of a more rigorous cell washing step.

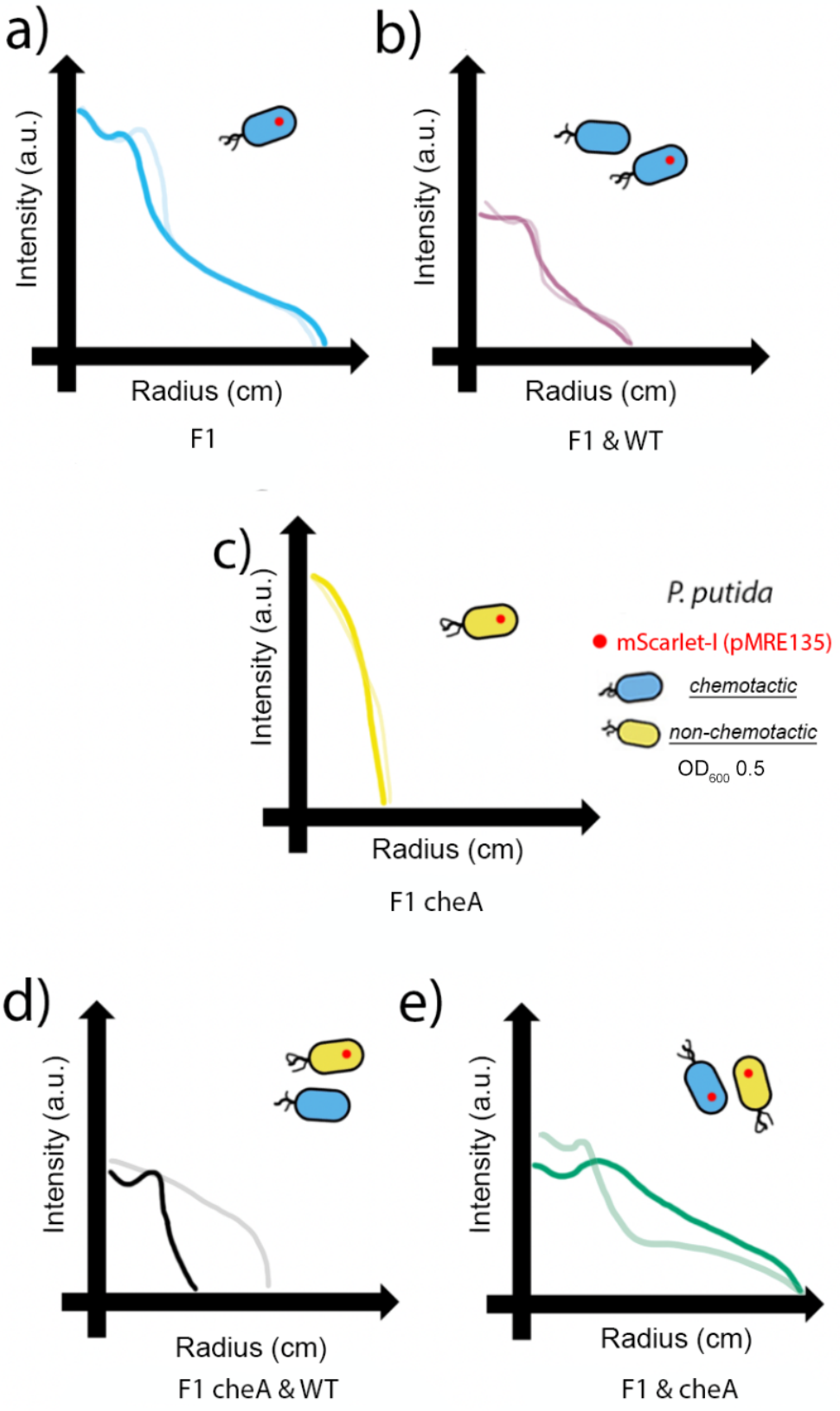


Fig. 5.10. Schematic comparing expected vs. measured radial intensity profiles. The lighter shaded curves reflect the corresponding expected intensity profile based on literature. This is shown to highlight the deviation from the expected curves. A) F1 (sky blue), B) F1 & WT (magenta), C) cheA mutant (yellow), D) cheA & WT (black), and E) F1 & cheA (forest green).

5.5.3 Microbial interactions, co-culture comparisons and biomobilisation

This subsection investigates the interactions of microbes of varying degrees of chemotactic ability and analyses evidence of biomobilisation. It is important to reinforce the fact here that succinate is being used as a proxy for a more toxic compound, such as naphthalene and how these mechanisms can be used to improve and develop NSZD models.

This study found that a co-culture of F1 & cheA formed a significantly greater colony perimeter across all treatments than mono-cultures of cheA, with a degree of biomobilisation expected to be occurring within this colony expansion (Fig. 5.1, 5.2, 5.9, 5.10, Table. 5.1, 5.5) (*184*, *190*, *289*). Table. 5.6 also shows that the mixed culture had a greater AUC across all treatments compared to the cheA, suggesting that the F1 strain within the co-culture may have provided nutrients to the cheA cell contributing to its growth (Table. 5.6) (*304*, *313*). This is significant as it suggests that a diverse population of chemotactic and non-chemotactic microbes may have increased biodegradation potential, over the same amount of non-chemotactic cells and highlights the benefit of chemotaxis, and could amplify the rate of NSZD (*98*, *103*, *176*). Moreover, the higher AUC across the different succinate treatments of the co-culture of F1 & cheA compared to the cheA strain supports this interpretation (Table. 5.6).

However, this study found a non-significant difference in the perimeter of co-cultures of F1 and cheA mutants compared to F1 mono-cultures, across all succinate treatments (Table. 5.1, 5.5). This suggests there is not a constructive interaction of chemotactic and non-chemotactic microbes causing a significantly greater perimeter, as would be expected if biomobilisation was occurring. The t-ratio is negative suggesting that the mixed-colony perimeter may be greater, however not significantly (Fig. 5.1) (*184*, *190*). The AUC of the co-culture is also less than the AUC for the F1 strain at 10 mM and 1 mM succinate, and a deviation from the relationship theorised in the introduction to this chapter, which was based on the study by

Gude et al., (2020) on bacterial coexistence (Fig. 5.4, Table. 5.1, 5.6) (*313*). This deviation could be due to a some other biomobilisation phenomena and/or a combative relationship caused by cells colliding and competing for resources (*101*, *346*). Therefore possibly impeding growth and leading to a net decrease in the amount of biomass capable of degradation (*101*, *346*). This could therefore concur with the aforementioned study by Gomes et al., (2005) (*37*).

An alternative explanation for this result is the F1 strain released bacteriocins upon the cheA mutants via a suicidal program (*313*, *347*). Bacteriocins inhibit or slow growth of similar strains. This response has been reported with another *Pseudomonas* species, *P. aeruginosa* (*347*). If such chemicals are released in this qSS-FCLSA it could provide an alternative explanation for the suspected quorum sensing patterns seen in figure 4.9.

Interestingly, the co-culture of F1 and cheA mutants had a significantly greater perimeter in the presence of succinate compared to when no succinate is present (Table. 5.1, 5.4). It followed the same trend in significance as the F1 mono-culture, which found a non-significant increase in colony size between 1-10 mM succinate (Table. 5.4). This suggests a degree of chemotactic response is also present within the F1 and cheA co-culture (Table. 5.1, 5.4). This is supported by the distinct curve co-culture curve in figure 5.8 and deviation from the expected curve (Fig. 5.8, 5.10). This curve is based on the bimodal distribution and segregation that is expected to occur, with cheA colonising the POI and the pioneering F1 migrating outwards (Fig. 5.8, 5.10) (*96*, *313*). However, the intensity profile displayed an elevated intensity over a greater spatial range than expected, suggesting some other phenomenon such as biomobilisation or collisions of cells may be occurring (Fig. 5.8, 5.10) (*184*, *190*, *289*).

It has recently been shown that collisions of chemotactic cells in certain cases can lead more random discohesive movement reducing chemotactic colony expansion (*289*). If the F1 cells are aligned in high abundances, they can migrate collectively as a wave and at a greater rate and range, especially at higher cell densities (*289*).

However, if random movement is introduced into the system, this may alter the chemotactic response, with collisions of cheA cells being a possible trigger, potentially leading to a dramatically reduced response. This could impact growth and explain the deviation from the expected curves and colony perimeters (Fig. 5.8, 5.10, Table, 5.1, 5.3, 5.4, 5.5, 5.6) (*289*). This may also explain the lower AUC recorded for the co-culture compared to the F1 mono-culture (Fig. 5.9 A, Table. 5.1, 5.5) (*289*).

Another reason for the F1 and cheA co-culture having a increased colony perimeter compared to the cheA cells, is the non-chemotactic cells simply fail to compete against the chemotactic cells for nutrients (Table. 5.1, 5.5). This has been shown previously when chemotactic *Pseudomonas* and *E. coli* strains outcompeted non-chemotactic mutants in plant root colonisation assays (*348*, *349*). A similar result occurred in the aforementioned study by Ni et al., (2020), when an *E. coli* WT strain outcompeted a non-chemotactic *E. coli* ΔcheY mutant in an unstirred culture, where the chemoattractant (12% casein hydrolysate) was delivered by a small (40μL) agarose bead (*101*). A further interesting result from the co-cultures is the vermilion curve (which represent the sum of the co-cultures of cheA & WT and F1 & WT) it gives an insight into how a different ratios of chemotactic to non-chemotactic cells may respond (1 non-chemotactic :3 chemotactic) (Fig. 5.9, Table. 5.1, 5.7). The curve exhibits the high initial peak characteristic of the cheA mutant which has not been masked by an increased proportion of chemotactic cells. The curve also has a comparably high AUC when an attractant is present, suggesting an increase in biodegradation potential (Fig. 5.9, Table. 5.1, 5.7) (*304*, *313*). The next subsection further investigates if there is any evidence of intra-colony biomobilisation within colonies composed of chemotactic and non-chemotactic co-cultures (Fig. 5.1).

5.5.4 Evidence of intra-colony biomobilisation

To ascertain if there is any evidence of biomobilisation effects within the F1 and cheA co-culture themselves, the perimeter of the co-culture of the cheA mutant and

WT strain can be compared to the cheA mutant mono-culture (Table. 5.1, 5.5, 5.6, 5.7). This result along with inspecting the intensity curves will provide any evidence of any microbial interaction or biomobilisation that may occur (Fig. 5.10). This study found that there is a non-significant difference in colony perimeter, across all treatments, suggesting no biomobilisation occurred (Table. 5.4). However, the intensity profiles of the co-culture of the cheA mutant and WT strain (illustrated by the black curve) contradicts this, with the presence of chemotactic hump structures, particularly at higher succinate concentrations (Fig. 5.4, 5.10). The chemotactic hump structures are present at a radius of 0.2 cm from the POI and are particularly clear at higher succinate concentrations and are characteristic of chemotactic cells (Fig. 5.4, 5.9 A, B, 5.10, Table. 5.1). The curve also deviates from the distinctive steep decline of the intensity curve shapes associated with the non-chemotactic mono-culture which follow Fisher–Kolmogorov wave dynamics, even with taking into account the expected enhanced radial movement and biomobilisation shown in figure 5.10, (Fig. 5.9 A, B, 5.10) (*304*, *313*). This suggests some other biomobilisation mechanism may be in operation in the colonies composed of co-cultures of the chemotactic and non-chemotactic cells as they respond chemotactically. Perhaps a entwining of flagella resulting in a combative "tug of war" biomobilisation effect, which mimics the effects of collisions mentioned above and results in a slightly more hindered expansion (Fig. 5.11) (*350*).

Further evidence of intra-colony biomobilisation and interaction, is visible when comparing the curve profiles of the F1 and the cheA mutant co-culture (forest green) against the navy curve, which represents the sum of half the F1 and cheA mono-cultures (Fig. 5.9). The navy curve is theorised to have a similar shape and AUC, as they should have the same amount of fluorescent cells, however it deviates from the expected curve shape and bimodal distribution (Fig. 5.9, Table. 5.1, 5.7) (*304*, *313*). The forest green curve has a lower initial intensity compared to the navy curve in the 10 mM succinate treatment (∼10000 a.u) (Fig. 5.9 A). However, the forest green curve shows a greater median radial intensity past 0.2 cm, decreasing

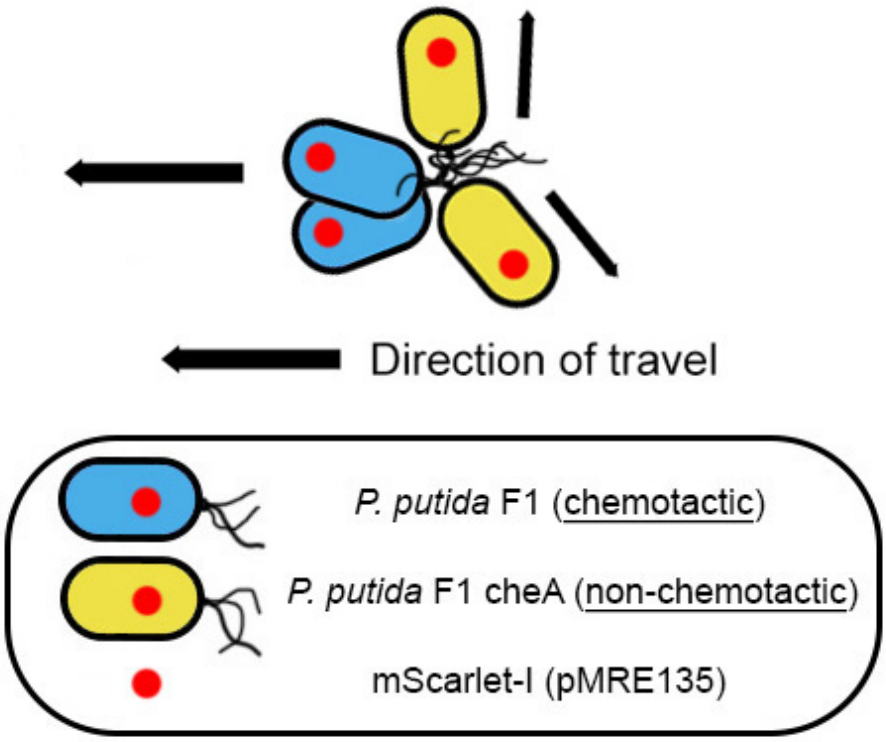


Fig. 5.11. "Tug of war" biomobilisation mechanism. Illustrates the theorised "tug of war" biomobilisation mechanism. This mechanism may form as a result of the cells' flagella entwining, resulting in a combative relationship, with the F1 cells responding chemotactically and transporting the cheA cells along a chemical gradient, with the random smooth swimming behaviour of the cheA cells hindering the rate of biomobilisation (Table. 5.2).

gradually towards 0, with the navy curve having a more marked decline, a lower AUC and decreased spatial range (Fig. 5.9 A, Table. 5.1, 5.7). This result provides further evidence that intra-colony biomobilisation and interaction effect may occur within colonies consisting of chemotactic and non-chemotactic cells (Fig. 5.11).

This inferred intra-colony biomobilisation effect decreases with decreased chemoattractant concentrations as expected (Fig. 5.1, 5.9, Table. 5.1, 5.7). There is an also general trend in the pattern of the chemotactic rings with the co-culture humps being approximately 0.5 cm further out than the F1 mono-culture (Fig. 5.8). These results suggest that further research needs to be undertaken to determine the exact nature of the biomobilisation mechanism and how best to incorporate this phenomena within current NZSD models, which expect there to be a more bimodal distribution driven by spatial segregation than is witnessed, with the microbial transport parameter solely based on the classical advection and diffusion of cells (*31*, *313*). Nevertheless, this study provides evidence supporting that biomobilisation may operate within communities of varying degrees of chemotactic ability (Fig. 1.3, 5.8, B, C, 5.10) (*96*, *304*, *313*).

It must also be stated that the co-culture of F1 & WT did not respond to succinate as expected, this is potentially due to the fact only half the amount of cells are fluorescent (Fig. 5.9 A, B, C, Table. 5.1, 5.4). However, it may also be due to a different growth rate of the WT compared to the F1 strain. The F1 and WT strains functionality should be identical, with the only difference being the insertion of the mScarlet-I (pMRE135) plasmid, however the plasmid may impact the metabolic rate of the F1 strain (*351*). Plasmids can cause a metabolic burden that is triggered by the expression of the fluorescence, resulting in wild-type strains having a faster growth rate and slightly different behaviour (*351*). Despite this the magenta intensity curve profiles for the F1 & WT co-culture maintain chemotactic hump structures, with the curves producing a similar shape to those expected. Suggesting their chemotactic nature is unhindered and some other phenomenon may be occurring, as would also be the case in the cheA & WT co-culture (Fig. 5.9 A, B, C, 5.10,

Table. 5.1, 5.4). This is further supported by the commonality in the significance trend of F1 vs. cheA and F1 & WT vs. F1 & cheA in table 5.5, despite the presence of the WT (Table. 5.5).

Chapter 6

General discussion

6.1 Summary of key questions and objectives

This chapter integrates the field and laboratory studies described in chapters 3 to 5 and considers their relevance to the current literature. A summary of the thesis's key questions and objectives is provided for context in figure 6.1. This figure also outlines the three overarching research questions of the thesis and the links between the two studies (Fig. 1.3, 6.1).

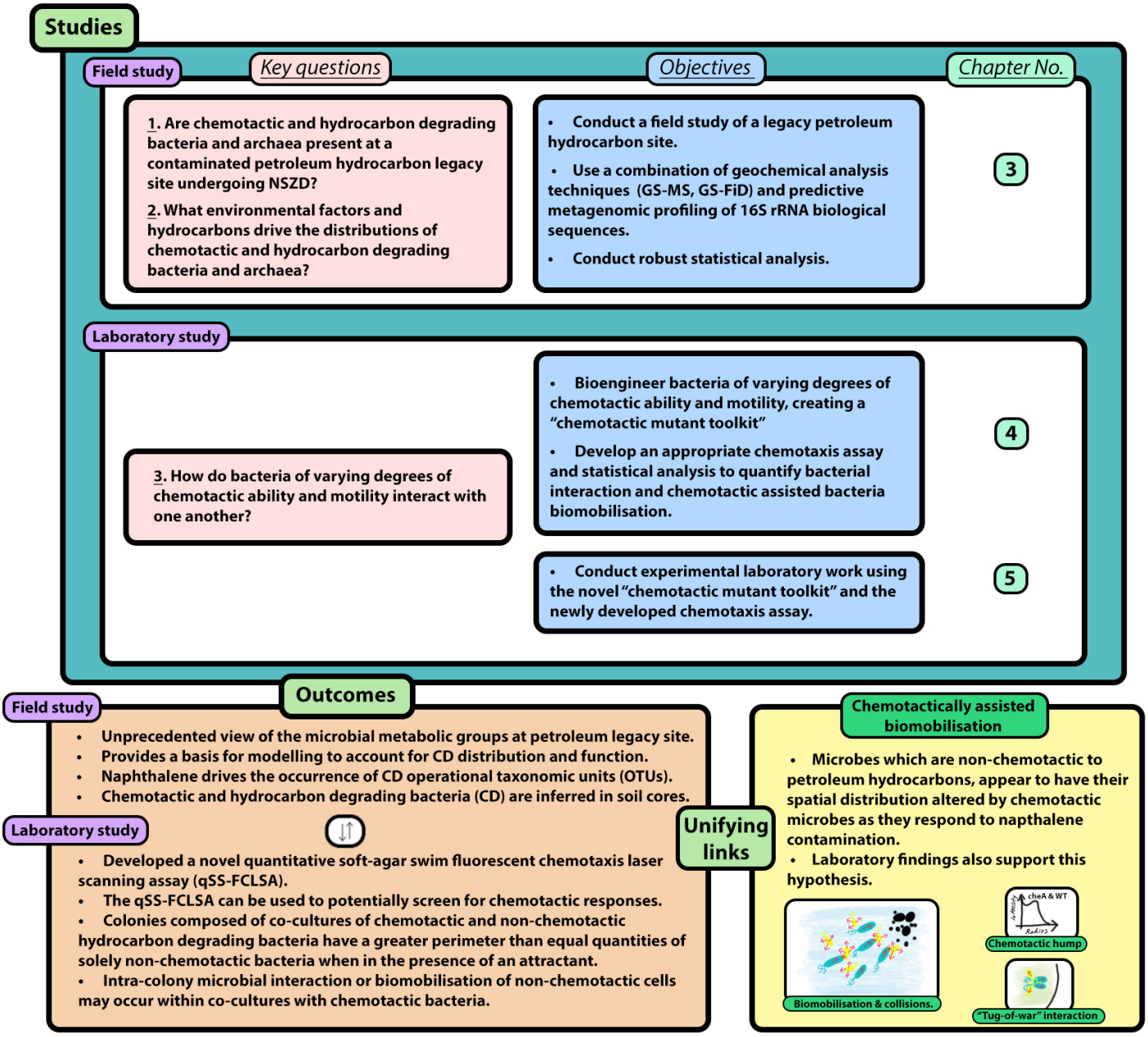


Fig. 6.1. General discussion summary. This figure shows the key questions, objectives, study linkages, key results and outcomes of the thesis, as well as their relevant chapter number.

6.2 Unification of the field and laboratory studies

One of the primary aims of this research was to investigate the impact of chemotactically-induced biomobilisation on the spatial arrangement of non-chemotactic microbial populations within the environment. This holds significant importance for understanding processes like natural source zone depletion (NSZD) that rely on manipulating the taxonomic and functional make-up of indigenous microbial communities within the subsurface (Fig. 6.1).

This thesis employed both field and laboratory methodologies to address this aim (Fig. 6.1). The field study investigated the distribution and patterns of chemotactic and non-chemotactic microorganisms involved in hydrocarbon degradation at a legacy site, which has a history of petroleum processing and storage. Meanwhile, the laboratory component focused on examining the outcomes of biomobilisation among chemotactic and non-chemotactic variants of the same microbial species in the presence of a chemoattractant (Fig. 6.1).

To be able to actually track and monitor the chemotactic response of microbes, a novel quantitative soft-agar swim fluorescent chemotaxis laser scanning assay (qSS-FCLSA) and a "chemotaxis mutant toolkit" was developed, which allows us further explore this link at first hand. This technique provided some of the first observed evidence of intra-colony biomobilisation. This was tested in the field by assessing the spatial distribution of taxa which are non-chemotactic to petroleum hydrocarbons, such as *Geobacteraceae*. Other taxa such as *Pseudomonadaceae*, which are chemotactic and hydrocarbon degrading, are thought to have potentially altered the spatial distribution of *Geobacteraceae*, through biomobilisation. This field study is the first to investigate the distribution of chemotactic and hydrocarbon degrading microbes (CD) in the subsurface, and explore any evidence of biomobilisation. The only prior inference of spatial distribution of chemotaxis in the subsurface is via modelling techniques, such as modified Keller-Segel models (*155–157*).

Another gap in literature that is tackled by both studies is the distances and general

movement in which chemotactic responses operate and how microbes navigate the subsurface. Utilising the contaminant depth profiles in figure 3.2 and distances travelled by microbes using the soft swim assay in figure 4.11, one can postulate expected movement and interactions (Fig. 3.2, 4.11, 5.10). This new qSS-FCLSA also provides the tools to explore community dynamics and plasmid exchange with unparalleled clarity, which is highlighted in the literature review in chapter 2 and field study, as areas with a deficit of data. Common taxa identified in the literature review and field study, such as members of the *Rhizobiaceae* family could be utilised for this in future laboratory work (Fig. 3.3) (*168*, *171–175*).

Overall, by combining field observations and laboratory experiments, this thesis aims to deepen our understanding of how chemotactic behaviour influences the distribution dynamics of microbial populations in environments, including those impacted by petroleum hydrocarbons. This section highlights the links between the studies, as well as their interlinked nature. Improving the understanding of chemotaxis and biomobilisation and the role they play in the degradation of petroleum hydrocarbons, will in-turn assist in the improved quantification of risk posed to human health from such contamination events. The next sections assess if the key questions outlined in figure 1.3 have been addressed and discusses their outcomes (Fig. 1.3, 6.1).

6.3 Field and laboratory studies in context with current literature

6.3.1 1. Are chemotactic and hydrocarbon degrading bacteria and archaea present at a contaminated petroleum hydrocarbon legacy site undergoing NSZD?

The field study conducted in chapter 3 of this thesis provides fresh insights into

the detection and distribution of chemotactic and hydrocarbon degrading taxa at a legacy petroleum hydrocarbon site in Kwinana, Western Australia undergoing NSZD. Thereby addressing the first key question of this thesis (Fig. 6.1). This is significant, as it is the first time that this has been done and paves the way for further functionality research. As an example of its relevance, the work has been recently cited in a review of functional microbiome strategies for bioremediation by Haque et al., (2022), in the context of providing an increased awareness of the impact of chemotaxis on biodegradation rates (*352*, *353*).

The "bioinformatic pipeline" developed in chapter 3 can now be tested on other NSZD sites, such as the aforementioned site in Bemidji, Minnesota (*10*, *43–46*, *55*). This bioinformatic pipeline and inferred functionality technique has recently been adopted by Lv et al., (2023), in a study into microbial functionality and hydrocarbon remediation (*354*). The study also used PICRUSt functional gene prediction to assign pathways to individual OTUs (*354*). The pipeline is also highly adaptable and versatile, and can be altered to incorporate other inferred traits, such as antibiotic resistance, using the KEGG pathway "ko00998". Such an approach could investigate the prevalence of antibiotic resistance at contaminated petroleum hydrocarbon sites, and assist in the search for new antibiotics (*305*, *355*).

Key taxa assigned to the chemotactic and degrading (CD) group in the field study (chapter 3); *Pseudomonadaceae*, *Desulfocapsaceae*, *Comamonadaceae* and *Geobacteraceae*, have all been detected in contaminated sites and locations previously, bolstering their taxonomic assignment and inferred presence at the legacy site in Kwinana (*356–358*).

Pseudomonadaceae and *Comamonadaceae* have been recorded at an abandoned legacy petrochemical plant in Lanzhou City, China in a study by Sun et al., (2017) (*356*). The *Comamonadaceae* family has also been reported at other legacy contaminated sites in Kuwait (*241*). *Desulfocapsaceae* have recently been detected in hypoxic microcosms, constructed using samples collected in the Caspian Sea by BP, during a study by Griffiths et al., (2023) on crude oil degradation (*357*). *Geobac-*

teraceae has also been detected in elevated abundances at an abandoned chemical factory site located in Changzhou, China, during a study by Xiao et al., (2022) (*358*). Further analysis and "deeper sequencing" could also further investigate the complex interplay between the CD communities and members of the hydrocarbon degrading (D) communities and their intrinsic methanogenic hydrocarbon degrading ability outlined in chapter 3 (*177*, *266*, *359*).

6.3.2 2. What environmental factors and hydrocarbons drive the distributions of chemotactic and hydrocarbon degrading bacteria and archaea?

The key result that naphthalene was found to drive the distribution of chemotactic and hydrocarbon degrading microbes (CD) inferred to be present across the site, helps address the second key question of this thesis (Fig. 6.1). This result supports the conclusions obtained from column experiments conducted in a study by Velasco-Casal et al., (2008) (*180*). The study found that naphthalene promotes the distribution of CD microbes in porous microcosms (*177*, *180*).

The CD taxa at the legacy site also showed a significantly negative relationship with benzene and phenanthrene. The negative response with benzene could be explained by the concentration being too high and therefore toxic to microbial cells (*103*, *166*, *250*, *360*). In particular in the jet fuel cores D9 and T5, where benzene is recorded on the order of ∼1000 mg/kg (Fig. 3.2). This has previously been witnessed during studies by the "Ford Research Group" at the University of Virginia, where *P. putida* F1 responded positively at low, but negatively at higher benzene concentrations (*52*). The negative relationship with phenanthrene could be associated with its poor solubility effecting the bioavailability (*361*). This would potentially favour the degradation of other chemoattractants by CD taxa, with other non-CD taxa which are distributed randomly within the subsurface being unable to swim away from areas of phenanthrene contamination. The non-CD taxa's distribution would predominately driven by percolation (fluid movement downward through saturated

zones) and associated advection/diffusion & dispersion (*177*, *361*).

The negative relationship with depth could be explained by CD bacteria moving towards hydrocarbon compounds located closer to the surface and to any hydrocarbons which have been partially volatilised and re-condensed at shallower depths. This also infers that the CD population could be primarily oxic, due to their spatial distribution (Fig. 3.2, 3.3) (*177*). However, this is complicated by oxygen also being an attractant to certain bacteria, as mentioned in chapter 2 and in a review on *Pseudomonas* chemotaxis by Sampedro et al., (2015) (*103*, *177*, *269*). These observations have important implications for process-based models used to simulate hydrocarbon biodegradation at contaminated field sites, such as the TMVOCBio model mentioned in chapter 2. Here, the effect of inferred CD accumulation in areas where naphthalene is present and is being degraded, along with the negative relationship with benzene, phenanthrene and depth could be represented by altering the biodegradation module (BIODG) parameter within the TMVOCBio model (*362*).

This TMVOCBio quasi-chemotaxis model simulation could include an inhibitory value for areas of phenanthrene and benzene contamination, as well as one related to depth below ground level and soil water status. This could then be compared against a standard TMVOCBio fed with data from the Kwinana site. The hypothesis being the TMVOCBio quasi-chemotaxis model may provide a closer estimation of CD activity, and biodegradation in general, than the standard model, further validating the outcomes of the field study (*55*, *362*, *363*). The significance of this chemotactic work, and its link with model simulations, is further highlighted in a recent citation by Davis et al., (2023), where chemotaxis is noted as a key process, whose function and importance is vital to understand, in order to better represent contaminant and environmental coupling at legacy sites undergoing NSZD (*364*).

6.3.3 3. How do bacteria of varying degrees of chemotactic ability and motility interact with one another?

The field study in Kwinina, Western Australia, also found possible evidence of biomobilisation and bacteria-bacteria transport (Fig. 6.1) (*177*). An OTU, assigned to the obligately anaerobic *Geobacteraceae* family, was detected at shallower depths within the subsurface than expected (*177*). It was theorised that this shift and change in their normal distribution was triggered by biomobilisation and transport by other CD taxa, such as *Pseudomonadaceae*, *Desulfocapsaceae*, and *Comamonadaceae*, as they responded chemotactically to hydrocarbons present at the site (*177*, *190*). It was then decided to investigate chemotaxis and biomobilisation further in the laboratory setting, through the development of a new chemotaxis assay.

A novel quantitative soft-agar swim fluorescent chemotaxis laser scanning assay (qSS-FCLSA) was developed, and chosen ahead of other methods outlined in figures 4.1 and 4.12. (Fig. 4.1, 4.12). This approach allows for fine detail of the colony structure to be captured at the edges of the colony (Fig. 4.1, 4.9, 4.11, 4.12) (*147*). This pioneering assay is recommended as an alternative to the "bucket of light" approach, which requires manual construction of materials in a metal workshop, developed by Parkinson (2007) (*147*).

A key finding from the qSS-FCLSA was the atypical intensity profiles of co-cultures of chemotactic WT and non-chemotactic cheA mutants, compared to the typical cheA intensity profile (Fig. 5.10, 6.1). This result provides evidence of bacteria-bacteria transport in the presence of an attractant, inferring intra-colony biomobilisation (Fig. 5.10, 6.1). This interaction between a chemotactic and non-chemotactic bacteria has never before been witnessed, and is a key outcome from this work. It also raises the question "How does such an interaction occur?".

A study by Seymour et al., (2024) recently highlighted the importance of cell-to-cell chemotactic sensing, showing the vast amount of unknowns surrounding this

intriguing phenomenon (*365*). Whilst a study by Balseiro-Romero et al., (2022), referenced in the literature review in chapter 2, describes the biomobilisation of non-chemotactic and non-motile hydrocarbon degrading bacteria by chemotactic hydrocarbon degrading bacteria. Suggesting such an interaction is feasible, possibly via a "tug-of-war" mechanism (*184*). A variation of this "tug-of-war" mechanism has been witnessed before through the tangling of flagella of motile bacteria in a study by Cairns et al., (2013) (*366*). In the study the flagellar filament protein of *Bacillus subtilis* was interfered with by anti-Hag antibodies, which caused the tangling of bacterial flagella. Videos of the interaction are available in the supplementary information of the paper (*366*). This interaction is similar to the "tug-of-war" biomobilisation mechanism theorised in this thesis, between the F1 and cheA strains (*366*) (Fig. 5.1, 5.11, 6.1).

The median normalised radial intensity profiles generated using the qSS-FCLSA could be used to "fingerprint" chemotactic, non-chemotactic or mixed activity within cultures, by inspecting and identifying distinct characteristics in the signal (*284*). Similar agar assay screening mechanisms, have been used to identify *Pseudomonas* strains capable of polyester hydrolysis in a study by Molitor et al., (2019) (*367*). This type of fingerprinting, could also act as a screening tool for assessing chemotactic behaviour of microbes of unknown abilities sampled from a petroleum hydrocarbon sites, such as the legacy site studied in chapter 3 (Fig. 5.8, 5.10) (*284*).

Samples taken directly from the the site should have had their chemotactic ability further scrutinised using this assay, possibly comparing the response of strains of *Pseudomonadaceae* to *Desulfocapsaceae*, *Comamonadaceae* and *Geobacteraceae* phyla, as well as co-cultures. These strains would also be bioengineered in a similar way, by deleting the fliM gene, using a similar methodology to that developed in chapter 4, when developing the "chemotaxis mutant toolkit". This could provide valuable information on how different phyla interact and support this studies inference of intra-colony biomobilisation and microbial interaction within colonies composed of petroleum hydrocarbon degrading bacteria of varying degrees of chemo-

tactic ability.

Furthermore, strains constructed as part of the chemotaxis mutant toolkit in chapter 4 are currently being utilised by the Stanley Lab, Department of Bioengineering, Imperial College London, to investigate microbial interactions with fungal systems, to further explore biomobilisation. A methods paper on the experimental methodology and analysis using the qSS-FCLSA is also in preparation. New chemotaxis methodologies, assays and approaches are being trailed and tested across multiple fields, and are recently designated as "hot topics" in microbiology. An example of this is a study by Scheidweiler et al., (2024), in which the spatial structure of communities of varying degrees of chemotactic ability and motility was investigated in systems containing a dead-end porous networks (*368*). The paper found that chemotaxis and quorum sensing play a significant role in the heterogeneous accumulation of bacterial biomass (*368*).

Further development of this work will assist in assessing the exact proportions of actively degrading bacteria within co-cultures and provide vital data, which can be used to modulate the chemotaxis and microbial transport parameters within NSZD models. Further research investigating the exact nature and mechanisms of the suspected intra-colony biomobilisation and could also have applications outside the field of bioremediation and NSZD, such as the enhancement of the delivery of certain drugs (*369*).

Given the scarcity in literature pertaining to interactions between chemotactic and non-chemotactic hydrocarbon degrading bacteria as they swim towards an chemoattractant, it is difficult to elaborate further, so there is a pressing need for further research to further validate the work conducted in this thesis. With this in mind, the next chapter outlines future research recommendations and validation techniques that can be tested to address this need. It also provides a set of overall conclusions and identifies some of the associated limitations of the thesis.

Chapter 7

Conclusions

This chapter outlines the conclusions of the thesis. It then provides an outline of the limitations of both the field and laboratory studies and provides recommendations for future research and assesses if the aim of the thesis has been met.

7.1 Conclusions of field-study

This novel study defines the distribution and associations of indigenous microbes based on their predicted chemotactic and hydrocarbon degrading ability across the water table of a legacy petroleum hydrocarbon site. It provides an unprecedented view of the microbial functional metabolic groups operating across the water table of an unconfined superficial sand aquifer undergoing NSZD spanning a range of LNAPL types, water saturations, LNAPL component concentrations and air phase conditions. Critical distributions and associations have been defined for three petroleum types, crude oil, diesel fuel and jet fuel, and compared to a background location in the same hydrogeochemical and lithological setting. This forms a valuable foundation for future research to explore this important biological phenomenon. Naphthalene concentration was found to be a driver for the presence of potentially chemotactic and hydrocarbon degrading microbes. Further investigation is required to confirm this association and to assess the role of OTUs identified as being influenced by naphthalene concentrations during LNAPL NSZD. Moreover, further research is required to investigate how the CD and D group OTUs, including methanogens,

interact to promote NSZD. Addressing these challenges will enable the development of more sophisticated models incorporating such biological processes to more accurately predict NSZD outcomes (*55*). Although the study has focused on inferred chemotaxis assisted hydrocarbon degradation, the role of other non-chemotactic functional groups in NSZD is of interest.

The study combined 16S rRNA sequencing, gas chromatography and predictive metagenomic profiling (PMP) via PICRUSt2 analysis, to infer chemotactic and petroleum degradation function. The PMP predicted the abundance of functional gene families present in microbial communities. This paper provides a pioneering insight into chemotaxis, with the methodology providing a "bioinformatic pipeline" that can be applied to petroleum contaminated sites worldwide, to investigate if similar patterns in distributions occur. However, the geology of the site should also be taken into account (Fig. 3.1).

This field-based study identified naphthalene contamination as a driving factor in the occurrence of chemotactic and petroleum hydrocarbon degrading microbes at a real-world site. The study also presented a comprehensive bioinformatic pipeline that can be applied to similar sites undergoing NZSD worldwide, further highlighting the versatility of the research (Fig. 3.1).

7.2 Conclusions of laboratory-based study

The laboratory-based study genetically engineered a chemotaxis mutant toolkit, which can be used in conjunction with a novel qSS-FCLSA to investigate the interactions of microbes of varying degrees of chemotactic abilities and motility (Fig. 4.9, 4.11, 5.1, Table. 4.1). This revealed that co-cultures of chemotactic and non-chemotactic petroleum hydrocarbon degrading microbes exhibited a significantly greater perimeter compared to an equal biomass of non-chemotactic microbes in the presence of an attractant (Table. 5.5).

Chemotactic mono-cultures displayed similar perimeters and spatial ranges to the co-cultures, but their intra-colony spatial distribution differed (Fig. 5.9 A, B, C, 5.10, 6.1, Table. 5.7). Comparative analysis of intensity profiles suggested that the chemotactic strain altered the typical radial distribution of the non-chemotactic strain through an intra-colony biomobilisation mechanism (Fig. 5.1, 5.10, 5.11). It is important to next assess how the thesis can be approved, its limitations, as well as future research recommendations.

7.3 Summary of field and laboratory limitations

7.3.1 Data analysis limitations

- Advances in sequencing and the development of more advanced taxonomic and functional libraries, such as the taxonomic Silva database and KEGG pathway libraries, could improve the accuracy and precision of PiCRUSt2 predictive metagenomic sequencing outlined in the thesis. This advancement would contribute to a better understanding of the distribution of chemotactic and degrading microbes at legacy sites (*176*, *215*, *227*, *228*, *370*).

7.3.2 Laboratory limitations

- A limitation involved in the use of the novel qSS-FCLSA is the placement of the petri-dish into the assay by hand, this could potentially result in human error artificially altering the perimeter and shape of the bacterial colonies. Perhaps robotisation, along with enhanced sterilisation techniques may improve consistency of results, therefore bolstering the statistcial power of the perimeter and intensity profile analysis.

7.4 Research recommendations

7.4.1 Bioinformatic approaches and future work based on fieldwork

- Recommendations for future analysis of the data from the field study, could include the "flagellar assembly" KEGG pathways in the CD and C groups to assess the impact of flagellation on the spatial distribution of the different functional groups, along with the incorporation of KEGG pathways associated with quorum sensing and biofilm formation (*176*, *371–375*).

- Alternatively, combining shotgun metagenomics sequencing with the 16S rRNA amplicon and meta-transcriptomics could improve knowledge of the functional behaviour of microbes within the subsurface. This multi-omic approach could also be used to determine gene expression, and the chemotactic and hydrocarbon degrading potential of microbial communities across legacy sites (*376*, *377*).

- Furthermore, the planned re-coring of the legacy site near Perth, Western Australia when the water table is lower should provide valuable information on how the distribution of chemotactic and hydrocarbon degrading taxa is influenced by changes in seasonality and fluctuations in the water table. This would also provide vital data on how functional communities react to variation within the groundwater systems, and determine if naphthalene remains as a key driver in their distribution, or if fluid flow influences the outcome (*177*). A greater understanding as to the exact nature of the relationship of CD communities and naphthalene, could be explored by re-sampling of the relevant cores and undertaking metagenomic and proteomic analysis. Microcosm assays and column experiments using material from the site would also assist in investigating this (*177*). This work could also explore the CD communities relationship with depth and the negative relationship with phenanthrene and benzene (*177*). The positioning of the bacteria is hypothesised to be driven in-part due to el-

evated toxicity. It is thought this may elicit a negative "necrotactic" response away from such areas, where the CD microbes sense cell death; even though phenanthrene and benzene are known chemoattractants, the concentrations may be too toxic (*103*, *166*, *250*, *360*). This could be investigated by packing columns with porous material from the site and tagging the CD microbes with magnetic particles, similar to the work which was undertaken in the Olson et al. (2004) paper mentioned in chapter two. The CD microbes would then be exposed to a step-wise increase in phenanthrene and benzene concentration and their distribution shift would be assessed by MRI (*90*). This would provide an improved understanding of the spatial distribution of a necrotactic response at depth (*90*).

- The bioinformatic pipeline developed in chapter three could be compared and trialed on other petroleum hydrocarbon sites, providing a clearer understanding about how these systems will respond to climate change and how chemotactic and hydrocarbon functional communities will migrate within contaminated aquifers (*29*, *89*, *177*). It is worth noting that confirming chemotaxis at the genomic level is challenging due to a couple of factors. Bacteria could stop swimming at a post-translational level and their behaviour could change rather quickly from a motile to sessile behaviour, which is especially hard to determine in a mixed microbial community (*96*). This highlights how important a multi-omic approach is, which includes laboratory-based research to verify chemotactic responses.

- Further research could also investigate the relationship between the chemotactic and hydrocarbon degrading microbes recorded at the site undergoing NSZD and the interplay they have with the methanogenic hydrocarbon degrading consortia present at the site (*177*, *266*). The role of acidogenic microbes, which also work in a partnership with the CD and methanogenic communities could also be confirmed (*177*). This would allow for improved understanding

of the degradation profile of petroleum hydrocarbons in aerobic and anaerobic systems, and the key microbes and taxa that play a role in the degradation process (*177*).

7.4.2 Laboratory-based bioengineering approaches

- In future, the novel non-chemotactic and non-motile *P. putida* F1 cheA ΔfliM mScarlet-I (pMRE135) mutant constructed in chapter four as part of the chemotaxis mutant toolkit, could be assessed in the qSS-FCLSA (Fig. 4.9, 4.11). The colony perimeters and median radial intensity profiles in the different succinate treatments (10 mM, 1 mM, and 0 mM) could then be compared to the other strains constructed (Table. 4.1).

- There could be an increase amount of experimental runs which could also include an increased amount of biological and technical replicates (n=20) to improve the robustness of the statistical analysis. Scanning colonies at different timescales could also be implemented, such as scanning every 12 hours for 36 hours. However, once the lids of the petri-dishes are removed, it is not practical to replace them and then return the plate to the incubator. This is due to issues with sterility and the fact frequent manual movement alters the rigidity of the soft-agar and could trigger artificial expansion of the colony due to agar structural failure. Instead, sub-sampling the various strains and mutants from a set point around the POI and exploring the growth rate over time, might be an alternative option (Table. 4.1). This could also assist in assessing the growth, death and reproduction rate of the mutants created, this could also be run in parallel with flow cytometry analysis to improve understanding of the cells shape, distinct phases and fluorescence (*269*). The results of the *Pseudomonas putida* cheA F1 mutant could then be compared to the response of the other *Pseudomonas putida* F1 strains constructed to provide more evidence as to why there is a significant decreased in the AUC

for the non-chemotactic mutants *P. putida* F1 cheA mScarlet-I compared to the *P. putida* F1 mScarlet-I chemotactic cells (Fig. 5.8, 5.9 A, B, C, Table 5.5, 5.6).

- Moreover, to further examine the spatial distribution of the non-chemotactic strain, PCRs could be conducted at different distances from the POI using the primer list recently provided by Rebecca Parales, The University of California, Davis, USA, using the "mid" primers, since the F1 cheA HindIII F and F1cheA BamHI R were unsuccessful during trials (Supplementary Information Data. S12) (*378*). This could also be used to investigate the distribution of the non-chemotactic and non-motile *Pseudomonas* using the primers for the fliM gene (Table. 4.3). Perhaps using these, in combination with spatial sequencing at set distances from the POI, would give an idea about the spatial community dynamics of how the chemotactic bacteria interact (*379*).

- It would also be beneficial to run co-cultures of *P. putida* F1 cheA ΔfliM mScarlet-I (pMRE135) mutant with the *P. putida* F1 WT strain, to explore biomobilisation further. If the perimeter of the non-motile and non-chemotactic *P. putida* F1 cheA ΔfliM mScarlet-I (pMRE135) mutant in co-culture with the *P. putida* F1 WT strain was significantly greater than the *P. putida* F1 cheA ΔfliM mScarlet-I (pMRE135) mono-culture in the presence of a succinate, then it could be inferred that the distribution had been influenced by the movement of *P. putida* F1 WT. This would likely be due to a biomobilisation effect, either by hydrodynamic entrapment, push / pull effects, piggybacking or the newly proposed "tug of war" effect (*184*, *189*, *190*). Evidence of this would support the biomobilisation outcome of the Balseiro-Romero et al., (2022) paper, with high magnification microscopy being the best way to visualise the exact nature of the biomobilisation mechanism (*184*). If the biomobilisation mechanism, was determined to be due to physical attachment, this is significant. Since in theory this would lead to the further transfer

of plasmids essential to chemotaxis and degradation within the subsurface. This is outlined in the literature review and is worthy of future investigation (Fig. 2.2, 5.1).

- Another method of investigating biomobilisation and interaction using the qSS-FCLSA would be utilising other fluorescent wavelength channels on the Amersham Typhoon to study the fluorescent plasmids inside each of the co-cultures tested. However, this would require further bioengineering work to construct or purchase fluorescent plasmids so their emission spectrum would not overlap, as this might lead to false fluorescent results (*380*). This would provide a clearer understanding if there was any consumer/producer relationship that developed within the co-culture (*381*). Further work could focus on the colony edges and assess the degree of spatial segregation or mutualism by assessing the "fuziness" of the interaction zone between the chemotactic strain and one of the mutant strains in the chemotaxis mutant toolkit, using the slow scan feature on the scanner (Table. 4.1) (*313*, *382*). It is important to note that selecting more than one emission channel on the Amersham Typhoon could double scan time. However this could be remedied by decreasing the area of scan and the number of biological replicates or treatments per run.

- Construction of a *P. putida* F1 ΔfliM mScarlet-I (pMRE135) mutant would also allow for the quantification as to the extent of any pili or culi based movement. This would be achieved by bench-marking this new strains perimeter and median normalised radial intensity profile against the *P. putida* F1 cheA ΔfliM mScarlet-I (pMRE135) strain. This works because the *P. putida* F1 ΔfliM mScarlet-I (pMRE135) is still chemotactic by means of pili or culi based movement and the *P. putida* F1 cheA ΔfliM mScarlet-I (pMRE135) is rendered non-chemotacic and non-motile, with the pili or culi being unable to respond a chemical gradient (*383*). This could then be compared to other strains in the chemotaxis mutant toolkit (Table. 4.1). This work might also

assist in gauging the energy burden of a chemotactic response mentioned in the historical review in chapter two (*96*, *101*).

- Interestingly, if manipulation of the mScarlet-I (pMRE135) plasmid is required to reduce any metabolic burden on the cell to make its growth identical to the *P. putida* F1 WT strain, then no manipulation of the plasmid may be required in the case of the *P. putida* F1 cheA ΔfliM mScarlet-I (pMRE135) mutant. As it may already be less impacted by the metabolic burden, due to the fact it lacks flagella. Thus, the energy required to form flagella is minimal, potentially off-setting any energy expenditure associated with carrying the metabolic plasmid (*96*, *101*, *351*).

- Different ratios of strains and numbers of strains could also be tested, instead of 50:50 co-cultures along with different OD_{600nm} and chemoattractants, such as maleate, benzene, toluene and naphthalene (*103*). However, due to the volatility of some of the aromatics, they can impact the rigidity of the soft-agar and often evaporate quickly as previously highlighted. Altering the agar concentration, may remedy this to an extent, however this in-turn, could impact colony shape (*103*, *165*). Using OD_{600nm} of less than 0.3 and above 0.7 could confirm what the ideal ranges for chemotactic responses are, or if OD_{600nm} above 0.7 still produces similar results as reported by Tian et al., (2021) (*168*, *194*, *284*, *288*, *289*). Experimentation with different ratios would also provide valuable data on thresholds of any biomobilisation and microbial transport that may be occurring and shed light on the microbial interactions mentioned in the discussion of chapter five.

- A petri-dish with no bacteria should also be added as a control within the qSS-FCLSA for a more accurate reflection of background noise and autofluorescence throughout batches. Further controls such as an aerotactic *P. putida* F1 aer2 mScarlet-I (pMRE135) mutant, should also be bioengineered and included

(*103*, *269*). Aerotaxis has been shown to subtly mask chemotactic responses (*103*, *127*, *269*). Furthermore, screening for more active pioneering phenotypes and comparing their results by sub-sampling from different proximal radii might lead to different results (*146*, *303*).

- The FFI device could also be altered slightly, in an attempt to remove the unwanted flow mentioned in chapter four. Possible remedies for removing the unwanted flow and allowing for static equilibrium to occur are: adding a layer of hydrogel or modifying the device with a third hole to encourage equilibrium formation (*384*, *385*). This could remove the flow and offer an improved resolution and enable more precise assessment of any cell-to-cell interactions or interaction phenomena.

- Further research could also be undertaken to investigate the role direct interspecies electron transfer (DIET) has on the spatial distribution of *Geobacteraceae* mentioned in chapter three, which bolstered the interest in investigating microbial transport and interaction, especially biomobilisation (*177*). This DIET, would involve biofilm formation which could act as "liferafts" for *Geobacteraceae* to survive higher up in the subsurface and protect the cells from oxidation, therefore providing a possible alternative to the biomobilisation hypothesis (*386*, *387*). Sub-culturing from samples which contain the strongest *Geobacteraceae* and naphthalene affiliation is a possible research avenue. The samples could be tested and sequenced to see if they contained *Geobacter* and tested in the qSS-FCLSA. This is assuming that culturing from the cores was successful and an anaerobic qSS-FCLSA variant could be developed. Interestingly, applying a current to the system might also encourage enhanced DIET and petroleum hydrocarbon's degradation rate through improved kinetic enhancement (*388*, *389*).

- A final suggestion, would be the construction of promoter reporter constructs. These could be constructed to fluoresce when the cell: initiates metabolism and degradation of a petroleum hydrocarbon, initiates a chemotactic response, transfers a plasmid and/or starts formation of a biofilm (*390–393*). This would improve knowledge of the spatial community dynamics operating within communities of varying degrees of chemotactic ability. Thereby improving the resolution of how NSZD might occur in petroleum hydrocarbon sites.

7.5 Concluding statement

This thesis investigated role of chemotaxis in the natural source zone depletion of petroleum hydrocarbons, with the aim of addressing three key questions which have been answered (Fig. 6.1). Based on these findings, it is recommended to revise existing NSZD models to account for CD accumulation in areas affected by naphthalene contamination. Furthermore, the NSZD models should consider the interactions and biomobilisation between petroleum hydrocarbon, degrading chemotactic microbes and microbes of varying degrees of chemotactic ability, within the subsurface. It recommends further research into the biomobilisation of non-chemotactic microbes within the subsurface that may alter the proportion of petroleum hydrocarbon degrading microbes at the degradation interface. This could lead to an improved quantification of the risk posed by petroleum hydrocarbon contamination to groundwater supplies, therefore safeguarding the ecosystem and reducing the risk to human health.

References

(*1*) Hoogesteger, J. (2022). Regulating agricultural groundwater use in arid and semi-arid regions of the Global South: Challenges and socio-environmental impacts. *Current Opinion in Environmental Science & Health 27*, 100341, DOI: https://doi.org/10.1016/j.coesh.2022.100341, https://www.sciencedirect.com/science/article/pii/S2468584422000162.

(*2*) Li, P., Karunanidhi, D., Subramani, T., and Srinivasamoorthy, K. (2021). Sources and Consequences of Groundwater Contamination. *Archives of Environmental Contamination and Toxicology 80*, 1–10, DOI: 10.1007/s00244-020-00805-z, https://doi.org/10.1007/s00244-020-00805-z.

(*3*) Viaroli, S., Lancia, M., and Re, V. (2022). Microplastics contamination of groundwater: Current evidence and future perspectives. A review. *Science of The Total Environment 824*, 153851, DOI: https://doi.org/10.1016/j.scitotenv.2022.153851, https://www.sciencedirect.com/science/article/pii/S0048969722009433.

(*4*) He, X., Li, P., Wu, J., Wei, M., Ren, X., and Wang, D. (2021). Poor groundwater quality and high potential health risks in the Datong Basin, northern China: research from published data. *Environmental Geochemistry and Health 43*, 791–812, DOI: 10.1007/s10653-020-00520-7, https://doi.org/10.1007/s10653-020-00520-7.

(*5*) Elshall, A. S., Castilla-Rho, J., El-Kadi, A. I., Holley, C., Mutongwizo, T., Sinclair, D., and Ye, M. *Imperiled: The Encyclopedia of Conservation*; Elsevier Inc: 2022.

(*6*) Lapworth, D. J., Boving, T. B., Kreamer, D. K., Kebede, S., and Smedley, P. L. (2022). Groundwater quality: Global threats, opportunities and realising the potential of groundwater. *Science of The Total Environment 811*, 152471, DOI: https://doi.org/10.1016/j.scitotenv.2021.152471, https://www.sciencedirect.com/science/article/pii/S0048969721075495.

(*7*) Dike, C. C., Hakeem, I. G., Rani, A., Surapaneni, A., Khudur, L., Shah, K., and Ball, A. S. (2022). The co-application of biochar with bioremediation for the removal of petroleum hydrocarbons from contaminated soil. *Science of The Total Environment 849*, 157753, DOI: https://doi.org/10.1016/j.scitotenv.2022.157753, https://www.sciencedirect.com/science/article/pii/S0048969722048525.

(*8*) FAO, and UNEP (2021). Global assessment of soil pollution: summary for policymakers. *Rome*, https://www.fao.org/documents/card/en/c/cb4894en.

(*9*) FAO, and UNEP Global assessment of soil pollution: Report, 2021, https://www.fao.org/documents/card/en/c/cb4894en.

(*10*) Gkorezis, P., Daghio, M., Franzetti, A., Van Hamme, J. D., Sillen, W., and Vangronsveld, J. The interaction between plants and bacteria in the remediation of petroleum hydrocarbons: An environmental perspective, 2016, DOI: 10.3389/fmicb.2016.01836.

(*11*) Poi, G., Shahsavari, E., Aburto-Medina, A., Mok, P. C., and Ball, A. S. (2018). Large scale treatment of total petroleum-hydrocarbon contaminated groundwater using bioaugmentation. *Journal of Environmental Management 214*, 157–163, DOI: https://doi.org/10.1016/j.jenvman.2018.02.079, https://www.sciencedirect.com/science/article/pii/S0301479718301920.

(*12*) Hidalgo, K. J., Teramoto, E. H., Soriano, A. U., Valoni, E., Baessa, M. P., Richnow, H. H., Vogt, C., Chang, H. K., and Oliveira, V. M. (2020). Tax-

onomic and functional diversity of the microbiome in a jet fuel contaminated site as revealed by combined application of in situ microcosms with metagenomic analysis. *Science of The Total Environment 708*, 135152, DOI: https://doi.org/10.1016/j.scitotenv.2019.135152, https://www.sciencedirect.com/science/article/pii/S0048969719351447.

(*13*) Wang, J., Chen, X., Yan, W., Ning, C., and Gsell, T. (2021). Both artificial root exudates and natural Koelreuteria paniculata exudates modify bacterial community structure and enhance phenanthrene biodegradation in contaminated soils. *Chemosphere 263*, 128041.

(*14*) Hannam, M. L., Bamber, S. D., Galloway, T. S., John Moody, A., and Jones, M. B. (2010). Effects of the model PAH phenanthrene on immune function and oxidative stress in the haemolymph of the temperate scallop Pecten maximus. *Chemosphere 78*, 779–784, DOI: https://doi.org/10.1016/j.chemosphere.2009.12.049, https://www.sciencedirect.com/science/article/pii/S0045653509014726.

(*15*) Han, J., Liang, Y., Zhao, B., Wang, Y., Xing, F., and Qin, L. (2019). Polycyclic aromatic hydrocarbon (PAHs) geographical distribution in China and their source, risk assessment analysis. *Environmental Pollution 251*, 312–327, DOI: https://doi.org/10.1016/j.envpol.2019.05.022, https://www.sciencedirect.com/science/article/pii/S0269749119310383.

(*16*) Rand, S., and Strauss, K. *Significance of Tests for Petroleum Products, Seventh Edition*; ASTM International: 2008, pp 3–3, DOI: 10.1520/mnl10078m.

(*17*) Botero, M. L., Mosbach, S., and Kraft, M. (2014). Sooting tendency of paraffin components of diesel and gasoline in diffusion flames. *Fuel 126*, 8–15, DOI: https://doi.org/10.1016/j.fuel.2014.02.005, https://www.sciencedirect.com/science/article/pii/S001623611400132X.

(*18*) Reid, T., Chaganti, S. R., Droppo, I. G., and Weisener, C. G. (2018). Novel insights into freshwater hydrocarbon-rich sediments using metatranscriptomics: Opening the black box. *Water Research 136*, 1–11, DOI: https://

doi.org/10.1016/j.watres.2018.02.039, http://www.sciencedirect.com/science/article/pii/S0043135418301465.

(*19*) Besha, A. T., Bekele, D. N., Naidu, R., and Chadalavada, S. (2018). Recent advances in surfactant-enhanced In-Situ Chemical Oxidation for the remediation of non-aqueous phase liquid contaminated soils and aquifers. *Environmental Technology & Innovation 9*, 303–322, DOI: https://doi.org/10.1016/j.eti.2017.08.004, https://www.sciencedirect.com/science/article/pii/S2352186417300767.

(*20*) Ossai, I. C., Ahmed, A., Hassan, A., and Hamid, F. S. (2020). Remediation of soil and water contaminated with petroleum hydrocarbon: A review. *Environmental Technology & Innovation 17*, 100526, DOI: https://doi.org/10.1016/j.eti.2019.100526, https://www.sciencedirect.com/science/article/pii/S235218641830364X.

(*21*) Chang, J. I., and Lin, C.-C. (2006). A study of storage tank accidents. *Journal of Loss Prevention in the Process Industries 19*, 51–59, DOI: https://doi.org/10.1016/j.jlp.2005.05.015, http://www.sciencedirect.com/science/article/pii/S0950423005000641.

(*22*) Newell, C. J., Acree, S. D., Ross, R. R., and Huling, S. G. Ground Water Issue: Light Nonaqueous Phase Liquids, tech. rep., Washington, DC: .S. Environmental Protection Agency, 1995, pp 1–28, https://cfpub.epa.gov/si/si_public_record_report.cfm?Lab=NRMRL&dirEntryId=126070.

(*23*) Davis, G. B., Barber, C., Power, T. R., Thierrin, J., Patterson, B. M., Rayner, J. L., and Wu, Q. (1999). The variability and intrinsic remediation of a BTEX plume in anaerobic sulphate-rich groundwater. *Journal of Contaminant Hydrology 36*, 265–290, DOI: https://doi.org/10.1016/S0169-7722(98)00148-X, http://www.sciencedirect.com/science/article/pii/S016977229800148X.

(*24*) Jakuba, M. V., Kinsey, J. C., Yoerger, D. R., Camilli, R., Murphy, C. A., Steinberg, D., and Bender, A. *Proceedings of the International Conference*

on Intelligent Robots and Systems (IROS) Workshop on Robotics for Environmental Monitoring (WREM), San Francisco, CA, USA, 2011, pp 25–30.

(*25*) Camilli, R., Reddy, C. M., Yoerger, D. R., Van Mooy, B. A. S., Jakuba, M. V., Kinsey, J. C., McIntyre, C. P., Sylva, S. P., and Maloney, J. V. (2010). Tracking hydrocarbon plume transport and biodegradation at Deepwater Horizon. *Science 330*, 201–204.

(*26*) Shih, T., Rong, Y., Harmon, T., and Suffet, M. (2004). Evaluation of the impact of fuel hydrocarbons and oxygenates on groundwater resources. *Environmental Science & Technology 38*, 42–48.

(*27*) Manek, E. G., Putra, D. P. E., and Hendrayana, H. *IOP Conference Series: Earth and Environmental Science*, IOP Publishing: 2021; Vol. 851, p 012024.

(*28*) Setyaningsih, W. (2010). Model Pergerakan Bahan Pencemar Minyak Disel Padaakuifer Batupasir Formasi Volkanik Merapi Muda. *Jurnal Geografi: Media Informasi Pengembangan dan Profesi Kegeografian 7*.

(*29*) Ortega-Calvo, J.-J., Harmsen, J., Parsons, J. R., Semple, K. T., Aitken, M. D., Ajao, C., Eadsforth, C., Galay-Burgos, M., Naidu, R., and Oliver, R. (2015). From bioavailability science to regulation of organic chemicals.

(*30*) National Research Council *Groundwater and Soil Cleanup: Improving Management of Persistent Contaminants*, National Research Council. 1999, Ed.; The National Academies Press: Washington, DC, 1999, DOI: 10.17226/9615.

(*31*) Lari, K. S., Davis, G. B., Rayner, J. L., Bastow, T. P., and Puzon, G. J. (2019). Natural source zone depletion of LNAPL: A critical review supporting modelling approaches. *Water research 157*, 630–646.

(*32*) Brusseau, M., and Artiola, J. *Environmental and Pollution Science*; Elsevier: 2019, pp 175–190, DOI: 10.1016/B978-0-12-814719-1.00012-4, https://linkinghub.elsevier.com/retrieve/pii/B9780128147191000124.

(*33*) Blyth, D., Butler, A., and Fowler, G. Characterising the Haystack of Geogenic Organics arising from Hydraulic Fracturing, tech. rep., Imperial College London & CSIRO, 2019, 57 slides.

(*34*) U.S. Environmental Protection Agency Ethylbenzene, tech. rep., Washington, D.C., United States: EPA, 2016, pp 1–4, https://www.epa.gov/sites/production/files/2016-09/documents/ethylbenzene.pdf.

(*35*) Espitia-Perez, L., Sosa, M. Q., Salcedo-Arteaga, S., Leon-Mejia, G., Hoyos-Giraldo, L. S., Brango, H., Kvitko, K., da Silva, J., and Henriques, J. A. P. (2016). Polymorphisms in metabolism and repair genes affects DNA damage caused by open-cast coal mining exposure. *Mutation Research/Genetic Toxicology and Environmental Mutagenesis 808*, 38–51.

(*36*) Shukla, S. K., Mangwani, N., Rao, T. S., and Das, S. *Microbial Biodegradation and Bioremediation*, 2014, pp 201–230, DOI: 10.1016/B978-0-12-800021-2.00008-X, http://dx.doi.org/10.1016/B978-0-12-800021-2.00008-X.

(*37*) Gomes, N. C. M., Kosheleva, I. A., Abraham, W. R., and Smalla, K. (2005). Effects of the inoculant strain Pseudomonas putida KT2442 (pNF142) and of naphthalene contamination on the soil bacterial community. *FEMS Microbiology Ecology 54*, 21–33, DOI: 10.1016/j.femsec.2005.02.005.

(*38*) Johnston, C. D., Rayner, J. L., Patterson, B. M., and Davis, G. B. (1998). Volatilisation and biodegradation during air sparging of dissolved BTEX-contaminated groundwater. *Journal of Contaminant Hydrology*, DOI: 10.1016/S0169-7722(98)00079-5.

(*39*) Santonicola, S., De Felice, A., Cobellis, L., Passariello, N., Peluso, A., Murru, N., Ferrante, M. C., and Mercogliano, R. (2017). Comparative study on the occurrence of polycyclic aromatic hydrocarbons in breast milk and infant formula and risk assessment. *Chemosphere 175*, 383–390, DOI: https://doi.org/10.1016/j.chemosphere.2017.02.084, https://www.sciencedirect.com/science/article/pii/S004565351730262X.

(*40*) Kuppusamy, S., Maddela, N. R., Megharaj, M., Venkateswarlu, K., Kuppusamy, S., Maddela, N. R., Megharaj, M., and Venkateswarlu, K. (2020). Impact of total petroleum hydrocarbons on human health. *Total Petroleum Hydrocarbons: Environmental Fate, Toxicity, and Remediation*, 139–165.

(*41*) Li, J., Huang, G. H., Zeng, G., Maqsood, I., and Huang, Y. (2007). An integrated fuzzy-stochastic modeling approach for risk assessment of groundwater contamination. *Journal of Environmental Management 82*, 173–188, DOI: https://doi.org/10.1016/j.jenvman.2005.12.018, https://www.sciencedirect.com/science/article/pii/S0301479706000429.

(*42*) Johnston, C. D., Rayner, J. L., and Briegel, D. (2002). Effectiveness of in situ air sparging for removing NAPL gasoline from a sandy aquifer near Perth, Western Australia. *Journal of Contaminant Hydrology 59*, 87–111, DOI: https://doi.org/10.1016/S0169-7722(02)00077-3, http://www.sciencedirect.com/science/article/pii/S0169772202000773.

(*43*) Davis, G. B., Patterson, B. M., Barber, C., and Johnston, C. D. *1997 International Conference on Groundwater Quality Protection: Remedial Technology and Management Policy for NAPL Contamination*, ed. by Organised by Professor Chia-Shyun Chen, I. o. A. G., and National Central University, T., Chung-Li, Institute of Applied Geology: Taipei, Taiwan, 1997, pp 45–62.

(*44*) Commission on Geosciences, *Natural Attenuation for Groundwater Remediation*, 2000, DOI: 10.17226/9792.

(*45*) Sookhak Lari, K., Johnston, C. D., Rayner, J. L., and Davis, G. B. (2018). Field-scale multi-phase LNAPL remediation: Validating a new computational framework against sequential field pilot trials. *Journal of Hazardous Materials*, DOI: 10.1016/j.jhazmat.2017.11.006.

(*46*) An, D., Xi, B., Wang, Y., Xu, D., Tang, J., Dong, L., Ren, J., and Pang, C. (2016). A sustainability assessment methodology for prioritizing the technologies of groundwater contamination remediation. *Journal of Cleaner Production 112*, 4647–4656, DOI: 10.1016/j.jclepro.2015.08.020.

(*47*) Hu, L., Wu, X., Liu, Y., Meegoda, J. N., and Gao, S. (2010). Physical modeling of air flow during air sparging remediation. *Environmental science & technology 44*, 3883–3888.

(*48*) Benner, M. L., Mohtar, R. H., and Lee, L. S. (2002). Factors affecting air sparging remediation systems using field data and numerical simulations. *Journal of Hazardous Materials 95*, 305–329, DOI: https://doi.org/10.1016/S0304-3894(02)00144-9, https://www.sciencedirect.com/science/article/pii/S0304389402001449.

(*49*) Silva, A., Delerue-Matos, C., and Fiúza, A. (2005). Use of solvent extraction to remediate soils contaminated with hydrocarbons. *Journal of Hazardous Materials 124*, 224–229, DOI: https://doi.org/10.1016/j.jhazmat.2005.05.022, https://www.sciencedirect.com/science/article/pii/S0304389405002311.

(*50*) Li, X., Du, Y., Wu, G., Li, Z., Li, H., and Sui, H. (2012). Solvent extraction for heavy crude oil removal from contaminated soils. *Chemosphere 88*, 245–249, DOI: https://doi.org/10.1016/j.chemosphere.2012.03.021, https://www.sciencedirect.com/science/article/pii/S0045653512003359.

(*51*) Statham, T. M., Sumner, R., Hill, A. F. M., and Smith, J. W. N. (2023). Transition from active remediation to natural source zone depletion (NSZD) at a LNAPL-impacted site, supported by sustainable remediation appraisal. *Quarterly Journal of Engineering Geology and Hydrogeology*, 2022–140.

(*52*) Singh, R., and Olson, M. S. *Emerging Environmental Technologies*; Springer Netherlands: 2008, pp 149–172, DOI: 10.1007/978-1-4020-8786-8{_}7.

(*53*) Pishgar, R., Hettiaratchi, J. P., and Chu, A. (2022). Natural Source Zone Depletion (NSZD) Quantification Techniques: Innovations and Future Directions. *Sustainability 14*, 7027.

(*54*) Kulkarni, P. R., Walker, K. L., Newell, C. J., Askarani, K. K., Li, Y., and McHugh, T. E. (2022). Natural source zone depletion (NSZD) insights from

over 15 years of research and measurements: A multi-site study. *Water Research*, 119170.

(*55*) Sookhak Lari, K., Davis, G. B., and Rayner, J. L. (2022). Towards a digital twin for characterising natural source zone depletion: A feasibility study based on the Bemidji site. *Water Research 208*, 117853, DOI: https://doi.org/10.1016/j.watres.2021.117853, https://www.sciencedirect.com/science/article/pii/S0043135421010472.

(*56*) Franzmann, P. D., Zappia, L. R., Tilbury, A. L., Patterson, B. M., Davis, G. B., and Mandelbaum, R. T. Bioaugmentation of atrazine and fenamiphos impacted groundwater: Laboratory evaluation, 2000, DOI: 10.1080/10588330008951112.

(*57*) Scow, K. M., and Hicks, K. A. Natural attenuation and enhanced bioremediation of organic contaminants in groundwater, 2005, DOI: 10.1016/j.copbio.2005.03.009.

(*58*) Wackett, L. P., and Gibson, D. T. (1988). Degradation of trichloroethylene by toluene dioxygenase in whole-cell studies with Pseudomonas putida F1. *Applied and Environmental Microbiology 54*, 1703–1708.

(*59*) Woo, H. J., Sanseverino, J., Cox, C. D., Robinson, K. G., and Sayler, G. S. (2000). The measurement of toluene dioxygenase activity in biofilm culture of Pseudomonas putida F1. *Journal of Microbiological Methods 40*, 181–191, DOI: 10.1016/S0167-7012(00)00123-8.

(*60*) Methods in Biotechnology (Neil Willey), *Phytoremediation*, 1st; Willey, N., Ed.; Humana Press: Totowa, New Jersey, 2007, pp 1–478.

(*61*) Sookhak Lari, K., Davis, G. B., and Johnston, C. D. (2016). Incorporating hysteresis in a multi-phase multi-component NAPL modelling framework; a multi-component LNAPL gasoline example. *Advances in Water Resources*, DOI: 10.1016/j.advwatres.2016.07.012.

(*62*) Lekmine, G., Bastow, T. P., Johnston, C. D., and Davis, G. B. (2014). Dissolution of multi-component LNAPL gasolines: The effects of weathering

and composition. *Journal of Contaminant Hydrology*, DOI: 10.1016/j.jconhyd.2014.02.003.

(*63*) Wu, T. Application of computational fluid dynamics to the biopile treatment of hydrocarbon contaminated soil, Ph.D. Thesis, Edinburgh: University of Edinburgh, 2009, https://era.ed.ac.uk/handle/1842/5713.

(*64*) Hinchee, R. E., and Smith, L. A., *In situ thermal technologies for site remediation*, 1st ed.; Battelle Memorial Institute, CRC Press, Lewis Publishers: 1992.

(*65*) Rivett, M., and Sweeney, R. (2019). An introduction to natural source zone depletion at LNAPL sites.

(*66*) Vasileva-Tonkova, E., and Galabova, D. (2003). Hydrolytic enzymes and surfactants of bacterial isolates from lubricant-contaminated wastewater. *Zeitschrift für Naturforschung C 58*, 87–92.

(*67*) Ahmad, F., Zhu, D., and Sun, J. Bacterial chemotaxis: a way forward to aromatic compounds biodegradation, 2020, DOI: 10.1186/s12302-020-00329-2.

(*68*) Chakraborty, R., and Coates, J. D. (2004). Anaerobic degradation of monoaromatic hydrocarbons. *Applied microbiology and biotechnology 64*, 437–446.

(*69*) Budzinski, H., Raymond, N., Nadalig, T., Gilewicz, M., Garrigues, P., Bertrand, J. C., and Caumette, P. (1998). Aerobic biodegradation of alkylated aromatic hydrocarbons by a bacterial community. *Organic Geochemistry 28*, 337–348.

(*70*) Park, H., and Choi, I.-G. (2020). Genomic and transcriptomic perspectives on mycoremediation of polycyclic aromatic hydrocarbons. *Applied Microbiology and Biotechnology 104*, 6919–6928, DOI: 10.1007/s00253-020-10746-1, https://doi.org/10.1007/s00253-020-10746-1.

(*71*) Avesani, D., Dumbser, M., Chiogna, G., and Bellin, A. (2017). An alternative smooth particle hydrodynamics formulation to simulate chemotaxis in

porous media. *Journal of Mathematical Biology 74*, 1037–1058, DOI: 10.1007/s00285-016-1049-6.

(*72*) Adadevoh, J. S., Ramsburg, C. A., and Ford, R. M. (2018). Chemotaxis Increases the Retention of Bacteria in Porous Media with Residual NAPL Entrapment. *Environmental Science and Technology 52*, 7289–7295, DOI: 10.1021/acs.est.8b01172.

(*73*) Berg, H. C. (1975). Chemotaxis in bacteria. *Annu. Rev. Biophys. Bioeng. Online*, 119–138, www.annualreviews.org.

(*74*) Chisholm, H., *"Chemotaxis"*, 11th ed.; Cambridge University Press: Cambridge, UK, 1911, p 77.

(*75*) Eisenbach, M., Tamada, A., Omann, G. M., Segall, J. E., Firtel, R. A., Meili, R., Gutnick, D., Varon, M., Lengeler, J. W., and Murakami, F., *Chemotaxis*; World Scientific Publishing Company: 2004, https://books.google.co.uk/books?hl=en&lr=&id=ks42DwAAQBAJ&oi=fnd&pg=PR7&dq=chemotaxis+definition&ots=pcHThOhaJf&sig=oLw8ukWKo2wdhCkXO7_ujV-EP70#v=onepage&q=chemotaxis%20definition&f=false.

(*76*) Wadhwa, N., and Berg, H. C. (2022). Bacterial motility: machinery and mechanisms. *Nature Reviews Microbiology 20*, 161–173, DOI: 10.1038/s41579-021-00626-4, https://doi.org/10.1038/s41579-021-00626-4.

(*77*) Berg, H. C. (2003). The Rotary Motor of Bacterial Flagella. *Annual Review of Biochemistry 72*, 19–54, DOI: 10.1146/annurev.biochem.72.121801.161737, http://www.annualreviews.org/doi/10.1146/annurev.biochem.72.121801.161737.

(*78*) Claußnitzer, D. Bacterial chemotaxis: sensory adaptation, noise filtering, and information transmission, Ph.D. Thesis, Imperial College London, 2011, pp 1–187.

(*79*) Harwood, C. S., Fosnaugh, K., and Dispensa, M. (1989). Flagellation of Pseudomonas putida and analysis of its motile behavior. *Journal of Bacteriology 171*, 4063–4066, DOI: 10.1128/jb.171.7.4063-4066.1989.

(*80*) Pérez, E. E. A. A new factor in the regulation of polar flagellum synthesis in Vibrio parahaemolyticus, Ph.D. Thesis, Marburg: University of Marburg - Philipps-Universität Marburg, 2023, https://archiv.ub.uni-marburg.de/diss/z2023/0105/pdf/deeap.pdf.

(*81*) Waite, A. J., Frankel, N. W., and Emonet, T. (2018). Annual Review of Biophysics Behavioral Variability and Phenotypic Diversity in Bacterial Chemotaxis. DOI: 10.1146/annurev-biophys, https://www.annualreviews.org/doi/abs/10.1146/annurev-biophys-062215-010954.

(*82*) Yuan, J., Fahrner, K. A., Turner, L., and Berg, H. C. (2010). Asymmetry in the clockwise and counterclockwise rotation of the bacterial flagellar motor. *Proceedings of the National Academy of Sciences 107*, 12846–12849, DOI: 10.1073/pnas.1007333107.

(*83*) Mears, P. J., Koirala, S., Rao, C. V., Golding, I., and Chemla, Y. R. (2014). Escherichia coli swimming is robust against variations in flagellar number. *eLife 3*, DOI: 10.7554/elife.01916.

(*84*) Ludwig Maximilian University of Munich Biophysics of Systems, tech. rep., Munich: University of Munich, 2016, p 1, https://www.physik.uni-muenchen.de/lehre/vorlesungen/wise_16_17/Biophysics_of_Systems/013_BakterChemotaxis_DB_WS16.pdf.

(*85*) Elgamoudi, B. Motility and chemotaxis, 2019, https://www2.le.ac.uk/projects/vgec/schoolsandcolleges/Microbial%20Sciences/infectious-disease/campy-motility.

(*86*) Tambalo, D. D., Del Bel, K. L., Bustard, D. E., Greenwood, P. R., Steedman, A. E., and Hynes, M. F. (2010). Regulation of flagellar, motility and chemotaxis genes in Rhizobium leguminosarum by the VisN/R-Rem cascade. *Microbiology 156*, 1673–1685, DOI: 10.1099/mic.0.035386-0.

(*87*) Johnson, D. L., Maguire, K. L., Anderson, D. R., and McGrath, S. P. (2004). Enhanced dissipation of chrysene in planted soil: the impact of a rhizobial inoculum. *Soil Biology and Biochemistry 36*, 33–38, DOI: https://doi.

org/10.1016/j.soilbio.2003.07.004, https://www.sciencedirect.com/science/article/pii/S0038071703002888.

(*88*) Bhattacharjee, T., and Datta, S. S. (2019). Bacterial hopping and trapping in porous media. *Nature Communications 10*, 2075, DOI: 10.1038/s41467-019-10115-1, http://www.nature.com/articles/s41467-019-10115-1.

(*89*) Wang, X., Long, T., and Ford, R. M. (2012). Bacterial chemotaxis toward a NAPL source within a pore-scale microfluidic chamber. *Biotechnology and Bioengineering 109*, 1622–1628, DOI: 10.1002/bit.24437.

(*90*) Olson, M. S., Ford, R. M., Smith, J. A., and Fernandez, E. J. (2004). Quantification of bacterial chemotaxis in porous media using magnetic resonance imaging. *Environmental Science and Technology*, DOI: 10.1021/es035236s.

(*91*) Marx, R. B., and Aitken, M. D. (2000). Bacterial chemotaxis enhances naphthalene degradation in a heterogeneous aqueous system. *Environmental Science and Technology 34*, 3379–3383, DOI: 10.1021/es000904k.

(*92*) Chaudhary, P., Sahay, H., Sharma, R., Pandey, A. K., Singh, S. B., Saxena, A. K., and Nain, L. (2015). Identification and analysis of polyaromatic hydrocarbons (PAHs)—biodegrading bacterial strains from refinery soil of India. *Environmental Monitoring and Assessment 187*, 391, DOI: 10.1007/s10661-015-4617-0, https://doi.org/10.1007/s10661-015-4617-0.

(*93*) Hong, Y.-H., Ye, C.-C., Zhou, Q.-Z., Wu, X.-Y., Yuan, J.-P., Peng, J., Deng, H., and Wang, J.-H. (2017). Genome Sequencing Reveals the Potential of Achromobacter sp. HZ01 for Bioremediation. *Frontiers in Microbiology 8*, 1507, https://www.frontiersin.org/article/10.3389/fmicb.2017.01507.

(*94*) Toepfer, J. A., Ford, R. M., Metge, D., and Harvey, R. W. (2012). Impact of fluorochrome stains used to study bacterial transport in shallow aquifers on motility and chemotaxis of Pseudomonas species. *FEMS Microbiology Ecology 81*, 163–171, DOI: 10.1111/j.1574-6941.2012.01355.x.

(*95*) Guadayol, Ò., Thornton, K. L., and Humphries, S. (2017). Cell morphology governs directional control in swimming bacteria. *Scientific Reports 7*, 2061.

(*96*) Keegstra, J. M., Carrara, F., and Stocker, R. (2022). The ecological roles of bacterial chemotaxis. *Nature Reviews Microbiology 20*, 491–504, DOI: 10.1038/s41579-022-00709-w, https://doi.org/10.1038/s41579-022-00709-w.

(*97*) Wick, L. Y., Remer, R., Würz, B., Reichenbach, J., Braun, S., Schäfer, F., and Harms, H. (2007). Effect of Fungal Hyphae on the Access of Bacteria to Phenanthrene in Soil. *Environmental Science & Technology 41*, 500–505, DOI: 10.1021/es061407s, https://doi.org/10.1021/es061407s.

(*98*) Strobel, K. L., McGowan, S., Bauer, R. D., Griebler, C., Liu, J., and Ford, R. M. (2011). Chemotaxis increases vertical migration and apparent transverse dispersion of bacteria in a bench-scale microcosm. *Biotechnology and bioengineering 108*, 2070–2077.

(*99*) de Weert, S., Vermeiren, H., Mulders, I. H. M., Kuiper, I., Hendrickx, N., Bloemberg, G. V., Vanderleyden, J., De Mot, R., and Lugtenberg, B. J. J. (2002). Flagella-driven chemotaxis towards exudate components is an important trait for tomato root colonization by Pseudomonas fluorescens. *Molecular Plant-Microbe Interactions 15*, 1173–1180.

(*100*) Sourjik, V., and Berg, H. C. (2002). Receptor sensitivity in bacterial chemotaxis. *Proceedings of the National Academy of Sciences 99*, 123–127.

(*101*) Ni, B., Colin, R., Link, H., Endres, R. G., and Sourjik, V. (2020). Growth-rate dependent resource investment in bacterial motile behavior quantitatively follows potential benefit of chemotaxis. *Proceedings of the National Academy of Sciences 117*, 595–601, DOI: 10.1073/pnas.1910849117, https://doi.org/10.1073/pnas.1910849117.

(*102*) Paul, K., Nieto, V., Carlquist, W. C., Blair, D. F., and Harshey, R. M. (2010). The c-di-GMP binding protein YcgR controls flagellar motor direction and

speed to affect chemotaxis by a "backstop brake" mechanism. *Molecular cell 38*, 128–139.

(*103*) Sampedro, I., Parales, R. E., Krell, T., and Hill, J. E. (2015). Pseudomonas chemotaxis. *FEMS Microbiology Reviews 39*, 17–46, DOI: 10.1111/1574-6976.12081.

(*104*) Wu, X., Monchy, S., Taghavi, S., Zhu, W., Ramos, J., and van der Lelie, D. (2011). Comparative genomics and functional analysis of niche-specific adaptation in Pseudomonas putida. *FEMS Microbiology Reviews 35*, 299–323, DOI: 10.1111/j.1574-6976.2010.00249.x, https://doi.org/10.1111/j.1574-6976.2010.00249.x.

(*105*) Burrows, L. L. (2012). Pseudomonas aeruginosa twitching motility: type IV pili in action. *Annual review of microbiology 66*, 493–520.

(*106*) Lanfranconi, M. P., Alvarez, H. M., and Studdert, C. A. (2003). A strain isolated from gas oil-contaminated soil displays chemotaxis towards gas oil and hexadecane. *Environmental Microbiology 5*, 1002–1008, DOI: 10.1046/j.1462-2920.2003.00507.x.

(*107*) Kohlmeier, S., Smits, T. H. M., Ford, R. M., Keel, C., Harms, H., and Wick, L. Y. (2005). Taking the fungal highway: Mobilization of pollutant-degrading bacteria by fungi. *Environmental Science and Technology 39*, 4640–4646, DOI: 10.1021/es047979z.

(*108*) Pöritz, M., Schiffmann, C. L., Hause, G., Heinemann, U., Seifert, J., Jehmlich, N., von Bergen, M., Nijenhuis, I., and Lechner, U. (2015). Dehalococcoides mccartyi strain DCMB5 Respires a broad spectrum of chlorinated aromatic compounds. *Applied and environmental microbiology 81*, 587–596, DOI: 10.1128/AEM.02597-14, https://www.ncbi.nlm.nih.gov/pubmed/25381236.

(*109*) Cheng, C., Wang, Q., He, L. Y., Huang, Z., and Sheng, X. F. (2015). Chitinophaga qingshengii sp. nov., isolated from weathered rock surface. *In-*

ternational Journal of Systematic and Evolutionary Microbiology 65, 280–285, DOI: 10.1099/ijs.0.070516-0.

(*110*) Richter, F., Bindschedler, S., Calonne-Salmon, M., Declerck, S., Junier, P., and Stanley, C. E. (2022). Fungi-on-a-Chip: microfluidic platforms for single-cell studies on fungi. *FEMS Microbiology Reviews 46*, fuac039.

(*111*) Deveau, A., Bonito, G., Uehling, J., Paoletti, M., Becker, M., Bindschedler, S., Hacquard, S., Hervé, V., Labbé, J., Lastovetsky, O. A., Mieszkin, S., Millet, L. J., Vajna, B., Junier, P., Bonfante, P., Krom, B. P., Olsson, S., van Elsas, J. D., and Wick, L. Y. (2018). Bacterial–fungal interactions: ecology, mechanisms and challenges. *FEMS Microbiology Reviews 42*, 335–352, DOI: 10.1093/femsre/fuy008, https://doi.org/10.1093/femsre/fuy008.

(*112*) Yang, P., and van Elsas, J. D. (2018). Mechanisms and ecological implications of the movement of bacteria in soil. *Applied Soil Ecology 129*, 112–120, DOI: https://doi.org/10.1016/j.apsoil.2018.04.014, https://www.sciencedirect.com/science/article/pii/S0929139317312325.

(*113*) Nazir, R., Zhang, M., de Boer, W., and van Elsas, J. D. (2012). The capacity to comigrate with Lyophyllum sp. strain Karsten through different soils is spread among several phylogenetic groups within the genus Burkholderia. *Soil Biology and Biochemistry 50*, 221–233, DOI: https://doi.org/10.1016/j.soilbio.2012.03.015, https://www.sciencedirect.com/science/article/pii/S0038071712001253.

(*114*) Adler, J. (1975). Chemotaxis in bacteria. *Annual Reviews Online Annu. Rev. Biochem.* 341–356.

(*115*) Pfeffer, W., *Locomotorische Richtungsbewegungen durch chemische Reize:(Aus den" Untersuchungen aus dem botanischen Institut zu Tübingen Bd. I. Heft 3 p. 363-482).* W. Engelmann: 1884.

(*116*) Phillips, R. How Cells Decide Where to Go: The Case of Bacterial Chemotaxis, Pasadena, 2007, http://rpdata.caltech.edu/courses/aph161/2007/.

(*117*) Harris, H. (1960). Mobilization of defensive cells in inflammatory tissue. *Microbiology and Molecular Biology Reviews 24*, 3–15, http://mmbr.asm.org/.

(*118*) Adler J (1969). Chemoreceptors in bacteria. *Science 166*, 1588–1597.

(*119*) Rothert, W. (1901). Beobactungen und Betrachtungen tiber tactische Reizerscheinungen. *Flora 88*, 371–421.

(*120*) Salah Ud-Din, A. I. M., and Roujeinikova, A. Methyl-accepting chemotaxis proteins: a core sensing element in prokaryotes and archaea, 2017, DOI: 10.1007/s00018-017-2514-0.

(*121*) Krell, T., *Cellular Ecophysiology of microbe: hydrocarbon and lipid interactions*; Springer International Publishing: 2018.

(*122*) Parkinson, J. S. (2010). Signaling Mechanisms of HAMP Domains in Chemoreceptors and Sensor Kinases. *Annual Review of Microbiology 64*, 101–122, DOI: 10.1146/annurev.micro.112408.134215.

(*123*) Pandey, G., and Jain, R. K. Bacterial chemotaxis toward environmental pollutants: Role in bioremediation, 2002, DOI: 10.1128/AEM.68.12.5789-5795.2002.

(*124*) MBINFO What are two component regulatory systems?, 2019, https://www.mechanobio.info/pathogenesis/what-are-two-component-regulatory-systems.

(*125*) Parales, R. E., Luu, R. A., Hughes, J. G., and Ditty, J. L. Bacterial chemotaxis to xenobiotic chemicals and naturally-occurring analogs, 2015, DOI: 10.1016/j.copbio.2015.03.017.

(*126*) Derr, P., Boder, E., and Goulian, M. (2006). Changing the specificity of a bacterial chemoreceptor. *Journal of Molecular Biology 355*, 923–932, DOI: 10.1016/j.jmb.2005.11.025.

(*127*) Luu, R. A., Schneider, B. J., Ho, C. C., Nesteryuk, V., Ngwesse, S. E., Liu, X., Parales, J. V., Ditty, J. L., and Parales, R. E. (2013). Taxis of Pseudomonas putida F1 toward phenylacetic acid is mediated by the energy taxis receptor Aer2. *Applied and environmental microbiology 79*, 2416–2423.

(*128*) Mukherjee, T., Kumar, D., Burriss, N., Xie, Z., and Alexandre, G. (2016). Azospirillum brasilense chemotaxis depends on two signaling pathways regulating distinct motility parameters. *Journal of bacteriology 198*, 1764–1772.

(*129*) Fan, S., and Endres, R. G. (2014). A minimal model for metabolism-dependent chemotaxis in rhodobacter sphaeroides. *Interface Focus 4*, DOI: 10.1098/rsfs.2014.0002.

(*130*) Müller, H., Bosch, J., Griebler, C., Damgaard, L. R., Nielsen, L. P., Lueders, T., and Meckenstock, R. U. (2016). Long-distance electron transfer by cable bacteria in aquifer sediments. *ISME Journal 10*, 2010–2019, DOI: 10.1038/ismej.2015.250.

(*131*) Taylor, B., Zhulin, I., and Johnson, S. (1991). Aerotaxis and Other Energy Sensing Behavior in Bacteria. *Annual Review of Microbiology 53*, 103–128, DOI: https://doi.org/10.1146/annurev.micro.53.1.103.

(*132*) Luciano, A., Mancini, G., Torretta, V., and Viotti, P. (2018). An empirical model for the evaluation of the dissolution rate from a DNAPL-contaminated area. *Environmental Science and Pollution Research*, DOI: 10.1007/s11356-018-3193-6.

(*133*) Mazzag, B. C., Zhulin, B., and Mogilner, A. (2003). Model of Bacterial Band Formation in Aerotaxis. *Biophysical Journal 85*, 3558–3574, DOI: 10.1016/S0006-3495(03)74775-4.

(*134*) Müller, F. D., Schüler, D., and Pfeiffer, D. (2020). A compass to boost navigation: cell biology of bacterial magnetotaxis. *Journal of Bacteriology 202*, 00398–20.

(*135*) Marcos, Fu, H. C., Powers, T. R., and Stocker, R. (2012). Bacterial rheotaxis. *Proceedings of the National Academy of Sciences 109*, 4780–4785, DOI: 10.1073/pnas.1120955109, https://doi.org/10.1073/pnas.1120955109.

(*136*) Gao, B., Wang, X., and Ford, R. M. (2023). Chemotaxis along local chemical gradients enhanced bacteria dispersion and PAH bioavailability in a heterogenous porous medium. *Science of The Total Environment 859*, 160004, DOI: https://doi.org/10.1016/j.scitotenv.2022.160004, https://www.sciencedirect.com/science/article/pii/S0048969722071042.

(*137*) Yang, L., Chen, X., Zeng, X., Radosevich, M., Ripp, S., Zhuang, J., and Sayler, G. S. (2019). Surface-adsorbed contaminants mediate the importance of chemotaxis and haptotaxis for bacterial transport through soils. *Frontiers in microbiology 10*, 2691.

(*138*) Sourjik, V., and Wingreen, N. S. (2012). Responding to chemical gradients: bacterial chemotaxis. *Current Opinion in Cell Biology 24*, 262–268, DOI: https://doi.org/10.1016/j.ceb.2011.11.008, https://www.sciencedirect.com/science/article/pii/S0955067411001542.

(*139*) Mesibov, R., Ordal, G. W., and Adler, J. (1973). The range of attractant concentrations for bacterial chemotaxis and the threshold and size of response over this range: Weber law and related phenomena. *The Journal of general physiology 62*, 203–223.

(*140*) Eisenbach, M., Wolf, A., Welch, M., Caplan, S., Lapidus, I., Macnab, R. M., Aloni, H., and Asher, O. (1990). Pausing, switching and speed fluctuation of the bacterial flagellar motor and their relation to motility and chemotaxis. *Journal of Molecular Biology 211*, 551–563, DOI: https://doi.org/10.1016/0022-2836(90)90265-N, https://www.sciencedirect.com/science/article/pii/002228369090265N.

(*141*) Block, S. M., Blair, D. F., and Berg, H. C. (1989). Compliance of bacterial flagella measured with optical tweezers. *Nature 338*, 514–518.

(*142*) Segall, J. E., Block, S. M., and Berg, H. C. (1986). Temporal comparisons in bacterial chemotaxis. *Proceedings of the National Academy of Sciences 83*, 8987–8991.

(*143*) El Amrani, A., Dumas, A. S., Wick, L. Y., Yergeau, E., and Berthomé, R. (2015). "Omics" Insights into PAH Degradation toward Improved Green Remediation Biotechnologies. *Environmental Science and Technology 49*, 11281–11291, DOI: 10.1021/acs.est.5b01740.

(*144*) Dahlquist, F., Lovely, P., and Koshland, D. (1972). Quantitative Analysis of Bacterial Migration in Chemotaxis. *Nature New Biology 236*, 120–123.

(*145*) Tsang, N., Macnab, R., and Koshland, D. (1973). Common mechanism for repellents and attractants in bacterial chemotaxis. *Science 181*, 60–63.

(*146*) Parales, R. E., and Ditty, J. L. *Bacterial Chemosensing*; Springer: 2018, pp 255–280.

(*147*) Parkinson, J. S. (2007). A "bucket of light" for viewing bacterial colonies in soft agar. *Methods in enzymology 423*, 432–435.

(*148*) Salek, M. M., Carrara, F., Fernandez, V., Guasto, J. S., and Stocker, R. (2019). Bacterial chemotaxis in a microfluidic T-maze reveals strong phenotypic heterogeneity in chemotactic sensitivity. *Nature Communications 10*, 1877, DOI: 10.1038/s41467-019-09521-2, https://doi.org/10.1038/s41467-019-09521-2.

(*149*) Oliveira, N. M., Foster, K. R., and Durham, W. M. (2016). Single-cell twitching chemotaxis in developing biofilms. *Proceedings of the National Academy of Sciences 113*, 6532–6537.

(*150*) Schneider, C. A., Rasband, W. S., and Eliceiri, K. W. (2012). NIH Image to ImageJ: 25 years of image analysis. *Nature Methods 9*, 671–675, DOI: 10.1038/nmeth.2089, https://doi.org/10.1038/nmeth.2089.

(*151*) Singh, R., Paul, D., and Jain, R. K. Biofilms: implications in bioremediation, 2006, DOI: 10.1016/j.tim.2006.07.001.

(*152*) Valderrama-Gómez, M. Á., Schomer, R. A., Savageau, M. A., and Parales, R. E. (2020). TaxisPy: A Python-based software for the quantitative analysis of bacterial chemotaxis. *Journal of Microbiological Methods 175*, 105918, DOI: https://doi.org/10.1016/j.mimet.2020.105918, https://www.sciencedirect.com/science/article/pii/S0167701220300865.

(*153*) Ford, R. M., and Harvey, R. W. (2007). Role of chemotaxis in the transport of bacteria through saturated porous media. *Advances in Water Resources 30*, 1608–1617.

(*154*) Aufrecht, J. A., Fowlkes, J. D., Bible, A. N., Morrell-Falvey, J., Doktycz, M. J., and Retterer, S. T. (2019). Pore-scale hydrodynamics influence the spatial evolution of bacterial biofilms in a microfluidic porous network. *PLOS ONE 14*, e0218316–, https://doi.org/10.1371/journal.pone.0218316.

(*155*) Keller, E. F., and Segel, L. A. (1970). Initiation of slime mold aggregation viewed as an instability. *Journal of Theoretical Biology 26*, 399–415, DOI: https://doi.org/10.1016/0022-5193(70)90092-5, https://www.sciencedirect.com/science/article/pii/0022519370900925.

(*156*) Keller, E. F., and Segel, L. A. (1971). Model for chemotaxis. *Journal of Theoretical Biology 30*, 225–234, DOI: https://doi.org/10.1016/0022-5193(71)90050-6, https://www.sciencedirect.com/science/article/pii/0022519371900506.

(*157*) Arumugam, G., and Tyagi, J. (2020). Keller-Segel Chemotaxis Models: A Review. *Acta Applicandae Mathematicae 171*, 6, DOI: 10.1007/s10440-020-00374-2, https://doi.org/10.1007/s10440-020-00374-2.

(*158*) Gosztolai, A., and Barahona, M. (2020). Cellular memory enhances bacterial chemotactic navigation in rugged environments. *Communications Physics 3*, 47.

(*159*) Valdés-Parada, F. J., Porter, M. L., Narayanaswamy, K., Ford, R. M., and Wood, B. D. (2009). Upscaling microbial chemotaxis in porous media. *Ad-*

vances in Water Resources 32, 1413–1428, DOI: 10.1016/j.advwatres.2009.06.010.

(*160*) Lacal, J., Muñoz-Martínez, F., Reyes-Darías, J. A., Duque, E., Matilla, M., Segura, A., Calvo, J. J., Jímenez-Sánchez, C., Krell, T., and Ramos, J. L. (2011). Bacterial chemotaxis towards aromatic hydrocarbons in Pseudomonas. *Environmental Microbiology 13*, 1733–1744, DOI: 10.1111/j.1462-2920.2011.02493.x.

(*161*) Schulze-Makuch, D., Bowman, R., Pillai, S., and Guan, H. (2003). Groundwater Monitoring and Remediation. *Ground Water Monitoring & Remediation 23*, 68–75.

(*162*) Schmidt, R., Ahmetagic, A., Philip, D., and Pemberton, J. (2011). Catabolic plasmids. *eLS. 1*, 23–26, DOI: 10.1002/9780470015902.a0000471.pub3.

(*163*) Garbisu, C., Garaiyurrebaso, O., Epelde, L., Grohmann, E., and Alkorta, I. (2017). Plasmid-mediated bioaugmentation for the bioremediation of contaminated soils. *Frontiers in Microbiology 8*, DOI: 10.3389/fmicb.2017.01966.

(*164*) Registry of Standard Biological Parts DNA/Conjugation, 2017, http://parts.igem.org/DNA/Conjugation.

(*165*) Croze, O. A., Ferguson, G. P., Cates, M. E., and Poon, W. C. (2011). Migration of Chemotactic Bacteria in Soft Agar: Role of Gel Concentration. *Biophysical Journal 101*, 525–534, DOI: https://doi.org/10.1016/j.bpj.2011.06.023, https://www.sciencedirect.com/science/article/pii/S0006349511007211.

(*166*) Godheja, J., Shekhar, S. K., and Modi, D. R. *Plant-Microbe Interactions in Agro-Ecological Perspectives: Volume 2: Microbial Interactions and Agro-Ecological Impacts*, Singh, D. P., Singh, H. B., and Prabha, R., Eds.; Springer Singapore: Singapore, 2017, pp 495–519, DOI: 10.1007/978-981-10-6593-4{_}20, https://doi.org/10.1007/978-981-10-6593-4_20.

(*167*) Bjrklf, K., Suoniemi, A., Haahtela, K., and Romantschuk, M. (1995). High frequency of conjugation versus plasmid segregation of RP1 in epiphytic Pseudomonas syringae populations. *Microbiology 141*, 2719–2727.

(*168*) Parales, R. E., Ditty, J. L., and Harwood, C. S. Toluene-Degrading Bacteria Are Chemotactic towards the Environmental Pollutants Benzene, Toluene, and Trichloroethylene, tech. rep. 9, 2000, pp 4098–4104, http://aem.asm.org/.

(*169*) Dennis, J. J., and Zylstra, G. J. (2004). Complete Sequence and Genetic Organization of pDTG1, the 83 Kilobase Naphthalene Degradation Plasmid from Pseudomonas putida strain NCIB 9816-4. *Journal of Molecular Biology 341*, 753–768, DOI: https://doi.org/10.1016/j.jmb.2004.06.034, https://www.sciencedirect.com/science/article/pii/S0022283604007259.

(*170*) Simon, M. J., Osslund, T. D., Saunders, R., Ensley, B. D., Suggs, S., Harcourt, A., Wen-chen, S., Cruder, D. L., Gibson, D. T., and Zylstra, G. J. (1993). Sequences of genes encoding naphthalene dioxygenase in Pseudomonas putida strains G7 and NCIB 9816-4. *Gene 127*, 31–37, DOI: https://doi.org/10.1016/0378-1119(93)90613-8, https://www.sciencedirect.com/science/article/pii/0378111993906138.

(*171*) Lee, J.-Y., Jung, K.-H., and Kim, H.-S. (1995). Amplification of toluene dioxygenase genes in a hybrid Pseudomonas strain to enhance the biodegradation of benzene, toluene, and p-xylene mixture. *Biotechnology and bioengineering 45*, 488–494.

(*172*) Venkata, N. Y., Pierre, W., Stefan, W., Stephan, B., Venkata, M. S., A, W. P., and Martina, H. (2003). Dual Labeling of Pseudomonas putida with Fluorescent Proteins for In Situ Monitoring of Conjugal Transfer of the TOL Plasmid. *Applied and Environmental Microbiology 69*, 4846–4852, DOI: 10.1128/AEM.69.8.4846-4852.2003, https://doi.org/10.1128/AEM.69.8.4846-4852.2003.

(*173*) JGI Pseudomonas putida F1, 2019, https://genome.jgi.doe.gov/portal/psepu/psepu.home.htm.

(*174*) Jussila, M. M., Zhao, J., Suominen, L., and Lindström, K. (2007). TOL plasmid transfer during bacterial conjugation in vitro and rhizoremediation of oil compounds in vivo. *Environmental Pollution 146*, 510–524, DOI: https://doi.org/10.1016/j.envpol.2006.07.012, https://www.sciencedirect.com/science/article/pii/S0269749106004738.

(*175*) Yessica, G.-P., Alejandro, A., Ronald, F.-C., José, A. J., Esperanza, M.-R., Samuel, C.-S. J., Remedios, M.-L. M., and Ormeño-Orrillo, E. (2013). Tolerance, growth and degradation of phenanthrene and benzo[a]pyrene by Rhizobium tropici CIAT 899 in liquid culture medium. *Applied Soil Ecology 63*, 105–111, DOI: https://doi.org/10.1016/j.apsoil.2012.09.010, https://www.sciencedirect.com/science/article/pii/S0929139312002338.

(*176*) Murphy, C. W. M., Butler, A., Stanley, C., Lee, P.-H., Puzon, G., and Morgan, M. (2022). The role of chemotaxis in natural source zone depletion (NSZD) at a legacy petroleum hydrocarbon site. *Australasian Groundwater Conference (AGC) Perth, Western Australia, (Oral Presentation)*, http://agc2022.com.au/program/.

(*177*) Murphy, C. W. M., Davis, G. B., Rayner, J. L., Walsh, T., Bastow, T. P., Butler, A. P., Puzon, G. J., and Morgan, M. J. (2022). The role of predicted chemotactic and hydrocarbon degrading taxa in natural source zone depletion at a legacy petroleum hydrocarbon site. *Journal of Hazardous Materials 430*, 128482.

(*178*) Greg Davis, and BBC News Online 'Curtain' of bacteria to purify pollution, 1999.

(*179*) Samanta S K, S. O. V., and K, J. R. (2002). Polycyclic aromatic hydrocarbons: environmental pollution and bioremediation. *TRENDS in Biotechnology 20*, 243–248.

(*180*) Velasco-Casal, P., Wick, L. Y., and Ortega-Calvo, J.-J. (2008). Chemoeffectors decrease the deposition of chemotactic bacteria during transport in porous media. *Environmental science & technology 42*, 1131–1137.

(*181*) Crane, S. R., and Moore, J. A. (1984). Bacterial pollution of groundwater: a review. *Water, Air, and Soil Pollution 22*, 67–83.

(*182*) Joye, S., Kleindienst, S., and Peña-Montenegro, T. D. (2018). SnapShot: microbial hydrocarbon bioremediation. *Cell 172*, 1336.

(*183*) Desai, N., Dabiri, S., and Ardekani, A. M. (2018). Nutrient uptake by chemotactic bacteria in presence of rising oil drops. *International Journal of Multiphase Flow 108*, 156–168, DOI: https://doi.org/10.1016/j.ijmultiphaseflow.2018.06.016, https://www.sciencedirect.com/science/article/pii/S0301932217307462.

(*184*) Balseiro-Romero, M., Prieto-Fernández, Á., Shor, L. M., Ghoshal, S., Baveye, P. C., and Ortega-Calvo, J. J. (2022). Chemotactic Bacteria Facilitate the Dispersion of Nonmotile Bacteria through Micrometer-Sized Pores in Engineered Porous Media. *Environmental Science & Technology 56*, 13975–13984, DOI: 10.1021/acs.est.2c03149, https://doi.org/10.1021/acs.est.2c03149.

(*185*) Furuno, S., Päzolt, K., Rabe, C., Neu, T. R., Harms, H., and Wick, L. Y. (2010). Fungal mycelia allow chemotactic dispersal of polycyclic aromatic hydrocarbon-degrading bacteria in water-unsaturated systems. *Environmental Microbiology 12*, 1391–1398, DOI: 10.1111/j.1462-2920.2009.02022.x, https://doi.org/10.1111/j.1462-2920.2009.02022.x.

(*186*) Grenier, D. (2013). Porphyromonas gingivalis outer membrane vesicles mediate coaggregation and piggybacking of Treponema denticola and Lachnoanaerobaculum saburreum. *International Journal of Dentistry 2013*, DOI: 10.1155/2013/305476.

(*187*) Stanton, M. M., Park, B.-W., Miguel-López, A., Ma, X., Sitti, M., and Sánchez, S. (2017). Biohybrid Microtube Swimmers Driven by Single Cap-

tured Bacteria. *Small 13*, 1603679, DOI: 10.1002/smll.201603679, https://doi.org/10.1002/smll.201603679.

(*188*) Stuelten, C. H., Parent, C. A., and Montell, D. J. (2018). Cell motility in cancer invasion and metastasis: insights from simple model organisms. *Nature Reviews Cancer 18*, 296, https://doi.org/10.1038/nrc.2018.15%2010.1038/nrc.2018.15.

(*189*) Adi, S., Alin, F., Gil, A., Oren, K., Colin, I., and Eshel, B.-J. (2012). Collective navigation of cargo-carrying swarms. *Interface Focus 2*, 786–798, DOI: 10.1098/rsfs.2012.0029, https://doi.org/10.1098/rsfs.2012.0029.

(*190*) Sungthong, R., van West, P., Heyman, F., Jensen, D. F., and Ortega-Calvo, J. J. (2016). Mobilization of Pollutant-Degrading Bacteria by Eukaryotic Zoospores. *Environmental Science & Technology 50*, 7633–7640, DOI: 10.1021/acs.est.6b00994, https://doi.org/10.1021/acs.est.6b00994.

(*191*) Colin, R., Ni, B., Laganenka, L., and Sourjik, V. (2021). Multiple functions of flagellar motility and chemotaxis in bacterial physiology. *FEMS Microbiology Reviews*, DOI: 10.1093/femsre/fuab038, https://doi.org/10.1093/femsre/fuab038.

(*192*) Soby, S., and Bergman, K. (1983). Motility and chemotaxis of Rhizobium meliloti in soil. *Applied and environmental microbiology 46*, 995–998.

(*193*) Olson, M. S., Ford, R. M., Smith, J. A., and Fernandez, E. J. (2005). Analysis of Column Tortuosity for MnCl2 and Bacterial Diffusion Using Magnetic Resonance Imaging. *Environmental Science & Technology 39*, 149–154, DOI: 10.1021/es049577x, https://doi.org/10.1021/es049577x.

(*194*) McCarter, L. L. (2010). Bacterial acrobatics on a surface: swirling packs, collisions, and reversals during swarming. *Journal of bacteriology 192*, 3246–3248.

(*195*) Howard C Berg Re: Chemotaxis Research Question (Personal Communication), Cambridge, MA, 2019.

(*196*) Cf, S. F., Rebello, S., Mathachan Aneesh, E., Sindhu, R., Binod, P., Singh, S., and Pandey, A. (2021). Bioprospecting of gut microflora for plastic biodegradation. *Bioengineered 12*, 1040–1053.

(*197*) Li, J., Luo, C., Zhang, D., Song, M., Cai, X., Jiang, L., and Zhang, G. (2018). Autochthonous Bioaugmentation-Modified Bacterial Diversity of Phenanthrene Degraders in PAH-Contaminated Wastewater as Revealed by DNA-Stable Isotope Probing. *Environmental Science & Technology 52*, 2934–2944, DOI: 10.1021/acs.est.7b05646, https://doi.org/10.1021/acs.est.7b05646.

(*198*) Singh, C., and Lin, J. (2010). Bioaugmentation efficiency of diesel degradation by Bacillus pumilus JLB and Acinetobacter calcoaceticus LT 1 in contaminated soils. *African Journal of Biotechnology 9*, 6881–6888.

(*199*) Imperial College London (Scholary Communication) Reproducing your own published work, 2023, https://www.imperial.ac.uk/research-and-innovation/support-for-staff/scholarly-communication/open-access/theses/reproducing-your-own-published-work/.

(*200*) Singh, N. K., and Choudhary, S. (2021). Bacterial and archaeal diversity in oil fields and reservoirs and their potential role in hydrocarbon recovery and bioprospecting. *Environmental Science and Pollution Research*, DOI: 10.1007/s11356-020-11705-z, https://doi.org/10.1007/s11356-020-11705-z.

(*201*) Blanco-Enríquez, E. G., De La Serna, F. J. Z. D., Peralta-Pérez, M. D. R., Ballinas-Casarrubias, L., Salmerón, I., Rubio-Arias, H., and Rocha-Gutiérrez, B. A. (2018). Characterization of a microbial consortium for the bioremoval of polycyclic aromatic hydrocarbons (PAHs) in water. *International Journal of Environmental Research and Public Health 15*, DOI: 10.3390/ijerph15050975.

(*202*) Dobson, R., Schroth, M. H., and Zeyer, J. (2007). Effect of water-table fluctuation on dissolution and biodegradation of a multi-component, light

nonaqueous-phase liquid. *Journal of Contaminant Hydrology 94*, 235–248, DOI: https://doi.org/10.1016/j.jconhyd.2007.07.007, http://www.sciencedirect.com/science/article/pii/S0169772207000836.

(*203*) Maila, M. P., Randima, P., Surridge, K., Drønen, K., and Cloete, T. E. (2005). Evaluation of microbial diversity of different soil layers at a contaminated diesel site. *International Biodeterioration & Biodegradation 55*, 39–44, DOI: https://doi.org/10.1016/j.ibiod.2004.06.012, http://www.sciencedirect.com/science/article/pii/S0964830504001258.

(*204*) Essaid, H. I., Bekins, B. A., and Cozzarelli, I. M. (2015). Organic contaminant transport and fate in the subsurface: Evolution of knowledge and understanding. *Water Resources Research 51*, 4861–4902.

(*205*) Franzmann, P. D., Robertson, W. J., Zappia, L. R., and Davis, G. B. (2002). The role of microbial populations in the containment of aromatichydrocarbons in the subsurface. *Biodegradation 13*, 65–78, DOI: 10.1023/A:1016318706753, https://doi.org/10.1023/A:1016318706753.

(*206*) Chapelle, F. H., Bradley, P. M., Lovley, D. R., O'Neill, K., and Landmeyer, J. E. (2002). Rapid Evolution of Redox Processes in a Petroleum Hydrocarbon-Contaminated Aquifer. *Groundwater 40*, 353–360, DOI: 10.1111/j.1745-6584.2002.tb02513.x, https://doi.org/10.1111/j.1745-6584.2002.tb02513.x.

(*207*) Dell'Anno, A., Beolchini, F., Rocchetti, L., Luna, G. M., and Danovaro, R. (2012). High bacterial biodiversity increases degradation performance of hydrocarbons during bioremediation of contaminated harbor marine sediments. *Environmental Pollution 167*, 85–92, DOI: https://doi.org/10.1016/j.envpol.2012.03.043, http://www.sciencedirect.com/science/article/pii/S026974911200173X.

(*208*) Franzmann, P. D., Zappia, L. R., Patterson, B. M., Rayner, J. L., and Davis, G. B. (1998). Mineralisation of low concentrations of organic compounds and microbial biomass in surface and vadose zone soils from the Swan Coastal

Plain, Western Australia. *Soil Research 36*, 921–940, https://doi.org/10.1071/S97116.

(*209*) Bruckberger, M. C., Bastow, T. P., Morgan, M. J., Gleeson, D., Banning, N., Davis, G., and Puzon, G. J. (2018). Biodegradability of polar compounds formed from weathered diesel. *Biodegradation 29*, 443–461, DOI: 10.1007/s10532-018-9841-1.

(*210*) Lang, D. A., Bastow, T. P., Van Aarssen, B. G. K., Warton, B., Davis, G. B., and Johnston, C. D. (2009). Polar compounds from the dissolution of weathered diesel. *Groundwater Monitoring & Remediation 29*, 85–93.

(*211*) Lee, S.-J., Kong, M., St-Arnaud, M., and Hijri, M. (2020). Arbuscular Mycorrhizal Fungal Communities of Native Plant Species under High Petroleum Hydrocarbon Contamination Highlights Rhizophagus as a Key Tolerant Genus. *Microorganisms 8*, 872.

(*212*) Li, H., Martin, F. L., and Zhang, D. (2017). Quantification of Chemotaxis-Related Alkane Accumulation in Acinetobacter baylyi Using Raman Microspectroscopy. *Analytical Chemistry 89*, 3909–3918, DOI: 10.1021/acs.analchem.6b02297, https://doi.org/10.1021/acs.analchem.6b02297.

(*213*) Zhang, D., He, Y., Wang, Y., Wang, H., Wu, L., Aries, E., and Huang, W. E. (2012). Whole-cell bacterial bioreporter for actively searching and sensing of alkanes and oil spills. *Microbial biotechnology 5*, 87–97.

(*214*) Lloyd, K. G., Steen, A. D., Ladau, J., Yin, J., and Crosby, L. (2018). Phylogenetically novel uncultured microbial cells dominate earth microbiomes. *MSystems 3*, 10–1128.

(*215*) Douglas, G. M., Maffei, V. J., Zaneveld, J. R., Yurgel, S. N., Brown, J. R., Taylor, C. M., Huttenhower, C., and Langille, M. G. I. (2020). PICRUSt2 for prediction of metagenome functions. *Nature biotechnology 38*, 685–688.

(*216*) Crampon, M., Bodilis, J., and Portet-Koltalo, F. (2018). Linking initial soil bacterial diversity and polycyclic aromatic hydrocarbons (PAHs) degradation potential. *Journal of Hazardous Materials 359*, 500–509.

(*217*) Davis, G. B., Rayner, J. L., Trefry, M. G., Fisher, S. J., and Patterson, B. M. (2005). Measurement and modeling of temporal variations in hydrocarbon vapor behavior in a layered soil profile. *Vadose Zone Journal 4*, 225–239.

(*218*) King, A. Quantification of methanogenesis-dominated natural attenuation processes in a carbonate aquifer with complex sources, tech. rep., Perth: University of Western Australia, Masters Thesis, School of Earth and Environment, 2009.

(*219*) Wiedemeier, T. H., Rifai, H. S., Newell, C. J., and Wilson, J. T., *Natural attenuation of fuels and chlorinated solvents in the subsurface*; John Wiley & Sons: 1999.

(*220*) Bruckberger, M. C., Gleeson, D. B., Bastow, T. P., Morgan, M. J., Walsh, T., Rayner, J. L., Davis, G. B., and Puzon, G. J. (2021). Unravelling Microbial Communities Associated with Different Light Non-Aqueous Phase Liquid Types Undergoing Natural Source Zone Depletion Processes at a Legacy Petroleum Site. *Water 13*, 898.

(*221*) Rayment, G. E., and Lyons, D. J., *Soil chemical methods: Australasia*; CSIRO publishing: 2011; Vol. 3.

(*222*) Parada, A. E., Needham, D. M., and Fuhrman, J. A. (2016). Every base matters: assessing small subunit rRNA primers for marine microbiomes with mock communities, time series and global field samples. *Environmental microbiology 18*, 1403–1414.

(*223*) Bolyen, E. et al. (2019). Reproducible, interactive, scalable and extensible microbiome data science using QIIME 2. *Nature Biotechnology 37*, 852–857, DOI: 10.1038/s41587-019-0209-9, https://doi.org/10.1038/s41587-019-0209-9.

(*224*) Callahan, B., McMurdie, P., Rosen, M., Han, A., Johnson, A., and Holmes, S. (2016). DADA2: High-resolution sample inference from Illumina amplicon data. *Nat Methods 13*, 581–583, DOI: 10.1038/nmeth.3869.

(*225*) Rognes, T., Flouri, T., Nichols, B., Quince, C., and Mahé, F. (2016). VSEARCH: a versatile open source tool for metagenomics. *PeerJ 4*, e2584.

(*226*) Bokulich, N. A., Kaehler, B. D., Rideout, J. R., Dillon, M., Bolyen, E., Knight, R., Huttley, G. A., and Gregory Caporaso, J. (2018). Optimizing taxonomic classification of marker-gene amplicon sequences with QIIME 2's q2-feature-classifier plugin. *Microbiome 6*, 1–17.

(*227*) Quast, C., Pruesse, E., Yilmaz, P., Gerken, J., Schweer, T., Yarza, P., Peplies, J., and Glöckner, F. O. (2012). The SILVA ribosomal RNA gene database project: improved data processing and web-based tools. *Nucleic acids research 41*, D590–D596.

(*228*) Yilmaz, P., Parfrey, L. W., Yarza, P., Gerken, J., Pruesse, E., Quast, C., Schweer, T., Peplies, J., Ludwig, W., and Glöckner, F. O. (2014). The SILVA and "all-species living tree project (LTP)" taxonomic frameworks. *Nucleic acids research 42*, D643–D648.

(*229*) Team, R. (2020). RStudio: Integrated Development Environment for R (RStudio, PBC, Boston, MA, 2020). *URL http://www. rstudio. com*.

(*230*) Kanehisa, M., and Goto, S. (2000). KEGG: Kyoto Encyclopedia of Genes and Genomes. *Nucleic Acids Research 28*, 27–30, DOI: `10.1093/nar/28.1.27`, `https://doi.org/10.1093/nar/28.1.27`.

(*231*) Kanehisa, M. (2019). Toward understanding the origin and evolution of cellular organisms. *Protein Science 28*, 1947–1951, DOI: `10.1002/pro.3715`, `https://doi.org/10.1002/pro.3715`.

(*232*) Kanehisa Laboratories Bacterial chemotaxis PATHWAY: ko02030, 2009, `https://www.genome.jp/entry/ko02030#:~:text=KEGG%20PATHWAY%3A%20ko02030&text=Chemotaxis%20is%20the%20process%20by,move%20towards%20more%20favorable%20conditions.`.

(*233*) Oksanen, J., Blanchet, F. G., Kindt, R., Legendre, P., Minchin, P. R., O'hara, R. B., Simpson, G. L., Solymos, P., Stevens, M. H. H., and Wagner, H. (2013). Package 'vegan'. *Community ecology package, version 2*, 1–295.

(*234*) Mangse, G., Werner, D., Meynet, P., and Ogbaga, C. C. (2020). Microbial community responses to different volatile petroleum hydrocarbon class mixtures in an aerobic sandy soil. *Environmental Pollution 264*, 114738, DOI: https://doi.org/10.1016/j.envpol.2020.114738, http://www.sciencedirect.com/science/article/pii/S0269749119362451.

(*235*) Hamdan, H. Z., Salam, D. A., and Saikaly, P. E. (2019). Characterization of the microbial community diversity and composition of the coast of Lebanon: Potential for petroleum oil biodegradation. *Marine pollution bulletin 149*, 110508.

(*236*) Naimi, B., Hamm, N. A. S., Groen, T. A., Skidmore, A. K., and Toxopeus, A. G. (2014). Where is positional uncertainty a problem for species distribution modelling? *Ecography 37*, 191–203.

(*237*) Lundegard, P. D., and Sweeney, R. E. (2004). Total Petroleum Hydrocarbons in Groundwater—Evaluation of Nondissolved and Nonhydrocarbon Fractions. *Environmental Forensics 5*, 85–95, DOI: 10.1080/15275920490454346, https://doi.org/10.1080/15275920490454346.

(*238*) Venables, W. N., and Ripley, B. D., *Modern applied statistics with S-PLUS*; Springer Science & Business Media: 2013.

(*239*) Sharma, M., Nandy, A., Taylor, N., Venkatesan, S. V., Ozhukil Kollath, V., Karan, K., Thangadurai, V., Tsesmetzis, N., and Gieg, L. M. (2020). Bioelectrochemical remediation of phenanthrene in a microbial fuel cell using an anaerobic consortium enriched from a hydrocarbon-contaminated site. *Journal of Hazardous Materials 389*, 121845, DOI: https://doi.org/10.1016/j.jhazmat.2019.121845, https://www.sciencedirect.com/science/article/pii/S0304389419317996.

(*240*) Hassan, M., Fernandez, A. S., San Martin, I., Xie, B., and Moran, A. (2018). Hydrogen evolution in microbial electrolysis cells treating landfill leachate: Dynamics of anodic biofilm. *International Journal of Hydrogen Energy 43*, 13051–13063.

(*241*) Bruckberger, M. C., Morgan, M. J., Walsh, T., Bastow, T. P., Prommer, H., Mukhopadhyay, A., Kaksonen, A. H., Davis, G., and Puzon, G. J. (2019). Biodegradability of legacy crude oil contamination in Gulf War damaged groundwater wells in Northern Kuwait. *Biodegradation 30*, 71–85.

(*242*) Lessner, D. J., Parales, R. E., Narayan, S., and Gibson, D. T. (2003). Expression of the nitroarene dioxygenase genes in Comamonas sp. strain JS765 and Acidovorax sp. strain JS42 is induced by multiple aromatic compounds. *Journal of bacteriology 185*, 3895–3904.

(*243*) Wang, Y.-H., Huang, Z., and Liu, S.-J. (2019). Chemotaxis Towards Aromatic Compounds: Insights from Comamonas testosteroni. *International journal of molecular sciences 20*, 2701, DOI: 10.3390/ijms20112701, https://pubmed.ncbi.nlm.nih.gov/31159416%20https://www.ncbi.nlm.nih.gov/pmc/articles/PMC6600141/.

(*244*) Rabinovitch-Deere, C. A., and Parales, R. E. (2012). Three Types of Taxis Used in the Response of Acidovorax sp. Strain JS42 to 2-Nitrotoluene. *Applied and Environmental Microbiology 78*, 2306, DOI: 10.1128/AEM.07183-11, http://aem.asm.org/content/78/7/2306.abstract.

(*245*) Kunapuli, U., Jahn, M. K., Lueders, T., Geyer, R., Heipieper, H. J., and Meckenstock, R. U. (2010). Desulfitobacterium aromaticivorans sp. nov. and Geobacter toluenoxydans sp. nov., iron-reducing bacteria capable of anaerobic degradation of monoaromatic hydrocarbons. *International Journal of Systematic and Evolutionary Microbiology 60*, 686–695, DOI: 10.1099/ijs.0.003525-0.

(*246*) Zhang, T., Tremblay, P.-L., Chaurasia, A. K., Smith, J. A., Bain, T. S., and Lovley, D. R. (2014). Identification of genes specifically required for the anaerobic metabolism of benzene in Geobacter metallireducens. *Frontiers in microbiology 5*, 245, DOI: 10.3389/fmicb.2014.00245, https://pubmed.ncbi.nlm.nih.gov/24904558%20https://www.ncbi.nlm.nih.gov/pmc/articles/PMC4033198/.

(*247*) Childers, S., Ciufo, S., and Lovley D (2002). Geobacter metallireducens accesses insoluble Fe(III) oxide by chemotaxis. *Nature 416*, 767–769.

(*248*) Derek R. Lovley Chemotaxis Geobacter Q (Personal Communication), 2020.

(*249*) Bruckberger, M. Degradation of recalcitrant products from weathered petroleum contaminations in Western Australia and Kuwait, Ph.D. Thesis, University of Western Australia, 2020, p 303, https://api.research-repository.uwa.edu.au/files/79931940/TH20_110_THESIS_DOCTOR_OF_PHILOSOPHY_BRUCKBERGER_Melanie_Carina_2020.pdf.

(*250*) Lacal, J., Reyes-Darias, J. A., García-Fontana, C., Ramos, J.-L., and Krell, T. (2013). Tactic responses to pollutants and their potential to increase biodegradation efficiency. *Journal of Applied Microbiology 114*, 923–933, DOI: 10.1111/jam.12076, https://doi.org/10.1111/jam.12076.

(*251*) Luu, R. A., Kootstra, J. D., Nesteryuk, V., Brunton, C. N., Parales, J. V., Ditty, J. L., and Parales, R. E. (2015). Integration of chemotaxis, transport and catabolism in Pseudomonas putida and identification of the aromatic acid chemoreceptor PcaY. *Molecular Microbiology 96*, 134–147, DOI: 10.1111/mmi.12929.

(*252*) Semenec, L., Laloo, A. E., Schulz, B. L., Vergara, I. A., Bond, P. L., and Franks, A. E. (2018). Deciphering the electric code of Geobacter sulfurreducens in cocultures with Pseudomonas aeruginosa via SWATH-MS proteomics. *Bioelectrochemistry 119*, 150–160, DOI: https://doi.org/10.1016/j.bioelechem.2017.09.013, http://www.sciencedirect.com/science/article/pii/S1567539417302050.

(*253*) Zhuang, L., Tang, Z., Ma, J., Yu, Z., Wang, Y., and Tang, J. (2019). Enhanced Anaerobic Biodegradation of Benzoate Under Sulfate-Reducing Conditions With Conductive Iron-Oxides in Sediment of Pearl River Estuary. *Frontiers in Microbiology 10*, 374, https://www.frontiersin.org/article/10.3389/fmicb.2019.00374.

(*254*) Pilloni, G., Bayer, A., Ruth-Anneser, B., Fillinger, L., Engel, M., Griebler, C., and Lueders, T. (2019). Dynamics of hydrology and anaerobic hydrocarbon degrader communities in a tar-oil contaminated aquifer. *Microorganisms 7*, 46.

(*255*) Cambon-Bonavita, M.-A., Aubé, J., Cueff-Gauchard, V., and Reveillaud, J. (2020). Niche Partitioning in the Rimicaris Exoculata Holobiont: The Case of the First Symbiotic Zetaproteobacteria.

(*256*) Wawrik, B., Marks, C. R., Davidova, I. A., McInerney, M. J., Pruitt, S., Duncan, K. E., Suflita, J. M., and Callaghan, A. V. (2016). Methanogenic paraffin degradation proceeds via alkane addition to fumarate by 'Smithella' spp. mediated by a syntrophic coupling with hydrogenotrophic methanogens. *Environmental Microbiology 18*, 2604–2619, DOI: 10.1111/1462-2920.13374, https://doi.org/10.1111/1462-2920.13374.

(*257*) Embree, M., Nagarajan, H., Movahedi, N., Chitsaz, H., and Zengler, K. (2014). Single-cell genome and metatranscriptome sequencing reveal metabolic interactions of an alkane-degrading methanogenic community. *The ISME journal 8*, 757–767, DOI: 10.1038/ismej.2013.187, https://www.ncbi.nlm.nih.gov/pubmed/24152715.

(*258*) Tischer, K., Kleinsteuber, S., Schleinitz, K. M., Fetzer, I., Spott, O., Stange, F., Lohse, U., Franz, J., Neumann, F., Gerling, S., Schmidt, C., Hasselwander, E., Harms, H., and Wendeberg, A. (2013). Microbial communities along biogeochemical gradients in a hydrocarbon-contaminated aquifer. *Environmental Microbiology 15*, 2603–2615, DOI: 10.1111/1462-2920.12168, https://doi.org/10.1111/1462-2920.12168.

(*259*) Sakai, S., Conrad, R., Liesack, W., and Imachi, H. (2010). Methanocella arvoryzae sp. nov., a hydrogenotrophic methanogen isolated from rice field soil. *International journal of systematic and evolutionary microbiology 60*, 2918–2923, DOI: 10.1099/ijs.0.020883-0.

(*260*) Sakai, S., Takaki, Y., Shimamura, S., Sekine, M., Tajima, T., Kosugi, H., Ichikawa, N., Tasumi, E., Hiraki, A. T., Shimizu, A., Kato, Y., Nishiko, R., Mori, K., Fujita, N., Imachi, H., and Takai, K. (2011). Genome Sequence of a Mesophilic Hydrogenotrophic Methanogen Methanocella paludicola, the First Cultivated Representative of the Order Methanocellales. *PLOS ONE 6*, e22898–, https://doi.org/10.1371/journal.pone.0022898.

(*261*) Angel, R., Matthies, D., and Conrad, R. (2011). Activation of methanogenesis in arid biological soil crusts despite the presence of oxygen. *PloS one 6*, e20453.

(*262*) Zhang, L., Guo, B., Mou, A., Li, R., and Liu, Y. (2020). Blackwater biomethane recovery using a thermophilic upflow anaerobic sludge blanket reactor: Impacts of effluent recirculation on reactor performance. *Journal of Environmental Management 274*, 111157, DOI: https://doi.org/10.1016/j.jenvman.2020.111157, https://www.sciencedirect.com/science/article/pii/S0301479720310823.

(*263*) Tan, B., Jane Fowler, S., Laban, N. A., Dong, X., Sensen, C. W., Foght, J., and Gieg, L. M. (2015). Comparative analysis of metagenomes from three methanogenic hydrocarbon-degrading enrichment cultures with 41 environmental samples. *The ISME Journal 9*, 2028–2045, DOI: 10.1038/ismej.2015.22, https://doi.org/10.1038/ismej.2015.22.

(*264*) Zhang, T., Bain, T. S., Nevin, K. P., Barlett, M. A., and Lovley, D. R. (2012). Anaerobic benzene oxidation by Geobacter species. *Applied and environmental microbiology 78*, 8304–8310.

(*265*) Coates, J. D., Bhupathiraju, V. K., Achenbach, L. A., Mclnerney, M. J., and Lovley, D. R. (2001). Geobacter hydrogenophilus, Geobacter chapellei and Geobacter grbiciae, three new, strictly anaerobic, dissimilatory Fe (III)-reducers. *International Journal of Systematic and Evolutionary Microbiology 51*, 581–588.

(*266*) Murphy, C., Morgan, M., Butler, A., Rayner, J., Bastow, T., Walsh, T., Davis, G., and Puzon, G. (2019). Evaluating the presence of chemotaxic microbes at a hydrocarbon contaminated site undergoing remediation. *NCGRT/IAH Australasian Groundwater Conference (AGC) Brisbane, Queensland, (Poster Presentation)*, http://agc2019.p.agc.currinda.com/days/2019-11-26/abstract/489.

(*267*) Weimer, A., Kohlstedt, M., Volke, D. C., Nikel, P. I., and Wittmann, C. (2020). Industrial biotechnology of Pseudomonas putida: advances and prospects. *Applied Microbiology and Biotechnology 104*, 7745–7766, DOI: 10.1007/s00253-020-10811-9, https://doi.org/10.1007/s00253-020-10811-9.

(*268*) Gimeno, A., Stanley, C. E., Ngamenie, Z., Hsung, M.-H., Walder, F., Schmieder, S. S., Bindschedler, S., Junier, P., Keller, B., and Vogelgsang, S. (2021). A versatile microfluidic platform measures hyphal interactions between Fusarium graminearum and Clonostachys rosea in real-time. *Communications Biology 4*, 262, DOI: 10.1038/s42003-021-01767-1, https://doi.org/10.1038/s42003-021-01767-1.

(*269*) Parales, R. E., Luu, R. A., Chen, G. Y., Liu, X., Wu, V., Lin, P., Hughes, J. G., Nesteryuk, V., Parales, J. V., and Ditty, J. L. (2013). Pseudomonas putida F1 has multiple chemoreceptors with overlapping specificity for organic acids. *Microbiology (Reading, England) 159*, 1086–1096, DOI: 10.1099/mic.0.065698-0, https://pubmed.ncbi.nlm.nih.gov/23618999%20https://www.ncbi.nlm.nih.gov/pmc/articles/PMC4085986/.

(*270*) Ditty, J. L., Grimm, A. C., and Harwood, C. S. (1998). Identification of a chemotaxis gene region from Pseudomonas putida. *FEMS Microbiology Letters 159*, 267–273, DOI: 10.1111/j.1574-6968.1998.tb12871.x, https://doi.org/10.1111/j.1574-6968.1998.tb12871.x.

(*271*) Liu, X., Wood, P. L., Parales, J. V., and Parales, R. E. (2009). Chemotaxis to pyrimidines and identification of a cytosine chemoreceptor in Pseudomonas putida. *Journal of bacteriology 191*, 2909–2916.

(*272*) McCullock, T. W., MacLean, D. M., and Kammermeier, P. J. (2020). Comparing the performance of mScarlet-I, mRuby3, and mCherry as FRET acceptors for mNeonGreen. *PloS one 15*, e0219886.

(*273*) Bindels, D. S., Haarbosch, L., Van Weeren, L., Postma, M., Wiese, K. E., Mastop, M., Aumonier, S., Gotthard, G., Royant, A., and Hink, M. A. (2017). mScarlet: a bright monomeric red fluorescent protein for cellular imaging. *Nature methods 14*, 53–56.

(*274*) Choi, K.-H., and Schweizer, H. P. (2006). mini-Tn7 insertion in bacteria with single attTn7 sites: example Pseudomonas aeruginosa. *Nature Protocols 1*, 153–161, DOI: 10.1038/nprot.2006.24, https://doi.org/10.1038/nprot.2006.24.

(*275*) Martínez-García, E., and de Lorenzo, V. *Synthetic Gene Networks*; Springer: 2012, pp 267–283.

(*276*) Winsor, G. L., Griffiths, E. J., Lo, R., Dhillon, B. K., Shay, J. A., and Brinkman, F. S. L. (2016). Enhanced annotations and features for comparing thousands of Pseudomonas genomes in the Pseudomonas genome database. *Nucleic acids research 44*, D646–D653.

(*277*) Brinkman Lab Pseudomonas putida F1, Pput_1508 (fliM), 2023, https://www.pseudomonas.com/feature/show/?id=1495299&view=overview.

(*278*) Gjermansen, M., Ragas, P., Sternberg, C., Molin, S., and Tolker-Nielsen, T. (2005). Characterization of starvation-induced dispersion in Pseudomonas putida biofilms. *Environmental microbiology 7*, 894–904.

(*279*) Martínez-García, E., and de Lorenzo, V. (2011). Engineering multiple genomic deletions in Gram-negative bacteria: analysis of the multi-resistant antibiotic profile of Pseudomonas putida KT2440. *Environmental microbiology 13*, 2702–2716.

(*280*) Hueso-Gil, Á., Calles, B., and de Lorenzo, V. (2020). The Wsp intermembrane complex mediates metabolic control of the swim-attach decision of Pseudomonas putida. *Environmental Microbiology 22*, 3535–3547, DOI: https:

//doi.org/10.1111/1462-2920.15126, https://doi.org/10.1111/1462-2920.15126.

(*281*) Benchling Home Page, 2023, https://benchling.com..

(*282*) Hyakutake, A., Homma, M., Austin, M. J., Boin, M. A., Häse, C. C., and Kawagishi, I. (2005). Only one of the five CheY homologs in Vibrio cholerae directly switches flagellar rotation. *Journal of bacteriology 187*, 8403–8410.

(*283*) Hawkins, A. C., and Harwood, C. S. (2002). Chemotaxis of Ralstonia eutropha JMP134 (pJP4) to the herbicide 2, 4-dichlorophenoxyacetate. *Applied and environmental microbiology 68*, 968–972.

(*284*) Ditty, J. L., and Parales, R. E. (2017). Protocols for the measurement of bacterial chemotaxis to hydrocarbons. *Hydrocarbon and Lipid Microbiology Protocols: Activities and Phenotypes*, 7–42.

(*285*) Mosqueda, G., Ramos-González, M.-I., and Ramos, J. L. (1999). Toluene metabolism by the solvent-tolerant Pseudomonas putida DOT-T1 strain, and its role in solvent impermeabilization. *Gene 232*, 69–76, DOI: https://doi.org/10.1016/S0378-1119(99)00113-4, http://www.sciencedirect.com/science/article/pii/S0378111999001134.

(*286*) Tover, A., Ojangu, E.-L., and Kivisaar, M. (2001). Growth medium composition-determined regulatory mechanisms are superimposed on CatR-mediated transcription from the pheBA and catBCA promoters in Pseudomonas putida. *Microbiology 147*, 2149–2156, DOI: 10.1099/00221287-147-8-2149, https://www.microbiologyresearch.org/content/journal/micro/10.1099/00221287-147-8-2149.

(*287*) Phoenix, P., Keane, A., Patel, A., Bergeron, H., Ghoshal, S., and Lau, P. C. K. (2003). Characterization of a new solvent-responsive gene locus in Pseudomonas putida F1 and its functionalization as a versatile biosensor. *Environmental Microbiology 5*, 1309–1327, DOI: https://doi.org/10.1111/j.1462-2920.2003.00426.x, https://doi.org/10.1111/j.1462-2920.2003.00426.x.

(*288*) Nikel, P. I., Chavarría, M., Martínez-García, E., Taylor, A. C., and de Lorenzo, V. (2013). Accumulation of inorganic polyphosphate enables stress endurance and catalytic vigour in Pseudomonas putida KT2440. *Microbial cell factories 12*, 1–14.

(*289*) Tian, M., Zhang, C., Zhang, R., and Yuan, J. (2021). Collective motion enhances chemotaxis in a two-dimensional bacterial swarm. *Biophysical Journal 120*, 1615–1624, DOI: https://doi.org/10.1016/j.bpj.2021.02.021, https://www.sciencedirect.com/science/article/pii/S0006349521001594.

(*290*) Hintsche, M., Waljor, V., Großmann, R., Kühn, M. J., Thormann, K. M., Peruani, F., and Beta, C. (2017). A polar bundle of flagella can drive bacterial swimming by pushing, pulling, or coiling around the cell body. *Scientific Reports 7*, 16771, DOI: 10.1038/s41598-017-16428-9, https://doi.org/10.1038/s41598-017-16428-9.

(*291*) Tecon, R., and Or, D. (2017). Cooperation in carbon source degradation shapes spatial self-organization of microbial consortia on hydrated surfaces. *Scientific Reports 7*, DOI: 10.1038/srep43726.

(*292*) Martin, P., Redouan, B., Saskia, B., Sevasti, F., Y, W. L., Daniel, J., and Pilar, J. (2013). Gains of Bacterial Flagellar Motility in a Fungal World. *Applied and Environmental Microbiology 79*, 6862–6867, DOI: 10.1128/AEM.01393-13, https://doi.org/10.1128/AEM.01393-13.

(*293*) Pineda-Molina, E., Reyes-Darias, J.-A., Lacal, J., Ramos, J. L., García-Ruiz, J. M., Gavira, J. A., and Krell, T. (2012). Evidence for chemoreceptors with bimodular ligand-binding regions harboring two signal-binding sites. *Proceedings of the National Academy of Sciences of the United States of America 109*, 18926–18931, DOI: 10.1073/pnas.1201400109, https://pubmed.ncbi.nlm.nih.gov/23112148%20https://www.ncbi.nlm.nih.gov/pmc/articles/PMC3503224/.

(*294*) Zhao, L. H., Lee, J., and Sen, P. N. (2012). Long-term retention of hydrophilic behavior of plasma treated polydimethylsiloxane (PDMS) surfaces stored under water and Luria-Bertani broth. *Sensors and Actuators A: Physical 181*, 33–42, DOI: https://doi.org/10.1016/j.sna.2012.04.038, https://www.sciencedirect.com/science/article/pii/S0924424712002774.

(*295*) Murray, T. S., and Kazmierczak, B. I. (2006). FlhF is required for swimming and swarming in Pseudomonas aeruginosa. *Journal of bacteriology 188*, 6995–7004.

(*296*) Morales, M., Sentchilo, V., Bertelli, C., Komljenovic, A., Kryuchkova-Mostacci, N., Bourdilloud, A., Linke, B., Goesmann, A., Harshman, K., Segers, F., Delapierre, F., Fiorucci, D., Seppey, M., Trofimenco, E., Berra, P., El Taher, A., Loiseau, C., Roggero, D., Sulfiotti, M., Etienne, A., Ruiz Buendia, G., Pillard, L., Escoriza, A., Moritz, R., Schneider, C., Alfonso, E., Ben Jeddou, F., Selmoni, O., Resch, G., Greub, G., Emery, O., Dubey, M., Pillonel, T., Robinson-Rechavi, M., and van der Meer, J. R. (2016). The Genome of the Toluene-Degrading Pseudomonas veronii Strain 1YdBTEX2 and Its Differential Gene Expression in Contaminated Sand. *PLOS ONE 11*, e0165850–, https://doi.org/10.1371/journal.pone.0165850.

(*297*) Schlechter, R. O., Jun, H., Bernach, M., Oso, S., Boyd, E., Muñoz-Lintz, D. A., Dobson, R. C. J., Remus, D. M., and Remus-Emsermann, M. N. P. (2018). Chromatic Bacteria – A Broad Host-Range Plasmid and Chromosomal Insertion Toolbox for Fluorescent Protein Expression in Bacteria. *Frontiers in Microbiology 9*, https://www.frontiersin.org/article/10.3389/fmicb.2018.03052.

(*298*) Jia, Z. J., Xiaoyu, T., Michelle, Z., Darlene, N., and S, M. B. (2017). Broad-Host-Range Expression Reveals Native and Host Regulatory Elements That Influence Heterologous Antibiotic Production in Gram-Negative Bacteria. *mBio 8*, 01291–17, DOI: 10.1128/mBio.01291-17, https://doi.org/10.1128/mBio.01291-17.

(*299*) Herzberg, M., Dosoretz, C. G., Kuhn, J., Klein, S., and Green, M. (2006). Visualization of active biomass distribution in a BGAC fluidized bed reactor using GFP tagged Pseudomonas putida F1. *Water Research 40*, 2704–2712, DOI: https://doi.org/10.1016/j.watres.2006.05.006, https://www.sciencedirect.com/science/article/pii/S0043135406002715.

(*300*) Xiangsheng, Z., G, H. J., A, S. G., L, D. J., and E, P. R. (2019). Chemotaxis of Pseudomonas putida F1 to Alcohols Is Mediated by the Carboxylic Acid Receptor McfP. *Applied and Environmental Microbiology 85*, 01625–19, DOI: 10.1128/AEM.01625-19, https://doi.org/10.1128/AEM.01625-19.

(*301*) Bubendorfer, S., Koltai, M., Rossmann, F., Sourjik, V., and Thormann, K. M. (2014). Secondary bacterial flagellar system improves bacterial spreading by increasing the directional persistence of swimming. *Proceedings of the National Academy of Sciences 111*, 11485–11490.

(*302*) Giverso, C., Verani, M., and Ciarletta, P. (2016). Emerging morphologies in round bacterial colonies: comparing volumetric versus chemotactic expansion. *Biomechanics and Modeling in Mechanobiology 15*, 643–661, DOI: 10.1007/s10237-015-0714-9, https://doi.org/10.1007/s10237-015-0714-9.

(*303*) Liu, W., Cremer, J., Li, D., Hwa, T., and Liu, C. (2019). An evolutionarily stable strategy to colonize spatially extended habitats. *Nature 575*, 664–668, DOI: 10.1038/s41586-019-1734-x, https://doi.org/10.1038/s41586-019-1734-x.

(*304*) Cremer, J., Honda, T., Tang, Y., Wong-Ng, J., Vergassola, M., and Hwa, T. (2019). Chemotaxis as a navigation strategy to boost range expansion. *Nature 575*, 658–663, DOI: 10.1038/s41586-019-1733-y, https://doi.org/10.1038/s41586-019-1733-y.

(*305*) Das, N., and Chandran, P. (2011). Microbial degradation of petroleum hydrocarbon contaminants: an overview. *Biotechnology research international 2011*.

(*306*) Kanehisa Laboratories Degradation of aromatic compounds - Reference pathway, 2019, https://www.genome.jp/pathway/map01220.

(*307*) La Rosa, R., Nogales, J., and Rojo, F. (2015). The Crc/CrcZ-CrcY global regulatory system helps the integration of gluconeogenic and glycolytic metabolism in Pseudomonas putida. *Environmental Microbiology 17*, 3362–3378, DOI: https://doi.org/10.1111/1462-2920.12812, https://doi.org/10.1111/1462-2920.12812.

(*308*) Narla, A. V., Cremer, J., and Hwa, T. (2021). A traveling-wave solution for bacterial chemotaxis with growth. *Proceedings of the National Academy of Sciences 118*, e2105138118.

(*309*) Venturi, V. (2006). Regulation of quorum sensing in Pseudomonas. *FEMS Microbiology Reviews 30*, 274–291, DOI: 10.1111/j.1574-6976.2005.00012.x, https://doi.org/10.1111/j.1574-6976.2005.00012.x.

(*310*) Natan, G., Worlitzer, V. M., Ariel, G., and Be'er, A. (2022). Mixed-species bacterial swarms show an interplay of mixing and segregation across scales. *Scientific Reports 12*, 16500.

(*311*) Oliveira, R. A., Cabral, V., Torcato, I., and Xavier, K. B. (2023). Deciphering the quorum-sensing lexicon of the gut microbiota. *Cell Host & Microbe 31*, 500–512, DOI: https://doi.org/10.1016/j.chom.2023.03.015, https://www.sciencedirect.com/science/article/pii/S1931312823001208.

(*312*) Adler, J. (1966). Chemotaxis in Bacteria. *Science 153*, 708–716, DOI: 10.1126/science.153.3737.708, https://doi.org/10.1126/science.153.3737.708.

(*313*) Gude, S., Pinçe, E., Taute, K. M., Seinen, A.-B., Shimizu, T. S., and Tans, S. J. (2020). Bacterial coexistence driven by motility and spatial competition. *Nature 578*, 588–592, DOI: 10.1038/s41586-020-2033-2, https://doi.org/10.1038/s41586-020-2033-2.

(*314*) Barnard, R. T. (2019). The Zone of Inhibition. *Clinical Chemistry 65*, 819, DOI: 10.1373/clinchem.2018.299800, https://doi.org/10.1373/clinchem.2018.299800.

(*315*) Lynch, W. H. (1980). Effect of temperature on Pseudomonas fluorescens chemotaxis. *Journal of Bacteriology 143*, 338–342, DOI: 10.1128/jb.143.1.338-342.1980, https://doi.org/10.1128/jb.143.1.338-342.1980.

(*316*) Podoleanu, A. G., Dobre, G. M., Webb, D. J., and Jackson, D. A. (1996). Coherence imaging by use of a Newton rings sampling function. *Optics Letters 21*, 1789–1791.

(*317*) Altuntas, V., Altuntas, S., and Gok, M. (2018). Automatic colony segmentation on agar surface by image processing. *CSIR-NIScPR Online Repository*, https://nopr.niscpr.res.in/bitstream/123456789/44804/1/JSIR%2077(8)%20451-456.pdf.

(*318*) Danielsen, J., and Nordenfelt, P. (2017). Computer vision-based image analysis of bacteria. *Bacterial Pathogenesis: Methods and Protocols*, 161–172.

(*319*) Liao, P.-S., Chen, T.-S., and Chung, P.-C. (2001). A fast algorithm for multilevel thresholding. *J. Inf. Sci. Eng. 17*, 713–727.

(*320*) Paul Baggethun Radial Profile Plot, Pittsburgh, PA, 2002, https://imagej.nih.gov/ij/plugins/radial-profile.html.

(*321*) Stavig, G. R., and Gibbons, J. D. (1977). Comparing the mean and the median as measures of centrality. *International Statistical Review/Revue Internationale de Statistique*, 63–70.

(*322*) Josse, G., Mias, C., Le Digabel, J., Filiol, J., Ipinazar, C., Villaret, A., Gomiero, C., Bevilacqua, M., Redoules, D., and Nocera, T. (2020). High bacterial colonization and lipase activity in microcomedones. *Experimental dermatology 29*, 168–176.

(*323*) Schlechter, R. O., Kear, E. J., Remus, D. M., and Remus-Emsermann, M. N. P. (2021). Fluorescent protein expression as a proxy for bacterial

fitness in a high-throughput assay. *Applied and Environmental Microbiology 87*, 00982–21.

(*324*) Murphy, C. W. M., Morgan, M. J., Stanley, C. E., Lee, P.-H., Puzon, G., and Butler, A. (2022). Investigating the biophysical interactions of hydrocarbon degrading microbial communities of varying chemotactic abilities. *ISME 22 - Microscale and biophysical interactions in microbial ecosystems (Poster, PS28)*.

(*325*) Chourey, K., Nissen, S., Vishnivetskaya, T., Shah, M., Pfiffner, S., Hettich, R. L., and Löffler, F. E. (2013). Environmental proteomics reveals early microbial community responses to biostimulation at a uranium-and nitrate-contaminated site. *Proteomics 13*, 2921–2930.

(*326*) Dallinger, A., and Horn, M. A. (2014). Agricultural soil and drilosphere as reservoirs of new and unusual assimilators of 2, 4-dichlorophenol carbon. *Environmental microbiology 16*, 84–100.

(*327*) Bansal, R., Liermann, L. J., Stanley, B. A., Brantley, S. L., and Tien, M. (2015). Characterization and proteomic analysis of Geobacter sulfurreducens PCA under long-term electron-donor starvation. *Geomicrobiology Journal*, 0.

(*328*) Grösbacher, M., Eckert, D., Cirpka, O. A., and Griebler, C. (2018). Contaminant concentration versus flow velocity: drivers of biodegradation and microbial growth in groundwater model systems. *Biodegradation 29*, 211–232.

(*329*) Sung, Y., Fletcher, K. E., Ritalahti, K. M., Apkarian, R. P., Ramos-Hernández, N., Sanford, R. A., Mesbah, N. M., and Löffler, F. E. (2006). Geobacter lovleyi sp. nov. strain SZ, a novel metal-reducing and tetrachloroethene-dechlorinating bacterium. *Applied and environmental microbiology 72*, 2775–2782.

(*330*) Yao, J., and Allen, C. (2006). Chemotaxis is required for virulence and competitive fitness of the bacterial wilt pathogen Ralstonia solanacearum. *Journal of bacteriology 188*, 3697–3708.

(*331*) Budrene, E. O., and Berg, H. C. (1995). Dynamics of formation of symmetrical patterns by chemotactic bacteria. *Nature 376*, 49–53.

(*332*) Chou, K.-T., Lee, D.-y. D., Chiou, J.-g., Galera-Laporta, L., Ly, S., Garcia-Ojalvo, J., and Süel, G. M. (2022). A segmentation clock patterns cellular differentiation in a bacterial biofilm. *Cell 185*, 145–157, DOI: https://doi.org/10.1016/j.cell.2021.12.001, https://www.sciencedirect.com/science/article/pii/S0092867421014045.

(*333*) Bosshard, L., Peischl, S., Ackermann, M., and Excoffier, L. (2019). Mutational and Selective Processes Involved in Evolution during Bacterial Range Expansions. *Molecular Biology and Evolution 36*, 2313–2327, DOI: 10.1093/molbev/msz148, https://doi.org/10.1093/molbev/msz148.

(*334*) Luong, N.-D. M., Jeuge, S., Coroller, L., Feurer, C., Desmonts, M.-H., Moriceau, N., Anthoine, V., Gavignet, S., Rapin, A., Frémaux, B., Robieu, E., Zagorec, M., Membré, J.-M., and Guillou, S. (2020). Spoilage of fresh turkey and pork sausages: Influence of potassium lactate and modified atmosphere packaging. *Food Research International 137*, 109501, DOI: https://doi.org/10.1016/j.foodres.2020.109501, https://www.sciencedirect.com/science/article/pii/S0963996920305263.

(*335*) Maier, L., Pruteanu, M., Kuhn, M., Zeller, G., Telzerow, A., Anderson, E. E., Brochado, A. R., Fernandez, K. C., Dose, H., Mori, H., Patil, K. R., Bork, P., and Typas, A. (2018). Extensive impact of non-antibiotic drugs on human gut bacteria. *Nature 555*, 623–628, DOI: 10.1038/nature25979, https://doi.org/10.1038/nature25979.

(*336*) Packard, G. C., and Boardman, T. J. (2008). Model selection and logarithmic transformation in allometric analysis. *Physiological and Biochemical Zoology 81*, 496–507.

(*337*) Barton, K., and Barton, M. K. (2015). Package 'mumin'. *Version 1*, 439.

(*338*) Deepika, D., Karmakar, R., Tirumkudulu, M. S., and Venkatesh, K. V. (2015). Variation in swimming speed of Escherichia coli in response to attractant. *Archives of Microbiology 197*, 211–222, DOI: 10.1007/s00203-014-1044-5, https://doi.org/10.1007/s00203-014-1044-5.

(*339*) Englert, D. L., Manson, M. D., and Jayaraman, A. (2009). Flow-based microfluidic device for quantifying bacterial chemotaxis in stable, competing gradients. *Applied and environmental microbiology 75*, 4557–4564.

(*340*) Adler, J. (1973). A method for measuring chemotaxis and use of the method to determine optimum conditions for chemotaxis by Escherichia coli. *Microbiology 74*, 77–91.

(*341*) Kojadinovic, M., Armitage, J. P., Tindall, M. J., and Wadhams, G. H. (2013). Response kinetics in the complex chemotaxis signalling pathway of Rhodobacter sphaeroides. *Journal of the Royal Society Interface 10*, 20121001.

(*342*) Tweedy, L., and Insall, R. H. (2020). Self-generated gradients yield exceptionally robust steering cues. *Frontiers in Cell and Developmental Biology 8*, 133.

(*343*) Gandhi, S. R., Yurtsev, E. A., Korolev, K. S., and Gore, J. (2016). Range expansions transition from pulled to pushed waves as growth becomes more cooperative in an experimental microbial population. *Proceedings of the National Academy of Sciences 113*, 6922–6927.

(*344*) Smakman, F. Effects of dead bacterial cells on growth, gene expression and evolution of surrounding microbes, Ph.D. Thesis, ETH Zurich, 2021, https://www.research-collection.ethz.ch/bitstream/handle/20.500.11850/500140/1/Effectsofdeadbacterialcellsongrowthgeneexpressionandevolutionc pdf.

(*345*) Peter, C., Wesselborg, S., Herrmann, M., and Lauber, K. (2010). Dangerous attraction: phagocyte recruitment and danger signals of apoptotic and necrotic cells. *Apoptosis 15*, 1007–1028.

(*346*) Amchin, D. B., Ott, J. A., Bhattacharjee, T., and Datta, S. S. (2022). Influence of confinement on the spreading of bacterial populations. *PLoS computational biology 18*, e1010063.

(*347*) Oliveira, N. M., Wheeler, J. H. R., Deroy, C., Booth, S. C., Walsh, E. J., Durham, W. M., and Foster, K. R. (2022). Suicidal chemotaxis in bacteria. *Nature Communications 13*, 7608.

(*348*) Oku, S., Komatsu, A., Tajima, T., Nakashimada, Y., and Kato, J. (2012). Identification of chemotaxis sensory proteins for amino acids in Pseudomonas fluorescens Pf0-1 and their involvement in chemotaxis to tomato root exudate and root colonization. *Microbes and Environments 27*, 462–469.

(*349*) Dublan, M. d. l. A., Ortiz-Marquez, J. C. F., Lett, L., and Curatti, L. (2014). Plant-adapted Escherichia coli show increased lettuce colonizing ability, resistance to oxidative stress and chemotactic response. *PLoS One 9*, e110416.

(*350*) Matsuzaki, R., Kawachi, M., Nozaki, H., Nohara, S., and Suzuki, I. (2020). Sexual reproduction of the snow alga Chloromonas fukushimae (Volvocales, Chlorophyceae) induced using cultured materials. *Plos one 15*, e0238265.

(*351*) Zhang, Y., Taiming, L., and Liu, J. (2003). Low temperature and glucose enhanced T7 RNA polymerase-based plasmid stability for increasing expression of glucagon-like peptide-2 in Escherichia coli. *Protein Expression and Purification 29*, 132–139, DOI: `https://doi.org/10.1016/S1046-5928(03)00002-0`, `https://www.sciencedirect.com/science/article/pii/S1046592803000020`.

(*352*) Haque, S., Srivastava, N., Pal, D. B., Alkhanani, M. F., Almalki, A. H., Areeshi, M. Y., Naidu, R., and Gupta, V. K. (2022). Functional microbiome strategies for the bioremediation of petroleum-hydrocarbon and heavy metal contaminated soils: A review. *Science of The Total Environment 833*, 155222, DOI: `https://doi.org/10.1016/j.scitotenv.2022.155222`, `https://www.sciencedirect.com/science/article/pii/S0048969722023154`.

(*353*) Davis, G. B. (2023). Reviewing the Bioremediation of Contaminants in Groundwater: Investigations over 40 Years Provide Insights into What's Achievable. *Frontiers in Bioscience-Elite 15*, 16.

(*354*) Lv, Y., Bao, J., Liu, D., Gao, X., Yu, Y., and Zhu, L. (2023). Synergistic effects of rice husk biochar and aerobic composting for heavy oil-contaminated soil remediation and microbial community succession evaluation. *Journal of Hazardous Materials 448*, 130929.

(*355*) Laboratories Kanehisa Biosynthesis of various antibiotics - Reference pathway, 2022, `https://www.genome.jp/pathway/map00998`.

(*356*) Sun, Y., Lu, S., Zhao, X., Ding, A., and Wang, L. (2017). Long-term oil pollution and in situ microbial response of groundwater in Northwest China. *Archives of environmental contamination and toxicology 72*, 519–529.

(*357*) Griffiths, Z. G., Miller, J. I., Campa, M. F., Putt, A., Joyner, D., Pelz, O. X., Garajayeva, N., Ceccopieri, M., Gardinali, P., and Hazen, T. C. (2023). Comparing the Response of the Indigenous Microbial Community to Native Crude Oil Amendment in Oxic versus Hypoxic Conditions. *Frontiers in Microbiomes 2*, 1270352.

(*358*) Xiao, X., Zheng, Q., Shen, R., Huang, K., Xu, H., Tu, B., and Zhao, Y. (2022). Patterns of groundwater bacterial communities along the petroleum hydrocarbon gradient. *Journal of Environmental Chemical Engineering 10*, 108773.

(*359*) Sengupta, K., and Pal, S. (2021). A review on microbial diversity and genetic markers involved in methanogenic degradation of hydrocarbons: futuristic prospects of biofuel recovery from contaminated regions. *Environmental Science and Pollution Research 28*, 40288–40307.

(*360*) Ragot, R. (1993). Negative necrotaxis. *Blood cells 19*, 81–8, `http://europepmc.org/abstract/MED/8400315`.

(*361*) Harms, H., and Wick, L. Y. Dispersing pollutant-degrading bacteria in contaminated soil without touching it, 2006, DOI: `10.1002/elsc.200620122`.

(*362*) Jung, Y., and Battistelli Saipem SpA, A. (2016). User's Guide for Biodegradation Reactions in TMVOCBio. DOI: 10.13140/RG.2.1.4529.1123, https://www.researchgate.net/publication/303983662.

(*363*) Sookhak Lari, K., Rayner, J. L., Davis, G. B., and Johnston, C. D. (2020). LNAPL Recovery Endpoints: Lessons Learnt Through Modeling, Experiments, and Field Trials. *Groundwater Monitoring & Remediation 40*, 21–29, DOI: 10.1111/gwmr.12400, https://doi.org/10.1111/gwmr.12400.

(*364*) Davis, G. B., Rayner, J. L., and Donn, M. J. (2023). Advancing "Autonomous" sensing and prediction of the subsurface environment: a review and exploration of the challenges for soil and groundwater contamination. *Environmental Science and Pollution Research*, 1–16.

(*365*) Seymour, J. R., Brumley, D. R., Stocker, R., and Raina, J.-B. (2024). Swimming towards each other: the role of chemotaxis in bacterial interactions. *Trends in Microbiology*, DOI: https://doi.org/10.1016/j.tim.2023.12.008, https://www.sciencedirect.com/science/article/pii/S0966842X23003608.

(*366*) Cairns, L. S., Marlow, V. L., Bissett, E., Ostrowski, A., and Stanley-Wall, N. R. (2013). A mechanical signal transmitted by the flagellum controls signalling in B acillus subtilis. *Molecular microbiology 90*, 6–21.

(*367*) Molitor, R., Bollinger, A., Kubicki, S., Loeschcke, A., Jaeger, K.-E., and Thies, S. (2020). Agar plate-based screening methods for the identification of polyester hydrolysis by Pseudomonas species. *Microbial biotechnology 13*, 274–284.

(*368*) Scheidweiler, D., Bordoloi, A. D., Jiao, W., Sentchilo, V., Bollani, M., Chhun, A., Engel, P., and de Anna, P. (2024). Spatial structure, chemotaxis and quorum sensing shape bacterial biomass accumulation in complex porous media. *Nature Communications 15*, 191.

(*369*) Sahari, A., Traore, M. A., Scharf, B. E., and Behkam, B. (2014). Directed transport of bacteria-based drug delivery vehicles: bacterial chemotaxis dom-

inates particle shape. *Biomedical Microdevices 16*, 717–725, DOI: 10.1007/s10544-014-9876-y, https://doi.org/10.1007/s10544-014-9876-y.

(*370*) Mukherjee, A., Chettri, B., Langpoklakpam, J. S., Basak, P., Prasad, A., Mukherjee, A. K., Bhattacharyya, M., Singh, A. K., and Chattopadhyay, D. (2017). Bioinformatic approaches including predictive metagenomic profiling reveal characteristics of bacterial response to petroleum hydrocarbon contamination in diverse environments. *Scientific reports 7*, 1–22.

(*371*) Kanehisa Laboratories Biofilm formation - Escherichia coli - Reference pathway, 2022, https://www.genome.jp/pathway/map02026.

(*372*) Kanehisa Laboratories Biofilm formation - Pseudomonas aeruginosa - Reference pathway, 2019, https://www.genome.jp/pathway/map02025.

(*373*) Kanehisa Laboratories Biofilm formation - Vibrio cholerae - Reference pathway, 2022, https://www.genome.jp/pathway/map05111#:~:text=The%20quorum%20sensing%20(QS)%20pathway,repressor)%20at%20high%20cell%20density..

(*374*) Kanehisa Laboratories Flagellar assembly - Reference pathway, 2020, https://www.genome.jp/pathway/map02040.

(*375*) Kanehisa Laboratories Quorum sensing - Reference pathway, 2020, https://www.genome.jp/pathway/map02024.

(*376*) Schweitzer, H. D., Smith, H. J., Barnhart, E. P., McKay, L. J., Gerlach, R., Cunningham, A. B., Malmstrom, R. R., Goudeau, D., and Fields, M. W. (2022). Subsurface hydrocarbon degradation strategies in low- and high-sulfate coal seam communities identified with activity-based metagenomics. *npj Biofilms and Microbiomes 8*, 7, DOI: 10.1038/s41522-022-00267-2, https://doi.org/10.1038/s41522-022-00267-2.

(*377*) Hallstrøm, S., Raina, J.-B., Ostrowski, M., Parks, D. H., Tyson, G. W., Hugenholtz, P., Stocker, R., Seymour, J. R., and Riemann, L. (2022). Chemotaxis may assist marine heterotrophic bacterial diazotrophs to find micro-

zones suitable for N2 fixation in the pelagic ocean. *The ISME Journal 16*, 2525–2534.

(*378*) Rebecca E Parales Re: Chemotaxis Research Question (Personal Communication), 2022.

(*379*) Jeckel, H., and Drescher, K. (2021). Advances and opportunities in image analysis of bacterial cells and communities. *FEMS Microbiology Reviews 45*, fuaa062, DOI: 10.1093/femsre/fuaa062, https://doi.org/10.1093/femsre/fuaa062.

(*380*) Maluchenko, N., Koshkina, D., Korovina, A., Studitsky, V., and Feofanov, A. (2022). Interactions of PARP1 Inhibitors with PARP1-Nucleosome Complexes. *Cells 11*, 3343.

(*381*) Borer, B., Ciccarese, D., Johnson, D., and Or, D. (2020). Spatial organization in microbial range expansion emerges from trophic dependencies and successful lineages. *Communications Biology 3*, 685.

(*382*) Müller, M. J. I., Neugeboren, B. I., Nelson, D. R., and Murray, A. W. (2014). Genetic drift opposes mutualism during spatial population expansion. *Proceedings of the National Academy of Sciences 111*, 1037–1042.

(*383*) Hughes, J. G. G. Chemotaxis and Energy Taxis in Pseudomonas putida F1, Ph.D. Thesis, Davis: University of California, Davis, 2018, https://search.proquest.com/openview/1d30b306eeded977572af4677d8ac883/1?pq-origsite=gscholar&cbl=18750&casa_token=AWs64pKMfVsAAAAA:cEO0H3T2M5fG5h241b5qHJ2PpjIdU1LjRTHsTI91UvqP5B4QVum0saPvugFXFyuNeFPvTlA5ug.

(*384*) Wu, H., Huang, B., and Zare, R. N. (2006). Generation of Complex, Static Solution Gradients in Microfluidic Channels. *Journal of the American Chemical Society 128*, 4194–4195, DOI: 10.1021/ja058530o, https://doi.org/10.1021/ja058530o.

(*385*) Has, C., Dhuriya, R., and Sunthar, P. (2019). A Simple Microfluidic Device for Generating Solute Concentration Gradients. *Materials Today: Proceedings 18*, 623–627, DOI: https://doi.org/10.1016/j.matpr.2019.

06.456, https://www.sciencedirect.com/science/article/pii/S2214785319318267.

(*386*) Rotaru, A.-E., Woodard, T. L., Nevin, K. P., and Lovley, D. R. (2015). Link between capacity for current production and syntrophic growth in Geobacter species. *Frontiers in Microbiology 6*, 744.

(*387*) Speers, A. M., and Reguera, G. (2021). Competitive advantage of oxygen-tolerant bioanodes of Geobacter sulfurreducens in bioelectrochemical systems. *Biofilm 3*, 100052, DOI: https://doi.org/10.1016/j.bioflm.2021.100052, https://www.sciencedirect.com/science/article/pii/S2590207521000101.

(*388*) Kwon, D., Beirns, E., Yoon, J., Lam, T. Y. C., Tan, G.-Y. A., Lee, P.-H., and Kim, J. (2022). Polyaniline-coated conductive media promotes direct interspecies electrons transfer (DIET) and kinetics enhancement of low-strength wastewater treatment in anaerobic fluidized bed membrane bioreactor (AFMBR). *Chemical Engineering Journal 446*, 136711, DOI: https://doi.org/10.1016/j.cej.2022.136711, https://www.sciencedirect.com/science/article/pii/S1385894722022069.

(*389*) Gill, R. T., Harbottle, M. J., Smith, J. W. N., and Thornton, S. F. (2014). Electrokinetic-enhanced bioremediation of organic contaminants: A review of processes and environmental applications. *Chemosphere 107*, 31–42, DOI: https://doi.org/10.1016/j.chemosphere.2014.03.019, https://www.sciencedirect.com/science/article/pii/S0045653514003683.

(*390*) Story, S. P., Parker, S. H., Kline, J. D., Tzeng, T.-R. J., Mueller, J. G., and Kline, E. L. (2000). Identification of four structural genes and two putative promoters necessary for utilization of phenanthrene naphthalene, fluoranthene, and by Sphingomonas paucimobilis var. EPA505. *Gene 260*, 155–169.

(*391*) Jiang, B., Song, Y., Liu, Z., Huang, W. E., Li, G., Deng, S., Xing, Y., and Zhang, D. (2021). Whole-cell bioreporters for evaluating petroleum hy-

drocarbon contamination. *Critical Reviews in Environmental Science and Technology 51*, 272–322, DOI: 10.1080/10643389.2020.1717907, https://doi.org/10.1080/10643389.2020.1717907.

(*392*) Yoshida, A., and Kuramitsu, H. K. (2002). Streptococcus mutans biofilm formation: utilization of a gtfB promoter–green fluorescent protein (PgtfB::gfp) construct to monitor development. *Microbiology 148*, 3385–3394.

(*393*) Southward, C. M., and Surette, M. G. (2002). The dynamic microbe: green fluorescent protein brings bacteria to light. *Molecular microbiology 45*, 1191–1196.

Journal of Hazardous Materials 430 (2022) 128482

Contents lists available at ScienceDirect

Journal of Hazardous Materials

journal homepage: www.elsevier.com/locate/jhazmat

Research Paper

The role of predicted chemotactic and hydrocarbon degrading taxa in natural source zone depletion at a legacy petroleum hydrocarbon site

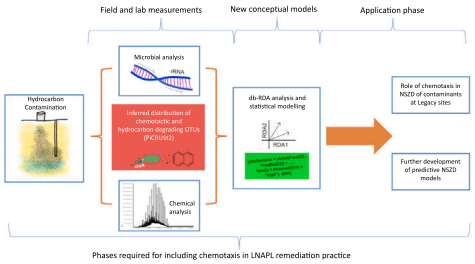
Cameron W.M. Murphy [a,b], Greg B. Davis [b], John L. Rayner [b], Tom Walsh [c], Trevor P. Bastow [b], Adrian P. Butler [a], Geoffrey J. Puzon [b,*], Matthew J. Morgan [c]

[a] Environmental and Water Resources Section, Department of Civil and Environmental Engineering, Imperial College of Science,Technology and Medicine, Exhibition Road, London, United Kingdom
[b] Centre for Environment and Life Sciences, CSIRO Land and Water, Private Bag No 5, Wembley, WA 6913, Australia
[c] Black Mountain Laboratories, CSIRO Land and Water, Acton, P.O. Box 1700, Canberra, ACT 2601, Australia

HIGHLIGHTS

- Unprecedented view of the microbial metabolic groups at petroleum legacy site.
- Chemotactic and hydrocarbon degrading bacteria (CD) are inferred in soil cores.
- Naphthalene drives the occurrence of CD operational taxonomic units (OTUs).
- Provides a basis for modelling to account for CD distribution and function.

GRAPHICAL ABSTRACT



ARTICLE INFO

Editor: Dr. R. Maria Sonia

Keywords:
Natural source zone depletion (NSZD)
Groundwater
Chemotaxis
Petroleum hydrocarbons

ABSTRACT

Petroleum hydrocarbon contamination is a global problem which can cause long-term environmental damage and impacts water security. Natural source zone depletion (NSZD) is the natural degradation of such contaminants. Chemotaxis is an aspect of NSZD which is not fully understood, but one that grants microorganisms the ability to alter their motion in response to a chemical concentration gradient potentially enhancing petroleum NSZD mass removal rates. This study investigates the distribution of potentially chemotactic and hydrocarbon degrading microbes (CD) across the water table of a legacy petroleum hydrocarbon site near Perth, Western Australia in areas impacted by crude oil, diesel and jet fuel. Core samples were recovered and analysed for hydrocarbon contamination using gas chromatography. Predictive metagenomic profiling was undertaken to infer functionality using a combination of 16 S rRNA sequencing and PICRUSt2 analysis. Naphthalene contamination was found to significantly increase the occurrence of potential CD microbes, including members of the *Comamonadaceae* and *Geobacteraceae* families, which may enhance NSZD. Further work to explore and define this link is important for reliable estimation of biodegradation of petroleum hydrocarbon fuels. Furthermore, the outcomes suggest that the chemotactic parameter within existing NSZD models should be reviewed to accommodate CD accumulation in areas of naphthalene contamination, thereby providing a more accurate quantification of risk from petroleum impacts in subsurface environments, and the scale of risk mitigation due to NSZD.

* Corresponding author.
E-mail address: Geoffrey.Puzon@csiro.au (G.J. Puzon).

https://doi.org/10.1016/j.jhazmat.2022.128482
Received 27 July 2021; Received in revised form 10 February 2022; Accepted 10 February 2022
Available online 12 February 2022
0304-3894/© 2022 The Authors. Published by Elsevier B.V. This is an open access article under the CC BY-NC-ND license (http://creativecommons.org/licenses/by-nc-nd/4.0/).

1. Introduction

Groundwater is an essential source of drinking water across the world, however the resource is vulnerable to anthropogenic petroleum hydrocarbon contamination. Petroleum hydrocarbons are released into the subsurface in the form of crude oil, gasoline, diesel fuels and jet range fuels (Gkorezis et al., 2016; Hidalgo et al., 2020), with their release commonly being associated with spills (Gkorezis et al., 2016) and leakages from storage tanks (Chang and Lin, 2006). These fuels differ significantly in their hydrocarbon composition, including polycyclic aromatic hydrocarbons (PAHs), such as naphthalene (Sulimov et al., 1965), and monoaromatic hydrocarbon compounds like benzene, toluene, ethylbenzene, and xylenes (BTEX). They are all generally described as being light non-aqueous phase liquids (LNAPLs), with a density generally less than that of water. LNAPLs are common contaminates at legacy sites (Reid et al., 2018) but with a carcinogenic risk profile (Li et al., 2007). LNAPLs also pose broad contamination risks because LNAPL components can partition into air and water phases creating pathways of exposure for human health and the environment. Since LNAPLs effectively "float" at the top of the capillary fringe, this promotes lateral and vertical proliferation of contaminants within the subsurface. These factors both enjoin remedial and management action be taken but also make LNAPLs very difficult to remediate (Johnston et al., 1998, 2002).

Multiple physical remediation techniques have been developed to clean up contaminated sites and limit the spread of LNAPL petroleum hydrocarbons, such as, air sparging and bioventing (Sookhak Lari et al., 2020). Air sparging is the injection of high pressurised air below the lowest level of contamination in the saturated zone (Hu et al., 2010). This creates a transient moment when pore spaces are filled with air, triggering partitioning to the air phase and transport of the contaminates from the saturated zone to the unsaturated zone above. Bioventing is a process which provides oxygen to the subsurface above the water table; this can stimulate the degradation rate of indigenous microorganisms (Frutos et al., 2010). However, these techniques can be expensive, and in some cases ineffective (Sookhak Lari et al., 2020). Biodegradation of petroleum hydrocarbons occurs naturally by indigenous microbes and is an inexpensive and sustainable option (Gupta and Yadav, 2019). During biodegradation petroleum hydrocarbons breakdown into less hazardous substances. The whole mass loss of LNAPLs due to partitioning and physical and biological degradation is termed natural source zone depletion (NSZD) (Sookhak Lari et al., 2019).

Understanding how microbial communities interact with specific chemical contaminants is an important step towards predictive modelling and manipulation of sites to promote NSZD. A number of studies have investigated the microbial communities and physical conditions that may contribute to the NSZD of petroleum hydrocarbon compounds (Blanco-Enríquez et al., 2018; Dobson et al., 2007; Maila et al., 2005). These studies have considered the role of different redox conditions on biodegradation (Chapelle et al., 2002) and the role of microorganisms in constraining contaminant expansion in the subsurface (Essaid et al., 2015; Franzmann et al., 2002). Research has also highlighted the role of microorganisms in degrading more recalcitrant contaminants (Davis et al., 1999; Lee et al., 2020), and the role of maintaining a diverse biodegrading population (Dell'Anno et al., 2012; Franzmann et al., 1998), along with investigating the formation of biodegradation by-products (e.g., polar compounds) in weathered diesel and their fate (Bruckberger et al., 2018; Lang et al., 2009).

Chemotaxis is an important mechanism used by microbes to exploit otherwise inaccessible resources, including petroleum hydrocarbons (Parales and Ditty, 2018). Many microbes have been demonstrated to be capable of chemotaxis-assisted degradation of alkanes and other hydrocarbon compounds (Li et al., 2017; Zhang et al., 2012). Microbial species that exhibit chemotaxis-assisted hydrocarbon degradation have been shown to enhance the rate of NSZD in column and microcosm experiments (Wang et al., 2012; Olson et al., 2004; Marx and Aitken, 2000). In a laboratory experiment, a chemotactic *Pseudomonas putida* G7 (PpG7) strain degraded 90% of naphthalene in six hours, compared to 30 h for a non-chemotactic mutant strain (C1) and a non-motile mutant strain (R2) (Marx and Aitken, 2000). Indigenous microbes present in the subsurface have been reported to possess the ability for chemotactic assisted petroleum hydrocarbon biodegradation, such as; *Alcaligenaceae* to alkanes extracted from a crude oil-polluted seawater in Daya Bay, South China Sea (Hong et al., 2017) and *Brevibacteriaceae* to anthracene and other PAHs isolated from a contaminated refinery in Mathura, India (Chaudhary et al., 2015). Exploitation of this chemotaxis mechanism to manipulate microbe-driven NSZD could therefore have far reaching bioremediation potential at sites undergoing NSZD (Wang et al., 2012; Olson et al., 2004; Marx and Aitken, 2000).

The distribution of chemotactic microbes and the exact nature of the role chemotaxis plays in the NSZD of petroleum hydrocarbons under field conditions remains unclear (Sookhak Lari et al., 2019). Addressing this challenge requires characterising microbial diversity, community composition and the functional potential of community members for hydrocarbon degradation and chemotaxis. Although culturing specific bacteria can provide direct evidence of chemotaxis and degrading functions, the vast majority of soil microbes are not culturable (Lloyd et al., 2018; Rappé and Giovannoni, 2003) and environmental samples are typically too diverse to make this feasible for characterising communities. Alternatively, shotgun metagenomic sequencing, which aims to assemble whole genomes from short fragments, can be used to determine gene content and thus functional potential of microbial communities. However, it is limited if there is little community biomass or host contamination, and remains a significant bioinformatic challenge (Douglas et al., 2020). An alternative approach indirectly infers the functional potential of individual species by comparing community-derived marker gene sequences against a database of reference genomes from organisms with known functions (Douglas et al., 2020). For example, Crampon et al. (2018) used this approach to infer that operational taxonomic units based on 16S rRNA amplicon sequences were abundant in metabolic pathways linked to higher polycyclic aromatic hydrocarbon degradation potential. The widespread use of this approach for inferring community functional potential and the recent improvements in database coverage and optimised genome prediction algorithms (Douglas et al., 2020) make this a robust option for microbial community functional inference.

The research presented here describes a field study of the inferred spatial distribution of predicted chemotactic and hydrocarbon degrading microbes linked with crude oil, diesel and jet fuel contamination at a legacy petroleum hydrocarbon site. The aim of the study was to explore the association of the predicted functional potential of microbial communities at these sites with these legacy contaminants, and test whether the distribution of petroleum hydrocarbon and LNAPL compounds influences the abundance of the inferred chemotactic and hydrocarbon degrading microbes. This was achieved by comparing the predicted metagenome profiles of operational taxonomic units (OTUs) derived from 16S rRNA marker gene sequences, to the distribution and concentration of legacy petroleum hydrocarbon and LNAPL compounds across the site. Investigating the preferential occurrence of the predicted chemotactic and hydrocarbon degrading microbes to various petroleum products and depth allows for the development of more accurate NSZD models (Sookhak Lari et al., 2021). The methodology applied in this study assists in potential bioprospecting and screening of chemotactic and hydrocarbon degrading microbes potentially capable of enhancing NSZD. This will provide a clearer picture of risk to groundwater resources (Singh and Choudhary, 2021).

2. Materials and methods

2.1. Site description and soil core recovery

The study site has stored significant volumes of crude oil, as well as

diesel and jet fuels. It is approximately 50 km south of Perth, Western Australia. The site overlies a shallow superficial unconfined sand aquifer (Johnston et al., 1998), which is located on the Swan Coastal Plain (Fig. 1). The dominant surficial lithology is a Safety Bay Sands unit with deeper Becher Sand units; these lithographic units are relatively homogenous and composed of sub-horizontal layered aeolian and littoral calcareous sands (Johnston et al., 1998). The sand is predominately fine to medium grained with some thin inter-bedded layers of course grained sands and gravel, with low concentrations of organic matter (Davis et al., 2005). Cores recovered from the site were taken from the predominantly homogenous aeolian and littoral calcareous sands as described in detail by Johnston et al. (1998). Limited air-sparging, bioventing, LNAPL skimming, slurping, vacuum extraction and a mixture of such remediation techniques have been trialled on the site over time, however the site is now undergoing assessment and management through NSZD (Johnston et al., 2002; Sookhak Lari et al., 2018).

Groundwater at the site is typically fresh with a low electrical conductivity (50–160 mS/m) and has a pH typically in the range 7.5–8.5 buffered by the calcareous nature of the superficial sand formation. Regionally nitrate and sulfate are present in groundwater due to agricultural and urban influences. However, within the site these electron acceptors (along with oxygen) are strongly depleted within groundwater due to natural attenuation processes (Davis et al., 1999). Bicarbonate ranges from 250 to 940 mg/L and dissolved methane is found across large areas of the groundwater due to hydrocarbon degradation processes (King, 2009). Methane production also indicates that other electron acceptors are strongly depleted (Wiedemeier et al., 1999).

Soil cores were recovered using a Geoprobe 6620 drilling rig (Bruckberger et al., 2021). One core was recovered from a representative background control area unaffected by petroleum hydrocarbon contamination (B6), three cores were recovered from the crude oil contaminated area (T7, D10a and D10b), two cores were recovered from the diesel contaminated area (D6, T3), and three cores were recovered from the jet fuel contaminated area (D7, D9 and T5) (Fig. 1). The nine core locations were sampled from depths of 1.50–5.10 m below ground level. Each core was cut into 0.05 m sections, sealed in tins and immediately transported on ice to the CSIRO laboratory. Upon arrival at the laboratory, tins were sub-sampled for chemical and biological analysis. For each core, four representative sections were selected from the Top section (above the water table at an average of 2.28 m in depth), Water Table section (an average of 3.05 m in depth), Middle section (an average of 3.78 m in depth and below the water table), and Bottom section (an average of 4.48 m in depth) (Bruckberger et al., 2021) (Fig. 1). Chemical analysis using GS-MS and GS-FID was undertaken on these 36 section samples. For biological analysis, triplicate samples (5 g), from each of the 36 sections, were collected using sterile techniques and stored at − 80 °C until DNA extraction. For chemical

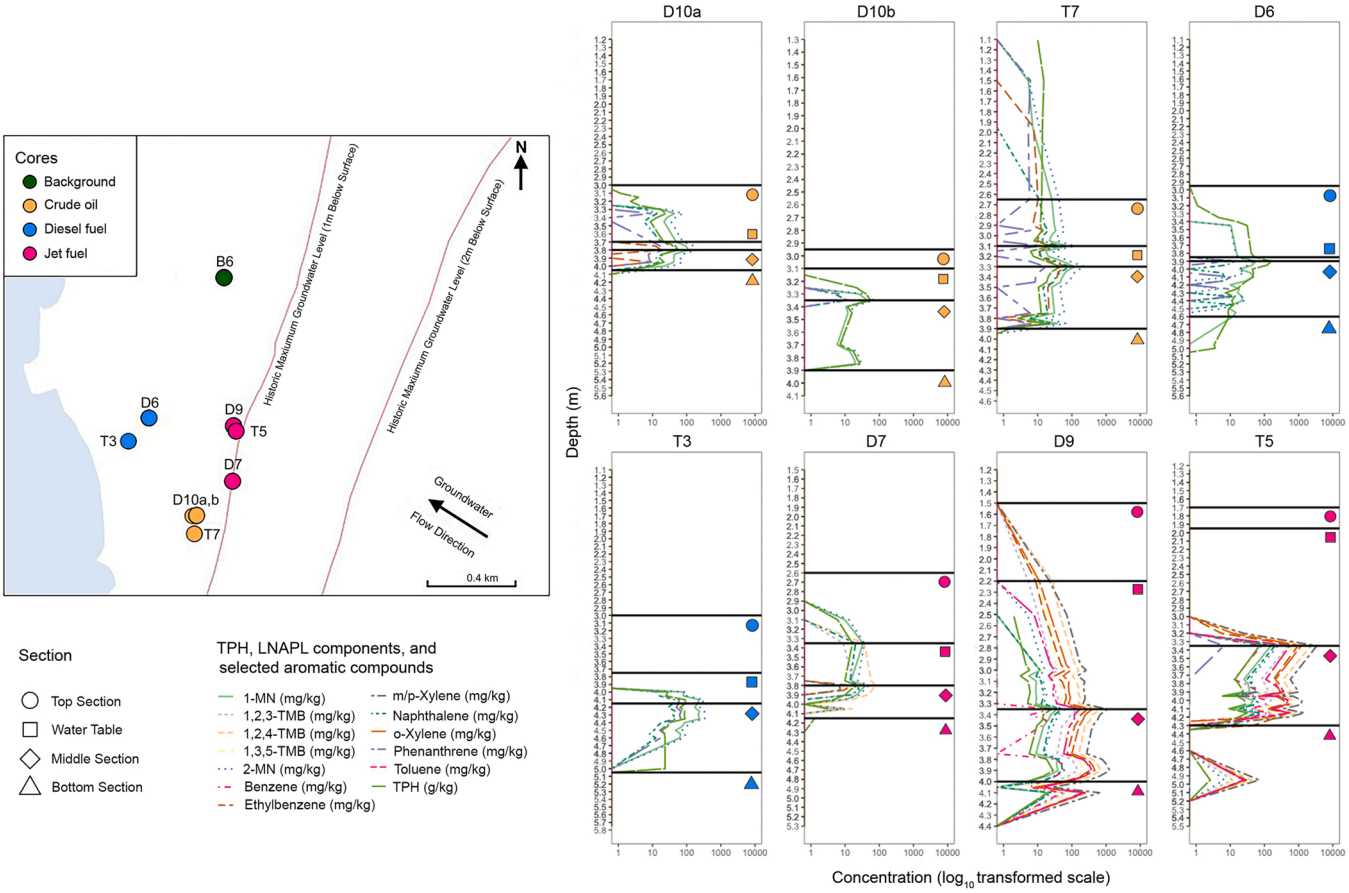


Fig. 1. Map of sampling sites showing position of contaminated zones relative to maximum historic groundwater levels, and proximity to the Indian Ocean. The figure also shows the depth profile of the contaminated core sections after GC-FID and GC-MS analysis. The concentrations of TPH and the selected aromatic LNAPL components identified (1-methylnaphthalene (1-MN), 1,3,5-trimethylbenzene (1,3,5-TMB), ethylbenzene, *o*-xylene, 1,2,3-trimethylbenzene (1,2,3-TMB), 2-methylnaphthalene (2-MN), *m/p*-xylene, phenanthrene, 1,2,4-trimethylbenzene (1,2,4-TMB), benzene, naphthalene, and toluene) are shown. The solid horizonal black lines indicate the subsections within the core, along with concentrations at each sample section. Inferred and extrapolated linear lines are then used to postulate concentrations between the core sample sections. Different line types are used to differentiate between individual contaminants. The Background core is green, the Crude Oil cores are orange, the Diesel Fuel cores are blue and the Jet Fuel cores are pink. On the right-hand side of the figure, circles represent the Top section, squares represent Water Table section, rhombuses represent the Middle section and triangles represent the Bottom section.

analysis, 3–5 g were sampled and immediately extracted using 4 mL of dichloromethane (containing deuterated internal standards) (d6-benzene, d8-toluene, d10-p-xylene, d8-naphthalene, d14-p-terphenyl) as described in Bruckberger et al. (2021). The Water Table section of the core was differentiated from the other core sections by re-weighing the remaining core samples before and after drying, and comparing the moisture loss (Bruckberger et al., 2018). This was achieved by initially air-drying a portion of the core section to remove excess chemicals for 48 h, and then heating it in an oven for 24 h at 105 °C to calculate moisture loss (%) (Bruckberger et al., 2021). Geochemical analysis of a subset of soil cores samples (24 in total) for a range of parameters (TOC, N, P, pH, moisture, electrical conductivity, Al, As, B, Ca, Cd, Co, Cr, Cu, Fe, K, Mg, Mn, Mo, Na, Ni, Pb, S, and Zn) was conducted at a government NATA accredited laboratory (ChemCentre Western Australia) using standard methods (Rayment and Lyons, 2011) (Fig. S1).

2.2. Petroleum hydrocarbon chemical analysis

Total petroleum hydrocarbon (TPH) analysis of the core sample extracts was carried out using an Agilent 6890 gas chromatography–flame ionisation detector (GC-FID) system (Bruckberger et al., 2021). Internal and petroleum hydrocarbon external standards were used. Gas chromatography–mass spectrometry (GC–MS) analysis of the core sample extracts was carried out using an Agilent 7890 gas chromatograph and an Agilent 7000B mass spectrometer (Bruckberger et al., 2021). Quantitation of selected analytes was performed using external standards (benzene, toluene, ethylbenzene, *m*-xylene, *p*-xylene, *o*-xylene, 1,3,5-trimethylbenzene (1,3,5-TMB), 1,2,4-trimethylbenzene (1,2,4-TMB), naphthalene, 2-methylnaphthalene (2-MN), 1-methylnaphthalene (1-MN) and phenanthrene) containing the same internal standards used for the samples (Fig. S1).

2.3. 16S rRNA gene amplification and bioinformatics

Genomic DNA was extracted from the 36 core sections in triplicate (36 × 3), using 0.5 g of soil and the PowerBiofilm DNA Isolation Kit (MoBio Laboratories, Inc., Carlsbad, CA, USA), and quantified with a Qubit fluorometer (Invitrogen) (Bruckberger et al., 2018). A 300 base pair (bp) area of the V4 region of the 16S rRNA was amplified using the 515f (5'-GTGCCAGCMGCCGCGGTAA-3') and 806rcbc (5'-GGACTACHVGGGTWTCTAAT-3') primer set (Parada et al., 2016), following the Earth Microbiome Project protocol (https://earthmicrobiome.org/protocols-and-standards/16s/) and barcoding and sequencing library preparation followed the Illumina 16S protocol (Illumina, USA). After amplification the PCR products were individually purified with SPRI beads (Ampure XP beads, Beckman Coulter) and then barcodes added through a second round of PCR. Following a second round of bead-based purification, samples were quantified and pooled in an equimolar manner ready for sequencing. Forward and reverse sequencing was undertaken on the Illumina MiSeq (v3 600 cycle), following the manufacturer's instructions (Illumina, USA) (Bruckberger et al., 2021). Data has been published online (https://data.csiro.au/collections/collection/CIcsiro:49662v1). Sequences were processed using QIIME2 version 2019.1 (Bolyen et al., 2019). The imported paired-end sequences were denoised and merged using the DADA2 workflow (Callahan et al., 2016), which involved trimming the first 19 nucleotide bases from each read and truncating at 190 bases. This process utilises exact amplicon sequence variants (ASVs) instead of conventional OTU workflows. The ASVs were clustered using the *de novo* "q2-vsearch" clustering algorithm (Rognes et al., 2016) at 97% similarity, with borderline chimeras being retained. Representative OTU sequences were classified against the Silva 138 515F/806R database (Quast et al., 2013; Yilmaz et al., 2014) using the "classify-sklearn" algorithm (Bokulich et al., 2018). OTUs which were not classified as prokaryotes were removed. R Studio version 4.0.3 (RStudio Team, 2020) was then used to merge the biological sample replicates and undertake further analysis with the "phyloseq" (McMurdie and Holmes, 2013) and "vegan" packages (Oksanen et al., 2020). Alpha diversity metrics (the number of OTUs and Chao1 estimator) were calculated from a single rarefaction at 10,000 reads per sample, this was selected after manual inspection of rarefaction curves and Good's coverage calculation (Figs. S2 and S3). The Water Table and Middle section of the Jet Fuel core T3 failed to pass the rarefaction threshold and were excluded from further analysis. Homogeneity of variance for each metric grouped by Zone (Background, Crude Oil, Diesel or Jet Fuel) and Section (Top, Water Table, Middle, Bottom) were tested with Levene's test implemented in the "car" package. Two-way ANOVA tests of the alpha diversity estimates were used to test for statistically significant differences in microbial diversity between Zone and Section.

2.4. Predictive metagenomic profiling

For further analyses the dataset was rarefied 1000 times at 10,000 reads and averaged relative abundances retained. The resulting OTUs were then imported into PICRUSt2 v2.3.0-b (Douglas et al., 2020) and placed into a reference phylogenetic tree, with metagenome content being predicted using an ancestral-state reconstruction algorithm to predict the metagenomes based on 16S marker gene information. The resulting tree was used for functional metabolic prediction, through the utilisation of Kyoto Encyclopedia of Genes and Genomes (KEGG) reaction pathways (Kanehisa and Goto, 2000; Kanehisa, 2019), with a minimal nearest-sequenced taxon index (NSTI) value of 2 set to improve accuracy of pathway assignment (Douglas et al., 2020). The OTUs were split into four groupings, based on the predicted presence of chemotaxis and petroleum hydrocarbon KEGG degradation pathways.

The chemotactic and hydrocarbon degrading (CD) group included OTUs inferred to possess the pathways associated with bacterial chemotaxis (ko02030), as well as at least one of the hydrocarbon degradation pathways; benzoate degradation (ko00362), bisphenol degradation (ko00363), chloroalkane and chloroalkene degradation (ko00625), chlorocyclohexane and chlorobenzene degradation (ko00361), toluene degradation (ko00623), nitrotoluene degradation (ko00633), xylene degradation (ko00622), caprolactam degradation (ko00930), ethylbenzene degradation (ko00642), naphthalene degradation (ko00626) and/or polycyclic aromatic hydrocarbon degradation (ko00624). It is important to highlight here that this does not explicitly mean that a given CD OTU is necessarily chemotactic directly towards one of the hydrocarbons, but that it may also include microbes that are chemotactic towards other compounds. The chemotactic (C) group included OTUs inferred to possess only the chemotaxis pathway and none of the hydrocarbon degradation pathways. The hydrocarbon degrading group (D) included OTUs inferred to possess at least one of the hydrocarbon degradation pathways and no bacterial chemotaxis pathway. Finally, the non-chemotactic and non-hydrocarbon degrading (NCND) group contains OTUs without inferred bacterial chemotaxis or any of the hydrocarbon degradation pathways. It is important to note that individual OTUs are assigned to a single group based on their inferred functionality. Since OTUs within the same family may differ in their inferred functional grouping, it is possible for a single family to contain OTUs assigned to different functional groups.

2.5. Molecular ecology, genetic diversity and statistical analysis

Family-level relative abundance heatmaps were generated to visualise the alpha diversity and taxonomic community composition of the predicted metagenomic groupings and their distribution across the site. A heatmap of the community composition of the groupings at a genera level is present in the supplementary information. The "vegan" package (Oksanen et al., 2020) was used to visualise the beta diversity among the samples through non-metric multidimensional scaling (NMDS) ordination of the Bray-Curtis dissimilarity matrix. This approach is commonly used to inspect the dissimilarity of contaminated petroleum

hydrocarbon sites (Mangse et al., 2020; Hamdan et al., 2019).

Environmental drivers of community composition and CD OTU distribution were identified independently using constrained ordination and Generalised Linear Modelling (GLM). For both analyses multicollinearity of the environmental variables was assessed using the vifcor function in the "usdm" package to calculate variance inflation factors (Naimi et al., 2014), with a correlation threshold of 0.7 being implemented to remove any strong multicollinear signals. Nine of the 13 variables had collinearity issues and were removed for further analyses. The remaining environmental variables were Depth, Naphthalene, Phenanthrene and Benzene. TPH was also omitted from further analysis due to a confounding relationship with the LNAPLs (Lundegard and Sweeney, 2004). This is because TPH can also be representative of colloids or sorbed phase hydrocarbons on particulate matter, as well as dissolved hydrocarbons and dissolved nonhydrocarbons, which leads to collinear relationships (Lundegard and Sweeney, 2004). The contaminant concentration and depth were standardised using the "decostand" function in the "vegan" package (Oksanen et al., 2020). Distance-based constrained redundancy analysis (db-RDA) of the Bray-Curtis dissimilarity matrix was performed using the "capscale" function in the "vegan" package in order to investigate which of the remaining parameters (Depth, Naphthalene, Phenanthrene and Benzene) drive structural differences between samples. Statistically significant variables were identified using step-wise model selection procedure implemented in the ordistep function in vegan with a cutoff p-value < 0.05). This analysis was also used to explore the difference in the distribution of the various inferred functional chemotactic and hydrocarbon degrading groups. To aid clarity, the OTUs from each group were visualised separately on the common db-RDA axes.

A generalised linear model (GLM) assuming a binomial distribution, with a logit link function, was used to test the association between CD group microbes, depth and contaminant concentration. The model counts OTUs assigned to the CD group, as "successes" and OTUs assigned to the C, D and NCND groups as "failures". Variable selection was undertaken using a bi-directional step-wise model using the "MASS" package (Venables and Ripley, 2002) and the AIC criterion to select significant variables and model with a p-value of < 0.05.

3. Results

3.1. Overview of the site and chemical analysis

Soil cores collected from the site had different ranges of petroleum hydrocarbon (crude oil, diesel fuel and jet fuel) contamination as well as a representative background core (Fig. 1). Cores were analysed for concentrations of TPH, LNAPL components, and selected aromatic compounds (the main water soluble aromatic compounds present in significant abundances) (Fig. 1). The representative background control location was found to contain negligible concentrations of TPH and LNAPL components (data not shown). Across all core locations contaminated with different petroleum types, TPH had peak concentrations of 20–100 g/kg, which generally occurred below the water table (Fig. 1). The Crude oil contaminated cores contained a limited range of identifiable LNAPL components; primarily these were the aromatic components 2-MN, naphthalene, 1-MN, phenanthrene and ethylbenzene. These were generally found in two of the three Crude oil cores. The diesel cores were generally dominated by 2-MN, 1-MN, naphthalene and phenanthrene, with a more diverse range of up to a dozen dominant aromatic components in the LNAPL detected in the Jet Fuel cores (Fig. 1). In the Water Table and Middle sections of the Crude oil cores (T7, D10a), concentrations peaked at approximately 10–100 mg/kg for ethylbenzene, naphthalene, 1-MN, 2-MN and phenanthrene, although highest concentrations were in the Middle section (Fig. 1). D10b was similar, however the core did not contain ethylbenzene and had lower concentrations of naphthalene and phenanthrene, with the highest concentrations in the Middle section. D10b also contained very low concentrations of 2-MN in the Bottom section. Concentrations in core T7 were above detection levels in the Top section, with low concentrations of 2-MN in the Bottom section. In the Diesel cores (T3, D6), naphthalene, phenanthrene, 1-MN and 2-MN had peak concentrations in the range 10–100 mg/kg. TPH and 1-MN were detected in the Bottom section of D6 (Fig. 1).

The two Jet Fuel cores, D9 and T5, were found to contain elevated concentrations of selected aromatic components in the Middle section of the cores, with concentrations ranging from approximately 10 to 3000 mg/kg (Fig. 1). Notably, all the BTEX (benzene, toluene, ethylbenzene and xylenes) and trimethylbenzene (TMB) isomers were detected in these cores, as well as 1-MN, 2-MN and naphthalene. Phenanthrene was only detected in T5. Exceptionally elevated concentrations of *m/p*-xylene and 1,2,4-TMB were recorded in the Middle section of both cores. In D9, the shallower Water Table section, a smaller range of the selected aromatic compounds were recorded (1,2,3-TMB, 1,3,4-TMB, 1,3,5-TMB, *m/p*-xylene, *o*-xylene, ethylbenzene), with toluene and benzene not being detected. However, all compounds were detected in the Bottom section of this core. In contrast, no TPH was detected in the Water Table section of the T5 Jet Fuel core, and ethylbenzene, 1-MN, naphthalene and 2-MN were the only LNAPL components detected in the Bottom section of this core (Fig. 1).

3.2. Molecular ecological genetic diversity analysis

3.2.1. Alpha diversity analysis

The 250 bp paired-end MiSeq run produced 5,057,077 reads, of which 4,786,072 reads passed all quality control, denoising and chimera removal steps. Rarefaction curves of observed and Shannon's diversity and a Good's coverage of 96.5–99.8% for all samples in the rarefied dataset suggest that 10,000 reads was appropriate and captures the vast majority of microbial diversity in most samples (Figs. S2 and S3). The Chao1 diversity estimator ranged from 169.5 (T5 Jet Fuel Bottom section) to 1377.003 (B6 Background Water Table) (Fig. S3). Background 'Zone' samples had the highest alpha diversity within each section, except the Top section of D10b (Fig. S3). Two-way ANOVA showed that the Zone (Background, Crude, Diesel or Jet Fuel) had a significant effect on the Chao1 diversity across the site ($F = 5.267$, $df = 3$, $P = 0.009$), but neither Section ($F = 2.665$, $df = 3$, $P = 0.08$) nor the interaction of Zone and Section ($F = 0.725$, $df = 9$, $P = 0.681$) had a statistically significant effect. Pairwise Wilcoxon rank sum tests using a Benjamin-Hochberg correction for multiple tests showed that Background samples had significantly higher alpha diversity than Diesel ($P = 0.048$) and Jet Fuel ($P = 0.024$) samples, but not Crude oil samples ($P = 0.059$) (Figs. S2 and S3). Multivariate dispersion was significantly lower for the Background Zone than all other Zones (betadisper $F = 13.26$, $df = 3$, $P < 0.001$; TukeyHSD $P < 0.001$ for all Background Zone pairwise comparisons), which indicated that Background sample Sections were highly similar to each other. After rarefaction, averaging and predictive metagenomic sequencing analysis, 7583 unique bacterial and archaeal OTUs were identified and were assigned to Prokaryote taxa (Figs. S2–S4).

3.2.2. Community composition analysis

Background Sections at all depths and Top Sections of most cores were characterised by high abundance of OTUs in the *Methylomirabilaceae*, *Nitrosopumilaceae*, *Nitrosotaleaceae*, *Nitrososphaeraceae*, and *Rokubacteriales*. Community composition was more variable in deeper sections of contaminated cores, but some common patterns were evident. The Middle and Bottom sections of most contaminated cores were charactersied by high abundance of OTUs in the *Anaerolineaceae*, *Methanocellaceae* and *Methanosaetaceae*. *Aminicenantales* OTUs were common in the Crude and Diesel cores only, whereas *Smithellaceae* and *Methanoreulaceae* were more abundant in Diesel and Jet Fuel cores. In contrast, the Middle Sections of Crude core T7 and Jet Fuel core D9 were characterised by communities that included a high abundance of OTUs

in the *Geobacteraceae* and *Pseudomonadaceae*. No *Geobacteraceae* OTUs were detected in the Background core, with *Pseudomonadaceae* OTUs only being detected in low abundances in the Bottom section. Methanogenic families (e.g., *Methanocellaceae* and *Methanosaetaceae*) were notably present throughout the site (Fig. 2).

After grouping by inferred functional potential, the CD group contained 1831 OTUs, and were most commonly assigned to *Geobacteraceae, Comamonadaceae, Smithellaceae, Methanoregulaceae, Methanocellaceae, Nitrosopumilaceae, Pseudomonadaceae,* and *Desulfocapsaceae* (Fig. S5a). The D group contained 3411 OTUs, which were most commonly assigned to families including *Nitrosotaleaceae, Anaerolineaceae, Methylomirabilaceae, Woesearchaeales, Methanocellaceae, Methanobacteriaceae, Rokubacteriales, Dysgonomonadaceae,* and *Nitrosopumilaceae*. The C group contained 938 OTUs, with high abundance families including *Rokubacteriales, Hungateiclostridiaceae* and *Omnitrophaceae*. Finally, the NCND contained 1403 OTUs with those assigned to *Anaerolineaceae, Aminicenantales* and *Methylomirabilaceae* being most abundant.

3.2.3. Beta diversity analysis

Non-metric multidimensional scaling (NMDS) ordination was undertaken on the cores across the site. NMDS enabled a way to condense information from multidimensional data, into an interpretable two-dimensional dissimilarity ordination plot. In this molecular ecological ordination, if the points were closer, then the corresponding OTUs within the samples were more closely related. The Background core samples from all depths clustered together, indicating that they were highly similar in composition (Fig. 3). The majority of the Top sections of the Jet fuel, Diesel and Crude Oil clustered with the Background. The other contaminated sections formed two loose clusters: one comprised the Middle and the Bottom sections of the Diesel and Crude Oil cores; the other comprised samples from the Jet Fuel cores, T7 core and Top section of D10a (both Crude Oil).

3.2.4. Environmental drivers of community structure and CD group OTU distribution

Constrained ordination analysis was performed in order to better understand the drivers of differences in community composition. The stepwise model selection procedure selected depth and naphthalene contamination as significant variables (Fig. 4A and S6). Constrained ordination of a subset of samples for which a more extensive chemical analysis was available further confirmed naphthalene and depth as significant variables in addition to pH and arsenic concentration (Fig S7). The following results and discussion focused on the results for the statistically robust full sample dataset since both analyses identified naphthalene as a major explanatory vector orthogonal to depth, and the pH vector was congruent with the depth vector. Congruent with the NMDS result, Background Zone samples clustered with samples from Top and Water Table Sections and were influenced by low naphthalene and depth with low contamination levels (Fig. 4A). The additional analysis of the subset of samples suggests that higher arsenic may also contribute to this observation (Fig. S7). However, the composition of samples from some Jet Fuel and Crude Oil Zones were strongly influenced by high naphthalene levels (Fig. 4A). The side-by-side comparison of the db-RDA plots enabled easier interpretation of the relationship between the OTUs in the predicted chemotactic and hydrocarbon degrading groups and depth and naphthalene (Fig. 4B). The distribution of a subset of OTUs appeared to be influenced by naphthalene contamination and all were assigned to the CD group (Fig. 4B). Separate subsets of OTUs assigned to the CD, D, and NCND groups were predicted to be influenced by depth. The OTUs assigned to the C group were not strongly influenced by either variable. The subset of CD OTUs influenced by naphthalene were assigned to the four microbial families, *Pseudomonadaceae, Desulfocapsaceae, Comamonadaceae* and *Geobacteraceae*. The subset of CD OTUs influenced by depth were assigned to three families, *Methanocellaceae, Nitrosopumilaceaes* and *Smithellaceae.*

A generalised linear model (GLM) assuming a binomial distribution with a logit link function was used to test the relationship between the occurrence of CD OTUs vs. Non-CD (C, D, NCND) OTUs and contaminant concentration and depth (Table 1). CD OTU occurrence was found to be significantly influenced by naphthalene contamination across the site, with a significantly negative relationship with depth, as well as the concentration of the soluble aromatic components, benzene and phenanthrene, across multiple vertical transects across the water table (Table 1).

4. Discussion

This study tested the association and distribution of microbes and petroleum LNAPL contaminants based on their inferred chemotactic and hydrocarbon degrading ability across multiple vertical transects across the water table of a legacy petroleum hydrocarbon site undergoing NSZD. Samples with low contaminant concentrations, including all Background sections and the Top sections of the Diesel, Crude Oil and Jet Fuel cores, tended to have similar community structure and composition, whereas the composition of deeper, more contaminated sections was more influenced by contaminant type. Two independent analyses identified naphthalene concentration as a driver of community structure and CD OTU distribution. Concentrations of naphthalene were found to have a significantly positive relationship with the occurrence of predicted CD group microbes, while concentrations of benzene and phenanthrene, along with depth, were significantly negatively related (Table 1). OTUs that were particularly influence by naphthalene concentration were assigned to the four microbial families, *Pseudomonadaceae, Desulfocapsaceae, Comamonadaceae* and *Geobacteraceae*. Existing NSZD models do not incorporate the role of CD microbial taxa and the results presented here provide further evidence supporting their inclusion to improve prediction of risk and remediation of petroleum in subsurface environments.

4.1. The role of predicted chemotactic and hydrocarbon degrading communities in NSZD

As expected, CD OTUs were found at higher abundance in the contaminated cores (Crude Oil, Jet Fuel and Diesel) in contrast to the Background core (Fig. 2). Naphthalene concentration was identified as a driver of CD OTUs distribution (Fig. 4A & B, Table 1). These CD OTUs were assigned to the microbial families *Geobacteraceae, Comamonadaceae, Pseudomonadaceae* and *Desulfocapsaceae* (Fig. 4B). In particular, *Pseudomonadaceae, Geobacteraceae* and *Comamonadaceae* appear to co-occur in samples with similar community composition (Fig. 2). Furthermore, the families *Pseudomonadaceae, Comamonadaceae* and *Geobacteraceae* have been noted to contain members which are electroactive microbes (Hassan et al., 2018) and family members are involved in the formation of biofilms which can further enhance the degradation of petroleum hydrocarbon compounds (Sharma et al., 2020).

Comamonadaceae family members have been reported in other legacy contaminated sites in Kuwait (Bruckberger et al., 2019). The family includes specific genera, such as *Comamonas* which is similar to some *Pseudomonas* species in its biology, ecology and ability to metabolise aromatic compounds (Lessner et al., 2003). However, they generally do not assimilate carbohydrates for growth, preferring organic acids and aromatic compounds (Wang et al., 2019). The *Acidovorax sp.* strain JS42 is a notable example of a CD group microbe of the *Comamonadaceae* family and has been specifically associated with aromatic and nitro-aromatic degradation at manufacturing sites (Rabinovitch-Deere and Parales, 2012).

All *Geobacteraceae* OTUs were classified as CD group taxa. Previous work has shown that members of this family can degrade multiple hydrocarbons in LNAPLs and are strictly anaerobic (Kunapuli et al., 2010; Zhang et al., 2014). However, chemotaxis towards hydrocarbons has not

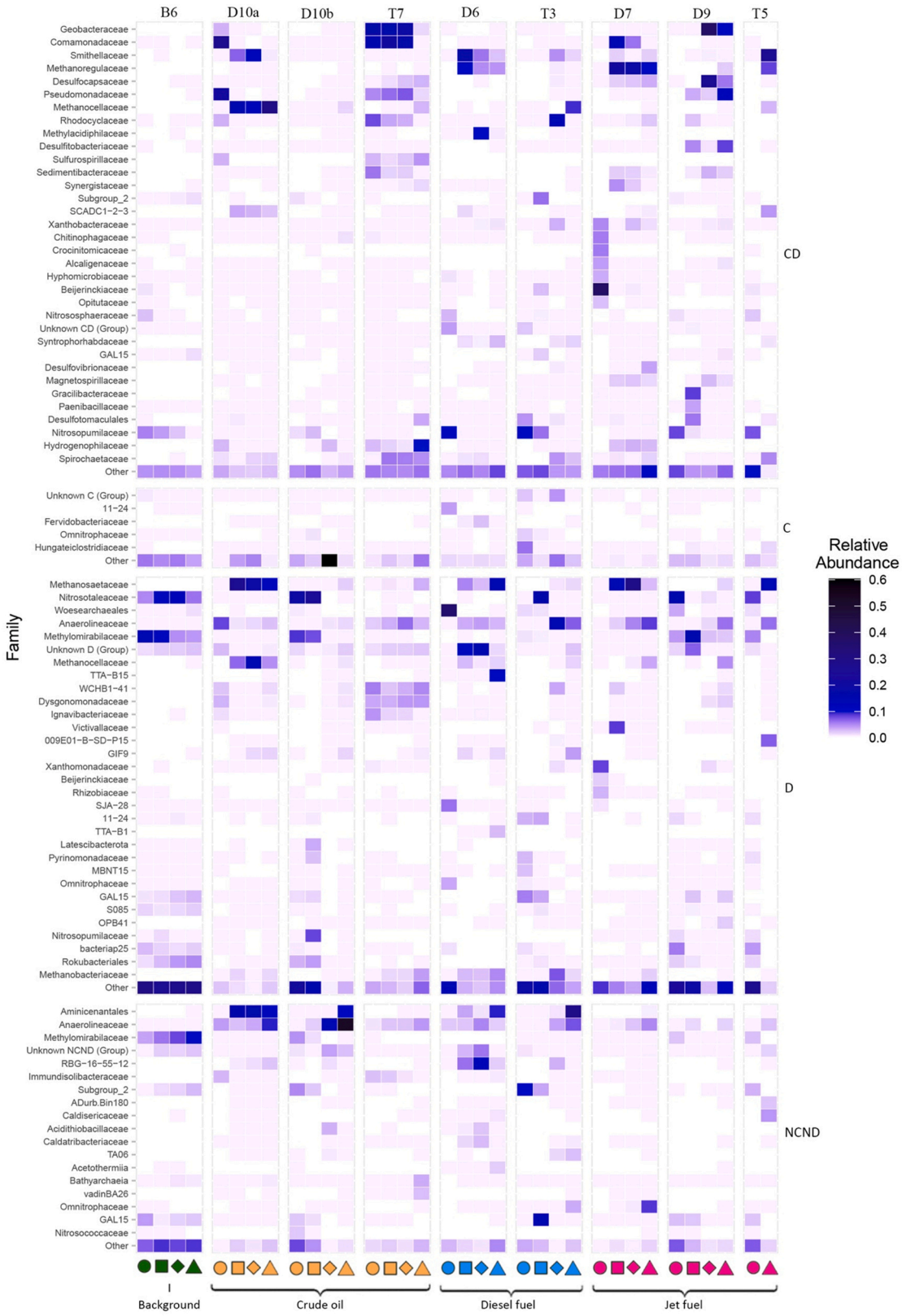


Fig. 2. Community composition heatmap of relative abundances arranged by similarity of distribution of the families in their chemotactic and hydrocarbon degrading groups based on predictive metagenomic profiling. The heatmap is faceted by group, with the purple shading representing their relative abundance. The Other taxa of each group contains microbes with a maximum relative abundance < 2%; including uncultured taxa, with unknown taxa also being shown. The y-axis is arranged by similarity of distribution, with the x-axis being arranged by core section and contamination zone. The Background core is green, the Crude Oil cores are orange, the Diesel Fuel cores are blue and the Jet Fuel cores are pink. On the right-hand side of the figure circles represent the Top section, squares represent Water Table section, rhombuses represent the Middle section and triangles represent the Bottom section.

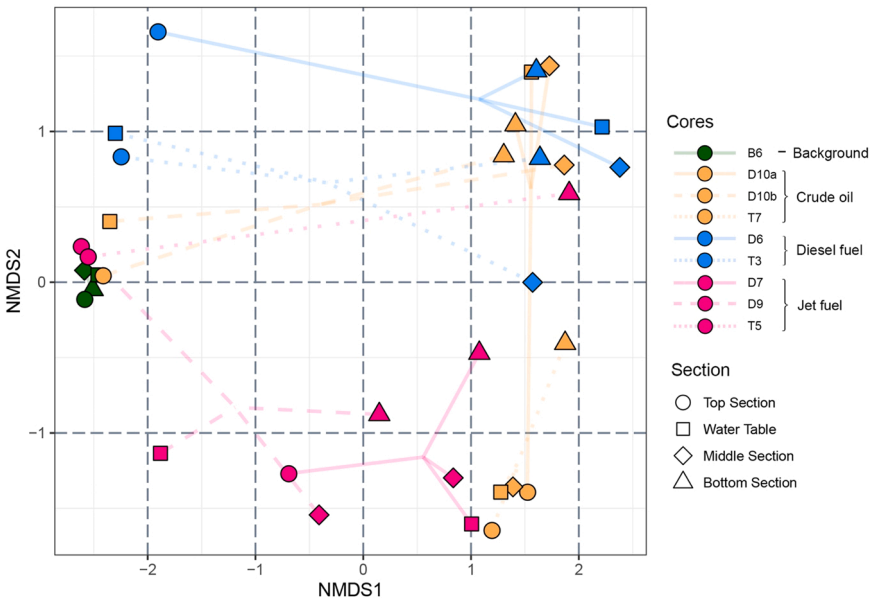


Fig. 3. Non-metric multidimensional scaling (NMDS) Bray-Curtis dissimilarity plot of core sections representing beta diversity. The stress of the ordination is 0.07 and has been computed in 3 dimensions, with the first and second axis being presented. The Background samples are green, Crude Oil is orange, Diesel Fuel is blue and Jet Fuel is pink. Circles represent the Top section, squares represent Water Table section, diamonds represent the Middle section and triangles represent the Bottom section, various line-types are used to connect samples from the same core.

been observed, but *Geobacteraceae* species have been shown to be chemotactic towards Fe (II) or Mn (II) oxide (Childers et al., 2002). It is therefore likely that *Geobacteraceae* OTUs are chemotactic towards compounds other than hydrocarbons, and that they may instead be considered part of the D group.

Pseudomonadaceae are part of the *Gammaproteobacteria* class of microbes, with this class being reported previously in high abundances throughout cores of a legacy petroleum hydrocarbon contaminated site in Kuwait (Bruckberger et al., 2019, 2020). All of the CD group OTUs from this family were from the genus *Pseudomonas* (Fig. S4), species of which are generally aerobic Gram-negative rod-like bacteria, however some members can also survive in certain anaerobic environments (Sampedro et al., 2015; Lacal et al., 2011). Many *Pseudomonas* species are able to degrade and/or metabolise many petroleum hydrocarbon compounds (Lacal et al., 2011; Sampedro et al., 2015; Luu et al., 2015), as well as being highly chemotactic towards aromatic hydrocarbons found in petroleum LNAPL zones (Sampedro et al., 2015), thereby potentially assisting in NSZD.

Members of *Geobacteraceae* and *Pseudomonadaceae*, *G. sulfurreducens* and *P. aeruginosa*, have been reported to facilitate interspecies electron transfer (IET). This permits extracellular electron exchange in environments of mixed resources (Semenec et al., 2018). *P. aeruginosa* has been reported to exhibit both direct interspecies electron transfer (DIET) and hydrogen interspecies electron transfer (IET) with *G. sulfurreducens* (Semenec et al., 2018). This could be another reason for their co-occurrence and is worthy of further investigation. The scope and nature of chemotaxis in the *Geobacteraceae* family poses compelling questions (Childers et al., 2002). Further research needs to be undertaken to determine if members of the *Geobacteraceae* family are chemotactic toward hydrocarbons, and their co-occurrence with *Pseudomonadaceae* species is due to their synergetic DIET relationship (Semenec et al., 2018). Alternatively, their positioning within the subsurface could be due to a bacteria-bacteria transport (Sungthong et al., 2016). This mode of transport is where *Pseudomonadaceae* or other microbes which are chemotactic directly towards petroleum hydrocarbons drag the generally non-motile *Geobacteraceae* along its chemotactic gradient towards hydrocarbon compounds (Sungthong et al., 2016; Grenier, 2013; Stanton et al., 2017).

The other CD OTU influenced by naphthalene is assigned to the genus *Desulfoprunum* (Figs. S5b and S5c) in the *Desulfocapsaceae* family (Fig. 4B). This genus has been recorded at hydrocarbon contaminated sites previously and are capable of using benzoate during sulfate reduction (Zhuang et al., 2019; Pilloni et al., 2019). Chemotactic responses of this family and genera however have not been directly observed but were inferred from the functional potential of genes present in metagenome-assembled genomes (MAGs) found as epibionts in *Rimicaris exoculata* shrimp in deep-sea hydrothermal vents and assigned to this family (Cambon-Bonavita et al., 2021). The KEGG pathway for naphthalene degradation includes benzoate degradation as a possible next step in naphthalene degradation, as well as being a central intermediary in the degradation of other petroleum hydrocarbons (Zhuang et al., 2019; Pilloni et al., 2019). OTUs assigned to the families *Pseudomonadaceae, Comamonadaceae* and *Geobacteraceae* all possess this pathway (Fig. S8). The negative relationship with depth and CD OTU presence could be explained by the fact many of the CD microbes are more tolerant of various environments and prefer to be where the attractant (food source) is present (Sampedro et al., 2015; Lacal et al., 2011; Kunapuli et al., 2010; Zhang et al., 2014).

Overall, these results indicate the presence of CD group OTUs (that is, OTUs that were predicted to have the functional potential for chemotaxis and hydrocarbon degradation) is positively associated with naphthalene contamination and thus suggests a role for chemotaxis assisted degradation contributing to NSZD of petroleum hydrocarbons. In addition, these results have generated novel hypotheses regarding the contribution of the four OTUs significantly associated with naphthalene. Further research is needed to characterise the role of the CD OTUs in the families *Pseudomonadaceae, Desulfocapsaceae, Comamonadaceae* and *Geobacteraceae* in order to define their contribution to NSZD. Further research will lead to a more accurate understanding of the role chemotaxis plays in NSZD and lead to better mitigation of risk from petroleum releases.

4.2. Community connections between CD and D group microbes

A subset of CD OTUs assigned to *Smithellaceae* (assigned to the genus *Smithella*) (Fig. S4) and *Methanocellaceae* (assigned to the genus *Methanocella*) (Fig S4) were found to be significantly associated with increasing depth. *Smithellaceae* were recorded throughout the site, however at an elevated presence in the cores D10a (Crude Oil), T5 (Jet Fuel), and D6 (Diesel). Members of the family are sulfate-reducing, strictly anaerobic and hydrocarbon degrading microbes (Embree et al., 2014; Tischer et al., 2013), which may possess the ability for chemotaxis (Wawrik et al., 2016). Family members have been linked with playing a role in anaerobic syntrophic food chains (Embree et al., 2014; Tischer

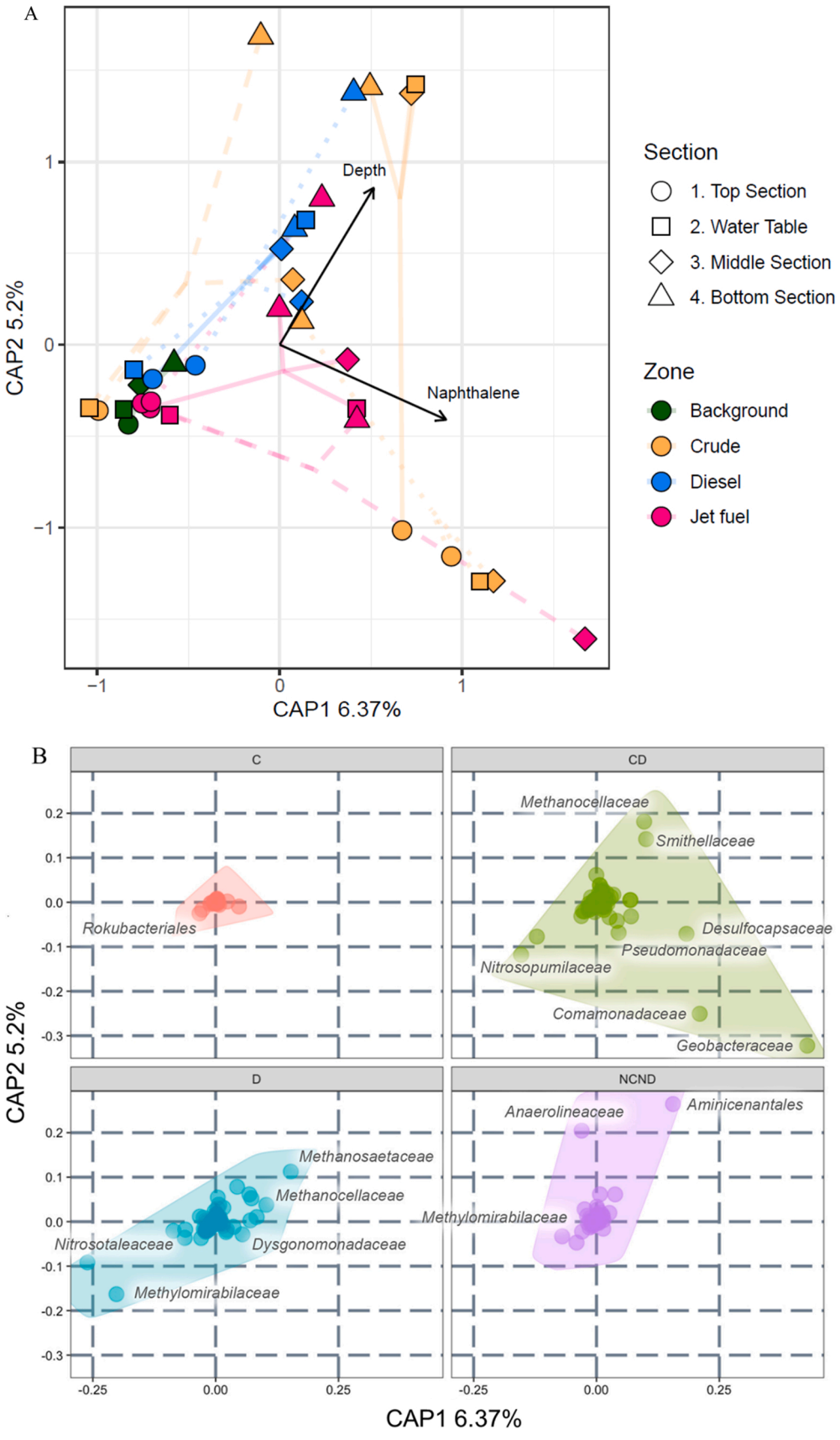


Fig. 4. Distance-based Bray-Curtis constrained redundancy ordination analysis (db-RDA) of samples and individual OTUs. In both figures naphthalene and depth are the significant variables, but only shown in panel A. (A) A db-RDA of samples and significant variables ($p < 0.05$) following stepwise model selection. Naphthalene and depth are the significant variables, with the length of the arrows gauging relative significance of each variable, the longer the arrow the greater the influence the variable has. The first axis (CAP1) explains 6.37% of variation across samples, with the second axis (CAP2) explaining 5.2% of variation, with the db-RDA explaining 13.2% of total variation. The Background samples are green, Crude Oil is orange, Diesel Fuel is blue and Jet Fuel is pink, with core sections through the water table being illustrated by shapes, and the different line types showing the differences between the cores. Circles represent the Top section, squares represent the Water Table section, diamonds represent the Middle section and triangles represent the Bottom section, line-types link core samples. (B) Different chemotactic and hydrocarbon degrading groups, the taxa of notable OTUs and how they are driven by significant variables within the db-RDA. The C group is red, the CD group is green, the D group is blue and the NCND group is purple.

Table 1
Statistical summary of the generalised linear model developed to investigate chemotaxis and hydrocarbon degradation across the legacy petroleum hydrocarbon site.

Dependent variable	
Frequency of CD OTUs vs. non-CD OTUs	
Depth	*Estimate* –0.040 Pr(>|z|) = 0.0137*
Benzene	*Estimate* –0.201 Pr(>|z|) = <2e-16***
Naphthalene	*Estimate* 0.273 Pr(>|z|) = <2e-16***
Phenanthrene	*Estimate* –0.125 Pr(>|z|) = 1.1e-11*
Constant	*Estimate* –0.936 Pr(>|z|) = <2e-16***
Observations	34
Log Likelihood	–545.707
Akaike Inf. Crit	1,101.413

Note: *p < 0.1; **p < 0.05; ***p < 0.01

et al., 2013). Interestingly, a CD OTU in the *Methanocellaceae*, a petroleum hydrocarbon degrading and potentially chemotactic family (Sakai et al., 2010, 2011) co-occurred with a CD OTU in the *Smithellaceae* (Fig. 2). Co-occurrence of these families has been previously reported by others (Tischer et al., 2013). Members of the *Methanocellaceae* are capable of both anoxic and oxic methanogenesis (Angel et al., 2011). Methanogenesis has been commonly reported in groundwater at the site (King, 2009). This could explain its presence above and below the water table in cores D6 and D7, where it has been hypothesised to act as scavengers for hydrogen, working with *Smithellaceae* and other related families (Tischer et al., 2013).

Although our study has focused on inferred chemotaxis assisted hydrocarbon degradation, the role of other non-chemotactic functional groups in NSZD is of interest. For example, Tischer et al. (2013), described a methanogenic and potentially hydrocarbon degrading consortium that included CD group taxa, such as *Smithellaceae* and *Methanocellaceae* and D grouped taxa such as members of the acetoclastic *Methanosaetaceae* family and the hydrogenotrophic family *Methanoregulaceae*. Interestingly, this consortium was able to reduce volatile fatty acid accumulation, therefore liberating the molecules required to enhance chemotactic activity within the subsurface (Zhang et al., 2020). Methanogenic families, such as *Methanobacteriaceae* have been reported previously at legacy petroleum hydrocarbon sites such as the Huabei Oilfield, China (Tan et al., 2015). Interestingly, some *Acinetobacter* species are known to be capable of chemotaxis assisted alkane and hydrocarbon degradation (Li et al., 2017; Zhang et al., 2012), however the OTUs assigned to *Acinetobacter* species in this study were found to be assigned to the D group which were predicted to be non-chemotactic. This further emphasises the importance of this functional group in NSZD. In summary, the D group microbes are potentially a valuable avenue of further study, both to evaluate CD community interaction and to understand their combined role in NSZD.

5. Conclusions

This novel study defines the distribution and associations of indigenous microbes based on their predicted chemotactic and hydrocarbon degrading ability across the water table of a legacy petroleum hydrocarbon site. It provides an unprecedented view of the microbial functional metabolic groups operating across the water table of an unconfined superficial sand aquifer undergoing NSZD spanning a range of LNAPL types, water saturations, LNAPL component concentrations and air phase conditions. Critical distributions and associations have been defined for three petroleum types, crude oil, diesel fuel and jet fuel, and compared to a background location in the same hydrogeochemical and lithological setting. This forms a valuable foundation for future research to explore this important biological phenomenon. Naphthalene concentration was found to be a driver for the presence of potentially chemotactic and hydrocarbon degrading microbes. Further investigation is required to confirm this association and to assess the role of OTUs identified as being influenced by naphthalene concentrations during LNAPL NSZD. Moreover, further research is required to investigate how the CD and D group OTUs, including methanogens, interact to promote NSZD. Addressing these challenges will enable the development of more sophisticated models (Sookhak Lari et al., 2021) incorporating such biological processes to more accurately predict NSZD outcomes.

CRediT authorship contribution statement

Cameron W. M. Murphy: Conceptualization, Methodology, Investigation, Formal analysis, Writing. **Greg B. Davis:** Investigation, Formal analysis, Writing. **John L. Rayner:** Investigation, Formal analysis. **Tom Walsh:** Investigation, Formal analysis, Writing. **Trevor P. Bastow:** Investigation, Formal analysis, Writing. **Adrian P. Butler:** Formal analysis, Writing, Supervision. **Geoffrey J. Puzon:** Investigation, Formal analysis, Writing, Supervision, Project administration. **Matthew J. Morgan:** Methodology, Investigation, Formal analysis, Writing, Supervision.

Declaration of Competing Interest

The authors declare that they have no known competing financial interests or personal relationships that could have appeared to influence the work reported in this paper.

Acknowledgment

Yasuko Geste is thanked for technical help with chemistry. Mike Donn, Jason Wylie, Melanie Bruckberger and Robert Woodbury are thanked for their help in sample processing. Suzanne Metcalfe is thanked for her assistance with amplicon sequencing. Kaveh Sookhak Lari is thanked for his help with the graphical abstract. BP Australia is acknowledged for supporting the investigation. This work is financially supported by the Commonwealth Scientific and Industrial Research Organisation (CSIRO).

Appendix A. Supporting information

Supplementary data associated with this article can be found in the online version at doi:10.1016/j.jhazmat.2022.128482.

References

Angel, R., Matthies, D., Conrad, R., 2011. Activation of methanogenesis in arid biological soil crusts despite the presence of oxygen. PLoS One 6 (5), e20453. https://doi.org/10.1371/journal.pone.0020453.

Blanco-Enríquez, E.G., de la Serna, Zavala-D.íaz, Peralta-Pérez, F.J., Ballinas-Casarrubias, M.D.R., Salmerón, L., Rubio-Arias, I., Rocha-Gutiérrez, B.A, H., 2018. Characterization of a microbial consortium for the bioremoval of polycyclic aromatic hydrocarbons (PAHs) in water. Int. J. Environ. Res. Public Health 15 (5), 975. https://doi.org/10.3390/ijerph15050975.

Bolyen, E., Rideout, J.R., Dillon, M.R., Bokulich, N.A., Abnet, C.C., Al-Ghalith, G.A., Alexander, H., Alm, E.J., Arumugam, M., Asnicar, F., Bai, Y., Bisanz, J.E., Bittinger, K., Brejnrod, A., Brislawn, C.J., Brown, C.T., Callahan, B.J., Caraballo-Rodríguez, A.M., Chase, J., Cope, E.K., Da Silva, R., Diener, C., Dorrestein, P.C., Douglas, G.M., Durall, D.M., Duvallet, C., Edwardson, C.F., Ernst, M., Estaki, M., Fouquier, J., Gauglitz, J.M., Gibbons, S.M., Gibson, D.L., Gonzalez, A., Gorlick, K., Guo, J., Hillmann, B., Holmes, S., Holste, H., Huttenhower, C., Huttley, G.A., Janssen, S., Jarmusch, A.K., Jiang, L., Kaehler, B.D., Kang, K.B., Keefe, C.R., Keim, P., Kelley, S.T., Knights, D., Koester, I., Kosciolek, T., Kreps, J., Langille, M.G.I., Lee, J., Ley, R., Liu, Y.X., Loftfield, E., Lozupone, C., Maher, M., Marotz, C., Martin, B.D., McDonald, D., McIver, L.J., Melnik, A.V., Metcalf, J.L., Morgan, S.C., Morton, J.T., Naimey, A.T., Navas-Molina, J.A., Nothias, L.F., Orchanian, S.B., Pearson, T., Peoples, S.L., Petras, D., Preuss, M.L., Pruesse, E., Rasmussen, L.B., Rivers, A., Robeson, M.S., Rosenthal, P., Segata, N., Shaffer, M., Shiffer, A., Sinha, R., Song, S.J., Spear, J.R., Swafford, A.D., Thompson, L.R., Torres, P.J., Trinh, P., Tripathi, A., Turnbaugh, P.J., Ul-Hasan, S., van der Hooft, J.J.J., Vargas, F., Vázquez-Baeza, Y., Vogtmann, E., von Hippel, M., Walters, W., Wan, Y., Wang, M., Warren, J., Weber, K.

C., Williamson, C.H.D., Willis, A.D., Xu, Z.Z., Zaneveld, J.R., Zhang, Y., Zhu, Q., Knight, R., Caporaso, J.G., 2019. Reproducible, interactive, scalable and extensible microbiome data science using QIIME 2. Nat. Biotechnol. 37, 852–857.

Bruckberger, M.C., Bastow, T.P., Morgan, M.J., Gleeson, D., Banning, N., Davis, G., Puzon, G.J., 2018. Biodegradability of polar compounds formed from weathered diesel. Biodegradation 29 (5), 443–461. https://doi.org/10.1007/s10532-018-9841-1.

Bruckberger, M.C., Gleeson, D.B., Bastow, T.P., Morgan, M.J., Walsh, T., Rayner, J.L., Davis, G.B., Puzon, G.J., 2021. Unravelling microbial communities associated with different light non-aqueous phase liquid types undergoing natural source zone depletion processes at a legacy petroleum site. Water 13 (7), 898.

Bruckberger, M.C., Morgan, M.J., Bastow, T.P., Walsh, T., Prommer, H., Mukhopadhyay, A., Kaksonen, A.H., Davis, G.B., Puzon, G.J., 2020. Investigation into the microbial communities and associated crude oil-contamination along a Gulf War impacted groundwater system in Kuwait. Water Res. 170, 115314 https://doi.org/10.1016/j.watres.2019.115314.

Bokulich, N.A., Kaehler, B.D., Rideout, J.R., Dillon, M., Bolyen, E., Knight, R., Huttley,, G.A., Caporaso, J.G., 2018. Optimizing taxonomic classification of marker-gene amplicon sequences with QIIME 2's q2-feature-classifier plugin. Microbiome 6 (1), 1–17.

Bruckberger, M.C., Morgan, M.J., Walsh, T., Bastow, T.P., Prommer, H., Mukhopadhyay, A., Kaksonen, A.H., Davis, G., Puzon, G.J., 2019. Biodegradability of legacy crude oil contamination in Gulf War damaged groundwater wells in Northern Kuwait. Biodegradation 30 (1), 71–85. https://doi.org/10.1007/s10532-019-09867-w.

Callahan, B.J., McMurdie, P.J., Rosen, M.J., Han, A.W., Johnson, A.J.A., Holmes, S.P., 2016. DADA2: high-resolution sample inference from Illumina amplicon data. Nat. Methods 13 (7), 581–583.

Cambon-Bonavita, M.-A., Aubé, J., Cueff-Gauchard, V., Reveillaud, J., 2021. Niche partitioning in the Rimicaris exoculata holobiont: the case of the first symbiotic Zetaproteobacteria. Microbiome 9 (1), 87. https://doi.org/10.1186/s40168-021-01045-6.

Chang, J.I., Lin, C.-C., 2006. A study of storage tank accidents. J. Loss Prev. Process Ind. 19 (1), 51–59. https://doi.org/10.1016/j.jlp.2005.05.015.

Chapelle, F.H., Bradley, P.M., Lovley, D.R., O'Neill, K., Landmeyer, J.E., 2002. Rapid evolution of redox processes in a petroleum hydrocarbon-contaminated aquifer. Ground Water 40 (4), 353–360. https://doi.org/10.1111/j.1745-6584.2002.tb02513.x.

Chaudhary, P., Sahay, H., Sharma, R., Pandey, A.K., Singh, S.B., Saxena, A.K., Nain, L., 2015. Identification and analysis of polyaromatic hydrocarbons (PAHs)–biodegrading bacterial strains from refinery soil of India. Environ. Monit. Assess. 187 (6), 391. https://doi.org/10.1007/s10661-015-4617-0.

Childers, S.E., Ciufo, S., Lovley, D.R., 2002. Geobacter metallireducens accesses insoluble Fe(III) oxide by chemotaxis. Nature 416 (6882), 767–769. https://doi.org/10.1038/416767a.

Crampon, M., Bodilis, J., Portet-Koltalo, F., 2018. Linking initial soil bacterial diversity and polycyclic aromatic hydrocarbons (PAHs) degradation potential. J. Hazard. Mater. 359, 500–509. https://doi.org/10.1016/j.jhazmat.2018.07.088.

Frutos, F.J.G., Escolano, O., García, S., Babín, M., Fernández,, M.D., 2010. Bioventing remediation and ecotoxicity evaluation of phenanthrene-contaminated soil. Journal of hazardous materials 183, 806–813 (1-3).

Davis, G.B., Barber, C., Power, T.R., Thierrin, J., Patterson, B.M., Rayner, J.L., Wu, Q., 1999. The variability and intrinsic remediation of a BTEX plume in anaerobic sulphate-rich groundwater. J. Contam. Hydrol. 36 (3), 265–290. https://doi.org/10.1016/S0169-7722(98)00148-X.

Davis, G.B., Rayner, J.L., Trefry, M.G., Fisher, S.J., Patterson, B.M., 2005. Measurement and modeling of temporal variations in hydrocarbon vapor behavior in a layered soil profile. Vadose Zone J. 4 (2), 225–239.

Dell'Anno, A., Beolchini, F., Rocchetti, L., Luna, G.M., Danovaro, R., 2012. High bacterial biodiversity increases degradation performance of hydrocarbons during bioremediation of contaminated harbor marine sediments. Environ. Pollut. 167, 85–92. https://doi.org/10.1016/j.envpol.2012.03.043.

Dobson, R., Schroth, M.H., Zeyer, J., 2007. Effect of water-table fluctuation on dissolution and biodegradation of a multi-component, light nonaqueous-phase liquid. J. Contam. Hydrol. 94 (3), 235–248. https://doi.org/10.1016/j.jconhyd.2007.07.007.

Douglas, G.M., Maffei, V.J., Zaneveld, J.R., Yurgel, S.N., Brown, J.R., Taylor, C.M., Huttenhower, C., Langille, M.G.I., 2020. PICRUSt2 for prediction of metagenome functions. Nat. Biotechnol. 38 (6), 685–688. https://doi.org/10.1038/s41587-020-0548-6.

Embree, M., Nagarajan, H., Movahedi, N., Chitsaz, H., Zengler, K., 2014. Single-cell genome and metatranscriptome sequencing reveal metabolic interactions of an alkane-degrading methanogenic community. ISME J. 8 (4), 757–767. https://doi.org/10.1038/ismej.2013.187.

Essaid, H.I., Bekins, B.A., Cozzarelli, I.M., 2015. Organic contaminant transport and fate in the subsurface: evolution of knowledge and understanding. Water Resour. Res. 51 (7), 4861–4902. https://doi.org/10.1002/2015WR017121.

Franzmann, P.D., Robertson, W.J., Zappia, L.R., Davis, G.B., 2002. The role of microbial populations in the containment of aromatichydrocarbons in the subsurface. Biodegradation 13 (1), 65–78. https://doi.org/10.1023/A:1016318706753.

Franzmann, P.D., Zappia, L.R., Patterson, B.M., Rayner, J.L., Davis, G.B., 1998. Mineralisation of low concentrations of organic compounds and microbial biomass in surface and vadose zone soils from the Swan Coastal Plain, Western Australia. Soil Res. 36 (6), 921–940. https://doi.org/10.1071/S97116.

Gkorezis, P., Daghio, M., Franzetti, A., Van Hamme, J.D., Sillen, W., Vangronsveld, J., 2016. The interaction between plants and bacteria in the remediation of petroleum hydrocarbons: an environmental perspective. Front. Microbiol. 7 (1836) https://doi.org/10.3389/fmicb.2016.01836.

Grenier, D., 2013. Porphyromonas gingivalis outer membrane vesicles mediate coaggregation and piggybacking of treponema denticola and lachnoanaerobaculum saburreum. Int J. Dent. 2013, 305476 https://doi.org/10.1155/2013/305476.

Gupta, P.K., Yadav, B.K., 2019. Remediation and Management of Petrochemical-Polluted Sites Under Climate Change Conditions. In: Bharagava, R.N. (Ed.), Environmental Contaminants: Ecological Implications and Management. Springer, Singapore, Singapore, pp. 25–47. https://doi.org/10.1007/978-981-13-7904-8_2.

Hamdan, H.Z., Salam, D.A., Saikaly, P.E., 2019. Characterization of the microbial community diversity and composition of the coast of Lebanon: potential for petroleum oil biodegradation. Mar. Pollut. Bull. 149, 110508 https://doi.org/10.1016/j.marpolbul.2019.110508.

Hassan, M., Fernandez, A.S., San Martin, I., Xie, B., Moran, A., 2018. Hydrogen evolution in microbial electrolysis cells treating landfill leachate: dynamics of anodic biofilm. Int. J. Hydrog. Energy 43 (29), 13051–13063. https://doi.org/10.1016/j.ijhydene.2018.05.055.

Hidalgo, K.J., Teramoto, E.H., Soriano, A.U., Valoni, E., Baessa, M.P., Richnow, H.H., Vogt, C., Chang, H.K., Oliveira, V.M., 2020. Taxonomic and functional diversity of the microbiome in a jet fuel contaminated site as revealed by combined application of in situ microcosms with metagenomic analysis. Sci. Total Environ. 708, 135152 https://doi.org/10.1016/j.scitotenv.2019.135152.

Hong, Y.-H., Ye, C.-C., Zhou, Q.-Z., Wu, X.-Y., Yuan, J.-P., Peng, J., Deng, H., Wang, J.-H., 2017. Genome sequencing reveals the potential of achromobacter sp. HZ01 for bioremediation. Front. Microbiol. 8, 1507. https://doi.org/10.3389/fmicb.2017.01507. –1507.

Hu, L., Wu, X., Liu, Y., Meegoda, J.N., Gao, S., 2010. Physical modeling of air flow during air sparging remediation. Environ. Sci. Technol. 44 (10), 3883–3888. https://doi.org/10.1021/es903853v.

Johnston, C.D., Rayner, J.L., Briegel, D., 2002. Effectiveness of in situ air sparging for removing NAPL gasoline from a sandy aquifer near Perth, Western Australia. J. Contam. Hydrol. 59 (1–2), 87–111. https://doi.org/10.1016/s0169-7722(02)00077-3.

Johnston, C.D., Rayner, J.L., Patterson, B.M., Davis, G.B., 1998. Volatilisation and biodegradation during air sparging of dissolved BTEX-contaminated groundwater. J. Contam. Hydrol. 33 (3), 377–404. https://doi.org/10.1016/S0169-7722(98)00079-5.

Kanehisa, M., 2019. Toward understanding the origin and evolution of cellular organisms. Protein Sci. 28 (11), 1947–1951. https://doi.org/10.1002/pro.3715.

Kanehisa, M., Goto, S., 2000. KEGG: kyoto encyclopedia of genes and genomes. Nucleic Acids Res. 28 (1), 27–30. https://doi.org/10.1093/nar/28.1.27.

King, A. 2009. Quantification of methanogenesis-dominated natural attenuation processes in a carbonate aquifer with complex sources. Master Thesis, University of Western Australia, 185 pp.

Kunapuli, U., Jahn, M.K., Lueders, T., Geyer, R., Heipieper, H.J., Meckenstock, R.U., 2010. Desulfitobacterium aromaticivorans sp. nov. and Geobacter toluenoxydans sp. nov., iron-reducing bacteria capable of anaerobic degradation of monoaromatic hydrocarbons. Int J. Syst. Evol. Microbiol. 60 (Pt 3), 686–695. https://doi.org/10.1099/ijs.0.003525-0.

Lacal, J., Muñoz-Martínez, F., Reyes-Darías, J.A., Duque, E., Matilla, M., Segura, A., Calvo, J.J., Jímenez-Sánchez, C., Krell, T., Ramos, J.L., 2011. Bacterial chemotaxis towards aromatic hydrocarbons in Pseudomonas. Environ. Microbiol. 13 (7), 1733–1744. https://doi.org/10.1111/j.1462-2920.2011.02493.x.

Lang, D.A., Bastow, T.P., Aarssen, B.G.Kv, Warton, B., Davis, G.B., Johnston, C.D., 2009. Polar compounds from the dissolution of weathered diesel. Groundw. Monit. Remediat. 29, 85–93.

Lee, S.-J., Kong, M., St-Arnaud, M., Hijri, M., 2020. Arbuscular mycorrhizal fungal communities of native plant species under high petroleum hydrocarbon contamination highlights rhizophagus as a key tolerant genus. Microorganisms 8 (6), 872.

Lessner, D.J., Parales, R.E., Narayan, S., Gibson, D.T., 2003. Expression of the nitroarene dioxygenase genes in Comamonas sp. strain JS765 and Acidovorax sp. strain JS42 is induced by multiple aromatic compounds. J. Bacteriol. 185 (13), 3895–3904. https://doi.org/10.1128/JB.185.13.3895-3904.2003.

Li, H., Martin, F.L., Zhang, D., 2017. Quantification of chemotaxis-related alkane accumulation in acinetobacter baylyi using raman microspectroscopy. Anal. Chem. 89 (7), 3909–3918. https://doi.org/10.1021/acs.analchem.6b02297.

Li, J., Huang, G.H., Zeng, G., Maqsood, I., Huang, Y., 2007. An integrated fuzzy-stochastic modeling approach for risk assessment of groundwater contamination. J. Environ. Manag. 82 (2), 173–188. https://doi.org/10.1016/j.jenvman.2005.12.018.

Lloyd, K.G., Steen, A.D., Ladau, J., Yin, J., Crosby, L., Neufeld, J.D., 2018. Phylogenetically novel uncultured microbial cells dominate earth microbiomes. MSystems 3 (5), e00055–00018. https://doi.org/10.1128/mSystems.00055-18.

Lundegard, P.D., Sweeney, R.E., 2004. Total petroleum hydrocarbons in groundwater—evaluation of nondissolved and nonhydrocarbon fractions. Environ. Forensics 5 (2), 85–95. https://doi.org/10.1080/15275920490454346.

Luu, R.A., Kootstra, J.D., Nesteryuk, V., Brunton, C.N., Parales, J.V., Ditty, J.L., Parales, R.E., 2015. Integration of chemotaxis, transport and catabolism in Pseudomonas putida and identification of the aromatic acid chemoreceptor PcaY. Mol. Microbiol. 96 (1), 134–147. https://doi.org/10.1111/mmi.12929.

Maila, M.P., Randima, P., Surridge, K., Drønen, K., Cloete, T.E., 2005. Evaluation of microbial diversity of different soil layers at a contaminated diesel site. Int. Biodeterior. Biodegrad. 55 (1), 39–44. https://doi.org/10.1016/j.ibiod.2004.06.012.

McMurdie, P.J., Holmes, S., 2013. phyloseq: an R package for reproducible interactive analysis and graphics of microbiome census data. PloS one 8 (4), e61217.
Mangse, G., Werner, D., Meynet, P., Ogbaga, C.C., 2020. Microbial community responses to different volatile petroleum hydrocarbon class mixtures in an aerobic sandy soil. Environ. Pollut. 264, 114738 https://doi.org/10.1016/j.envpol.2020.114738.
Marx, R.B., Aitken, M.D., 2000. Bacterial chemotaxis enhances naphthalene degradation in a heterogeneous aqueous system. Environ. Sci. Technol. 34 (16), 3379–3383. https://doi.org/10.1021/es000904k.
Naimi, B., Hamm, N.A.S., Groen, T.A., Skidmore, A.K., Toxopeus, A.G., 2014. Where is positional uncertainty a problem for species distribution modelling? Ecography 37 (2), 191–203. https://doi.org/10.1111/j.1600-0587.2013.00205.x.
Olson, M.S., Ford, R.M., Smith, J.A., Fernandez, E.J., 2004. Quantification of bacterial chemotaxis in porous media using magnetic resonance imaging. Environ. Sci. Technol. 38 (14), 3864–3870. https://doi.org/10.1021/es035236s.
Parada, A.E., Needham, D.M., Fuhrman, J.A., 2016. Every base matters: assessing small subunit rRNA primers for marine microbiomes with mock communities, time series and global field samples. Environ. Microbiol. 18 (5), 1403–1414. https://doi.org/10.1111/1462-2920.13023.
Parales, R.E., Ditty, J.L., 2018. Chemotaxis to Hydrocarbons. In: Krell, T. (Ed.), Cellular Ecophysiology of Microbe: Hydrocarbon and Lipid Interactions. Springer International Publishing, Cham, pp. 221–239. https://doi.org/10.1007/978-3-319-50542-8_43.
Pilloni, G., Bayer, A., Ruth-Anneser, B., Fillinger, L., Engel, M., Griebler, C., Lueders, T., 2019. Dynamics of hydrology and anaerobic hydrocarbon degrader communities in A tar-oil contaminated aquifer. Microorganisms 7 (2), 46. https://doi.org/10.3390/microorganisms7020046.
Quast, C., Pruesse, E., Yilmaz, P., Gerken, J., Schweer, T., Yarza, P., Peplies, J., Glöckner, F.O., 2013. The SILVA ribosomal RNA gene database project: improved data processing and web-based tools. Nucleic Acids Res. 41 (D1), D590–D596. https://doi.org/10.1093/nar/gks1219.
Rabinovitch-Deere, C.A., Parales, R.E., 2012. Three types of taxis used in the response of Acidovorax sp. strain JS42 to 2-nitrotoluene. Appl. Environ. Microbiol. 78 (7), 2306–2315. https://doi.org/10.1128/aem.07183-11.
Rappé, M.S., Giovannoni, S.J., 2003. The uncultured microbial majority. Annu Rev. Microbiol. 57, 369–394. https://doi.org/10.1146/annurev.micro.57.030502.090759.
Rayment, G.E., Lyons, D.J., 2011. Soil Chemical Methods: Australasia. CSIRO publishing.
Reid, T., Chaganti, S.R., Droppo, I.G., Weisener, C.G., 2018. Novel insights into freshwater hydrocarbon-rich sediments using metatranscriptomics: opening the black box. Water Res. 136, 1–11. https://doi.org/10.1016/j.watres.2018.02.039.
Rognes, T., Flouri, T., Nichols, B., Quince, C., Mahé, F., 2016. VSEARCH: a versatile open source tool for metagenomics. PeerJ 4, e2584.
Oksanen, J., Blanchet, F.G., Friendly, M., Kindt, R., Legendre, P., McGlinn, D., Minchin, P.R., O'Hara, R.B., Simpson, G.L., Solymos, P., Stevens, M.H.H., Wagner, H. and Wagner, H., **2020. vegan: Community Ecology Package. R package version 2.5-7. https://CRAN.R-project.org/package=vegan**.
RStudio Team 2020. RStudio: Integrated Development Environment for R. RStudio, PBC, Boston, MA URL ⟨http://www.rstudio.com/⟩.
Sakai, S., Conrad, R., Liesack, W., Imachi, H., 2010. Methanocella arvoryzae sp. nov., a hydrogenotrophic methanogen isolated from rice field soil. Int J. Syst. Evol. Microbiol. 60 (Pt 12), 2918–2923. https://doi.org/10.1099/ijs.0.020883-0.
Sakai, S., Takaki, Y., Shimamura, S., Sekine, M., Tajima, T., Kosugi, H., Ichikawa, N., Tasumi, E., Hiraki, A.T., Shimizu, A., Kato, Y., Nishiko, R., Mori, K., Fujita, N., Imachi, H., Takai, K., 2011. Genome sequence of a mesophilic hydrogenotrophic methanogen Methanocella paludicola, the first cultivated representative of the order Methanocellales. PloS One 6 (7). https://doi.org/10.1371/journal.pone.0022898 e22898–e22898.
Sampedro, I., Parales, R.E., Krell, T., Hill, J.E., 2015. Pseudomonas chemotaxis. FEMS Microbiol. Rev. 39 (1), 17–46. https://doi.org/10.1111/1574-6976.12081.
Semenec, L., Laloo, A.E., Schulz, B.L., Vergara, I.A., Bond, P.L., Franks, A.E., 2018. Deciphering the electric code of Geobacter sulfurreducens in cocultures with Pseudomonas aeruginosa via SWATH-MS proteomics. Bioelectrochemistry 119, 150–160. https://doi.org/10.1016/j.bioelechem.2017.09.013.
Sharma, M., Nandy, A., Taylor, N., Venkatesan, S.V., Ozhukil Kollath, V., Karan, K., Thangadurai, V., Tsesmetzis, N., Gieg, L.M., 2020. Bioelectrochemical remediation of phenanthrene in a microbial fuel cell using an anaerobic consortium enriched from a hydrocarbon-contaminated site. J. Hazard. Mater. 389, 121845 https://doi.org/10.1016/j.jhazmat.2019.121845.
Singh, N.K., Choudhary, S., 2021. Bacterial and archaeal diversity in oil fields and reservoirs and their potential role in hydrocarbon recovery and bioprospecting. Environ. Sci. Pollut. Res. Int. https://doi.org/10.1007/s11356-020-11705-z.
Sookhak Lari, K., Davis, G.B., Rayner, J.L., 2021. Towards a digital twin for characterising natural source zone depletion: a feasibility study based on the Bemidji site. Water Res. https://doi.org/10.1016/j.watres.2021.117853.
Sookhak Lari, K., Davis, G.B., Rayner, J.L., Bastow, T.P., Puzon, G.J., 2019. Natural source zone depletion of LNAPL: a critical review supporting modelling approaches. Water Res. 157, 630–646. https://doi.org/10.1016/j.watres.2019.04.001.
Sookhak Lari, K., Johnston, C.D., Rayner, J.L., Davis, G.B., 2018. Field-scale multi-phase LNAPL remediation: validating a new computational framework against sequential field pilot trials. J. Hazard. Mater. 345, 87–96. https://doi.org/10.1016/j.jhazmat.2017.11.006.
Sookhak Lari, K., Rayner, J.L., Davis, G.B., Johnston, C.D., 2020. LNAPL recovery endpoints: lessons learnt through modeling, experiments, and field trials. Groundw. Monit. Remediat. 40 (3), 21–29. https://doi.org/10.1111/gwmr.12400.
Stanton, M.M., Park, B.W., Miguel-López, A., Ma, X., Sitti, M., Sánchez, S., 2017. Biohybrid microtube swimmers driven by single captured bacteria. Small 13 (19). https://doi.org/10.1002/smll.201603679.
Sulimov, A.D., Kozhina, I.N., Trakhtenberg D. M, D.M., 1965. The production of naphthalene from petroleum crude. Chem. Technol. Fuels Oils 1 (1), 20–24.
Sungthong, R., van West, P., Heyman, F., Jensen, D.F., Ortega-Calvo, J.J., 2016. Mobilization of pollutant-degrading bacteria by eukaryotic zoospores. Environ. Sci. Technol. 50 (14), 7633–7640. https://doi.org/10.1021/acs.est.6b00994.
Tan, B., Jane Fowler, S., Laban, N.A., Dong, X., Sensen, C.W., Foght, J., Gieg, L.M., 2015. Comparative analysis of metagenomes from three methanogenic hydrocarbon-degrading enrichment cultures with 41 environmental samples. ISME J. 9 (9), 2028–2045. https://doi.org/10.1038/ismej.2015.22.
Tischer, K., Kleinsteuber, S., Schleinitz, K.M., Fetzer, I., Spott, O., Stange, F., Lohse, U., Franz, J., Neumann, F., Gerling, S., Schmidt, C., Hasselwander, E., Harms, H., Wendeberg, A., 2013. Microbial communities along biogeochemical gradients in a hydrocarbon-contaminated aquifer. Environ. Microbiol. 15 (9), 2603–2615. https://doi.org/10.1111/1462-2920.12168.
Venables, W.N., Ripley, B.D., 2002. Modern Applied Statistics with S, Fourth ed. Springer, New York. ISBN 0-387-95457-0. ⟨https://www.stats.ox.ac.uk/pub/MASS4/⟩.
Wang, X., Long, T., Ford, R.M., 2012. Bacterial chemotaxis toward a NAPL source within a pore-scale microfluidic chamber. Biotechnol. Bioeng. 109 (7), 1622–1628. https://doi.org/10.1002/bit.24437.
Wang, Y.-H., Huang, Z., Liu, S.-J., 2019. Chemotaxis towards aromatic compounds: insights from comamonas testosteroni. Int. J. Mol. Sci. 20 (11), 2701. https://doi.org/10.3390/ijms20112701.
Wawrik, B., Marks, C.R., Davidova, I.A., McInerney, M.J., Pruitt, S., Duncan, K.E., Suflita, J.M., Callaghan, A.V., 2016. Methanogenic paraffin degradation proceeds via alkane addition to fumarate by 'Smithella' spp. mediated by a syntrophic coupling with hydrogenotrophic methanogens. Environ. Microbiol. 18 (8), 2604–2619. https://doi.org/10.1111/1462-2920.13374.
Wiedemeier, T.H., Rifai, H.S., Newell, C.J., Wilson, J.T., 1999. Natural Attenuation of Fuels and Chlorinated Solvents in the Subsurface. John Wiley and Sons, Inc, New York.
Zhang, D., He, Y., Wang, Y., Wang, H., Wu, L., Aries, E., Huang, W.E., 2012. Whole-cell bacterial bioreporter for actively searching and sensing of alkanes and oil spills. Microb. Biotechnol. 5 (1), 87–97. https://doi.org/10.1111/j.1751-7915.2011.00301.x.
Yilmaz, P., Parfrey, L.W., Yarza, P., Gerken, J., Pruesse, E., Quast, C., Schweer, T., Peplies, J., Ludwig, W., Glöckner, F.O., 2014. The SILVA and "All-species Living Tree Project (LTP)" taxonomic frameworks. Nucleic Acids Res. 42 (D1), D643–D648. https://doi.org/10.1093/nar/gkt1209.
Zhang, L., Guo, B., Mou, A., Li, R., Liu, Y., 2020. Blackwater biomethane recovery using a thermophilic upflow anaerobic sludge blanket reactor: impacts of effluent recirculation on reactor performance. J. Environ. Manag. 274, 111157.
Zhang, T., Tremblay, P.L., Chaurasia, A.K., Smith, J.A., Bain, T.S., Lovley, D.R., 2014. Identification of genes specifically required for the anaerobic metabolism of benzene in Geobacter metallireducens. Front. Microbiol. 5, 245. https://doi.org/10.3389/fmicb.2014.00245.
Zhuang, L., Tang, Z., Ma, J., Yu, Z., Wang, Y., Tang, J., 2019. Enhanced anaerobic biodegradation of benzoate under sulfate-reducing conditions with conductive iron-oxides in sediment of Pearl River Estuary. Front. Microbiol. 10, 374. https://doi.org/10.3389/fmicb.2019.00374. –374.

Supporting Information

The role of predicted chemotactic and hydrocarbon degrading taxa in natural source zone depletion at a legacy petroleum hydrocarbon site

Cameron W. M. Murphy[a,b], Greg B. Davis[b], John L. Rayner[b], Tom Walsh[c], Trevor P. Bastow[b], Adrian P. Butler[a], Geoffrey J. Puzon[b*], Matthew J. Morgan[c]

[a]*Environmental and Water Resources Section, Department of Civil and Environmental Engineering, Imperial College of Science, Technology and Medicine, Exhibition Road, London, United Kingdom*
[b]*Centre for Environment and Life Sciences, CSIRO Land and Water, Private Bag No 5, Wembley, WA 6913, Australia*
[c]*Black Mountain Laboratories, CSIRO Land and Water, Acton, P.O. Box 1700, Canberra, ACT 2601, Australia*

*Corresponding author: E-mail address: Geoffrey.Puzon@csiro.au

Fig. S1. Site metadata. Contains general information of site characteristics, including sample depth (m), contamination zone and section, concentrations of contaminants, as well as geochemical analysis of selected core samples. These were recorded as g/kg of wet weight TPH and mg/kg of wet weight LNAPLs, with a reporting threshold of 0.5 g/kg for TPH and 5 mg/kg for LNAPL.

(File available :https://www.sciencedirect.com/science/article/pii/S0304389422002709#sec0105)

Fig. S2. Alpha Diversity (pre-rarefaction curves). Pre-rarefaction alpha diversity curves of observed mean and mean Shannon diversity of all 108 biological samples pre-merging replicates.

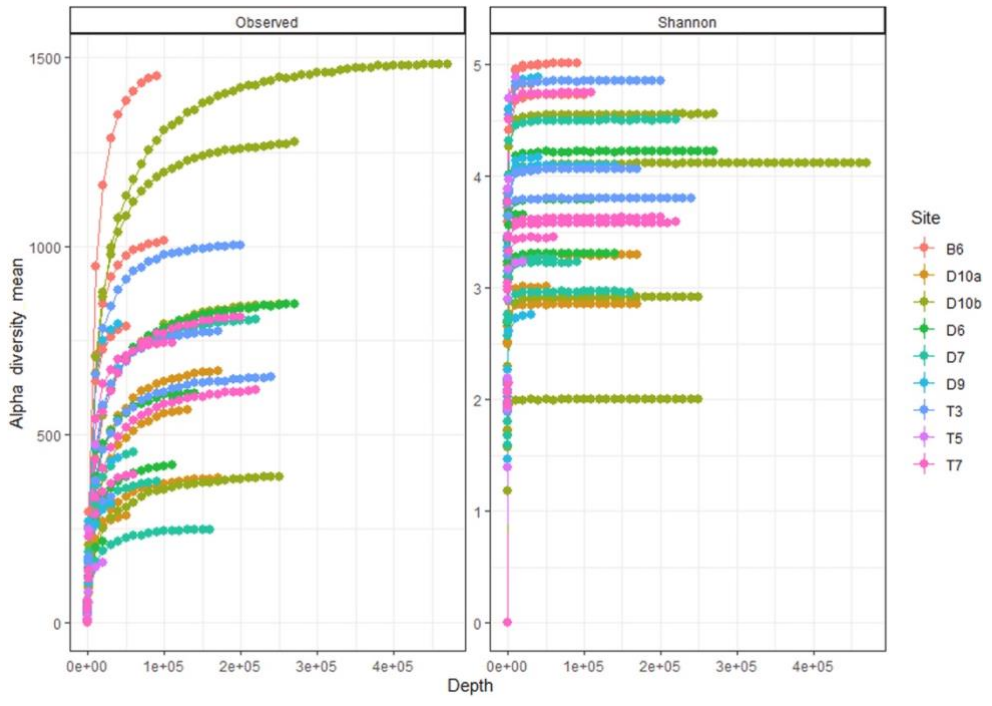


Fig S3. Alpha Diversity (post-rarefaction). Alpha diversity metrics (the number of OTUs and Chao1 estimator) were calculated from a single rarefaction at 10,000 reads per sample.

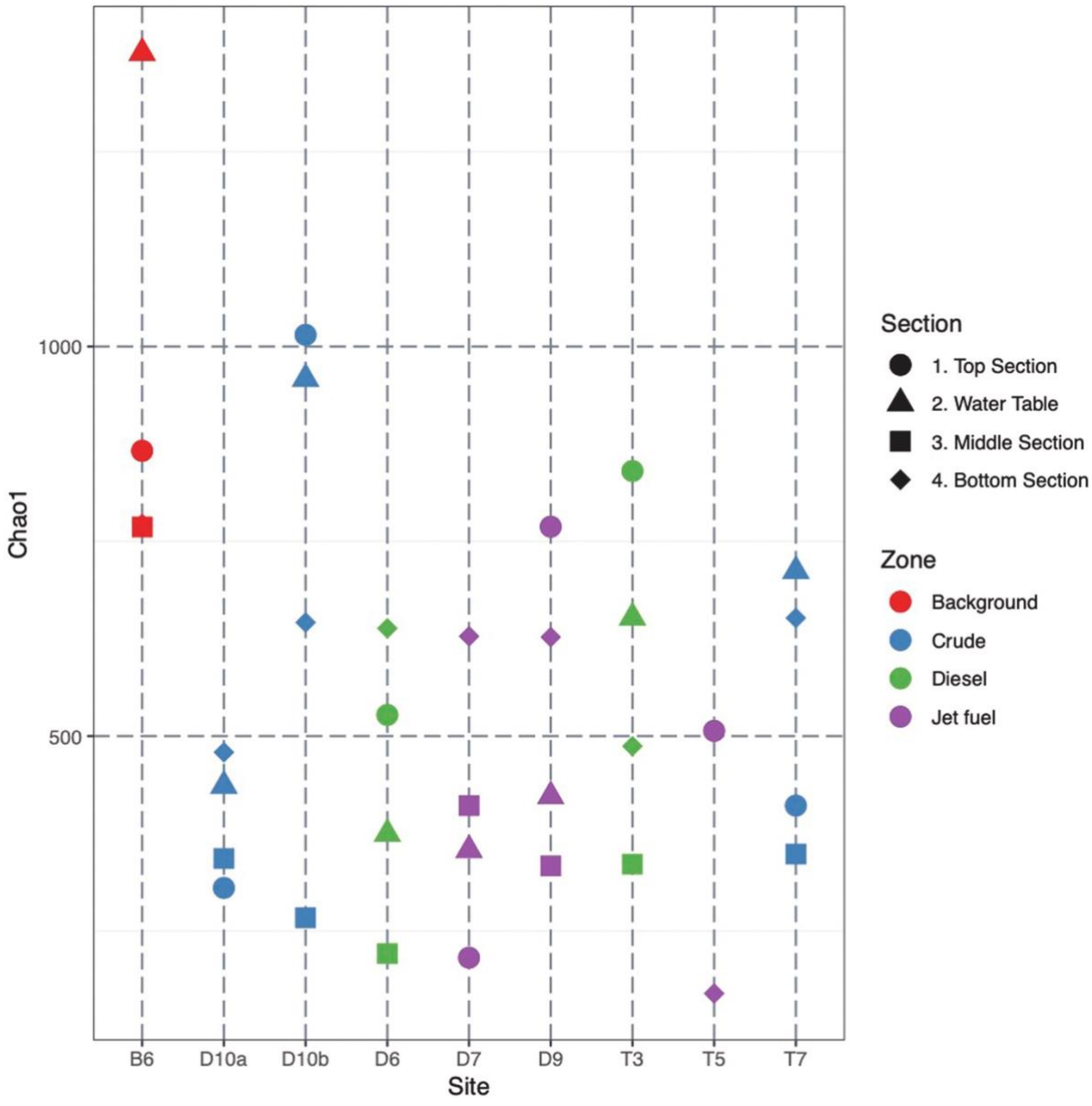
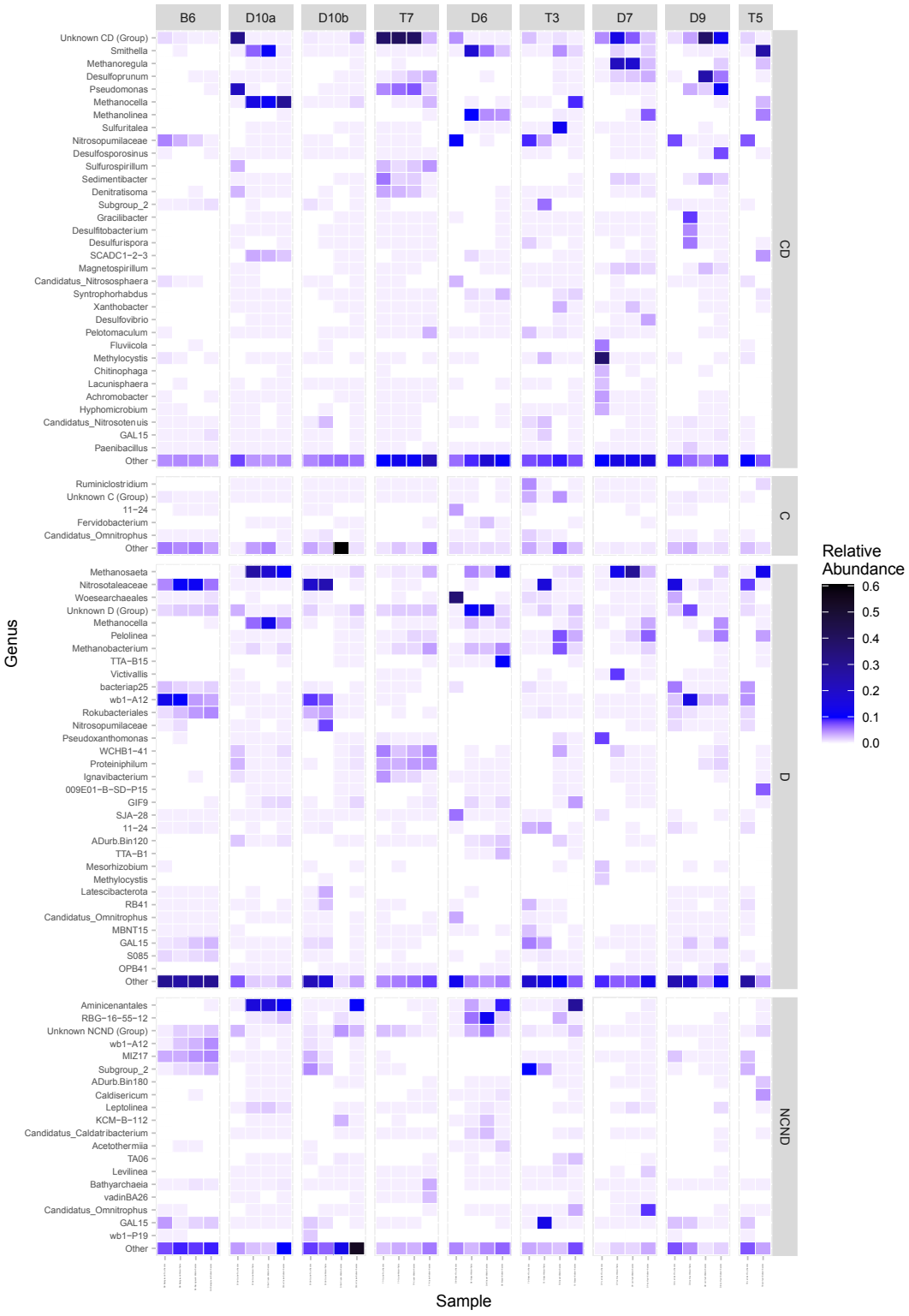


Fig S4. PICRUSt2 OTU Predictive metagenomic profiling. Contains data on each OTUs occurrence in a sample, specifically details on the functional pathways assigned to each OTU, their abundance and genomic function count (Douglas, 2019).

(File available :https://www.sciencedirect.com/science/article/pii/S0304389422002709#sec0105)

Fig S5 A), S5 B) S5 C). Community composition. 5a) Dataframe used to construct the family heatmap. 5b) Community composition heatmap of relative abundances arranged by similarity of distribution of the genera in their chemotactic and hydrocarbon degrading groups based on

predictive metagenomic profiling. The heatmap is faceted by group, with the purple shading representing their relative abundance. The Other taxa of each group contains microbes with a maximum relative abundance <2%; including uncultured taxa, with unknown taxa also being shown. The y-axis is arranged by similarity of distribution, with the x-axis being arranged by core section and contamination zone. 5c) Dataframe used to construct the heatmap composed by genera.

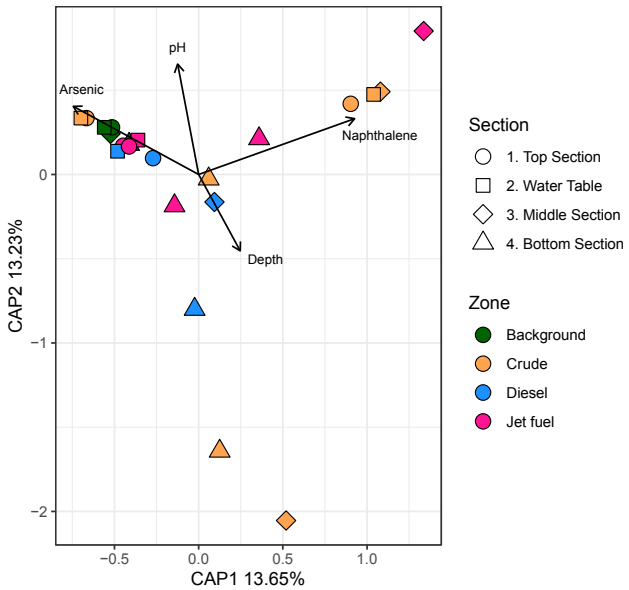


(Files available :https://www.sciencedirect.com/science/article/pii/S0304389422002709#sec0105)

Fig S6. Distance-based Bray-Curtis ANOVA. Analysis of various analysis (ANOVA) table of the significant variables, depth and naphthalene. The table displays the degrees of freedom (Df), Akaike information criterion (AIC), *F*-statistic along with the p-value and associated significance codes.

Analysis of variance analysis (ANOVA)				
Variables	Df	AIC	F	Pr(>F)
Depth	1	87.54	4.28	0.005**
Naphthalene	1	87.22	2.19	0.005**
Significance. codes: 0 '***' 0.001 '**' 0.01 '*' 0.05 '.' 0.1 ' ' 1				

Fig. S7. db-RDA analysis of subset of samples for which more extensive geochemical analysis was available. A db-RDA of samples and significant variables ($p < 0.05$) following step-wise model selection. Naphthalene, depth, pH and arsenic are the significant variables, with the length of the arrows gauging relative significance of each variable, the longer the arrow the greater the influence the variable has. The Background samples are green, Crude Oil is orange, Diesel Fuel is blue and Jet Fuel is pink, with core sections through the water table being illustrated by shapes, and the different line types showing the differences between the cores. Circles represent the Top section, squares represent the Water Table section, diamonds represent the Middle section and triangles represent the Bottom section, line-types link core samples.



Supporting Information (thesis)

Fig. S8. Taxonomy functional groupings. Contains data on OTU taxonomic assignment using Silva 138 515F/806R database (SILVA 138 SSU, 2019) and chemotactic and hydrocarbon group assignment, as well as db-RDA results for each OTU.

(File available :https://www.sciencedirect.com/science/article/pii/S0304389422002709#sec0105)

Data. S9. Gene deletion data. Contains data on the deletion of the fliM gene in *P. putida* F1.

(File: https://drive.google.com/file/d/17zcJwZPG-gmHStSKp0Vq588n95DbGSOr/view?usp=sharing)

Data. S10. Raw perimeter data. Contains the raw perimeter data.

(File: https://drive.google.com/file/d/17zcJwZPG-gmHStSKp0Vq588n95DbGSOr/view?usp=sharing)

Data. S11. Normalised fluorescent radial intensity profile data. Contains the intensity profiles data; radius in (cm) & intensity in (a.u.).

(File: https://drive.google.com/file/d/17zcJwZPG-gmHStSKp0Vq588n95DbGSOr/view?usp=sharing)

Data. S12. cheA primers. Contains on primers for the cheA mutation.

(File: https://drive.google.com/file/d/17zcJwZPG-gmHStSKp0Vq588n95DbGSOr/view?usp=sharing)